The Pennsylvania State University

The Graduate School

Eberly College of Science

PROBING STRUCTURE, MECHANISM, AND CONTROL OF OUTCOME IN METALLOENZYMES BY ADVANCED EPR AND X-RAY SPECTROSCOPIES

A Dissertation in

Chemistry

by

Ryan J. Martinie

Submitted in Partial Fulfillment

of the Requirements

for the Degree of

Doctor of Philosophy

December 2018

The dissertation of Ryan J. Martinie was reviewed and approved* by the following:

Joseph Martin Bollinger, Jr.
Professor of Chemistry and of Biochemistry and Molecular Biology
Dissertation Co-Advisor
Co-Chair of Committee

Carsten Krebs
Professor of Chemistry and of Biochemistry and Molecular Biology
Dissertation Co-Advisor
Co-Chair of Committee

Squire J. Booker
Howard Hughes Medical Investigator
Professor of Chemistry and of Biochemistry and Molecular Biology
Eberly Distinguished Chair in Science

Alexey Silakov
Assistant Professor of Chemistry

Amie K. Boal
Assistant Professor of Chemistry and of Biochemistry and Molecular Biology

Benjamin D. Allen
Assistant Research Professor of Biochemistry and Molecular Biology

Thomas E. Mallouk
Evan Pugh University Professor of Chemistry, Biochemistry and Molecular Biology, Physics, and Engineering Science and Mechanics
Head of the Chemistry Department

*Signatures are on file in the Graduate School.

Abstract

Metalloenzymes catalyze a broad range of nature's most challenging reactions, including C-H bond activation, nitrogen fixation, and water oxidation. My doctoral dissertation has centered around using spectroscopic tools to interrogate local structure in metalloenzyme active sites and relating this information to mechanism and function. The two primary variations on this central theme involve the ribonucleotide reductases (RNRs) and Fe(II)- and 2-oxoglutarate-dependent (Fe/2OG) oxygenases.

RNRs catalyze the reduction of ribonucleotides to deoxyribonucleotides, producing the precursors required for DNA replication and repair in organisms across all domains of life. These enzymes utilize a radical mechanism, which is initiated by the generation of a cysteine thiyl radical in the enzyme active site. In class I RNRs, this radical is generated by long-range electron transfer (ET) from the cysteine residue in the α subunit to a stable one-electron oxidant in the β subunit. The class I RNRs are further subdivided on the basis of the identity of the one-electron oxidant; class I-a and class I-b enzymes utilize a tyrosyl radical, generated in an activation reaction by a nearby dinuclear metal site. In the class I-c RNR from *Chlamydia trachomatis* (*Ct* RNR), the dinuclear metal site serves directly as the one-electron oxidant in the form of a heterodinuclear Mn(IV)/Fe(III) cofactor (**4/3**).

This **4/3** cofactor is generated when the Mn(II)/Fe(II) form of *Ct* RNR reacts with dioxygen to form a Mn(IV)/Fe(IV) (**4/4**) intermediate, which is reduced by an exogenous electron. This **4/4** intermediate is analogous to other high-valent metalloenzyme intermediates, such as the Fe(IV)/Fe(IV) intermediate "Q" in soluble methane monooxygenase, that have been subjected to intensive structural interrogation. In Appendix B, we examined **4/4** using extended x-ray absorption fine structure (EXAFS) analysis at both the Mn and Fe K-edges, which

indicated a Mn-Fe distance of 2.74-2.75 Å and a set of intensely scattering light atoms (C/N/O) at an average distance of 1.81 Å from Fe. Pulse electron paramagnetic resonance (EPR) studies on **4/4** revealed no detectable strong hyperfine couplings to exchangeable hydrons, though an exchangable hydron was detected at a position consistent with a terminal hydroxide ligand to Mn. Taken together, these observations are most consistent with a di-μ-oxo "diamond core" and a terminal hydroxide ligand to Mn(IV).

Although the agreement of these orthogonal spectroscopic techniques provides compelling evidence for such a di-μ-oxo core, this assignment relies on somewhat indirect observations (i.e. interatomic distances and a lack of strong, exchangable hyperfine couplings). In Appendix D, we sought to detect the μ-oxo ligands more directly using valence-to-core x-ray emission spectroscopy (VtC XES). In these spectra, μ-oxo ligands manifest as a distinct Kβ" peak in the Mn XES spectrum of **4/4**. Upon protonation of one of these -oxo bridges to form the μ-oxo/μ-hydroxo **4/3** state, this Kβ" intensity decreases. To our knowledge, these are the first VtC XES spectra to be reported for an enzyme intermediate, and allow for a more robust assignment of a di-μ-oxo **4/4** structure.

The Fe/2OG oxygenases are a diverse family of enzymes that catalyze a variety of reactions at unactivated carbon centers, including hydroxylation, halogenation, cyclization, desaturation, and stereoinversion. These enzymes generally bind iron via a $(His)_2(Glu/Asp)_1$ "facial triad" and couple the activation of oxygen to oxidative decarboxylation of 2OG to form an Fe(IV)-oxo (ferryl) intermediate. This ferryl intermediate initiates the reaction with the primary substrate by abstracting a hydrogen atom (H•). How different members of this family are able to direct the reactivity of this ferryl intermediate to the desired chemical outcome, avoiding undesired reactions, remains poorly understood.

The Fe/2OG halogenase SyrB2 chlorinates C4 of L-threonine (appended to the phosphopantetheine arm of the companion aminoacyl carrier protein SyrB1) in the biosynthesis of syringomycin E. The carboxylate ligand of the facial triad is replaced by alanine in the primary structure; the vacated coordination site is occupied by a chloride ligand. After the ferryl intermediate abstracts H• from C4, the resulting substrate radical attacks the *cis*-coordinated chlorine to produce the chlorinated product. In contrast, in Fe/2OG hydroxylases, the substrate radical attacks the hydroxide ligand generated by hydrogen atom abstraction (often termed "rebound"). Remarkably, SyrB2 deliberately sacrifices proficiency in H• abstraction in favor of chlorination selectivity. This led to the hypothesis that the partitioning between fast H• abstraction/hydroxylation and slow H• abstraction/chlorination is dictated by substrate positioning and that the non-native amino acid substrates 2-aminobutyric acid and norvaline are able to more closely approach the iron center. To investigate this hypothesis, in Appendix A I measured hyperfine couplings using hyperfine sublevel correlation (HYSCORE) spectroscopy between deuterium labeled substrates and an $\{FeNO\}^7$ complex in the SyrB2 active site. These experiments revealed that threonine is indeed held farther away from the iron center than other substrates. Moreover, the N_{NO}-Fe-$^2H_{Thr}$ angle is ~85°, placing the substrate in the plane *cis* to the Fe-N_{NO} bond, whereas other substrates exhibit more acute angles. If such a geometry is also present in the ferryl intermediate, the substrate radical would be primed to attack the *cis*-coordinated chloro ligand, rather than the hydroxo ligand.

These results underscored the importance of substrate positioning and *precise* local structural information in understanding the reactivity of Fe/2OG enzymes. To date, the best available structural information has come from 1) x-ray crystal structures of the reactant complex (i.e. with Fe(II), 2OG, and substrate bound) or 2) $\{FeNO\}^7$ complexes. Unfortunately, both these

states share dissimilarities with the ferryl intermediate (e.g. lower oxidation state of iron and 2OG bound instead of succinate) and might not reflect structural changes that occur upon ferryl formation. Because the stability and spin state of the ferryl intermediates generally preclude structural interrogation by either x-ray crystallography or pulse EPR spectroscopy, we sought a structural probe that would accurately mimic the ferryl intermediate and be amenable to both structural techniques. The vanadyl ion [V(IV)-oxo] is stable and EPR-active (d_1, S = 1/2); moreover, like the ferryl, it is a tetravalent first row transition metal with a single -oxo ligand. In Appendix C, we show using EPR and x-ray absorption spectroscopy that vanadyl binds to the model Fe/2OG enzyme TauD, along with succinate and substrate, adopting a distorted octahedral geometry nearly identical to that proposed for the ferryl intermediate. EXAFS analysis revealed M-oxo and M-L (first coordination sphere) distances of 1.60 and 2.05 Å, respectively, extremely similar to those of the ferryl intermediate in TauD (1.62 and 2.05 Å, respectively). For the L-arginine 3-hydroxylase, VioC, DFT calculations based on the x-ray crystal structure of the vanadyl complex correctly predict the ferryl Mössbauer parameters obtained in rapid-freeze-quench experiments. Moreover, the disposition of the substrate analog, L-homoarginine, relative to the vanadyl center in VioC is consistent with its altered reactivity (mixture of H• abstraction from C3 and C4), whereas its disposition in the corresponding x-ray crystal structure of the reactant complex is not. In the Fe/2OG halogenase, SyrB2, the vanadyl complex reproduces an effect previously observed only for the ferryl state: formation of a stable complex of SyrB2 with its protein substrate SyrB1. Taken together, these results suggest that the vanadyl ion is a faithful structural mimic of the ferryl intermediate in Fe/2OG enzymes suitable for characterization by x-ray crystalography and pulse EPR spectroscopy.

Based on results in the Fe/2OG halogenases, it has been suggested that an offline ferryl intermediate may be a general mechanism for reaction control in non-hydroxylating Fe/2OG enzymes. Hyoscyamine-6β-hydroxylase (H6H) provides an excellent system to test this hypothesis. H6H catalyzes installation of an epoxide across C6 and C7 of the tropane ring of the alkaloid hyoscyamine to furnish scopolamine. This reaction proceeds in two turnovers; the first turnover hydroxylates C6, whereas the second forms the epoxide in a 1,3-dehydrogenation/oxacyclization. In Chapter 2, we examine the mechanism of this second turnover and the structural factors that promote selectivity for expoxidation over a second hydroxylation. First, we utilize stopped-flow absorption spectrroscopy to observe a large ^{2}H-KIE on decay of the ferryl intermediate in the presence of 7-^{2}H-6-hydroxy-hyoscyamine; this result implicates H• abstraction from C7 in ferryl decay, ruling out H• abstraction from the newly-installed hydroxyl group, as has been proposed for a related Fe/2OG oxacyclase.

To test the hypothesis that the epoxidation turnover may proceed via an offline ferryl intermediate, we examined the disposition of the substrate relative to vanadyl in the presence of hyoscyamine and 6-hydroxy-hyoscyamine. In the H6H•vanadyl•succinate•hyscyamine complex, O_{oxo}-V-^{2}H angle and O_{oxo}-V/^{2}H-C angles of 40° and 25°, respectively, are observed for ^{2}H at C7. If H6H stabilizes an offline M(IV)-oxo in the epoxidation turnover, we would expect to observe less acute angles in the presence of 7-^{2}H-6-hydroxy-hyoscyamine (~53 and ~65°, respectively). Instead, nearly identical angles are observed. Given the sensitivity of these measurements to changes in the disposition of the C-H bond relative to V-O_{oxo} (or in this case, *vice versa*), these data provide no evidence for stabilization of an offline M(IV)-oxo in the presence of 6-hydroxy-hyoscyamine. We also examined the vanadyl complex of a variant of H6H (L290F) that catalyzes appreciable 6,7-dihydroxylation of hyoscyamine, along with diminution of the

epoxidized product; simulation of these data reveal a modest decrease in the V-^{2}H distance. Together, these observation suggests that the precise M-^{2}H distance, rather than wholesale offline rearrangement, is critical for efficient cyclization activity, and potentially other non-hydroxylation outcomes as well.

Table of Contents

List of Figures

Chapter 1

Chapter 2

Appendix A

Appendix B

Appendix C

Appendix D

List of Tables

Chapter 2.

Appendix A

Appendix B

Appendix C

Appendix D

Acknowledgements

I gratefully acknowledge that this thesis is the result of the efforts of many. Those who contributed to the experimental results are acknowledged in the appropriate chapter or appendix. Those who have contributed more indirectly, by enriching my life and time at Penn State, are acknowledged here. First and foremost, my wife Rachel, who has encouraged me in everything I've done, who has supported me in good times and bad. You make my life so rich. I also thank my parents, Randy and Cindy, who always nurtured my curiosity and have always supported me. Thank you to all my friends in State College and elsewhere for countless conversations, laughs, and meals. For always being willing to lend a listening ear, whether the topic is science or life, I especially thank Josiah Sinclair, David Witwer, and Dr. Nate Romero.

I also thank everyone on the third floor of the Chemistry building at Penn State, the current and former members of the Bollinger-Krebs, Boal, Booker, Silakov, and Green labs. You have made this a remarkable place to do science: one that is fun, helpful, and collaborative. I especially thank all the current and former members of the Bollinger-Krebs group, along with a few individuals in particular. I thank Prof. Wei-chen Chang, who trained me as a rotation student, taught me how to work with the SyrB2/SyrB1 system, and who was always ready with a joke and a laugh. Prof. Maria Pandelia, who taught me about spectroscopy and freeze-quench and who inspires me with her passion, intelligence, and kindness. Dr. Juan Pan, a great desk neighbor always ready with a smile or a conversation. Eli Wenger, a new graduate student, who has an easy laugh and puts up with my sarcasm. Dr. Beth Blasei, for a lot of lunchtime laughs and for putting up with my sleep-deprived beam-time personality with more grace than it probably deserved.

Most especially, I thank my good friend and coworker Dr. Chris Pollock. I am grateful for your appreciation of a properly-steeped cup of tea; for before-noon freeze quench; for early morning conversations in an otherwise dark, empty lab; for a lot of sarcasm and much laughter. In addition to these everyday things, Chris was the leader of the beam team, and like Beth had to put up with my sleep-deprived antics. Just as importantly, he taught me everything I know about x-ray spectroscopy; all the x-ray data reported here are a result, directly or indirectly, of Chris' influence. He has helped me tremendously in my growth as a spectroscopist and as a scientist.

I also thank Prof. Alexey Silakov, who contributed to this work in countless ways. When I first started in the lab, he was a postdoc down the hall; he trained me in the use of the pulse EPR spectrometer, how to analyze EPR data, and how to present it in a compelling way. Through it all, he was remarkably generous with his time, always willing to help me with problems small and large. His patience in teaching me about spins, tensors, and pulses was, particularly in retrospect, remarkable. As his role at Penn State has evolved, his willingness to teach and assist me has remained the same; he is has been an invaluable mentor to me scientifically, and his fingerprints are present in much of this work.

Finally, I thank my co-advisors Prof. Marty Bollinger and Prof. Carsten Krebs. They have created and fostered a remarkable environment for research in mechanistic bioinorganic chemistry. I thank them for giving me the opportunity to learn from them and other members of their group; it has been a remarkable privilege to spend my time trying to understand these enzymes. I thank Marty for many mentoring conversations, for always finding time to talk about the future and what's next. I also thank Marty for helping to develop my writing; it has been truly gratifying to work together on manuscripts, at least once we got around to working on them... In all seriousness, it has been so much fun to work with someone as intereted in grammar minutiae

as I am. The care you devote to the presentation of ideas inspires me and always pushes me towards my best writing. I am indebted to Carsten for many beers; over soccer, science, or otherwise. You foster an atmosphere here where people want to have fun and don't take themselves too seriously. I am also grateful for the times when Carsten pushed me to understand what I was doing more deeply, and for when he pushed me not to be satisfied with what I already knew or had already done. Thank you both, from the bottom of my heart; I owe so much of who I am today, as a scientist and otherwise, to the two of you.

Maybe the knowledge is too great and maybe men are growing too small. Maybe, kneeling down to atoms, they're becoming atom-sized in their souls. Maybe a specialist is only a coward, afraid to look out of his little cage. And think what any specialist misses -
the whole world over his fence.

- John Steinbeck

Chapter 1

Control of Diverse Reaction Outcomes in the Fe(II)- and 2-oxoglutarate-Dependent Oxygenases.

Acknowledgements

This introductory chapter was originally drafted in the form of a review article. This original draft was co-written by myself and Noah Dunham, a fellow graduate student in the Bollinger-Krebs group. In particular, sections 1.4-1.7 were largely written by Noah, with minor editorial input from myself. I am greatly indebted to Noah for his work on these sections. I also thank Marty Bollinger and Carsten Krebs, who were extensively involved in creating the original outline for this review/chapter, and who originally developed much of the intellectual foundation contained herein.

1.1 - Fe(II)- and 2-oxoglutarate-dependent oxygenases: diversity and function

Mononuclear iron-dependent oxygenases harness the oxidative power of molecular oxygen to carry out a diverse array of chemically challenging reactions in biological systems. These systems activate O_2 at an Fe(II) cofactor to form an Fe(IV)-oxo (ferryl) intermediate that can abstract a hydrogen atom (H•) or act as an electrophile to initiate a variety of transformations. One manifestation of this flexible strategy, employed by an important and diverse subset of iron-dependent oxygenases, couples the activation of O_2 to the oxidative decarboxylation of 2-oxoglutarate (2OG) to produce succinate and CO_2, along with the ferryl intermediate.[1–4] In the best characterized examples, including all characterized examples in humans, the ferryl intermediate carries out a hydroxylation reaction, generally at an unactivated, aliphatic carbon center. These hydroxylation reactions play crucial roles in human health, including collagen synthesis,[5] repair of DNA damage,[6,7] oxygen sensing,[8–10] iron homeostasis,[11] body mass homeostasis,[12] and control of transcription, differentiation, development and epigenetic inheritance.[13–17] Plants and microbes also employ these Fe(II)- and 2OG-dependent (Fe/2OG) enzymes for metabolism and regulation.[2,4] These organisms have leveraged the Fe/2OG platform for a variety of non-hydroxylation reactions, including olefin epoxidations,[18] aliphatic halogenations,[19,20] 1,2-dehydrogenations,[21,22] oxacycle-installing 1,3- and 1,5-dehydrogenations,[23–27] complex cyclic rearrangements,[28] endoperoxidation,[29,30] and a redox-neutral stereoinversion (Figure 1).[31] Many of these transformations are involved in the biosynthesis of pharmacologically-active compounds; a thorough understanding of the divergent mechanisms of these alternative biochemical transformations and the factors which direct a given enzyme toward the desired outcome has the potential to inform the design of bioinspired

catalysts, selective inhibition of medically relevant Fe/2OG enzymes, and the development and production of new natural product-based drug compounds.

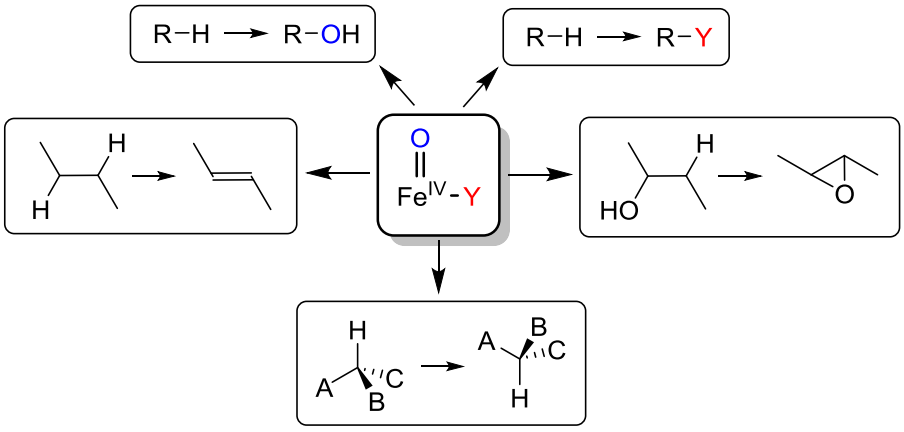

Figure 1. Chemical transformations catalyzed by Fe/2OG enzymes.

Herein, we summarize recent developments in understanding the mechanism of hydroxylation, as well as two alternative reactivities (halogenation and stereoinversion), in Fe/2OG enzymes. Next, we will examine two more alternative reactions (dehydrogenation and oxacyclization), reviewing mechanistic hypotheses and outlining methods by which these mechanisms might be elucidated. Finally, we propose a framework for reaction control of Fe/2OG reactivity, suggesting that avoiding hydroxylation by utilizing an "offline" ferryl is central to controlling the diversity of alternative Fe/2OG reactivity.

1.2 - Hydroxylation

As a result of their prominence in human health (*vide supra*), the Fe/2OG hydroxylases have been subject to prolonged inquiry and have served as models for the Fe/2OG family. The first comprehensive reaction mechanism for the Fe/2OG hydroxylases was proposed by

Hanauske-Abel and Günzler (sometimes referred to as the "HAG mechanism"), albeit on the basis of minimal experimental data.[32] Although initially speculative, this mechanism has largely been borne out by subsequent experimental validation.[4] The mononuclear, non-heme Fe(II) center is coordinated facially by a $(His)_2$,$(Glu/Asp)_1$ motif (Scheme 1), the so-called "facial triad",[33,34] with water ligands occupying three additional sites to form an octahedral geometry. Two of these water ligands are displaced by bidentate coordination of 2OG. Finally, extensive work by Solomon and coworkers has shown that addition of the primary substrate causes dissociation of the final water ligand to form a square pyramidal complex with an open coordination site available for oxygen addition (Scheme 1).[1] Reaction with oxygen putatively yields a ferric-superoxide complex [$\{FeOO\}^8$], which attacks C2 of 2OG; this attack initiates poorly understood chemistry which includes oxidative decarboxylation of 2OG and O-O bond cleavage, producing CO_2 and an Fe(IV)-oxo (ferryl) complex coordinated by succinate (Scheme 1). The ferryl then abstracts a hydrogen atom (H•) from the target position of the substrate, producing a carbon-based substrate radical and a ferric hydroxide. Finally, the substrate radical attacks the coordinated hydroxide, yielding the hydroxylated product and a ferrous complex (via formal homolysis of the Fe-O(H) bond and radical recombination of the substrate radical with •OH). Co-product dissociation returns the cycle to its origin. Prior to work in our laboratory, and that of Hausinger and coworkers, on taurine:2OG dioxygenase (TauD), none of the steps following oxygen addition had been validated.

Scheme 1. Mechanism of hydroxylation, catalyzed by Fe/2OG oxygenases. R' = $CH_2CH_2COO^-$.

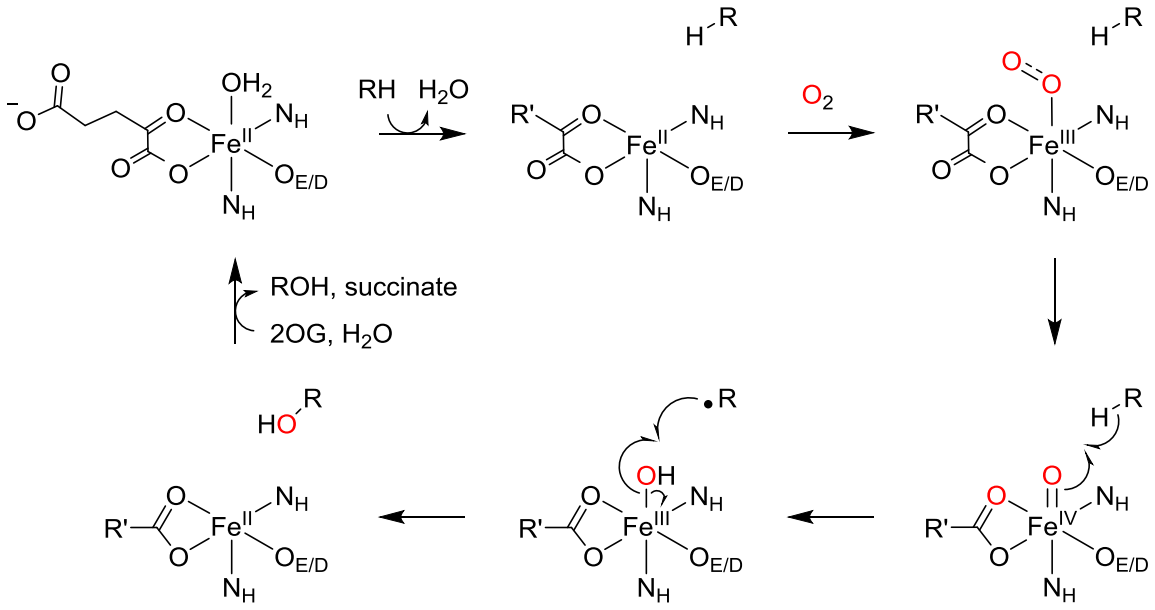

1.2.1 - Evidence for intermediates in the reaction cycle of TauD

Upon rapid mixing of the TauD•Fe(II)•2OG•taurine complex (sometimes referred to as the quaternary complex) with oxygen-saturated buffer, the accumulation of two intermediates is apparent when monitored by stopped-flow absorption spectroscopy (SF-abs).[35] The first intermediate absorbs at 320 nm, whereas the second has no appreciable absorbance in the UV/visible region and is thus distinguished by the absence of the 520 nm charge transfer band which characterizes the TauD•Fe(II)•2OG complex. The formation of the first intermediate, termed **J**, is first order with respect to the concentration of oxygen and the quaternary complex (second order rate constant 1.5 x 10^5 $M^{-1}s^{-1}$ at 5 °C),[35,36] indicating that it is that it is the first intermediate to accumulate following oxygen addition.

*1.2.2 - Mössbauer characterization of **J** reveals a high spin Fe(IV)*

Insight into the chemical nature of intermediate **J** was obtained via rapid-freeze-quench Mössbauer spectroscopy. Mössbauer spectroscopy is a powerful tool for the investigation of Fe/2OG enzymes, as all of the proposed intermediates in the HAG mechanism have integer spin ground states (S = 0, 1, 2, etc.) and are therefore readily detected and quantified.[37,38] Upon rapid mixing with oxygen-saturated buffer, the starting ferrous complex is converted to a new species which exhibits a quadrupole doublet in the Mössbauer spectrum with an isomer shift (δ) of 0.30 mm/s and a quadrupole splitting (ΔE_q) of 0.88 mm/s.[35] By comparing the intensity of this doublet after differing reaction times, it is clear that this species is associated with **J** in the SF-abs experiments. Moreover, the parameters of the doublet, in particular the low isomer shift, are consistent with an Fe(IV) oxidation state. This was confirmed by cryoreduction experiments in which disappearance of the putative Fe(IV) doublet was accompanied by development of broad, paramagnetically-split features in the Mössbauer spectrum and an S = 5/2 signal in the electron paramagnetic resonance (EPR) spectrum, both indicative of conversion to Fe(III) upon reduction.[35] Additional insight was obtained by examination of Mössbauer spectra collected at high magnetic fields, which indicated that the Fe(IV) center is in the high-spin (S = 2) state.[35] An intermediate with similar features, including an absorbance feature at ~320 nm in SF-abs and Mössbauer parameters indicative of a high-spin Fe(IV) species, has also been observed in the viral prolyl-4-hydroxylase (P4H), suggesting that such an intermediate is a general strategy in the Fe/2OG hydroxylases.[39]

1.2.3 - The Fe(IV) intermediate abstracts a hydrogen atom from the substrate

Comparison of the decay kinetics of **J** in the presence of taurine and 1,1-$[^2H]_2$-taurine indicate that this step involves abstraction of H• from the C1 position of taurine.[40] Specifically,

the 320-nm feature in SF-abs experiments decays much more slowly in the presence of 1,1-[^{2}H]$_2$-taurine than in the presence of taurine with natural abundance of all isotopes; the ratio of the observed decay rates ($k_{obs,H}/k_{obs,D}$) is 37 at 5 °C, a lower limit for the intrinsic deuterium kinetic isotope effect (KIE) associated with C-H/D cleavage. Substantially higher than the classical limit, this observation implicates tunneling in the decay of **J**, a hallmark of H• abstraction. A more rigorous analysis recognizes that the rate of decay of **J** is not identical to the rate of H• abstraction, but rather represents the sum of the rate of H• abstraction and the rate of unproductive decay. Measuring the proportion of productive ferryl decay events in the presence of taurine and 1,1-[^{2}H]$_2$-taurine to better approximate the intrinsic H• abstraction rates yields an estimate of ~50 for the KIE.[36]

1.2.4 - The Fe(IV) intermediate possesses an -oxo moiety

The above evidence indicates that **J** is an Fe(IV) complex which cleaves the C-H bond of taurine. In the HAG mechanism, the C-H cleaving complex was suggested to be a ferryl (Fe(IV)-oxo) intermediate. This hypothesis was confirmed by complementary spectroscopic results. First, Hausinger, Proshlyakov, and coworkers detected an oxygen-isotope-sensitive band (821 cm^{-1} with $^{16}O_2$; 789 cm^{-1} with $^{18}O_2$) in continuous-flow resonance Raman (CF-rR) experiments following rapid mixing of the TauD quaternary complex with O_2-saturated buffer for 0.22 s at -38 °C, consistent with an Fe(IV)-oxo moiety.[41] In addition, X-ray absorption spectroscopy experiments conducted with samples enriched in **J** exhibited an Fe *K*-edge shifted higher in energy relative to the Fe(II) quaternary complex, as expected for a high-valent intermediate.[42] More importantly, analysis of the X-ray absorption fine structure (EXAFS) region indicated the presence of a light atom (C/N/O) scatterer at 1.62 Å,[42] consistent with Fe-O_{oxo} distances

observed in inorganic ferryl complexes. Together, these experiments provide strong evidence that the C-H cleaving intermediate in TauD is an Fe(IV)-oxo (ferryl) complex.

1.2.5 - Intermediates preceding ferryl formation

The chemical steps which precede ferryl formation in Fe/2OG enzymes remain comparatively enigmatic. However, computational studies have suggested that oxygen attack at C2 by the putative Fe(III)-superoxo intermediate is followed by C1-C2 cleavage (releasing CO_2), producing an Fe(II)-peroxysuccinate complex.[43,44] Recent *in crystallo* reaction of the Fe/2OG hydroxylase VioC produced a number of crystals exhibiting density consistent with formation of this species, the first experimental evidence concerning the mechanistic steps preceding ferryl formation.[45] This observation was particularly striking, given the low barrier predicted for decay of this intermediate, suggesting that constraints arising from reaction *in crystallo* may play a role in stabilizing the complex.

1.2.6 - Intermediates following C-H cleavage

As noted above, *two* intermediates accumulate upon mixing the TauD quaternary complex with oxygen-saturated buffer, the first of which is **J**, the C-H cleaving ferryl complex. The second intermediate was assigned as possessing an Fe(II) oxidation state on the basis of freeze-quench Mössbauer experiments.[36] Moreover, the isomer shift and quadrupole splitting of this ferrous complex are distinct from those of other ferrous complexes observed prior to O_2 binding to TauD, suggesting that the second intermediate is, in fact, a product complex. The decay of this intermediate is kinetically limited by product release; correspondingly, this rate is dependent on solvent viscosity, presumably because greater solvent viscosity slows down protein rearrangements required for product dissociation.[36] The steps following C-H cleavage have also been probed by continuous-flow rR spectroscopy.[46,47] These experiments detected two

intermediates which followed the ferryl, which were assigned as an Fe(III)-oxo followed by an Fe(II)-alkoxo (product) complex. Mechanistically, these assignments would imply that the oxygen transfer from the iron to the substrate does not occur by the canonical "rebound", but rather by deprotonation of the Fe(III)-OH (formed via H• abstraction by the ferryl) to form the putative Fe(III)-oxo. This complex then decays by the substrate radical attacking the coordinated -oxo to form the putative Fe(II)-alkoxide product complex. Freeze-quench Mössbauer experiments on TauD have shown no evidence for significant accumulation of an Fe(III)-oxo,[35] though the lower temperature of the reaction in the CF-rR might account for this discrepancy. The assignment of an Fe(II)-alkoxide product complex is bolstered by the observation of such complexes *in crystallo*.[45]

1.3 - Halogenation

Halogens are present in a wide variety of natural products and are often essential to the biological and clinical efficacy of these compounds.[48] Members of the Fe/2OG halogenase subfamily are competent to install carbon-halogen bonds at unactivated carbon centers en route to these halogenated natural products. The first examples of this subfamily were characterized by Walsh and coworkers and are associated with non-ribosomal polypeptide synthetases (NRPS), functioning as tailoring enzymes to modify substrates presented by a corresponding aminoacyl carrier protein. Related fatty acyl halogenases have also been described for which the carrier protein is present as a domain within the halogenase polypeptide.[49,50] Finally, the Fe/2OG halogenase, WelO5, acts on a freestanding, small-molecule substrate in welwitindolinone biosynthesis and has recently been characterized.[51,52]

1.3.1 - The Fe/2OG halogenase SyrB2 lacks the acidic residue of the facial triad

The first Fe/2OG halogenase to be characterized was SyrB2, a carrier-protein-dependent halogenase involved in the synthesis of the phytotoxin syringomycin.[19] SyrB2 catalyzes the chlorination of C4 of L-threonine, appended via a thioester linkage to the phosphopantethine arm of the companion aminoacyl carrier protein SyrB1 (such aminoacyl constructs will be designated by the bolded three letter code of the amino acid, e.g. **Thr**). SyrB1 contains an adenylation domain which activates threonine for attachment to the phosphopantetheine arm of the thiolation domain responsible for delivery to SyrB2. Soon after its discovery, the three-dimensional structure of SyrB2 was solved in the presence of iron and 2OG (though lacking SyrB1) using X-ray crystallographic methods.[53] Remarkably, the structure revealed that the carboxylate ligand of the canonical "facial triad" of iron ligands is absent in SyrB2; the sequence position is occupied by a non-coordinating alanine residue. The substitution results in an open coordination site which is occupied by chlorine. This structural insight led to the proposal of a halogenation mechanism in which a *cis*-haloferryl intermediate forms, in direct analogy to the Fe/2OG hydroxylases (Scheme 2). Following H• abstraction, the mechanism diverges from that of the hydroxylases, as the substrate radical attacks the *cis*-coordinated chloride (Scheme 2, blue arrows), instead of the hydroxide ligand (Scheme 2, red arrows). This mechanism is directly analogous to that of the second cyclization step in isopenicillin-N-synthase (IPNS), originally proposed by Baldwin and coworkers and recently experimentally validated in our group, in which a ferryl intermediate abstracts a hydrogen atom and the resulting substrate radical attacks a *cis*-coordinated heteroatom (although in the case of IPNS, this coordinated heteroatom is substrate derived, making the overall reaction a cyclization).[54]

Scheme 2. Mechanism of halogenation catalyzed by Fe/2OG enzymes. R' = $CH_2CH_2COO^-$. Blue arrows in the radical attack step designate chlorination, whereas red arrows designate hydroxylation.

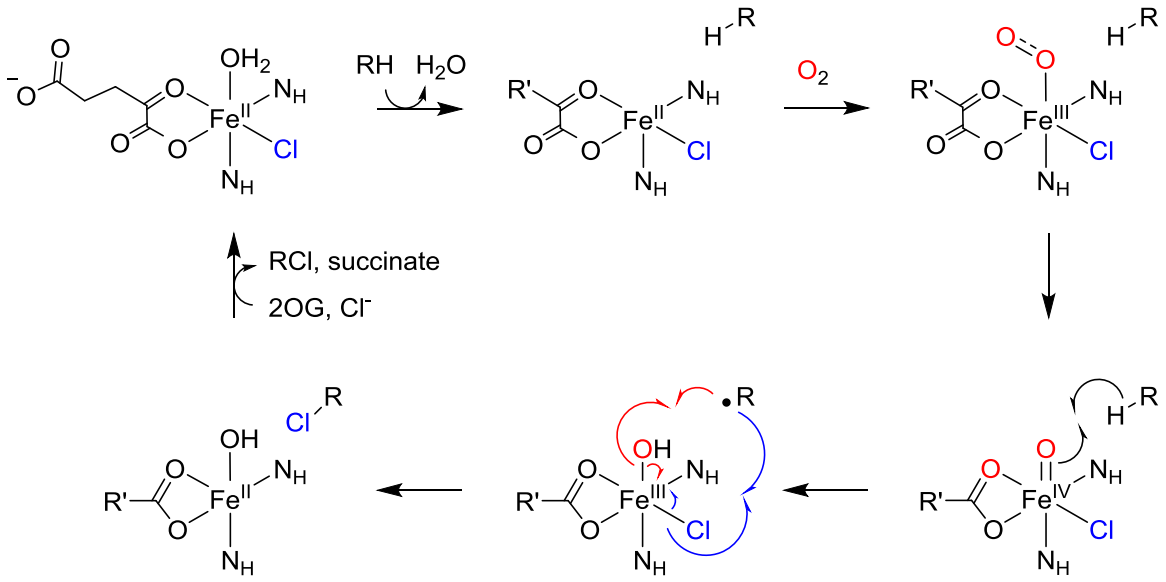

1.3.2 - Fe/2OG halogenation is mediated by a ferryl intermediate

Using the methods developed in the study of the Fe/2OG hydroxylases, the hypothesized ferryl intermediate was detected in the Fe/2OG halogenase SyrB2 and its close relative, CytC3. When the halogenase•Fe(II)•Cl^-•2OG•substrate complex is mixed with O_2-saturated buffer, an intermediate which absorbs at 320 nm develops, in direct analogy to observations in TauD and P4H.[55,56] Moreover, freeze-quench Mössbauer experiments revealed the presence of *two* quadrupole doublets with isomer shifts similar to those observed in TauD and P4H (0.25-0.30 mm/s), which accumulate and decay in association with the 320 nm feature.[55,56] Mössbauer spectra collected in the presence of high magnetic fields again reveal a high-spin (S = 2) ground state. EXAFS analysis of samples enriched in the Fe(IV) intermediate(s) revealed a light atom

(C/N/O) scatterer at a short distance (1.61 and 1.66 Å for CytC3 and SyrB2, respectively), attributed to an oxo group.[56,57] Examining the kinetics of the Fe(IV)-associated features showed that the decay of this intermediate is slowed 20-fold when the substrate is labeled with deuterium, indicating that the intermediate is implicated in H• abstraction. Notably, the absolute rates of decay are significantly (100-1000-fold) slower than those observed in the Fe/2OG hydroxylases.[4] The coincident accumulation and decay of the two quadrupole doublets indicates that both are present in a single kinetic state, suggesting that they are in rapid equilibrium. Although a number of explanations have been proposed, including an altered disposition of the oxo group or differential hydrogen bonding interactions, the chemical rationale for the two doublets remains an intriguing puzzle.[4] Overall however, the direct detection of a ferryl intermediate(s) in two Fe/2OG halogenases provides strong corroborating evidence for the proposed halogenation mechanism (Scheme 2).

1.3.3 - Controlling hydroxylation in Fe/2OG halogenases

The corroboration of the *cis*-ligand-transfer mechanism raised another striking question. Both the hydroxide ligand and the chloride ligand are coordinated to the iron following H• abstraction and could, theoretically, be attacked by the substrate radical, yielding a hydroxylated (Scheme 2, red arrows) or chlorinated product (blue arrows), respectively. How the enzyme differentiates between these two possibilities is thus a central mechanistic question. This question has been the subject of a number of computational investigations, with corresponding mechanistic proposals for reaction control.[58–60] Proposals included protonation of the hydroxide ligand to form water and discourage radical attack, capture of the hydroxide by CO_2 released in the oxidative decarboxylation of 2OG, and differing Fe-ligand bond strengths.

The first experimental clues to this conundrum came from further investigation of the reactivity of SyrB2. Contrary to previous reports, the adenylation domain of SyrB1 was found to be strikingly promiscuous, attaching a variety of aliphatic amino acids to the thiolation domain.[56] Surprisingly, when presented to SyrB2 as alternative substrates, all amino acids which underwent attachment to SyrB1 were able to trigger ferryl formation in SyrB2.[56] Substrate triggering is the phenomenon, observed for all Fe/2OG enzymes examined to date, of significant increase in rate of reaction with O_2 in the presence of substrate, compared to its absence.[4] This phenomenon can be rationalized by the work of Solomon and coworkers, which has shown that prior to substrate binding the ferrous center remains six-coordinate, unable to react with O_2.[1] The magnitude of this triggering effect is larger in SyrB2 than in any other Fe/2OG enzyme tested, allowing significant modification of the substrate without adverse consequences on reactivity.[56] Intriguingly, modification of the amino acid substrate resulted in changes in chemical outcome. Some were chlorinated, as in the native reaction; others displayed hydroxylation, or a mixture of the two outcomes.[56,61] Finally, in the presence of **Ala** and **Cpg** (L-cyclopropylglycinyl-*S*-SyrB1), SyrB2 generates the ferryl intermediate, but this intermediate displays unprecendented stability, with half-lives for decay of 30 and 110 min at 4°C, respectively.[56]

Comparing the reactivity of three substrates specifically provided an important set of clues in unraveling the halogenation selectivity of SyrB2: **Thr**, L-2-aminobutyryl-*S*-SyrB1 (**Aba**), and L-norvalinyl-*S*-SyrB1 (**Nva**). **Thr** is almost exclusively chlorinated, although some (<5%) hydroxylated product was observed,[61] contrary to previous reports.[19,20] As noted above, H• abstraction from **Thr** occurs quite slowly compared to the rates observed in the Fe/2OG hydroxylases. **Aba**, on the other hand, yielded hydroxylated and chlorinated products in comparable yields. However, the decay of the ferryl intermediate was accelerated 10-fold in the

presence of **Aba** compared to **Thr**.[61] For an enzyme to process a non-native substrate that has not been in some way chemically activated at a greater rate than the native substrate was most striking. Moreover, the ferryl intermediate decays even more rapidly in the presence of **Nva**: 10-fold faster than in the presence of **Aba** and 130-fold faster than in the presence of **Thr**. Furthermore, **Nva** is exclusively hydroxylated. Overall, in this series, chlorination efficiency is *anti*-correlated with H• abstraction rate. These observations suggested that the native reaction with **Thr** relies on a programmed inefficiency in H• abstraction in order to facilitate efficient chlorination selectivity.[61]

In light of these observations, it was suggested that differential substrate positioning might be the factor controlling reaction selectivity in SyrB2. That is, the native substrate **Thr** is held far from the iron center, resulting in comparatively sluggish H• abstraction by the ferryl intermediate; however, in the subsequent step, a long distance would also discourage coupling of the carbon centered radical with the hydroxide ligand and resultant hydroxylation. In contrast, extending the substrate by a single methlyene unit (i.e. **Nva**) projects the target carbon farther into the active site, closer to the iron center, resulting in rapid and efficient H• abstraction, but correspondingly exclusive hydroxylation. Thus, SyrB2 trades efficiency of H• abstraction in favor of selectivity for chlorination in the subsequent step.[61] This conclusion was bolstered by the observation that redirecting **Nva** reactivity from C5 to C4 (by deuterium labeling hydrons at C5) resulted in a significant decrease in H• abstraction rate (relative to C5) and a mixture of chlorination and hydroxylation.

This substrate positioning hypothesis was investigated more directly by defining the positions of **Thr**, **Aba**, and **Nva** relative to $\{Fe\text{-}NO\}^7$ complexes, EPR-active analogs of the relevant reaction intermediates, in SyrB2 using deuterium hyperfine sublevel correlation

spectroscopy (^{2}H-HYSCORE) (**Appendix A**).[62] These studies indicated that the target position of **Thr** is indeed more distant (4.2 Å) from the iron than those of **Aba** and **Nva** (3.7 and 3.4 Å, respectively), in excellent correlation with the H• abstraction rates observed for these substrates.[62] Moreover, the N_{NO}-Fe-^{2}H angle for **Thr** was found to be nearly perpendicular (85°); if such an angle is representative of the analogous angle in the ferryl complex (O_{oxo}-Fe-H), it would place the target hydron nearly in the equatorial plane, potentially directly adjacent to the *cis*-coordinated chloride ligand, primed for facile transfer. In contrast, a smaller angle (65°) is observed for **Nva**.[62] This structural information, and its excellent correlation with the available reactivity data, substantiate the hypothesis that substrate positioning controls reaction selectivity in the Fe/2OG halogenases and suggests that both the distance and angle relative to the ferryl intermediate may be relevant.

Although the above studies showed that substrate positioning is essential to reaction control in the Fe/2OG halogenases, detailed information concerning how this delicate positioning is enforced remained unavailable (Figure 2). Structural characterization of the SyrB1•SyrB2 complex by X-ray crystallography has proven elusive; however, the discovery of the first carrier-protein-independent halogenase WelO5, provided the opportunity to examine a system with a more crystallographically-tractable substrate. Indeed, the structure of WelO5 in complex with its substrate, 12-*epi*-fischerindole U, revealed that the halogenated carbon is positioned directly above the iron center, in similar position to substrates of Fe/2OG hydroxylases (Figure 2A and 2C).[52] Such a position is seemingly in conflict with the perpendicular position inferred from the ^{2}H-HYSCORE results in SyrB2. However, these two experimental observations could potentially be rationalized by invoking an "offline" ferryl oxo (Figure 2C).[2] Oxygen binding to Fe/2OG enzymes has generally been assumed to occur *trans* to the C-terminal histidine of the facial triad

(i.e. *cis* to the residues of the N-terminal HxD/E motif), i.e. "inline". Formation of the ferryl is assumed to occur without significant ligand rearrangement, resulting in an inline ferryl, also *trans* to the C-terminal histidine (Figure 2A and 2B). Such a ferryl is in excellent position to perform H• abstraction on a substrate in the typical binding pocket, which is also *trans* to the C-terminal histidine (Figure 2A). However, if oxygen were to bind "offline", *cis* to the C-terminal histidine, or if rearrangement following online oxygen binding were to occur, in each case producing an *offline* ferryl oxo, this arrangement would be perpendicular to the substrate binding pocket observed in WelO5 (Figure 2C), reconciling the two key experimental observations. Previous computational work had suggested that an offline ferryl could readily form in SyrB2,[59] and that reaction with the substrate proceeds via a π-type frontier molecular orbital,[63] which favors transfer of the halogen ligand to the resulting substrate radical.[64] Such a hypothesis is particularly intriguing, as it could potentially provide a generalizable strategy for avoiding hydroxylation in Fe/2OG enzyme catalysis (see Section 1.8).

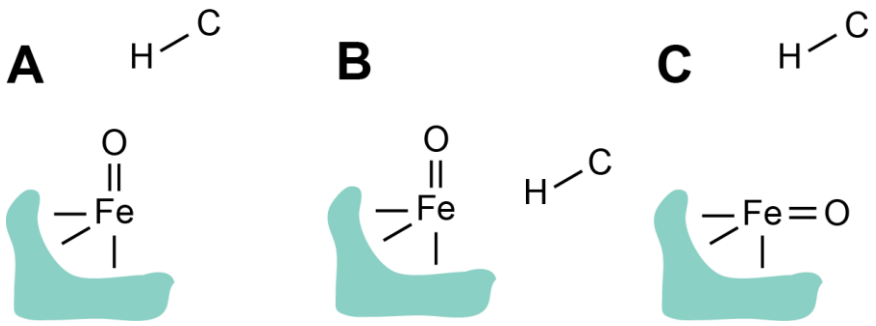

Figure 2. Possibilities for the relative dispositions of substrate C-H bond and ferryl oxo. (**A**) Canonical configuration for hydroxylation, with substrate above the inline ferryl oxo group; (**B**) hypothetical configuration with offline substrate and inline oxo (**C**) configuration postulated for the halogenases, with inline substrate and offline oxo.

1.4 - 1,2-dehydrogenation reactions

1,2-dehydrogenation reactions converting a C-C single bond into a double bond are found in numerous biosynthetic pathways of natural products and the generation of unsaturated fatty acids.[21,65] The desaturation between two completely unactivated carbon centers is typically achieved by generation of a high-valent metal species capable of initiating radical chemistry. Formally, the 2 e^- oxidation of the substrate requires the removal of two adjacent hydrogen atoms (H•). Both heme-containing P450 enzymes[66] and non-heme diiron oxygenases[65] are known to catalyze this transformation. In the former case, the Fe(IV)-oxo/ligand radical complex (compound I) can remove the first H•, whereas the second H• is removed by the high-valent Fe(IV)-OH complex (compound II).[66] In the latter case, the fatty acid desaturases react with O_2 to form a Fe_2(IV/IV) complex, similar to **Q** in sMMO,[67] that is capable of abstracting the first H•.[65] The second is removed by the resulting Fe_2(III/IV) cofactor to complete the reaction. In both systems, removal of each H• is rationalized through involvement of a reactive high-valent iron species.

The Fe/2OG oxygenases CarC,[31,68] CAS,[69] NapI,[22,70] and AsqJ[71] have also been shown to catalyze the 1,2-desaturation, although in each case a heteroatom (O or N) is adjacent to the double bond (Scheme 3). Similar to the systems described above, a mechanism involving two formal H• transfers, one from the ferryl complex and one by the Fe(III)-OH complex, is frequently cited in the literature (Scheme 4a, "HAT" pathway).[69,71] This proposal presents two major issues: (i) a second high-valent iron species analogous to the P450 desaturases and fatty acid desaturases is not present, replaced by the Fe(III)-OH complex, a modest oxidant at best, and (ii) a competing hydroxylation reaction would have to be effectively suppressed to facilitate

removal of the second H•. Below we discuss investigations leading to new mechanistic possibilities.

Scheme 3. Examples of 1,2-dehydrogenations catalyzed by Fe/2OG enzymes.

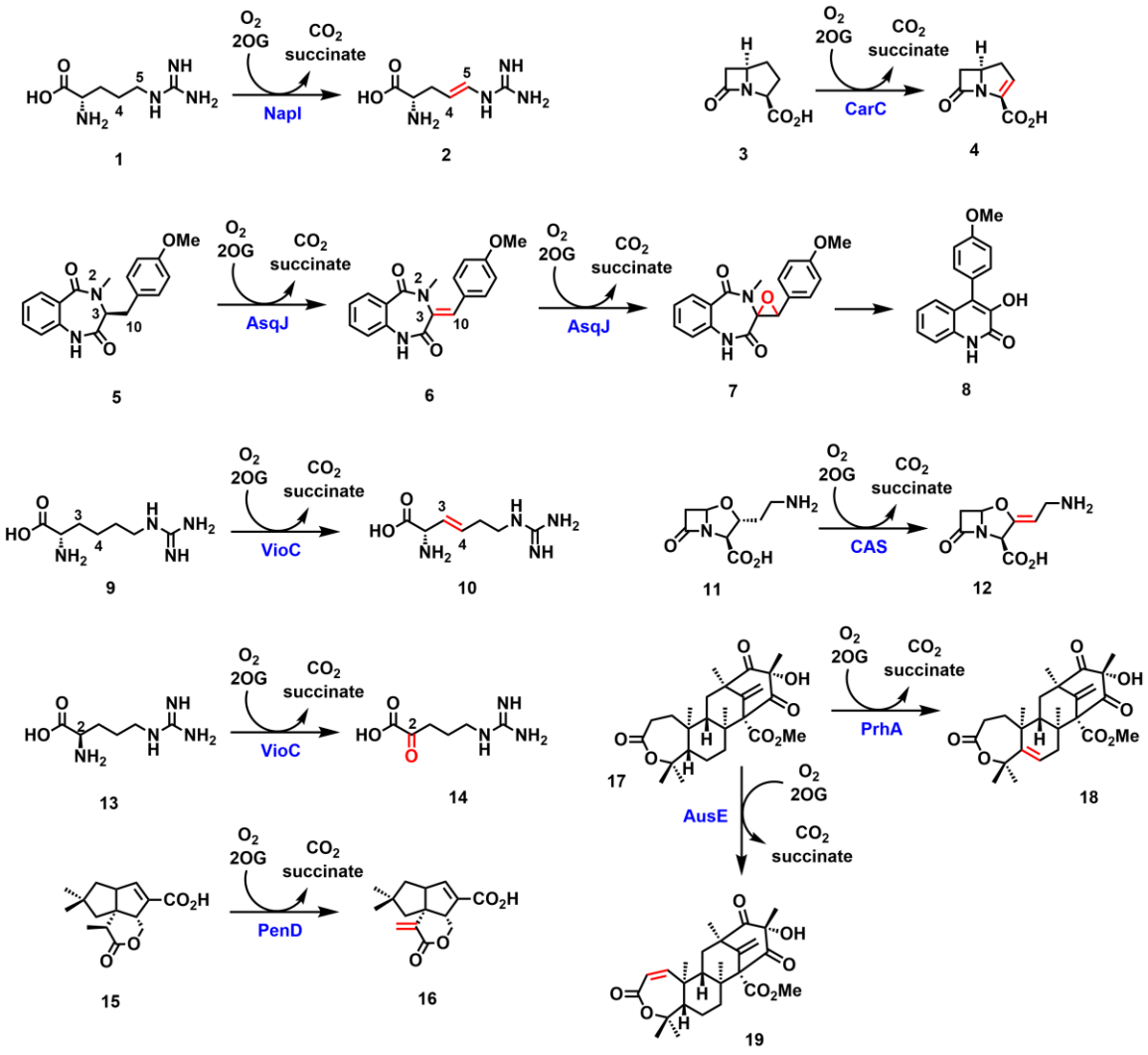

Scheme 4. Possible 1,2-dehydrogenation mechanisms catalyzed by Fe/2OG enzymes (**a**) and mechanism of guanidine production by NapI (**b**).

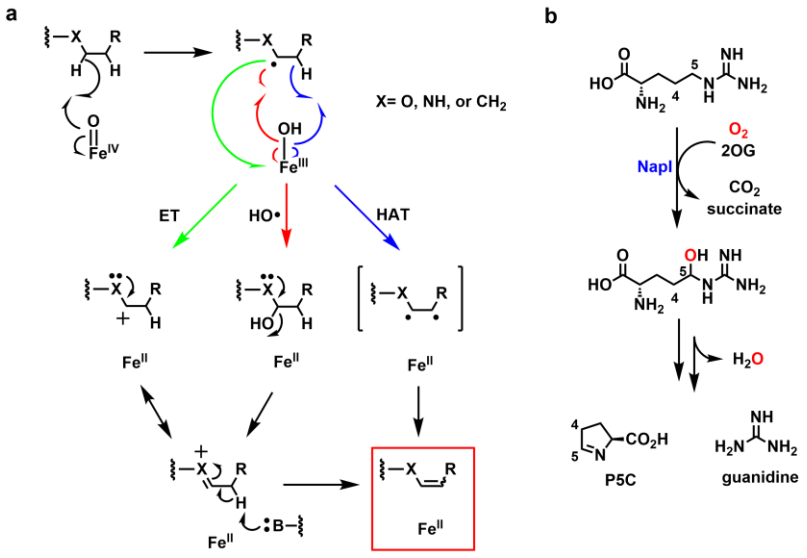

1.4.1 - NapI dehydrogenation of L-arginine

The orthologous Fe/2OG desaturases NapI, Cya18, and Qcn18 catalyze the 1,2-dehydrogenation between C4 and C5 of L-arginine (**1**) forming *trans*-4,5-dehydroarginine (**2**, Scheme 3). The product is crucial in the biosynthesis of the tetrahydroisoquinoline core of naphthyridinomycin, cyanocycline A, and quinocarcin; natural products exhibiting anti-cancer properties.[22]

Investigation into the NapI reaction proved to be an effective avenue for understanding dehydrogenation reactions catalyzed by Fe/2OG enzymes.[72] To elucidate the initial site of H• abstraction by the ferryl complex, L-arginine containing deuterium at C4 (4-[^{2}H]$_2$-L-Arg) and C5 (5-[^{2}H]$_2$-L-Arg) were synthesized. Each substrate reaction with NapI was initiated by rapid-

mixing with O_2 and monitoring ferryl complex decay at 320 nm (SF-Abs), confirmed by freeze-quench Mössbauer experiments. Results showed incorporation of deuterium at C5 produced a ^{2}H-KIE on ferryl decay of ~50 compared to the all-protium substrate.[72] Deuterium at C5 also triggered ~40% uncoupling of 2OG decarboxylation to L-arginine consumption, suggesting that slowed kinetics of H• abstraction at C5 redirected the reaction to an unproductive pathway. A 2.1 Å crystal structure of NapI in complex with L-arginine revealed a close approach of C5 to the iron center (3.9 Å).[72] Taken together, these data establish that NapI initiates the reaction by H• abstraction from C5 of L-arginine.

Removal of the H• from C5 opens up two additional mechanistic possibilities that posit a crucial role for the adjacent nitrogen. In the first, hydroxylation of C5 is followed by heteroatom-driven loss of the –OH group resulting in positive charge delocalization about C5-N6 (Scheme 4a, "HO•" pathway). In the second scenario, the C5 radical intermediate transfers an electron directly to the Fe(III)-OH generating the same resonance-stabilized carbocation as the HO• pathway (Scheme 4a, "ET" pathway). In both cases, the olefin double bond is then generated by removal of a proton from C4. Of the three possibilities, only the "HAT" pathway depends on a second H• abstraction. If a second H• abstraction were to occur during the reaction cycle, deuterium at C4 would likely redirect a portion of the reaction to hydroxylate the C5•, which ultimately results in production of pyrroline-5-carboxylate (P5C) and guanidine (Scheme 4b). This redirecting effect has been well-documented with the halogenase SyrB2 (*vide supra*).[61] Further investigation revealed no difference in product distribution when NapI was reacted with the all-protium or 4-d_2-L-Arg substrates, suggesting that productive reaction does not require H• abstraction from C4, disfavoring the HAT pathway (Scheme 4A).[72] In a further experiment, product analysis using the substrate analog L-indospicine, which contains a methylene unit in

place of N6, showed the presence of only hydroxylation, confirming the requirement of the heteroatom for the 1,2-dehydrogenation reaction.[72] Thus, NapI desaturates L-arginine via the "ET" or "HO•" pathways, not the frequently proposed "HAT" pathway.

1.4.2 - VioC dehydrogenation of L-homoarginine

The native L-arginine hydroxylase, VioC, from *Streptomyces vinaceus* shares 45% sequence identity with NapI and participates in the biosynthesis of the antibiotic viomycin.[73] Initial studies of VioC demonstrated the enzyme's ability to utilize multiple substrate analogs.[74] Further investigation determined that VioC is capable of catalyzing a 1,2-dehydrogenation on the substrate L-homoarginine (**9**), which contains an additional side-chain methylene unit relative to the native substrate L-arginine. Interestingly, VioC generates the C-C double bond between C3 and C4 of L-homoarginine, a position lacking any adjacent activating groups, producing *trans*-3,4-dehydrohomoarginine (**10**, Scheme 3). Specifically labeling substrates at C3 or C4 with deuterium revealed that competing hydroxylation reactions occur at both C3 and C4. The labeling experiments also revealed the presence of two ^{2}H-KIEs by directly measuring ratios of dehydrogenation/hydroxylation products; whether deuterium is present at C3, C4, or all non-exchangeable positions (*perD*), product ratios are always biased towards hydroxylation and disfavor dehydrogenation, relative to the all-protium substrate. This observation suggests that H• abstraction is required at both C3 and C4, consistent with the "HAT" pathway and presumably implicating the Fe(III)-OH complex in H• abstraction.[72] These conclusions are most easily understood by comparison of the all-protium and *perD* product profiles. The first H• abstraction step is not significantly altered because all positions are uniformly ^{1}H or ^{2}H; however, a bias towards hydroxylated products with the *perD* substrate suggests a ^{2}H-KIE is present during conversion of the Fe(III)-OH intermediate radical state to the product state. As observed with

SyrB2 (*vide supra*),[61] the ^{2}H-KIE of the second H• abstraction redirects a large portion of the reaction to hydroxylate the adjacent position. Although L-homoarginine is a non-native substrate to VioC, this study concludes that the "HAT" pathway is viable and indicates mechanistic diversity amongst Fe/2OG enzymes capable of the 1,2-dehydrogenation reaction. Furthermore, the viability of the Fe(III)-OH complex for H• abstraction suggests a significant activating effect of the adjacent carbon-centered radical on the homolytic bond dissociation energy (BDE) for the site of the second H• abstraction.

1.4.3 - AsqJ dehydrogenation of 4'-methoxycyclopeptin

AsqJ from *Aspergillus nidulans* effects the 1,2-dehydrogenation of 4'-methoxycyclopeptin (**5**) and subsequent epoxidation of 4'-methoxydehydrocyclopeptin (**6**) to 4'-methoxycyclopenin (**7**, Scheme 3).[71] The "spring-loaded" **7** product then undergoes a non-enzymatic rearrangement/elimination reaction to generate the final 4'-methoxyviridicatin product (**8**). Although AsqJ forms an epoxide similar to H6H (*vide infra*),[26] the reaction occurs on an already activated C-C double bond and will not be discussed here in detail.

The 1,2-dehydrogenation reaction between C3 and C10 of **5** provides another interesting case to investigate dehydrogenation mechanisms by Fe/2OG enzymes. In contrast to the NapI reaction, C3 and C10 of **5** are partially activated: C3 by the adjacent nitrogen and C10 by the methoxybenzene group. Initial characterization of the enzyme showed that the dehydrogenation and epoxidation reactions proceed in two separate steps, each requiring an equivalent of O_2 and 2OG.[71] Efforts by Bräuer and co-workers yielded multiple high resolution crystal structures with different substrates and substrate mimics.[75] The structure of AsqJ with **5** bound showed C3 and C10 in similar proximity to the metal center, 4.4 Å and 4.3 Å away, respectively, offering up either position for the initial H• abstraction. In a scenario analogous to the NapI reaction, initial

H• abstraction from C3 followed by further oxidation of the intermediate by either the "ET" or "HO•" pathways could be enacted by the neighboring nitrogen. In support of this, a substrate analog lacking the N2 methyl group is incapable of double bond formation. The co-crystal structure of the analog with AsqJ reveals identical binding compared to the **5** structure suggesting the altered reactivity is due primarily to an electronic effect rather than altered substrate position. Moreover, the dehydrogenation reaction still occurs in the absence of the benzyl methoxy group (cyclopeptin), which renders C10 less activated. This observation is consistent with initial H• abstraction of C3. Using coordinates from the crystal structures, Liu and co-workers performed computations that suggest C3 is the initial site of H• abstraction; however, a predicted low energy barrier for H• abstraction from C10 by the Fe(III)-OH complex suggests AsqJ proceeds via the "HAT" mechanism.[76] However, hydroxylation and dehydrogenation via the "HAT" pathway were the only scrutinized pathways. Further experimental work will be critical in evaluating these more detailed mechanistic possibilities.

Chang and co-workers detected the presence of the ferryl complex by rapid freeze-quench Mössbauer during the AsqJ epoxidation reaction.[77] Unfortunately, the authors were unable to detect the ferryl complex by UV/vis absorption due to strong absorbance features in the near UV region by the substrate and/or products. Determination of C3 or C10 as the initial site of H• abstraction for the dehydrogenation reaction may, however, be possible by comparing the coupling of 2OG decarboxylation to product formation using the all-protium substrate and substrates specifically labeled at C3 or C10, analogous to the NapI experiments. Further analysis of product distributions using the labeled substrates may be sufficient in detecting the presence/absence of a second ^{2}H-KIE.

1.4.4 - Dehydrogenation outlook

The studies presented above highlight the mechanistic diversity of the 1,2-dehydrogenation of a C-C bond catalyzed by Fe/2OG oxygenases. Future investigation focusing on enzymes that catalyze the reaction between two unactivated carbon centers will be critical in improving our understanding of these transformations. The studies with VioC and L-homoarginine demonstrated that 1,2-dehydrogenation can proceed through the "HAT" pathway, although the selectivity of dehydrogenation over hydroxylation is very poor. In another example, the reaction of claviminate synthase (CAS) with the substrate analog deoxyproclaviminic acid yielded a C-C double bond between to unactivated carbon centers; however, hydroxylation was also detected.[69] The Fe/2OG oxygenases PenD,[78] PrhA,[79] and AusE involved in the biosynthesis of pentalenolactone, paraherquonin, and acetoxydehydroaustin, respectively, represent natural cases where the dehydrogenation reaction is between two unactivated carbons. Unfortunately, the complexity of the substrates renders detailed investigation of these enzymes very challenging.

1.5 - Epimerization and Endoperoxidation

5.1 - CarC epimerization of (3S,5S)-carbapenam

The increased frequency of infection by multiple-drug-resistant strains of bacteria has been an impetus for research into new strategies of antibiotic targeting and drug development.[80] Carbapenem antibiotics are part of a diminishing class of drugs that are still effective against harmful and multi-drug resistant Gram-positive and Gram-negative pathogens.[21] Large scale production of carbapenem antibiotics has proved challenging, however, because (i) only small

quantities can be isolated from the native organisms, mainly due to instability during the purification processes, and (ii) the complex structure of the bicyclic β-lactam ring system, which includes multiple chiral centers, is a barrier to large-scale synthesis.[81] Engineering the biosynthetic pathways of these antibiotics presents a potentially more efficient route to large-scale production and global use as effective drugs. Here we discuss the role of the Fe/2OG enzyme CarC in the biosynthetic pathway ultimately resulting in (5R)-carbapenem, the simplest of the carbapenem antibiotics.

CarC catalyzes the C5 epimerization of (3*S*,5*S*)-carbapenam (Scheme 5a, **20**) followed by the 1,2-dehydrogenation of the product (**3**) (*vide supra*) to yield (5R)-carbapenem (Scheme 3, **4**).[68,82] Here, we will focus on mechanistic studies concerning the epimerization reaction. In contrast to most other reactions catalyzed by Fe/2OG enzymes, conversion of **20** to **3** is a redox neutral process. If CarC abides by canonical O_2 activation and ferryl generation, like all other Fe/2OG oxygenases currently known, the reaction would require an external reductant to enable multiple turnovers. Indeed, Mössbauer results from a sample prepared by rapidly mixing the CarC reactant complex with O_2 and freezing after 0.15 s displayed a quadrupole doublet with isomer shift (δ) of 0.28 mm s^{-1} and quadrupole splitting (ΔE_Q) of 0.87 mm s^{-1}, consistent with parameters of the ferryl complex previously observed with other Fe/2OG enzymes.[83]

Scheme 5. Epimerization reaction (**a**) and mechanism of epimerization (**b**) catalyzed by CarC.

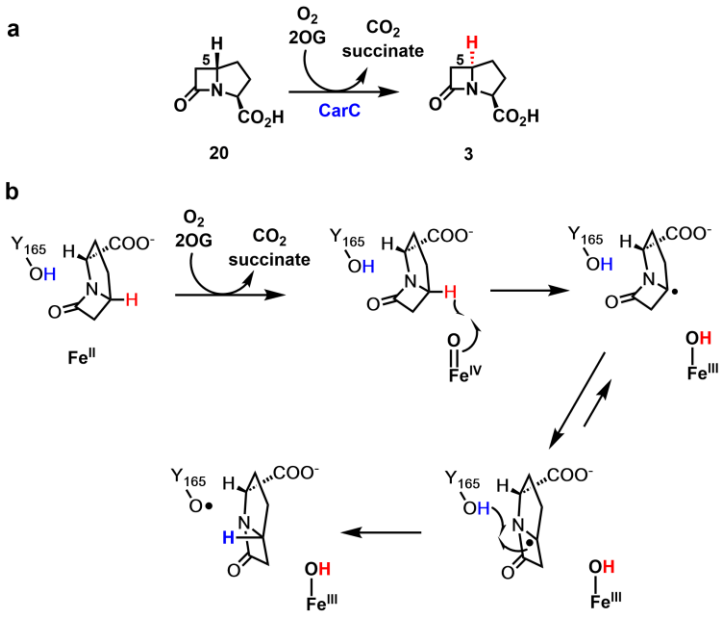

The most feasible epimerization mechanism involves H• abstraction from C5 by the ferryl complex followed H• donation to the opposite face of the C5•, completing the stereoinversion (Scheme 5b). Indeed, SF-Abs experiments initiated by mixing the CarC reactant complex with O_2 showed that decay of the ferryl complex at 320 nm is accompanied by formation of another species exhibiting a sharp band at 410 nm and a broader peak at 390 nm, hallmarks of a tyrosyl radical (Y•).[83] X-band EPR spectra of samples freeze-quenched at time points corresponding to the formation and decay of the new intermediate species presented more evidence for its identity as a Y•. The collected spectra at 10K displayed two signals assigned as the Fe(III) center (S = 5/2) and the Y•. The unusual line shape of the Y• signal was rationalized by dipolar coupling of the Y• with the metal center. This was confirmed by spectra collected at 100 K which showed considerable sharpening of the Y• signal accompanied by disappearance of the Fe(III) signal, consistent with rapid relaxation of the metal center and, thus, uncoupling of the

two spin centers. The two experiments taken together suggest the H• donating species to complete the reaction cycle is an active site tyrosine residue.[83]

To establish that **3** is formed after the ferryl complex and concurrent with Y•, chemically quenched samples were analyzed by LC-MS. The results showed only a small amount of **3** present in samples quenched at 0.15 s, the point of maximum ferryl accumulation.[83] However, the product peak intensity maximized in samples quenched at 3 s, the time point corresponding to maximal accumulation of Y•. Samples quenched at 10 s accumulated only a small amount of additional product. These results confirm the order of events during the CarC reaction cycle.

X-ray crystal structures of CarC solved without substrate and in the presence of substrate analogs revealed multiple tyrosine residues present in or near the active site.[84] Only when the complete substrate-complex crystal structure of CarC bound with **20** was solved to 2.1 Å resolution could the tyrosine implicated in the reaction be unquestionably identified.[83] The structure showed ordering of a loop region poising Y165 in close proximity to the opposite face of C5. SF-Abs experiments of the Y165F variant showed complete disappearance of the 410 nm species, which was preserved in variants removing other nearby tyrosine residues. Interestingly, the Y165F variant now catalytically consumed the substrate suggesting a unique, off-pathway oxidized product is formed.

In 2015, computational studies by Liu and co-workers suggested the presence of an additional intermediate between the H• abstraction and H• donation steps (Scheme 5b).[85] QM/MM calculations using the coordinates of the substrate-bound crystal structure predicted the strained bicyclic ring undergoes facile inversion after H• abstraction at C5. The resulting intermediate brings the C5• markedly closer to Y165, agreeing well with the experiments implicating Y165 as the H• donating species. Thus, in the CarC reaction, the hydroxylation

outcome is avoided by substrate positioning as in SyrB2 (i.e. positioning the substrate radical away from the ferric hydroxide), but this positioning is dynamic and relies on the intrinsic chemical properties of the substrate. That is, initial positioning allows for ferryl-mediated H• abstraction, but the substrate-radical intermediate is "spring loaded" and the radical moves away from the ferric hydroxide following H• abstraction, towards Y165, promoting the desired epimerization and avoiding hydroxylation.

1.5.2 - SnoN epimerization of 21

The discovery of SnoN represents only the second example of a Fe/2OG enzyme-enacted epimerization reaction. SnoN epimerizes C4'' of **21** during the biosynthesis of nogalamycin, a compound included in the anthracyclin class of natural products, many of which exhibit potent anticancer activity and show promise as drug candidates (Scheme 6). Metsä-Ketelä and co-workers solved the 2.20 Å crystal structure of SnoN in complex with iron, 2OG, and **21** which showed C4'' of the substrate 3.7 Å away from an iron-coordinated water, presumably representing the position of the ferryl oxo during catalysis.[86] Similar to CarC, the Y74 residue is poised on the opposite face of C4''; however, the Y74-OH is nearly 6.0 Å away and is obstructed by other atoms in the ring system. Moreover, mutagenesis studies of Y74 and other tyrosine and tryptophan residues in the active site did not significantly affect the activity of SnoN epimerization.

Scheme 6. Epimerization reaction catalyzed by SnoN.

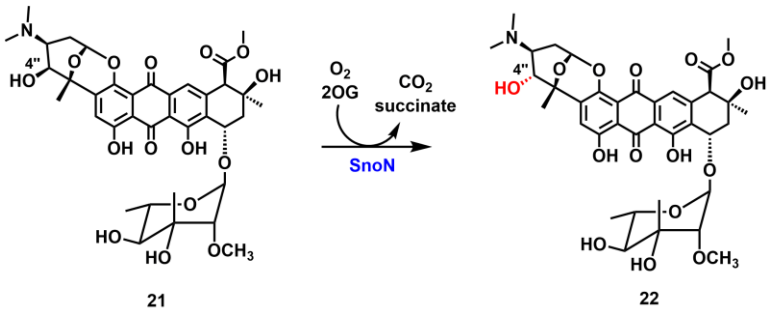

Further experiments measuring 2OG consumption in comparison with consumption of **21** aimed at determining the stoichiometry of the reactants.[86] Surprisingly, the results suggested only one equivalent of 2OG is necessary for the production of two equivalents of **22**. As a result, the authors propose a mechanism involving H• abstractions by both the ferryl and Fe(III)-OH complexes on two separate substrate molecules. Each resulting substrate radical leaves the active site and is reduced and epimerized by a currently unknown source. This proposal suggests SnoN possesses little to no control over the reaction following H• abstraction. During the protein purification process, SnoN was not exposed to a chelating agent to remove any bound metal. It is possible that adventitiously bound 2OG carried over from the purification process caused an underestimation of the amount of 2OG necessary for the reaction. Measuring the production of succinate rather than consumption of 2OG may be necessary to confirm the reaction stoichiometry, as a significant quantity of succinate is unlikely to be present from the purification process. Although there seem to be important structural differences between SnoN and CarC, a more detailed investigation is necessary to elucidate a complete reaction mechanism.

1.5.3 - FtmOx1 endoperoxidation of fumitremorgin B

Many interesting and potentially useful natural products possess an endoperoxide moiety.[87] Artemisinin and derivatives of artemisinin, sesquiterpene lactone endoperoxide natural

products from *Artemisia annua*, are frequently used clinically against the malaria parasite *Plasmodium falciparum*. Additionally, these compounds have been shown to exhibit anticancer properties.[88] The biosynthesis of artemisinin, particularly the endoperoxide formation, is currently not fully understood. Determining the enzymatic mechanism of endoperoxide formation may aid greatly in developing synthetic methods or engineering biosynthetic pathways to more efficiently produce these useful compounds. FtmOx1 (FtmB), an Fe/2OG oxygenase from *Aspergillus fumigatus*, catalyzes the formation of an eight-membered peroxide ring by introducing O_2 into an unactivated C-H bond.[29]

FtmOx1 catalyzes the endoperoxidation of fumitremorgin B (**23**) to form verruculogen (**24**) and is the only Fe/2OG enzyme known enact such a transformation (Scheme 7a). Preliminary studies aimed to determine the origin of the oxygen atoms present in the endoperoxide product.[29] Assays carried out with an atmosphere containing a mixture of $^{16}O_2$ and $^{18}O_2$ yielded product masses of +32 and +36 relative to **23**. This experiment elucidated two crucial aspects of the reaction. First, two molecules of O_2 are required for the reaction; one to generate the reactive ferryl species and the other to be inserted into the product. Second, the oxygen atoms inserted into the product structure originate from a single O_2 molecule of which the O-O bond is never cleaved. Subsequently, a mechanism was proposed in which the ferryl complex abstracts a H• from C21. Instead of HO• rebound, a second molecule of O_2 interacts with the substrate radical. The new peroxyl radical species reacts with the alkene of the neighboring prenyl arm forming the endoperoxide ring and generating a second carbon-based radical on C26. Reduction of the second radical species results in formation of **24** (Scheme 7b). The reaction is strikingly similar to the CarC epimerization with the inclusion of O_2 addition

between the H• abstraction and donation steps. FtmOx1 should then be limited to a single turnover in the absence of an external reductant.

Scheme 7. Endoperoxidation reaction (**a**) and mechanism of endoperoxide formation (**b**) catalyzed by FtmOx1.

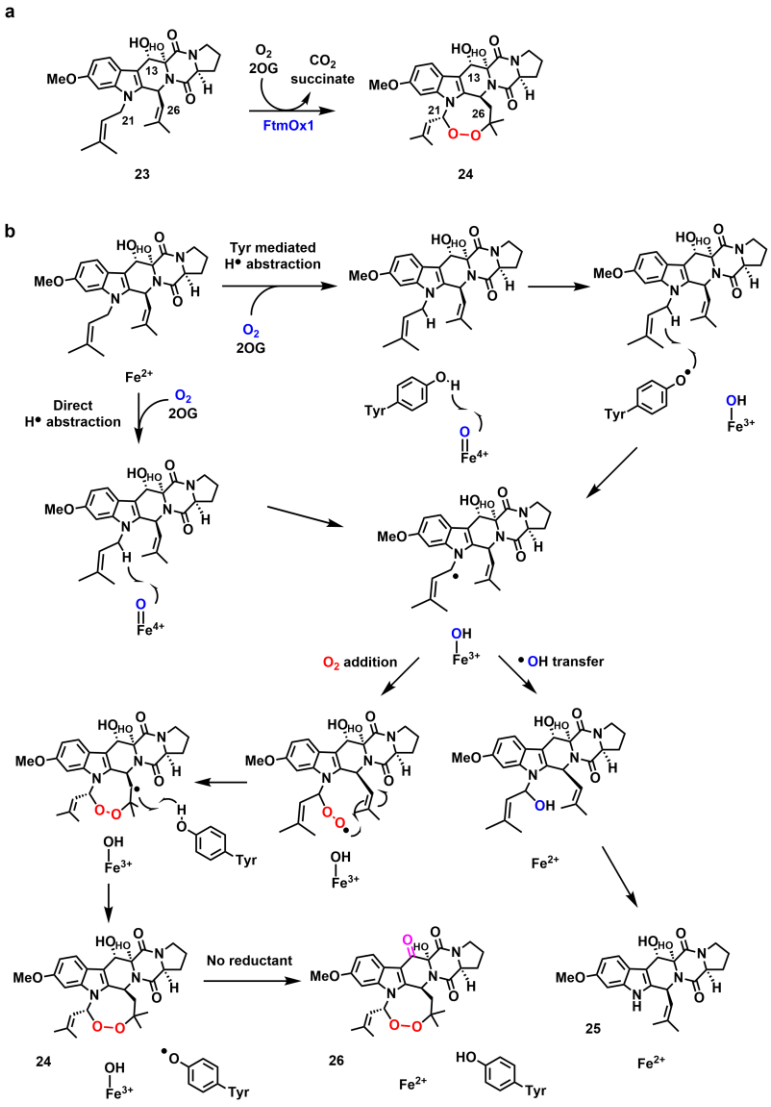

Osada and co-workers identified a number of side products that provide clues to discerning the mechanism.[89] The identification of the N1-dealkylated product (**25**) suggests a side pathway in which canonical hydroxylation of C21 is followed by non-enzymatic C-N bond cleavage (Scheme 7b, "•OH transfer" pathway). Interestingly, this reaction pathway would render the enzyme capable further turnover. FtmOx1 also produces a product in which the endoperoxide ring has formed, but the C13 hydroxyl group is oxidized to a ketone (**26**, Scheme 7b). The presence of **26** suggests the enzyme may be able to oxidize **24** to regenerate the cofactor for a subsequent turnover.

In 2015, Zhang and co-workers solved the first substrate-bound crystal structure of FtmOx1 to 2.2 Å resolution.[30] As modeled, C21 of **23** is located 5.9 Å from the iron. The hydroxyl group of a nearby tyrosine residue (Y224) is located only 4.5 Å from the iron and 3.9 Å from C21. As a consequence, the authors proposed a mechanism in which Y224 mediates the H• abstraction from C21 by the ferryl complex. Following O_2 addition to the C21•, Y224 reduces the C26• to form **24** (Scheme 7b). This mechanism describes a novel strategy for Fe/2OG enzymes to suppress the hydroxylation pathway. Additionally, the authors do not rule out the possibility that Y224• is capable of multiple turnovers without the further requirement of 2OG, reminiscent of ribonucleotide reductase (RNR) enzymes.

Supplementing the structural experiments, SF-Abs experiments revealed the presence of an intermediate with maximal absorbance around 420 nm.[30] Accompanying freeze-quench EPR experiments revealed a broad signal around $g = 2$ with matching kinetics of the intermediate detected by SF-Abs. Intriguingly, both the UV/Vis and EPR signals are not identical to other characterized Y• species. Further study is necessary to fully characterize this intermediate, which is undoubtedly key to understanding the endoperoxidation mechanism.

Given that the mechanistic hypothesis is almost solely based on structural observations, we examined the structural coordinates and electron density map more closely and conclude that the published experimental data and the proposed mechanism are not in agreement. First, the electron density map published on the protein data bank (PDB: 4ZON) exhibits a very poor fit to the proposed model. In fact, performing a refinement of the published data omitting the substrate produces *Fo-Fc* difference electron density *not* consistent with fumitremorgin B (Figure 3). Our analysis suggests either very low occupancy or complete absence of the substrate from the FtmOx1 active site. Furthermore, the Y224F and Y224A FtmOx1 variants still produce the endoperoxide products and exhibit similar product profiles to WT enzyme. According to the published structure, Y224 is also involved in a significant π-stacking interaction with the indole moiety of **23**, yet mutation of this residue to an alanine does not appear to significantly alter the activity. Taken together, the published model does not accurately reflect many aspects of the experimental data. Thus, it is our opinion that the endoperoxidation mechanism remains unresolved.

Our own structural investigation of FtmOx1 yielded similar results to those of the Zhang lab, suggesting there may be unique challenges to obtaining the substrate-bound crystal structure. Attempts at both co-crystallization with **23** and soaking of **23** into FtmOx1 crystals did not yield significant electron density consistent with the substrate, even across a number of crystallization conditions that produced different space groups and unit cell parameters. Intriguingly, our crystal structures almost perfectly overlay with the crystal structure solved by the Zhang group (Figure 3B). It is possible that FtmOx1 crystallizes in a physiologically irrelevant state that excludes the substrate for reasons currently not understood. Further efforts at obtaining the substrate-bound structure are ongoing in our lab.

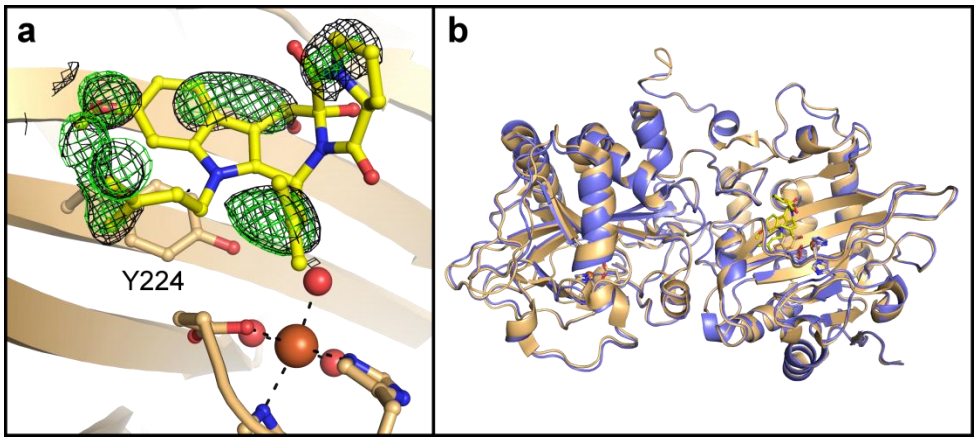

Figure 3. (**a**) FtmOx1 crystal structure in complex with **23** (PDB: 4ZON). The 2*Fo-Fc* map of the published coordinates is contoured to 1.0 σ (black mesh) and the *Fo-Fc* map from the refined data set in the absence of **23** is contoured to 3.0 σ (green mesh). (**b**) Overlay of the 4ZON (tan) coordinates with an FtmOx1 crystal structure solved by our lab (blue) from unique crystallization conditions.

1.6 - Oxacyclization reactions

Numerous oxacycle-bearing natural products, compounds that contain heterocyclic ring systems that include oxygen, exhibit useful bioactivities and the oxacycle is installed in a number of cases by Fe/2OG enzymes. For instance, the C-O bond of clavulanic acid, a bacterially produced serine β-lactamase inhibitor, is formed by CAS (Scheme 8a).[23,24] Intriguingly, CAS also catalyzes two other transformations in the clavulanic acid biosynthetic pathway. The enzyme LolO catalyzes an oxacyclization in the biosynthesis of norloline, a fungal insecticide (Scheme 8a).[90] Hyoscyamine 6β-hydroxylase (H6H) catalyzes the oxacyclization of hyoscyamine to generate scopolamine, a plant-derived anesthetic (Scheme 8a).[26] Recently, a number of Fe/2OG enzymes were discovered that catalyze oxacyclization reactions in

orthomycin biosynthetic pathways.[91] Many orthomycins have exhibited potent antibacterial properties against methicillin and vancomycin resistant strains of bacteria.

Scheme 8. Reactions catalyzed by CAS, LolO, and H6H (**a**). Electron transfer (ET) mechanism (**b**) and β-scission mechanism of oxacyclization (**c**).

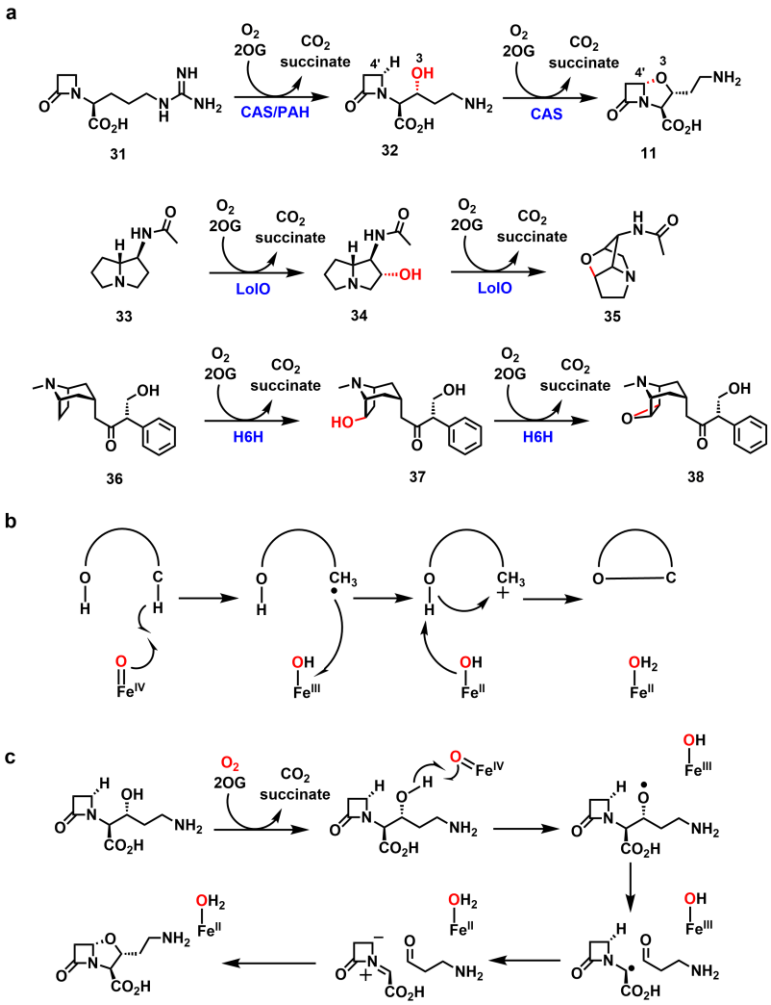

1.6.1 - IPNS and HppE

Isopenicillin N synthase (IPNS)[92] and (*S*)-2-hydroxypropyl-1-phosphate epoxidase (HppE)[93] are mononuclear non-heme iron oxygenases that differ from the Fe/2OG-dependent superfamily discussed here; however, they catalyze transformations analogous to those of the aforementioned oxacyclization enzymes, but without the requirement of 2OG. The mechanisms used by IPNS and HppE are comparatively well understood and will serve as a foundation for mechanistic discussions of the Fe/2OG-dependent oxacyclases.

IPNS utilizes L-δ-(α-aminoadipoyl)-L-cysteinyl-D-valine (ACV, **27**) to produce isopenicillin N (**28**), the common core to all penicillin antibiotics (Scheme 9a).[92] During the reaction cycle, the reduction of O_2 to water is balanced by a four electron oxidation of **27**, abolishing the necessity of an external electron source; the ferryl complex is generated by the first cyclization event. H• abstraction from C1 of **27** by an Fe(III)-O-O• complex and radical coupling from the metal-coordinated thiol generates an Fe(II)-O-OH complex and a thioaldehyde. Subsequent O-O bond cleavage and generation of the ferryl complex is accompanied by nucleophilic attack of the amide on the thioaldehyde effectively generating the β-lactam ring. Ferryl-mediated H• abstraction from C6 is followed by radical transfer of the coordinated sulfur atom to complete the thiazolidine ring of **28** and regenerate the Fe(II) cofactor (Scheme 9c).[54]

Scheme 9. Reactions catalyzed by IPNS (**a**) and HppE (**b**). The mechanisms of the transformations are shown in **c** and **d**, respectively.

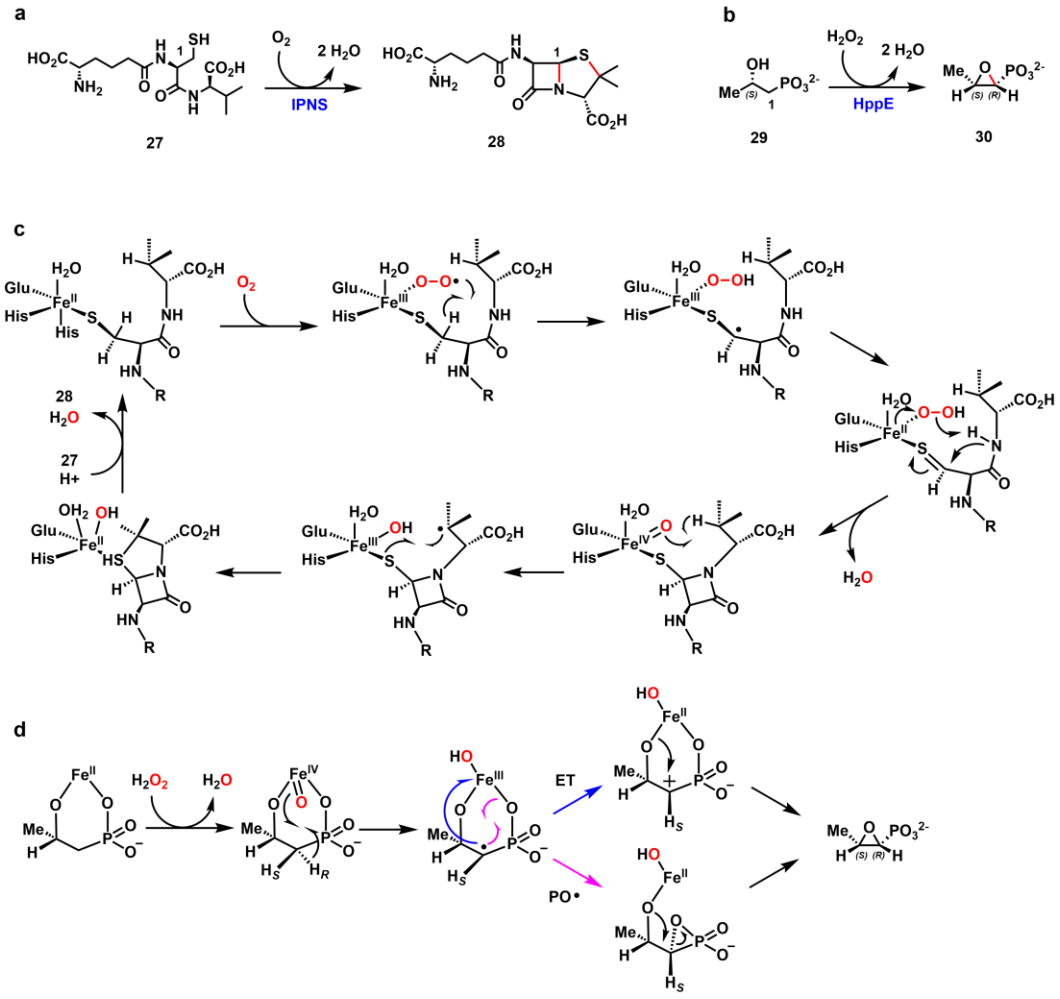

HppE catalyzes the transformation of (*S*)-2-hydroxypropyl-1-phosphonate (**29**) to the antibiotic fosfomycin (**30**, Scheme 9b).[93] Recent findings demonstrated that HppE utilizes H_2O_2, rather than O_2, as the oxidizing co-substrate.[94] This observation rationalizes the electron imbalance between the O_2 activation and substrate oxidation half reactions hypothesized previously. Therefore, the ferryl complex is directly formed from H_2O_2 and subsequently abstracts the *pro-R* H• from C1. The inversion of stereochemistry at C1 during the reaction cycle

suggests a two-step process that can be rationalized by two mechanistic possibilities. In the first, the C1• transfers an electron directly to the iron followed by nucleophilic attack of the C2-O^- to generate the product (Scheme 9d, blue arrows). Alternatively, radical coupling of the metal-coordinated phosphonate O atom effectively reduces the iron center. The phosphonate moiety leaving group departs as C2-O^- attacks C1 furnishing **30** (Scheme 9d, purple arrows).

The thiazolidine formation by IPNS and "PO•" pathway by HppE are analogous to the Fe/2OG halogenase mechanism in which a unique metal-coordinated atom is coupled with the substrate radical instead of the hydroxyl group. However, this strategy is unlikely for the Fe/2OG oxacyclases without a significant ligand rearrangement because the remaining iron coordination sites of the reactant complex are occupied by the co-substrate 2OG. In contrast, the "ET" pathway described for the HppE reaction provides a viable strategy for oxacyclization catalyzed by the Fe/2OG enzymes and will be discussed in more detail below.

1.6.2 - CAS, LolO, and H6H

CAS,[23,24] LolO,[90,95] and H6H[25,26] each catalyze sequential hydroxylation and oxacyclization reactions to furnish claviminic acid (**11**), *N*-acetylnorloline (**35**), and scopolamine (**38**), respectively (Scheme 8a). Of the three enzymes, CAS is perhaps the most extensively studied. Precedent set by the HppE "PO•" pathway presents an attractive oxacyclization mechanism viable for all three systems. In this framework, the CAS reaction is initiated by ferryl-mediated H• abstraction from C4' of proclaviminic acid (**32**) followed by direct electron transfer, reducing the iron cofactor to the 2+ state. The resulting carbocation may be partially resonance stabilized by the neighboring amine of the strained β-lactam ring. Closure of the oxacycle ring is then achieved by attack of O3 on the C4' carbocation to furnish **11** (Scheme 8b). However, the crystal structure of CAS in complex with **32** solved to 2.1 Å resolution reveals O3

only 4.2 Å away from the iron and better positioned for initial H• abstraction.[96] Conversely, C4' is 5.4 Å from the iron and likely out of line with the expected position of ferryl formation. Inspired by these findings, Schofield and co-workers proposed a unique mechanism beginning with ferryl-mediated H• abstraction from O3 followed by radical β-scission generating a carboxylato(2-oxoazetidin-1-yl)methyl radical and 3-aminopropanal. A proton transfer from C4' accompanied by radical transfer to the Fe(III)-OH cofactor results in ylide formation that reacts with 3-aminopropanal through a [3+2] dipolar cycloaddition to furnish **11** (Scheme 8c). Computations based on the structural coordinates supported this mechanism over the "ET" pathway.[97] However, this mechanism does not support a common strategy between CAS, LolO, and H6H as this sequence of events would not be possible in the latter two reactions.

Additional experimentation on these three enzymes is clearly necessary to buttress a single, viable mechanism. Analogous to the NapI experiments (*vide supra*), deuterium labeling of the atoms likely targeted for H• abstraction should discern the initiating step. Labeling of the carbon center will require chemical synthesis, whereas labeling the O-H group can be achieved using $^{2}H_2O$ solvent. Transient kinetic analysis using SF-Abs could reveal which substrate extends the life of the ferryl complex, and thus which position is subject to H• abstraction. In the event that the ferryl complex does not significantly accumulate, even when challenged with deuterium, a measurement of uncoupling of the 2OG oxidation and substrate activation half reactions should provide insight, as in the study of NapI. These experiments should aid in differentiating between the viable mechanisms. Results of such a study in H6H are presented in Chapter 2.

6.3 - Orthoester and dioxymethylene formation in orthomycin biosynthesis

Recently, the Fe/2OG enzymes HygX, AviO1, EvdO1, and EvdO2 have been discovered and implicated in the orthoester and dioxymethylene oxacyclization reactions in the biosynthesis of orthomycin natural products (Scheme 10). Although *in vivo* knockout experiments and *in vitro* oxacyclization activity have not been demonstrated, the apo x-ray crystal structures of AviO1, EvdO1, and EvdO2 and the crystal structure of HygX bound to **41** have been solved by Iverson and co-workers.[91] Intriguingly, HygX exhibits the modified iron-binding facial triad common to the Fe/2OG halogenases which is devoid of the coordinating acidic residue. Instead, the structure shows two open coordination sites about the octahedral iron geometry that are occupied by waters. Presumably, one site is reserved for O_2 binding; however, the existence of the second site expands the scope of mechanistic possibilities.

Scheme 10. The orthmycin antibiotics avilamycin A (**39**), everninomicin D (**40**), and hygromycin B (**41**).

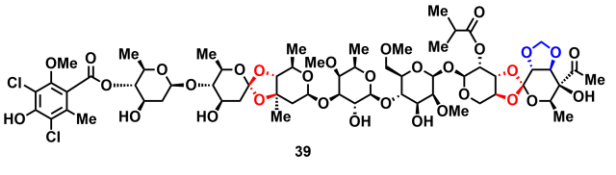

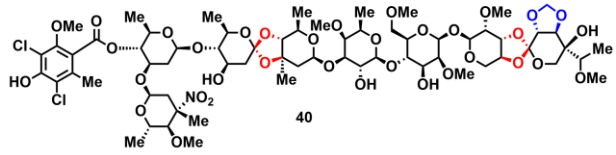

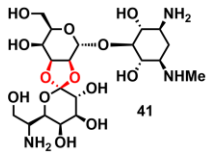

One possibility of orthoester formation by HygX is coupling of a carbon-centered radical to the iron-coordinated hydroxyl moiety of the substrate following H• abstraction, a mechanism analogous to thiazolidine ring formation by IPNS. The "ET" or "HO•" mechanisms described for both HppE and the Fe/2OG-dependent oxacyclases and desaturases are other viable pathways. In this case, however, the adjacent oxygen atom would likely resonance stabilize the carbocation intermediate through formation of an oxonium. A third, and very exciting, possibility is that HygX could be a cryptic halogenase.[91] According to this hypothesis, after H• abstraction from the target carbon, an iron-coordinated halide is transferred to the carbon center. The halogenated intermediate is then poised for cyclization by nucleophilic attack of the hydroxyl group. These newly discovered enzymes present a great opportunity to expand our understanding of Fe/2OG enzyme-mediated oxacyclization reactions.

1.7 - C-C cyclization reactions

Three novel Fe/2OG enzymes have recently been discovered that catalyze ring closure transformations by forming a new C-C bond; however, all of the known enzymes utilize structurally complex natural products making detailed mechanistic investigations very challenging. SnoK, the enzyme prior to SnoN in the nogalamycin biosynthetic pathway (*vide supra*), catalyzes the formation of a bond between C5'' and C2 of **42** to complete **21** (Scheme 11). Metsä-Ketelä and co-workers solved the crystal structure of SnoK to 2.20 Å; however, attempts to include substrate were unsuccessful.[86] EasH from *Aspergillus japonicus* participates in the biosynthesis of cycloclavine (**45**) and performs a unique C-C bond-forming ring closure reaction on **43** (Scheme 11).[98] Subsequently, NADPH-dependent reduction of **44** by EasG yields **45**. Lastly, Sattely and co-workers showed the enzyme 2-ODD catalyzes the C-C bond ring

closure in the biosynthetic pathway of (-)-podophyllotoxin, a natural precursor to the synthetic chemotherapeutic drug etoposide (Scheme 11).[99,100] Interestingly, their work presents a pathway to a new etoposide precursor, allowing an abbreviated synthetic procedure to the desired compound.

Scheme 11. C-C bond-forming ring closures catalyzed by Fe/2OG enzymes.

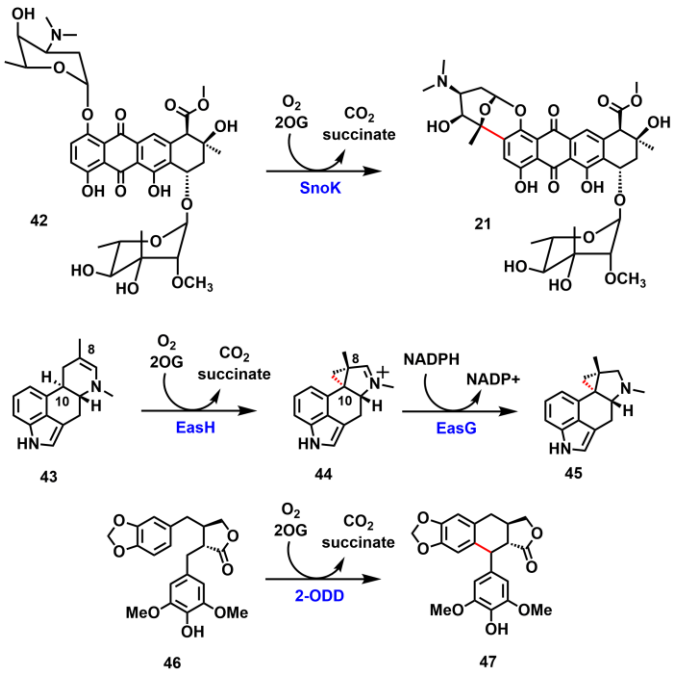

The mechanistic possibilities for C-C bond formation we discuss are common to SnoK, EasH, and 2-ODD and, thus, are simplified and displayed in Scheme 12. It is important to note that activating groups are located adjacent to each carbon center (depicted as **X** and **Y**). The reaction is initiated by ferryl-mediated H• abstraction from C1 yielding state **I**. This state is a branch point to three unique mechanisms. In one pathway, an electron is transferred from C1 reducing the Fe(III)-OH cofactor and generating a resonance stabilized carbocation (Scheme 12,

red arrows). A second option is coupling of the C1• to the iron-coordinated hydroxyl group followed by loss of water (blue arrows). In both pathways, nucleophilic attack by C2 forms the C-C bond (state **III**). In a third pathway, the initial C1• first couples with the C2-C3 double bond (green arrows). The resulting state **II** represents another branch point where electron transfer or hydroxylation events are possible (purple and teal arrows, respectively). In this scenario, loss of water is driven by activating group **Y** leading to state **III**. In the SnoK and 2-ODD reactions, state **III** is a tautomer with the product; however, state **III** in the EasH reaction is further reduced in the EasG-catalyzed reaction.

Scheme 12. Possible mechanisms of C-C bond-forming ring closure reaction.

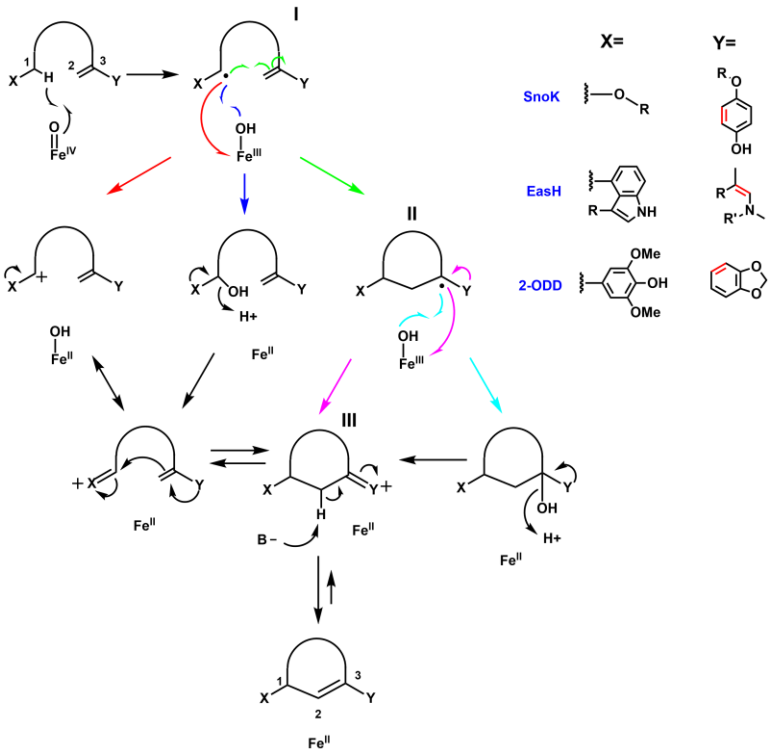

1.8 - Offline Ferryl Intermediates: A Unified Mechanism for Avoiding Hydroxylation?

Work in the Fe/2OG halogenases established that hydroxylation functions as a "default" outcome in Fe/2OG catalysis; when the substrate is modestly altered, halogenation selectivity is lost and hydroxylation prevails.[61] Thus, strategies for avoiding hydroxylation have been a central theme of our discussion of mechanistic hypotheses in other non-hydroxylating Fe/2OG enzymes. In the halogenases, it was established that delicate substrate positioning, specifically a relatively long distance between the iron and the target hydron and a nearly perpendicular angle between the Fe-oxo vector and the Fe-hydron vector, is critical for halogenation selectivity, presumably because it is essential for the substrate radical to not approach the hydroxide ligand too closely. The structure of WelO5 in complex with its substrate established that perpendicular positioning is achieved without radical repositioning of the substrate relative to the facial triad framework,[52] substantiating prior suggestions that an "offline" ferryl might be operant.[59,63]

Although similar experiments have not been reported for other non-hydroxylation members of this family, it is tempting to speculate that offline ferryl intermediates might provide a common framework for avoiding hydroxylation, and thereby promoting the productive reaction. All Fe/2OG reactions are believed to begin with formation of the ferryl intermediate, followed by an H• abstraction. All therefore have the opportunity for an unproductive hydroxylation reaction to occur if the substrate radical attacks the coordinated hydroxide (unless this hydroxylated product undergoes additional processing to yield the desired product, as in Scheme 4, "HO• pathway"). Deploying offline ferryl intermediates to avoid this unproductive pathway could thus be a strategy applicable to all non-hydroxylating Fe/2OG enzymes.

1.9 - Summary of Dissertation

1.9.1 - Assessing substrate positioning in SyrB2 via {FeNO}^{7} ^{2}H-HYSCORE, Appendix A.

As described in section 1.3.3, it had been hypothesized that substrate positioning was a key factor in controlling reaction selectivity in the Fe/2OG halogenase SyrB2. However, no experimental structural data had been reported to substantiate this hypothesis. The x-ray crystal structure of SyrB2 in the presence of iron and 2OG was critically lacking the substrate, SyrB1, which delivers L-threonine to the active site via a phosphopantetheine cofactor. In Appendix A, we addressed the positioning of the SyrB2 substrates **Thr**, **Aba**, and **Nva** relative to an EPR-active {FeNO}^{7} complex, formed by reaction of the SyrB2•Fe(II)•2OG•SyrB1 complex with nitric oxide (NO) gas. By measuring orientation-selective deuterium hyperfine sublevel correlation spectra (^{2}H-HYSCORE), we were able to measure the dipolar hyperfine coupling between the {FeNO}^{7} complex and specifically-deuterium-labeled amino acid substrates. By simulating these orientation-selective spectra, we were able to extract the Fe-^{2}H distances and N_{NO}-Fe-^{2}H angles. Using this method, we showed that the Fe-^{2}H distances follow the trend **Nva**<**Aba**<**Thr**, in excellent agreement with the rates of H• abstraction observed for these substrates. Furthermore, we showed that the N_{NO}-Fe-^{2}H angle for **Thr** is ~85°. If such an angle is representative of the analogous angle in the ferryl complex (O_{oxo}-Fe-H), it would place the target hydron nearly in the equatorial plane, potentially directly adjacent to the *cis*-coordinated chloride ligand, primed for facile transfer. In contrast, a more acute angle (65°) is observed for **Nva**, potentially allowing closer approach to the oxo ligand. These observations strongly corroborate the assertion that substrate positioning controls chemoselectivity in SyrB2. Moreover, the structural perturbations observed for **Nva** relative to **Thr**, including a ~0.8 Å closer approach and ~20° tilt toward the Fe−N(O) bond, are relatively modest but sufficient to unleash both the

H•-abstraction potency of the ferryl and the default hydroxylation outcome. This suggests that precise control of substrate positioning is essential to reaction control in non-hydroxylating Fe/2OG enzymes; correspondingly, precise structural information is required in order to understand their reactivity.

1.9.2 - Vanadyl as a Stable Structural Mimic of Reactive Ferryl Intermediates in Fe/2OG Enzymes, Appendix C.

The study outlined above underscored the importance of substrate positioning and precise local structural information in understanding the reactivity of Fe/2OG enzymes. To date, the best available structural information has come from 1) x-ray crystal structures of the reactant complex (i.e. with Fe(II), 2OG, and substrate bound) or 2) $\{FeNO\}^7$ complexes. Unfortunately, both these states share dissimilarities with the ferryl intermediate (e.g. lower oxidation state of iron and 2OG bound instead of succinate) and might not reflect structural changes that occur upon ferryl formation, such as formation of an offline ferryl intermediate. Because the stability and spin state of the ferryl intermediates generally preclude structural interrogation by either x-ray crystallography or pulse EPR spectroscopy, we sought a structural probe that would accurately mimic the ferryl intermediate and be amenable to both structural techniques.

The vanadyl ion [V(IV)-oxo] is stable and EPR-active (d_1, S = 1/2); moreover, like the ferryl, it is a tetravalent first row transition metal with a single oxo ligand. In Appendix C, we show using EPR, x-ray absorption spectroscopy, and x-ray crystallography that vanadyl binds to the model Fe/2OG enzyme TauD, along with succinate and substrate, adopting a distorted octahedral geometry nearly identical to that proposed for the ferryl intermediate.[101] EXAFS analysis revealed M-oxo and M-L (first coordination sphere) distances of 1.60 and 2.05 Å, respectively, extremely similar to those of the ferryl intermediate in TauD (1.62 and 2.05 Å,

respectively).[42] For the L-arginine 3-hydroxylase, VioC, DFT calculations based on the x-ray crystal structure of the vanadyl complex correctly predict the ferryl Mössbauer parameters obtained in rapid-freeze-quench experiments.[45] Moreover, the disposition of the substrate analog, L-homoarginine, relative to the vanadyl center in VioC is consistent with its altered reactivity (mixture of H• abstraction from C3 and C4), whereas its disposition in the corresponding x-ray crystal structure of the reactant complex is not.[72] In the Fe/2OG halogenase, SyrB2, the vanadyl complex reproduces an effect previously observed only for the ferryl state (not in lower oxidation states of iron or in the presence of other metals): formation of a stable complex of SyrB2 with its carrier protein substrate (L-aminoacyl-*S*-SyrB1). Taken together, these results suggest that the vanadyl ion is a faithful structural mimic of the ferryl intermediate in Fe/2OG enzymes suitable for characterization by x-ray crystalography and pulse EPR spectroscopy.

1.9.3 - Structural factors controlling epoxidation selectivity in hyoscyamine-6β-hydroxylase, Chapter 2

As described in section 1.8, it has been suggested that an offline ferryl intermediate may be a general mechanism for reaction control in non-hydroxylating Fe/2OG enzymes. Hyoscyamine-6β-hydroxylase (H6H, section 1.6.2) provides an excellent system to test this hypothesis. H6H catalyzes installation of an epoxide across C6 and C7 of the tropane ring of hyoscyamine to furnish the alkaloid scopolamine. This reaction proceeds in two turnovers; the first turnover hydroxylates C6, whereas the second forms the epoxide in a 1,3-dehydrogenation/oxacyclization. In Chapter 2, we examine the mechanism of this second turnover and the structural factors that promote selectivity for expoxidation over a second hydroxylation. First, we utilize SF-abs to observe a large ^{2}H-KIE on decay of the ferryl intermediate in the presence of 7-^{2}H-6-hydroxy-hyoscyamine; this result implicates H•

abstraction from C7 in ferryl decay, ruling out H• abstraction from the newly-installed hydroxyl group, as has been proposed for CAS (see section 1.6).

To test the hypothesis that the epoxidation turnover may proceed via an offline ferryl intermediate, we examined the disposition of the substrate relative to vanadyl in the presence of hyoscyamine and 6-hydroxy-hyoscyamine. In the H6H•vanadyl•succinate•hyscyamine complex, O_{oxo}-V-^{2}H angle and O_{oxo}-V//^{2}H-C angles of 40 and 25°, respectively, are observed for ^{2}H at C7. If H6H stabilizes an offline M(IV)-oxo in the epoxidation turnover, we would expect to observe less acute angles in the presence of 7-^{2}H-6-hydroxy-hyoscyamine (~53 and 65°, respectively). Instead, nearly identical angles are observed. Given the sensitivity of these measurements to changes in the disposition of the C-H bond relative to V-O_{oxo} (or in this case, *vice versa*), these data provide no evidence for the stabilization of an offline M(IV)-oxo in the presence of 6-hydroxy-hyoscyamine. We also examined the vanadyl complex of a variant of H6H (L290F) that catalyzes appreciable 6,7-dihydroxylation of hyoscyamine, along with diminution of the epoxidized product; HYSCORE data reveal a modest decrease in the V-^{2}H distance. Together, these observations suggest that the precise M-^{2}H distance, rather than wholesale offline rearrangement, is critical for efficient cyclization activity, and potentially other non-hydroxylation outcomes as well: too close results in hydroxylation derailing the desired function, too far leads to inefficient H• abstraction.

1.9.4 - Structure of the inorganic core of the Mn(IV)/Fe(IV) activation intermediate from Chlamydia trachomatis ribonucleotide reductase, Appendix B

The studies outlined above focused on the application of spectroscopic tools (in particular, pulse EPR and x-ray spectroscopy) to answer structural question in Fe/2OG enzymes.

In my dissertation research, I have also applied these techniques to outstanding questions in the ribonucleotide reductases (RNRs).

RNRs catalyze the reduction of ribonucleotides to deoxyribonucleotides, producing the precursors required for DNA replication and repair in organisms across all domains of life.[102] These enzymes utilize a radical mechanism, which is initiated by the generation of a cysteine thiyl radical in the enzyme active site. In class I RNRs, this radical is generated by long-range electron transfer (ET) from the cysteine residue in the α subunit to a stable one-electron oxidant in the β subunit.[103] The class II and III RNRs utilize and adenosylcobalamin and glycyl radical cofactors, respectively, to generate the radical. The class I RNRs are further subdivided on the basis of the identity of the one-electron oxidant. Class I-a and class I-b enzymes utilize a tyrosyl radical; this tyrosyl radical is generated in an activation reaction by a nearby dinuclear metal site.[104,105] In the class I-c RNR from *Chlamydia trachomatis* (*Ct* RNR), the dinuclear metal site serves directly as the one-electron oxidant in the form of a Mn(IV)/Fe(III) heterodinuclear cofactor (**4/3**).[106]

This **4/3** cofactor is generated when the Mn(II)/Fe(II) form of *Ct* RNR reacts with dioxygen to form a Mn(IV)/Fe(IV) (**4/4**) intermediate, which is reduced by an exogenous electron to form **4/3**.[33] This **4/4** intermediate is analogous to other high-valent metalloenzyme intermediates, such as the Fe(IV)/Fe(IV) intermediate "Q" in soluble methane monooxygenase,[67] that have been subjected to intensive structural interrogation.[67,107–111] In Appendix B, we examined **4/4** using EXAFS analysis at both the Mn and Fe K-edges, which indicated a Mn-Fe distance of 2.74-2.75 Å and a set of intensely scattering light atoms (C/N/O) at an average distance of 1.81 Å from Fe. Pulse EPR studies on **4/4** revealed no detectable strong hyperfine couplings to exchangeable hydrons, though an exchangable hydron was detected at a position

consistent with a terminal hydroxide ligand to Mn. Taken together, these observations are most consistent with a di-μ-oxo "diamond core" and a terminal hydroxide ligand to Mn(IV).

1.9.5 - Two-Color Valence-to-Core X-ray Emission Spectroscopy Tracks Cofactor Protonation State in Ct RNR, Appendix D

Although the agreement of these orthogonal spectroscopic techniques provides compelling evidence for such a di-μ-oxo core, this assignment relies on somewhat indirect observations (i.e. interatomic distances and a lack of strong, exchangable hyperfine couplings). In Appendix D, we sought to detect the μ-oxo ligands more directly using valence-to-core x-ray emission spectroscopy (VtC XES). In this element selective technique, a high energy x-ray photon generates a 1s core hole on an absorbing metal atom. Following ionization, electrons from higher-lying orbitals fill the core hole, emitting x-ray fluorescence; when these electrons originate in ligand-localized valence orbitals (i.e. valence-to-core transitions), the resulting spectra are sensitive to the electronic structure of the ligands. In these spectra, μ-oxo ligands manifest as a distinct Kβ" peak in the Mn XES spectrum of **4/4**. Upon protonation of one of these oxo bridges to form the μ-oxo/μ-hydroxo **4/3** state, this Kβ" intensity decreases. By directly probing the ligand electronic structure, these data allow for a more robust assignment of the protonation state of **4/4** and **4/3**. For these experiments, we utilized the dual array valence emission spectrometer (DAVES) at CHESS C-line to simultaneously collect both Mn and Fe VtC XES, minimizing the sample quantity required and avoiding difficulties arising from sample variability. To the authors' knowledge, these are the first "two-color" VtC XES to be reported, and the first VtC XES of any kind for an enzyme intermediate.

1.10 - Outlook

1.10.1 - Structural characterization of the Fe/2OG halogenases

The study outlined in section 1.9.1 (Appendix A), demonstrated that the halogenase SyrB2 enforces nearly perpedicular approach of the substrate to the $\{FeNO\}^7$ complex and, presumably, the oxidized intermediates in the catalytic cycle. However, how the enzyme dictates this positioning remains unclear, since the available crystallographic data lacks the substrate SyrB1. Several studies have endeavored to computationally dock the phosphopantetheine arm of SyrB1 into the SyrB2 crystal structure; however, such docking models are inherently speculative and lack any contributions or conformational changes arising from contact between SyrB1 and SyrB2. That these contacts are influential is clear, as they contribute to the observed substrate triggering in SyrB2.[56] Therefore, structural characterization of the SyrB1•SyrB2 complex remains an intriguing target. Stabilization of the complex using vanadyl (as described in Appendix C) may offer a viable route to crystallization. Preventing hydrolysis of the thioester amino acid-phosphopantetheine linkage (by substitution with an amide or other functionality) might also extend the lifetime of the complex. Alternatively, advances in cryo-electron microscopy (cryoEM) could potentially furnish a high resolution structure of the complex.

1.10.2 - Vibrational spectroscopy of SyrB2 ferryl intermediates in the presence of different substrates.

In 2013, Solomon and coworkers reported nuclear resonance vibrational spectra (NRVS) on the SyrB2 ferryl intermediate, prepared in the presence of **Cpg**.[63] NRVS spectra exclusively probe vibrational modes that include motion of ^{57}Fe. They used these spectra to validate a density functional theory (DFT) method, and then used this method to calculate reaction pathways for SyrB2 in the presence of **Thr** and **Nva**. These DFT calculation suggested that **Thr**

causes SyrB2 to stabilize an offline ferry geometry, whereas an online ferryl arises in the presence of **Nva**. A more direct probe of this hypothesis would be to measure NRVS spectra for the ferryl intermediates in the presence of **Thr** and **Nva** (rather than **Cpg**). Although these intermediates cannot be prepared in the remarkable concentration and purity achieved for **Cpg**, sufficient purity (60-80%) and concentration (~2 mM) should be achievable,[56] particularly with the use of chlorite dismutase as an O_2 source.[112] This more direct probe of the ferryl intermediate geometry could prove very illuminating in understanding the partitioning between online and offline ferryl intermediates in SyrB2, as well as other Fe/2OG enzymes.

1.10.3 - Using vanadyl to probe for offline ferryl intermediates in non-hydroxylating Fe/2OG enzymes

The use of the vanadyl ion as a structural mimic of ferryl intermediates has the potential to provide useful structural data in a wide variety of Fe/2OG enzymes. In particular, two different types of data are available from x-ray crystallography and pulse EPR. X-ray crystal structures of vanadyl complexes provide critical information about the overall placement of the substrate in the active site, protein-substrate interactions that enforce this positioning, and changes in these interactions that arise in the vanadyl complex compared to complexes with Fe(II) and 2OG. The power of this information has been demonstrated powerfully for the Fe/2OG hydroxylase VioC.[45] By contrast, pulse EPR studies can only yield information concerning positions of specifically-labeled positions, but this information can be extremely precise and detailed. Vanadyl complexes have been characterized by one or both of these techniques in the hydroxylases TauD and VioC, as well as the oxacyclase H6H. However, the investigation of vanadyl complexes in other Fe/2OG enzymes has the potential to be a rich source of mechanistic insight.

The positioning of **Thr**, **Aba**, and **Nva** in the active site has been examined using $\{FeNO\}^7$ complexes, but complementing these observations with vanadyl pulse EPR could confirm the previously observed trend with a probe more representative of the ferryl intermediate. Alternatively, any discrepancies could yield mechanistic insight. These studies are ongoing in our laboratory.

The role of substrate positioning in the Fe/2OG dehydrogenases is less clear than in the halogenases. However, comparison of vanadyl complexes of the L-arginine 4,5-dehydrogenase NapI to the related L-arginine hydroxylases VioC and OrfP could help to explain their differential reactivity (and regioselectivity). These experiments are also ongoing in our laboratory.

Vanadyl experiments in H6H indicate that this Fe/2OG oxacyclase does not stabilize an offline M(IV)-oxo in its second, epoxide forming turnover. Whether this is a general property of the oxacyclase class or Fe/2OG enzymes or a unique property of H6H is unknown. Examination of vanadyl complexes of the Fe/2OG oxacyclases LolO and CAS (see section 1.6.2) will be essential in answering this question. These experiments are also ongoing in our laboratory.

The presence of an offline ferryl intermediate in the Fe/2OG halogenase WelO5 has been assumed on the basis of observations in SyrB2. However, experiments with vanadyl have the potential to provide more direct evidence. A crystal structure of the vanadyl complex would perhaps be most direct. Pulse EPR experiments have not been feasible, because the complexity of the substrate does not lend itself to specific deuterium labeling. However, the orientation of vanadyl relative to the protein frame could be established by measuring orientation selective double electron-electron resonance (DEER) between vanadyl and strategically located spin

probes installed on the surface of the protein. These experiments are also ongoing in our laboratory.

1.11 - Literature Cited

(1) Solomon, E. I.; Brunold, T. C.; Davis, M. I.; Kemsley, J. N.; Lee, S.-K.; Lehnert, N.; Neese, F.; Skulan, A. J.; Yang, Y.-S.; Zhou, J. Geometric and Electronic Structure/Function Correlations in Non-Heme Iron Enzymes. *Chem. Rev.* **2000**, *100*, 235–350.

(2) Hausinger, R. P. Fe(II)/α-Ketoglutarate-Dependent Hydroxylases and Related Enzymes. *Crit. Rev. Biochem. Mol. Biol.* **2004**, *39*, 21–68.

(3) Costas, M.; Mehn, M. P.; Jensen, M. P.; Que, L., Jr. Dioxygen Activation at Mononuclear Nonheme Iron Active Sites: Enzymes, Models, and Intermediates. *Chem. Rev.* **2004**, *104*, 939–986.

(4) Bollinger, J. M., Jr.; Chang, W.-c.; Matthews, M. L.; Martinie, R. J.; Boal, A. K.; Krebs, C. Mechanisms of 2-Oxoglutarate-Dependent Oxygenases: The Hydroxylation Paradigm and Beyond. In *2-Oxoglutarate-Dependent Oxygenases*; Hausinger, R. P.; Schofield, C. J., Eds.; Royal Society of Chemistry, 2015.

(5) Kivirikko, K. I.; Myllyharju, J. Prolyl 4-Hydroxylases and Their Protein Disulfide Isomerase Subunit. *Matrix Biol.* **1998**, *16*, 357–368.

(6) Trewick, S. C.; Henshaw, T. F.; Hausinger, R. P.; Lindahl, T.; Sedgwick, B. Oxidative Demethylation by *Escherichia Coli* AlkB Directly Reverts DNA Base Damage. *Nature* **2002**, *419*, 174–178.

(7) Falnes, P. Ø.; Johansen, R. F.; Seeberg, E. AlkB-Mediated Oxidative Demethylation Reverses DNA Damage in Escherichia Coli. *Nature* **2002**, *419*, 178–182.

(8) Ivan, M.; Kondo, K.; Yang, H.; Kim, W.; Valiando, J.; Ohh, M.; Salic, A.; Asara, J. M.; Lane, W. S.; Jr, W. G. K. HIFα Targeted for VHL-Mediated Destruction by Proline Hydroxylation: Implications for O2 Sensing. *Science* **2001**, *292*, 464–468.

(9) Jaakkola, P.; Mole, D. R.; Tian, Y.-M.; Wilson, M. I.; Gielbert, J.; Gaskell, S. J.; Kriegsheim, A. von; Hebestreit, H. F.; Mukherji, M.; Schofield, C. J.; Maxwell, P. H.; Pugh, C. W.; Ratcliffe, P. J. Targeting of HIF-α to the von Hippel-Lindau Ubiquitylation Complex by O_2-Regulated Prolyl Hydroxylation. *Science* **2001**, *292*, 468–472.

(10) Epstein, A. C. R.; Gleadle, J. M.; McNeill, L. A.; Hewitson, K. S.; O'Rourke, J.; Mole, D. R.; Mukherji, M.; Metzen, E.; Wilson, M. I.; Dhanda, A.; Tian, Y; Masson, N.; Hamilton, D. L.; Jaakkola, P.; Barstead, R.; Hodgkin, J.; Maxwell, P. H.; Pugh, C. W.; Schofield, C. J.; Ratcliffe, P. J. *C. Elegans* EGL-9 and Mammalian Homologs Define a Family of Dioxygenases That Regulate HIF by Prolyl Hydroxylation. *Cell* **2001**, *107*, 43–54.

(11) Donovan, A.; Lima, C. A.; Pinkus, J. L.; Pinkus, G. S.; Zon, L. I.; Robine, S.; Andrews, N. C. The Iron Exporter Ferroportin/Slc40a1 Is Essential for Iron Homeostasis. *Cell Metab.* **2005**, *1*, 191–200.

(12) Gerken, T.; Girard, C. A.; Tung, Y.-C. L.; Webby, C. J.; Saudek, V.; Hewitson, K. S.; Yeo, G. S. H.; McDonough, M. A.; Cunliffe, S.; McNeill, L. A.; Galvanovkis, J.; Rorsman, P.; Robins, P.; Prieur, X.; Coll, A. P.; Ma, M.; Jovanovic, Z.; Farooqui, I. S.; Dedgwick, B.; Barroso, I.; Lindahl, T.; Ponting, C. P.; Ashcroft, F. M.; O'Rahilly, S.; Schofield, C. J. The Obesity-Associated FTO Gene Encodes a 2-Oxoglutarate-Dependent Nucleic Acid Demethylase. *Science* **2007**, *318*, 1469–1472.

(13) Tsukada, Y.; Fang, J.; Erdjument-Bromage, H.; Warren, M. E.; Borchers, C. H.; Tempst, P.; Zhang, Y. Histone Demethylation by a Family of JmjC Domain-Containing Proteins. *Nature* **2006**, *439*, 811–816.

(14) Cloos, P. A. C.; Christensen, J.; Agger, K.; Maiolica, A.; Rappsilber, J.; Antal, T.; Hansen, K. H.; Helin, K. The Putative Oncogene GASC1 Demethylates Tri- and Dimethylated Lysine 9 on Histone H3. *Nature* **2006**, *442*, 307–311.
(15) Klose, R. J.; Yamane, K.; Bae, Y.; Zhang, D.; Erdjument-Bromage, H.; Tempst, P.; Wong, J.; Zhang, Y. The Transcriptional Repressor JHDM3A Demethylates Trimethyl Histone H3 Lysine 9 and Lysine 36. *Nature* **2006**, *442*, 312–316.
(16) Ito, S.; Shen, L.; Dai, Q.; Wu, S. C.; Collins, L. B.; Swenberg, J. A.; He, C.; Zhang, Y. Tet Proteins Can Convert 5-Methylcytosine to 5-Formylcytosine and 5-Carboxylcytosine. *Science* **2011**, *333*, 1300–1303.
(17) He, Y.-F.; Li, B.-Z.; Li, Z.; Liu, P.; Wang, Y.; Tang, Q.; Ding, J.; Jia, Y.; Chen, Z.; Li, L.; Sun, Y.; Li, X.; Dai, Q.; Song, C.; Zhang, K.; He, C.; Xu, G. Tet-Mediated Formation of 5-Carboxylcytosine and Its Excision by TDG in Mammalian DNA. *Science* **2011**, *333*, 1303–1307.
(18) Hollenhorst, M. A.; Bumpus, S. B.; Matthews, M. L.; Bollinger, J. M.; Kelleher, N. L.; Walsh, C. T. The Nonribosomal Peptide Synthetase Enzyme DdaD Tethers N(β)-Fumaramoyl-L-2,3-Diaminopropionate for Fe(II)/α-Ketoglutarate-Dependent Epoxidation by DdaC during Dapdiamide Antibiotic Biosynthesis. *J. Am. Chem. Soc.* **2010**, *132*, 15773–15781.
(19) Vaillancourt, F. H.; Yin, J.; Walsh, C. T. SyrB2 in Syringomycin E Biosynthesis Is a Nonheme FeII α-Ketoglutarate- and O2-Dependent Halogenase. *Proc. Natl. Acad. Sci. U. S. A.* **2005**, *102*, 10111–10116.
(20) Vaillancourt, F. H.; Yeh, E.; Vosburg, D. A.; Garneau-Tsodikova, S.; Walsh, C. T. Nature's Inventory of Halogenation Catalysts: Oxidative Strategies Predominate. *Chem. Rev.* **2006**, *106*, 3364–3378.
(21) Hamed, R. B.; Gomez-Castellanos, J. R.; Henry, L.; Ducho, C.; McDonough, M. A.; Schofield, C. J. The Enzymes of β-Lactam Biosynthesis. *Nat. Prod. Rep.* **2013**, *30*, 21–107.
(22) Hiratsuka, T.; Koketsu, K.; Minami, A.; Kaneko, S.; Yamazaki, C.; Watanabe, K.; Oguri, H.; Oikawa, H. Core Assembly Mechanism of Quinocarcin/SF-1739: Bimodular Complex Nonribosomal Peptide Synthetases for Sequential Mannich-Type Reactions. *Chem. Biol.* **2013**, *20*, 1523–1535.
(23) Salowe, S. P.; Marsh, E. N.; Townsend, C. A. Purification and Characterization of Clavaminate Synthase from Streptomyces Clavuligerus: An Unusual Oxidative Enzyme in Natural Product Biosynthesis. *Biochemistry* **1990**, *29*, 6499–6508.
(24) Salowe, S. P.; Krol, W. J.; Iwata-Reuyl, D.; Townsend, C. A. Elucidation of the Order of Oxidations and Identification of an Intermediate in the Multistep Clavaminate Synthase Reaction. *Biochemistry* **1991**, *30*, 2281–2292.
(25) Hashimoto, T.; Yamada, Y. Hyoscyamine 6β-Hydroxylase, a 2-Oxoglutarate-Dependent Dioxygenase, in Alkaloid-Producing Root Cultures. *Plant Physiol.* **1986**, *81*, 619–625.
(26) Hashimoto, T.; Matsuda, J.; Yamada, Y. Two-Step Epoxidation of Hyoscyamine to Scopolamine Is Catalyzed by Bifunctional Hyoscyamine 6β-Hydroxylase. *FEBS Lett.* **1993**, *329*, 35–39.
(27) Schardl, C. L.; Grossman, R. B.; Nagabhyru, P.; Faulkner, J. R.; Mallik, U. P. Loline Alkaloids: Currencies of Mutualism. *Phytochemistry* **2007**, *68*, 980–996.

(28) Matsuda, Y.; Wakimoto, T.; Mori, T.; Awakawa, T.; Abe, I. Complete Biosynthetic Pathway of Anditomin: Nature's Sophisticated Synthetic Route to a Complex Fungal Meroterpenoid. *J. Am. Chem. Soc.* **2014**, *136*, 15326–15336.
(29) Steffan, N.; Grundmann, A.; Afiyatullov, S.; Ruan, H.; Li, S.-M. FtmOx1, a Non-Heme Fe(II) and α-Ketoglutarate-Dependent Dioxygenase, Catalyses the Endoperoxide Formation of Verruculogen in Aspergillus Fumigatus. *Org. Biomol. Chem.* **2009**, *7*, 4082–4087.
(30) Yan, W.; Song, H.; Song, F.; Guo, Y.; Wu, C.-H.; Sae Her, A.; Pu, Y.; Wang, S.; Naowarojna, N.; Weitz, A.; Hendrich, M. P.; Costello, C. E.; Zhang, L.; Liu, P.; Zhang, Y. J. Endoperoxide Formation by an α-Ketoglutarate-Dependent Mononuclear Non-Haem Iron Enzyme. *Nature* **2015**, *527*, 539–543.
(31) Li, R.; Stapon, A.; Blanchfield, J. T.; Townsend, C. A. Three Unusual Reactions Mediate Carbapenem and Carbapenam Biosynthesis. *J. Am. Chem. Soc.* **2000**, *122*, 9296–9297.
(32) Hanauske-Abel, H. M.; Günzler, V. A Stereochemical Concept for the Catalytic Mechanism of Prolylhydroxylase: Applicability to Classification and Design of Inhibitors. *J. Theor. Biol.* **1982**, *94*, 421–455.
(33) Que, L., Jr. One Motif — Many Different Reactions. *Nat. Struct. Mol. Biol.* **2000**, *7*, 182–184.
(34) Koehntop, K. D.; Emerson, J. P.; Que, L., Jr. The 2-His-1-Carboxylate Facial Triad: A Versatile Platform for Dioxygen Activation by Mononuclear Non-Heme iron(II) Enzymes. *J. Biol. Inorg. Chem.* **2005**, *10*, 87–93.
(35) Price, J. C.; Barr, E. W.; Tirupati, B.; Bollinger, J. M., Jr.; Krebs, C. The First Direct Characterization of a High-Valent Iron Intermediate in the Reaction of an α-Ketoglutarate-Dependent Dioxygenase: A High-Spin Fe(IV) Complex in Taurine/α-Ketoglutarate Dioxygenase (TauD) from Escherichia Coli†. *Biochemistry* **2003**, *42*, 7497–7508.
(36) Price, J. C.; Barr, E. W.; Hoffart, L. M.; Krebs, C.; Bollinger, J. M., Jr. Kinetic Dissection of the Catalytic Mechanism of Taurine:α-Ketoglutarate Dioxygenase (TauD) from *Escherichia Coli*. *Biochemistry* **2005**, *44*, 8138–8147.
(37) Krebs, C.; Galonić Fujimori, D.; Walsh, C. T.; Bollinger, J. M., Jr. Non-Heme Fe(IV)–Oxo Intermediates. *Acc. Chem. Res.* **2007**, *40*, 484–492.
(38) Krebs, C.; Price, J. C.; Baldwin, J.; Saleh, L.; Green, M. T.; Bollinger, J. M., Jr. Rapid Freeze-Quench ^{57}Fe Mössbauer Spectroscopy: Monitoring Changes of an Iron-Containing Active Site during a Biochemical Reaction. *Inorg. Chem.* **2005**, *44*, 742–757.
(39) Hoffart, L. M.; Barr, E. W.; Guyer, R. B.; Bollinger, J. M., Jr.; Krebs, C. Direct Spectroscopic Detection of a C-H-Cleaving High-Spin Fe(IV) Complex in a Prolyl-4-Hydroxylase. *Proc. Natl. Acad. Sci. U. S. A.* **2006**, *103*, 14738–14743.
(40) Price, J. C.; Barr, E. W.; Glass, T. E.; Krebs, C.; Bollinger, J. M., Jr. Evidence for Hydrogen Abstraction from C1 of Taurine by the High-Spin Fe(IV) Intermediate Detected during Oxygen Activation by Taurine:α-Ketoglutarate Dioxygenase (TauD). *J. Am. Chem. Soc.* **2003**, *125*, 13008–13009.
(41) Proshlyakov, D. A.; Henshaw, T. F.; Monterosso, G. R.; Ryle, M. J.; Hausinger, R. P. Direct Detection of Oxygen Intermediates in the Non-Heme Fe Enzyme Taurine/α-Ketoglutarate Dioxygenase. *J. Am. Chem. Soc.* **2004**, *126*, 1022–1023.
(42) Riggs-Gelasco, P. J.; Price, J. C.; Guyer, R. B.; Brehm, J. H.; Barr, E. W.; Bollinger, J. M., Jr.; Krebs, C. EXAFS Spectroscopic Evidence for an FeO Unit in the Fe(IV) Intermediate

Observed during Oxygen Activation by Taurine:α-Ketoglutarate Dioxygenase. *J. Am. Chem. Soc.* **2004**, *126*, 8108–8109.
(43) Ye, S.; Riplinger, C.; Hansen, A.; Krebs, C.; Bollinger, J. M., Jr.; Neese, F. Electronic Structure Analysis of the Oxygen-Activation Mechanism by Fe(II)- and α-Ketoglutarate (αKG)-Dependent Dioxygenases. *Chem. Eur. J.* **2012**, *18*, 6555–6567.
(44) Wójcik, A.; Radoń, M.; Borowski, T. Mechanism of O_2 Activation by α-Ketoglutarate Dependent Oxygenases Revisited. A Quantum Chemical Study. *J. Phys. Chem. A* **2016**, *120*, 1261–1274.
(45) Mitchell, A. J.; Dunham, N. P.; Martinie, R. J.; Bergman, J. A.; Pollock, C. J.; Hu, K.; Allen, B. D.; Chang, W.-c.; Silakov, A.; Bollinger, J. M., Jr.; Krebs, C.; Boal, A. K. Visualizing the Reaction Cycle in an Iron(II)- and 2-(Oxo)-Glutarate-Dependent Hydroxylase. *J. Am. Chem. Soc.* **2017**, *139*, 13830–13836.
(46) Grzyska, P. K.; Appelman, E. H.; Hausinger, R. P.; Proshlyakov, D. A. Insight into the Mechanism of an Iron Dioxygenase by Resolution of Steps Following the FeIV═O Species. *Proc. Natl. Acad. Sci. U. S. A.* **2010**, *107*, 3982–3987.
(47) Proshlyakov, D. A.; McCracken, J.; Hausinger, R. P. Spectroscopic Analyses of 2-Oxoglutarate-Dependent Oxygenases: TauD as a Case Study. *J. Biol. Inorg. Chem.* **2017**, *22*, 367–379.
(48) Gribble, G. W. Natural Organohalogens: A New Frontier for Medicinal Agents? *J. Chem. Educ.* **2004**, *81*, 1441.
(49) Pratter, S. M.; Ivkovic, J.; Birner-Gruenberger, R.; Breinbauer, R.; Zangger, K.; Straganz, G. D. More than Just a Halogenase: Modification of Fatty Acyl Moieties by a Trifunctional Metal Enzyme. *ChemBioChem* **2014**, *15*, 567–574.
(50) Pratter, S. M.; Light, K. M.; Solomon, E. I.; Straganz, G. D. The Role of Chloride in the Mechanism of O_2 Activation at the Mononuclear Nonheme Fe(II) Center of the Halogenase HctB. *J. Am. Chem. Soc.* **2014**, *136*, 9385–9395.
(51) Hillwig, M. L.; Liu, X. A New Family of Iron-Dependent Halogenases Acts on Freestanding Substrates. *Nat. Chem. Biol.* **2014**, *10*, 921–923.
(52) Mitchell, A. J.; Zhu, Q.; Maggiolo, A. O.; Ananth, N. R.; Hillwig, M. L.; Liu, X.; Boal, A. K. Structural Basis for Halogenation by Iron- and 2-Oxo-Glutarate-Dependent Enzyme WelO5. *Nat. Chem. Biol.* **2016**, *12*, 636–640.
(53) Blasiak, L. C.; Vaillancourt, F. H.; Walsh, C. T.; Drennan, C. L. Crystal Structure of the Non-Haem Iron Halogenase SyrB2 in Syringomycin Biosynthesis. *Nature* **2006**, *440*, 368–371.
(54) Tamanaha, E.; Zhang, B.; Guo, Y.; Chang, W.-c.; Barr, E. W.; Xing, G.; St. Clair, J.; Ye, S.; Neese, F.; Bollinger, J. M., Jr.; Krebs, C. Spectroscopic Evidence for the Two C–H-Cleaving Intermediates of Aspergillus Nidulans Isopenicillin N Synthase. *J. Am. Chem. Soc.* **2016**, *138*, 8862–8874.
(55) Galonić, D. P.; Barr, E. W.; Walsh, C. T.; Bollinger, J. M., Jr.; Krebs, C. Two Interconverting Fe(IV) Intermediates in Aliphatic Chlorination by the Halogenase CytC3. *Nat. Chem. Biol.* **2007**, *3*, 113–116.
(56) Matthews, M. L.; Krest, C. M.; Barr, E. W.; Vaillancourt, F. H.; Walsh, C. T.; Green, M. T.; Krebs, C.; Bollinger, J. M., Jr. Substrate-Triggered Formation and Remarkable Stability of the C−H Bond-Cleaving Chloroferryl Intermediate in the Aliphatic Halogenase, SyrB2. *Biochemistry* **2009**, *48*, 4331–4343.

(57) Galonić Fujimori, D.; Barr, E. W.; Matthews, M. L.; Koch, G. M.; Yonce, J. R.; Walsh, C. T.; Bollinger, J. M., Jr.; Krebs, C.; Riggs-Gelasco, P. J. Spectroscopic Evidence for a High-Spin Br-Fe(IV)-Oxo Intermediate in the α-Ketoglutarate-Dependent Halogenase CytC3 from Streptomyces. *J. Am. Chem. Soc.* **2007**, *129*, 13408–13409.
(58) de Visser, S. P.; Latifi, R. Carbon Dioxide: A Waste Product in the Catalytic Cycle of α-Ketoglutarate Dependent Halogenases Prevents the Formation of Hydroxylated By-Products. *J. Phys. Chem. B* **2009**, *113*, 12–14.
(59) Borowski, T.; Noack, H.; Radoń, M.; Zych, K.; Siegbahn, P. E. M. Mechanism of Selective Halogenation by SyrB2: A Computational Study. *J. Am. Chem. Soc.* **2010**, *132*, 12887–12898.
(60) Kulik, H. J.; Drennan, C. L. Substrate Placement Influences Reactivity in Non-Heme Fe(II) Halogenases and Hydroxylases. *J. Biol. Chem.* **2013**, *288*, 11233–11241.
(61) Matthews, M. L.; Neumann, C. S.; Miles, L. A.; Grove, T. L.; Booker, S. J.; Krebs, C.; Walsh, C. T.; Bollinger, J. M., Jr. Substrate Positioning Controls the Partition between Halogenation and Hydroxylation in the Aliphatic Halogenase, SyrB2. *Proc. Natl. Acad. Sci. U. S. A.* **2009**, *106*, 17723–17728.
(62) Martinie, R. J.; Livada, J.; Chang, W.-c.; Green, M. T.; Krebs, C.; Bollinger, J. M., Jr.; Silakov, A. Experimental Correlation of Substrate Position with Reaction Outcome in the Aliphatic Halogenase, SyrB2. *J. Am. Chem. Soc.* **2015**, *137*, 6912–6919.
(63) Wong, S. D.; Srnec, M.; Matthews, M. L.; Liu, L. V.; Kwak, Y.; Park, K.; Bell, C. B. I.; Alp, E. E.; Zhao, J.; Yoda, Y.; Kitao, S.; Seto, M.; Krebs, C.; Bollinger, J. M., Jr.; Solomon, E. I. Elucidation of the Fe(IV)=O Intermediate in the Catalytic Cycle of the Halogenase SyrB2. *Nature* **2013**, *499*, 320–323.
(64) Srnec, M.; Wong, S. D.; Matthews, M. L.; Krebs, C.; Bollinger, J. M., Jr.; Solomon, E. I. Electronic Structure of the Ferryl Intermediate in the α-Ketoglutarate Dependent Non-Heme Iron Halogenase SyrB2: Contributions to H Atom Abstraction Reactivity. *J. Am. Chem. Soc.* **2016**, *138*, 5110–5122.
(65) Fox, B. G.; Lyle, K. S.; Rogge, C. E. Reactions of the Diiron Enzyme Stearoyl-Acyl Carrier Protein Desaturase. *Acc. Chem. Res.* **2004**, *37*, 421–429.
(66) Meunier, B.; de Visser, S. P.; Shaik, S. Mechanism of Oxidation Reactions Catalyzed by Cytochrome P450 Enzymes. *Chem. Rev.* **2004**, *104*, 3947–3980.
(67) Lee, S. K.; Fox, B. G.; Froland, W. A.; Lipscomb, J. D.; Munck, E. A Transient Intermediate of the Methane Monooxygenase Catalytic Cycle Containing an FeIVFeIV Cluster. *J. Am. Chem. Soc.* **1993**, *115*, 6450–6451.
(68) Sleeman, M. C.; Smith, P.; Kellam, B.; Chhabra, S. R.; Bycroft, B. W.; Schofield, C. J. Biosynthesis of Carbapenem Antibiotics: New Carbapenam Substrates for Carbapenem Synthase (CarC). *ChemBioChem* **2004**, *5*, 879–882.
(69) Zhou, J.; Kelly, W. L.; Bachmann, B. O.; Gunsior, M.; Townsend, C. A.; Solomon, E. I. Spectroscopic Studies of Substrate Interactions with Clavaminate Synthase 2, a Multifunctional α-KG-Dependent Non-Heme Iron Enzyme: Correlation with Mechanisms and Reactivities. *J. Am. Chem. Soc.* **2001**, *123*, 7388–7398.
(70) Pu, J.-Y.; Peng, C.; Tang, M.-C.; Zhang, Y.; Guo, J.-P.; Song, L.-Q.; Hua, Q.; Tang, G.-L. Naphthyridinomycin Biosynthesis Revealing the Use of Leader Peptide to Guide Nonribosomal Peptide Assembly. *Org. Lett.* **2013**, *15*, 3674–3677.
(71) Ishikawa, N.; Tanaka, H.; Koyama, F.; Noguchi, H.; Wang, C. C. C.; Hotta, K.; Watanabe, K. Non-Heme Dioxygenase Catalyzes Atypical Oxidations of 6,7-Bicyclic Systems To

Form the 6,6-Quinolone Core of Viridicatin-Type Fungal Alkaloids. *Angew. Chem. Int. Ed.* **2014**, *53*, 12880–12884.
(72) Dunham, N. P.; Chang, W.-c.; Mitchell, A. J.; Martinie, R. J.; Zhang, B.; Bergman, J. A.; Rajakovich, L. J.; Wang, B.; Silakov, A.; Krebs, C.; Boal, A. K.; Bollinger, J. M., Jr. Two Distinct Mechanisms for C–C Desaturation by Iron(II)- and 2-(Oxo)glutarate-Dependent Oxygenases: Importance of α-Heteroatom Assistance. *J. Am. Chem. Soc.* **2018**, *140*, 7116–7126.
(73) Yin, X.; Zabriskie, T. M. VioC Is a Non-Heme Iron, α-Ketoglutarate-Dependent Oxygenase That Catalyzes the Formation of 3S-Hydroxy-L-Arginine during Viomycin Biosynthesis. *ChemBioChem* **2004**, *5*, 1274–1277.
(74) Helmetag, V.; Samel, S. A.; Thomas, M. G.; Marahiel, M. A.; Essen, L.-O. Structural Basis for the Erythro-Stereospecificity of the L-Arginine Oxygenase VioC in Viomycin Biosynthesis. *FEBS J.* **2009**, *276*, 3669–3682.
(75) Bräuer, A.; Beck, P.; Hintermann, L.; Groll, M. Structure of the Dioxygenase AsqJ: Mechanistic Insights into a One-Pot Multistep Quinolone Antibiotic Biosynthesis. *Angew. Chem. Int. Ed.* **2016**, *55*, 422–426.
(76) Su, H.; Sheng, X.; Zhu, W.; Ma, G.; Liu, Y. Mechanistic Insights into the Decoupled Desaturation and Epoxidation Catalyzed by Dioxygenase AsqJ Involved in the Biosynthesis of Quinolone Alkaloids. *ACS Catal.* **2017**, *7*, 5534–5543.
(77) Chang, W.-c.; Li, J.; Lee, J. L.; Cronican, A. A.; Guo, Y. Mechanistic Investigation of a Non-Heme Iron Enzyme Catalyzed Epoxidation in (−)-4′-Methoxycyclopenin Biosynthesis. *J. Am. Chem. Soc.* **2016**, *138*, 10390–10393.
(78) Cane, D. E.; Ikeda, H. Exploration and Mining of the Bacterial Terpenome. *Acc. Chem. Res.* **2012**, *45*, 463–472.
(79) Matsuda, Y.; Iwabuchi, T.; Fujimoto, T.; Awakawa, T.; Nakashima, Y.; Mori, T.; Zhang, H.; Hayashi, F.; Abe, I. Discovery of Key Dioxygenases That Diverged the Paraherquonin and Acetoxydehydroaustin Pathways in Penicillium Brasilianum. *J. Am. Chem. Soc.* **2016**, *138*, 12671–12677.
(80) The Antibiotic Alarm. *Nat. News* **2013**, *495*, 141.
(81) Parker, W. L.; Rathnum, M. L.; Wells, J. J. S.; Trejo, W. H.; Principe, P. A.; Sykes, R. B. SQ 27,860, a Simple Carbapenem Produced by Species of Serratia and Erwinia. *J. Antibiot.* **1982**, *35*, 653–660.
(82) Stapon, A.; Li, R.; Townsend, C. A. Carbapenem Biosynthesis: Confirmation of Stereochemical Assignments and the Role of CarC in the Ring Stereoinversion Process from L-Proline. *J. Am. Chem. Soc.* **2003**, *125*, 8486–8493.
(83) Chang, W.-c.; Guo, Y.; Wang, C.; Butch, S. E.; Rosenzweig, A. C.; Boal, A. K.; Krebs, C.; Bollinger, J. M., Jr. Mechanism of the C5 Stereoinversion Reaction in the Biosynthesis of Carbapenem Antibiotics. *Science* **2014**, *343*, 1140–1144.
(84) Clifton, I. J.; Doan, L. X.; Sleeman, M. C.; Topf, M.; Suzuki, H.; Wilmouth, R. C.; Schofield, C. J. Crystal Structure of Carbapenem Synthase (CarC). *J. Biol. Chem.* **2003**, *278*, 20843–20850.
(85) Ma, G.; Zhu, W.; Su, H.; Cheng, N.; Liu, Y. Uncoupled Epimerization and Desaturation by Carbapenem Synthase: Mechanistic Insights from QM/MM Studies. *ACS Catal.* **2015**, *5*, 5556–5566.

(86) Siitonen, V.; Selvaraj, B.; Niiranen, L.; Lindqvist, Y.; Schneider, G.; Metsä-Ketelä, M. Divergent Non-Heme Iron Enzymes in the Nogalamycin Biosynthetic Pathway. *Proc. Natl. Acad. Sci. U. S. A.* **2016**, *113*, 5251–5256.
(87) Dembitsky, V. M. Bioactive Fungal Endoperoxides. *Med. Mycol. Open Access* **2015**, *1*.
(88) Covello, P. S.; Teoh, K. H.; Polichuk, D. R.; Reed, D. W.; Nowak, G. Functional Genomics and the Biosynthesis of Artemisinin. *Phytochemistry* **2007**, *68*, 1864–1871.
(89) Kato, N.; Suzuki, H.; Takagi, H.; Uramoto, M.; Takahashi, S.; Osada, H. Gene Disruption and Biochemical Characterization of Verruculogen Synthase of Aspergillus Fumigatus. *ChemBioChem* **2011**, *12*, 711–714.
(90) Pan, J.; Bhardwaj, M.; Faulkner, J. R.; Nagabhyru, P.; Charlton, N. D.; Higashi, R. M.; Miller, A.-F.; Young, C. A.; Grossman, R. B.; Schardl, C. L. Ether Bridge Formation in Loline Alkaloid Biosynthesis. *Phytochemistry* **2014**, *98*, 60–68.
(91) McCulloch, K. M.; McCranie, E. K.; Smith, J. A.; Sarwar, M.; Mathieu, J. L.; Gitschlag, B. L.; Du, Y.; Bachmann, B. O.; Iverson, T. M. Oxidative Cyclizations in Orthosomycin Biosynthesis Expand the Known Chemistry of an Oxygenase Superfamily. *Proc. Natl. Acad. Sci. U. S. A.* **2015**, *112*, 11547–11552.
(92) Baldwin, J. E.; Bradley, M. Isopenicillin N Synthase: Mechanistic Studies. *Chem. Rev.* **1990**, *90*, 1079–1088.
(93) Liu, P.; Murakami, K.; Seki, T.; He, X.; Yeung, S.-M.; Kuzuyama, T.; Seto, H.; Liu, H. Protein Purification and Function Assignment of the Epoxidase Catalyzing the Formation of Fosfomycin. *J. Am. Chem. Soc.* **2001**, *123*, 4619–4620.
(94) Wang, C.; Chang, W.-c.; Guo, Y.; Huang, H.; Peck, S. C.; Pandelia, M. E.; Lin, G.; Liu, H.; Krebs, C.; Bollinger, J. M., Jr. Evidence That the Fosfomycin-Producing Epoxidase, HppE, Is a Non–Heme-Iron Peroxidase. *Science* **2013**, *342*, 991–995.
(95) Pan, J.; Bhardwaj, M.; Zhang, B.; Chang, W.-c.; Schardl, C. L.; Krebs, C.; Grossman, R. B.; Bollinger, J. M., Jr. Installation of the Ether Bridge of Lolines by the Iron- and 2-Oxoglutarate-Dependent Oxygenase, LolO: Regio- and Stereochemistry of Sequential Hydroxylation and Oxacyclization Reactions. *Biochemistry* **2018**, *57*, 2074–2083.
(96) Zhang, Z.; Ren, J.; Stammers, D. K.; Baldwin, J. E.; Harlos, K.; Schofield, C. J. Structural Origins of the Selectivity of the Trifunctional Oxygenase Clavaminic Acid Synthase. *Nat. Struct. Biol.* **2000**, *7*, 127–133.
(97) Borowski, T.; de Marothy, S.; Broclawik, E.; Schofield, C. J.; Siegbahn, P. E. M. Mechanism for Cyclization Reaction by Clavaminic Acid Synthase. Insights from Modeling Studies. *Biochemistry* **2007**, *46*, 3682–3691.
(98) Jakubczyk, D.; Caputi, L.; Stevenson, C. E. M.; Lawson, D. M.; O'Connor, S. E. Structural Characterization of EasH (Aspergillus Japonicus) – an Oxidase Involved in Cycloclavine Biosynthesis. *Chem. Commun.* **2016**, *52*, 14306–14309.
(99) Lau, W.; Sattely, E. S. Six Enzymes from Mayapple That Complete the Biosynthetic Pathway to the Etoposide Aglycone. *Science* **2015**, *349*, 1224–1228.
(100) Tang, M.-C.; Zou, Y.; Watanabe, K.; Walsh, C. T.; Tang, Y. Oxidative Cyclization in Natural Product Biosynthesis. *Chem. Rev.* **2017**, *117*, 5226–5333.
(101) Sinnecker, S.; Svensen, N.; Barr, E. W.; Ye, S.; Bollinger, J. M., Jr.; Neese, F.; Krebs, C. Spectroscopic and Computational Evaluation of the Structure of the High-Spin Fe(IV)-Oxo Intermediates in Taurine: α-Ketoglutarate Dioxygenase from *Escherichia Coli* and Its His99Ala Ligand Variant. *J. Am. Chem. Soc.* **2007**, *129*, 6168–6179.

(102) Stubbe, J.; van der Donk, W. A. Protein Radicals in Enzyme Catalysis. *Chem. Rev.* **1998**, *98*, 705–762.
(103) Stubbe, J.; Nocera, D. G.; Yee, C. S.; Chang, M. C. Y. Radical Initiation in the Class I Ribonucleotide Reductase: Long-Range Proton-Coupled Electron Transfer? *Chem. Rev.* **2003**, *103*, 2167–2202.
(104) Bollinger, J. M., Jr.; Edmondson, D. E.; Huynh, B. H.; Filley, J.; Norton, J. R.; Stubbe, J. Mechanism of Assembly of the Tyrosyl Radical-Dinuclear Iron Cluster Cofactor of Ribonucleotide Reductase. *Science* **1991**, *253*, 292–298.
(105) Cotruvo, J. A., Jr.; Stich, T. A.; Britt, R. D.; Stubbe, J. Mechanism of Assembly of the Dimanganese-Tyrosyl Radical Cofactor of Class Ib Ribonucleotide Reductase: Enzymatic Generation of Superoxide Is Required for Tyrosine Oxidation via a Mn(III)Mn(IV) Intermediate. *J. Am. Chem. Soc.* **2013**, *135*, 4027–4039.
(106) Jiang, W.; Yun, D.; Saleh, L.; Barr, E. W.; Xing, G.; Hoffart, L. M.; Maslak, M.-A.; Krebs, C.; Bollinger, J. M., Jr. A Manganese(IV)/Iron(III) Cofactor in Chlamydia Trachomatis Ribonucleotide Reductase. *Science* **2007**, *316*, 1188–1191.
(107) Shu, L.; Nesheim, J. C.; Kauffmann, K.; Münck, E.; Lipscomb, J. D.; Que, L., Jr. An $Fe_2^{IV}O_2$ Diamond Core Structure for the Key Intermediate Q of Methane Monooxygenase. *Science* **1997**, *275*, 515–518.
(108) Mitić, N.; Clay, M. D.; Saleh, L.; Bollinger, J. M., Jr.; Solomon, E. I. Spectroscopic and Electronic Structure Studies of Intermediate X in Ribonucleotide Reductase R2 and Two Variants: A Description of the FeIV-Oxo Bond in the FeIII−O−FeIV Dimer. *J. Am. Chem. Soc.* **2007**, *129*, 9049–9065.
(109) Dassama, L. M. K.; Silakov, A.; Krest, C. M.; Calixto, J. C.; Krebs, C.; Bollinger, J. M., Jr.; Green, M. T. A 2.8 Å Fe–Fe Separation in the $Fe_2^{III/IV}$ Intermediate, X, from *Escherichia Coli* Ribonucleotide Reductase. *J. Am. Chem. Soc.* **2013**, *135*, 16758–16761.
(110) Doan, P. E.; Shanmugam, M.; Stubbe, J.; Hoffman, B. M. Composition and Structure of the Inorganic Core of Relaxed Intermediate X(Y122F) of Escherichia Coli Ribonucleotide Reductase. *J. Am. Chem. Soc.* **2015**, *137*, 15558–15566.
(111) Younker, J. M.; Krest, C. M.; Jiang, W.; Krebs, C.; Bollinger, J. M., Jr.; Green, M. T. Structural Analysis of the Mn(IV)/Fe(III) Cofactor of Chlamydia Trachomatis Ribonucleotide Reductase by Extended X-Ray Absorption Fine Structure Spectroscopy and Density Functional Theory Calculations. *J. Am. Chem. Soc.* **2008**, *130*, 15022–15027.
(112) Dassama, L. M. K.; Yosca, T. H.; Conner, D. A.; Lee, M. H.; Blanc, B.; Streit, B. R.; Green, M. T.; DuBois, J. L.; Krebs, C.; Bollinger, J. M., Jr. O_2-Evolving Chlorite Dismutase as a Tool for Studying O_2-Utilizing Enzymes. *Biochemistry* **2012**, *51*, 1607–1616.

Chapter 2

Structural Factors Controlling Epoxidation Selectivity in Hyoscyamine 6β-Hydroxylase.

Acknowledgements

This material is based upon work supported by the National Science Foundation Graduate Research Fellowship Program under Grant No. DGE1255832. I gratefully acknowledge Ailiena Maggiolo, who performed all the crystallographic experiments under the supervision of Prof. Amie Boal. I also thank Prof. Ben Allen and his laboratory, who provided several of the contructs used to express H6H and who discovered the dihydroxylation activity of the L290F variant. We also thank our synthetic collaborators Richiro Ushimaru and Prof. Hung-wen Liu, who provided the deuterium-labeled substrates for this study. I thank Eli Wenger, who has taken over the H6H project and will be carrying it forward in the future; he performed several of the activity assays described here. Prof. Carsten Krebs and Prof. J. Martin Bollinger, Jr. provided critical feedback on the manuscript and throughout the study. Prof. Alexey Silakov provided valuable guidance in the analysis and presentation of the EPR data, in particular in mapping the EPR data onto the crystallographic data. Finally, Dr. Chris Pollock was the driving force behind the protein preparation, activity measurements, and stopped-flow measurements in this study. We designed some of the EPR experiments and prepared the samples together. In short, Chris was extensively involved throughout the project and it would not have been possible without his contributions.

Abstract

The Fe(II)- and 2-oxoglutarate-dependent (Fe/2OG) oxygenases catalyze a diverse array of chemical transformations, including hydroxylation, halogenation, oxacyclization, desaturation, endoperoxidation, and stereoinversion. The mechanisms by which these enzymes direct their reactivity to only one of these available outcomes are currently enigmatic, though it has been proposed that formation of an "offline" ferryl [Fe(IV)-oxo] oxo may be essential to avoiding hydroxylation. Hyoscyamine 6β-Hydroxylase (H6H) catalyzes an epoxidation of the alkaloid hyoscyamine to form scopolamine in two steps. In the first step, H6H hydroxylates hyoscyamine as is typical for Fe/2OG enzymes; the second step is a formal 1,3-dehydrogenation to form the epoxide. In this work, we show that this second turnover proceeds via hydrogen atom abstraction from C7, rather than from the newly-installed hydroxide as has been proposed for a related oxacyclase. Using vanadyl [V(IV)-oxo] as a structural mimic of the ferryl intermediates, we show that H6H does not stabilize an "offline" M(IV)-oxo in the second turnover, contrary to previous expectations. Finally, we show that H6H L290F catalyzes hydroxylation in the second turnover to much greater degree than WT; the modest perturbation of the substrate position relative to vanadyl suggests that fidelity for oxacyclization relies on precise positioning of an in-line oxo.

Introduction

The Fe(II)- and 2-oxoglutarate-dependent (Fe/2OG) oxygenases catalyze a diverse array of challenging chemical transformations in organisms across all domains of life.[1–4] These enzymes generally catalyze hydroxylation of an unactivated C-H bond; in humans and other organisms, these reactions play crucial roles in the biosynthesis of connective tissue,[5] iron homeostasis,[6] oxygen sensing,[7–9] regulation of body mass,[10] repair of DNA damage,[11–13] and control of transcription, differentiation, development and epigenetic inheritance.[14–18] Fe/2OG enzymes can also catalyze a number of alternative reaction outcomes, such as halogenation, oxacyclization, desaturation, endoperoxidation, and stereoinversion.[1] Plants, fungi, bacteria, and archaea leverage these reactions for secondary metabolism; in many cases, the resulting natural products have pharmaceutical potential as anti-cancer or anti-infective treatments.[1] However, the mechanisms that underlie these alternative transformations, and the methods by which the enzymes are able to direct powerful reactive intermediates towards a particular, desired chemical outcome, remain poorly understood.

The mechanism of action in the Fe/2OG enzyme family was first elucidated in the hydroxylase subclass.[19] The ferrous iron is coordinated by a $(His)_2(Glu/Asp)_1$ "facial triad" of protein ligands and bidentate 2OG;[20] oxygen activation occurs concomitant with oxidative decarboxylation of 2OG to form a succinate-coordinated Fe(IV)-oxo (ferryl) intermediate.[19,21–24] The ferryl intermediate abstracts a hydrogen atom (H•) from the target position of the substrate,[25] producing a substrate radical and an Fe(III)-hydroxo. The substrate radical then attacks the coordinated hydroxo (sometimes termed "oxygen rebound") to produce the hydroxylated product and Fe(II).[26]

All non-hydroxylating Fe/2OG enzymes characterized to date also activate oxygen to form a ferryl intermediate that performs an H• abstraction.[1,27–29] However, the mechanisms diverge after formation of the substrate radical. In the Fe/2OG halogenases, instead of attacking the coordinated hydroxo ligand, the substrate radical attacks a *cis* coordinated chlorine ligand.[28,30] Efficient H• abstraction would seemingly imply proximity of the target carbon to the ferryl oxo and, by extension, the hydroxo ligand in the radical attack step; such proximity would seemingly favor hydroxylation over the observed halogenation.[31] However, the Fe/2OG halogenases sacrifice proficiency in H• abstraction in favor of chlorination selectivity by enforcing a perpendicular approach of the target C-H bond relative to the ferryl oxo.[32] This arrangement has been suggested not to occur by structural repositioning of the substrate, but instead by repositioning the ferryl oxo in an "offline" configuration (i.e. *cis* to the distal His, rather than the standard *trans* configuration).[32–36]

The mechanisms of oxacycle-installing Fe/2OG oxygenases are less well understood. Several examples of this reactivity have been reported: hyoscyamine 6β-hydroxylase (H6H) installs an epoxide on hyoscyamine to produce the plant-derived alkaloid scopolamine,[37,38] clavaminic acid synthase (CAS) installs the five-membered ring of the β-lactamase inhibitor clavulanic acid,[39,40] and *N*-acetylnorloline synthase (LolO) catalyzes an oxacyclization in the biosynthesis of norloline, a fungal insecticide.[41–43] In this work, we examine the mechanism of epoxide formation in H6H, and delineate the structural factors that control selectivity for oxacycle formation in the second turnover. In each oxacycle forming enzyme, installation is proposed to proceed in two turnovers; the substrate is hydroxylated in the first turnover, followed by oxacycle formation (formally a 1,3 or 1,5-dehydrogenation) in the second turnover. In the case of H6H, the hydroxylation is proposed to occur at C6 of hyoscyamine (Scheme 1A).[37,38]

Following hydroxylation, two primary mechanisms have been proposed for oxacycle installation. In the first mechanism, the ferryl intermediate forms and abstracts H• from the carbon center to be coupled to oxygen (C7 in the case of H6H); the resulting carbon centered radical, instead of attacking the iron-coordinated hydroxo, participates in an intramolecular coupling with the hydroxide group installed in the first turnover, accompanied by electron transfer (ET) to the iron center (Scheme 1B and 1C). This mechanism is partially analogous to that of the Fe/2OG halogenases, with the exception that the hydroxo group is not coordinated to iron (Scheme 1E; the oxacyclases, unlike the halogenases, retain the full facial triad of protein ligands, making direct coordination unlikely), necessitating a through-space, rather than through-bond ET. Such a mechanism could proceed via a standard, in-line ferryl intermediate (Scheme 1B) or an offline ferryl, as proposed for the Fe/2OG halogenases (Scheme 1C). A second mechanism was proposed following the report of the crystal structure of CAS with the hydroxylated intermediate revealed that the C-H bond of the substrate is poorly positioned for H• abstraction, whereas the newly-installed oxygen is only 4.2 Å from iron, in good position for reaction with the ferryl intermediate.[44] Inspired by these findings, Borowski et al. proposed a unique mechanism beginning with ferryl-mediated H• abstraction from O3 and invoking a radical β-scission followed by a [3+2] dipolar cycloaddition to furnish the cyclized product (Scheme 1D).[45] Computations based on the structural coordinates supported this mechanism over the "ET" pathway.

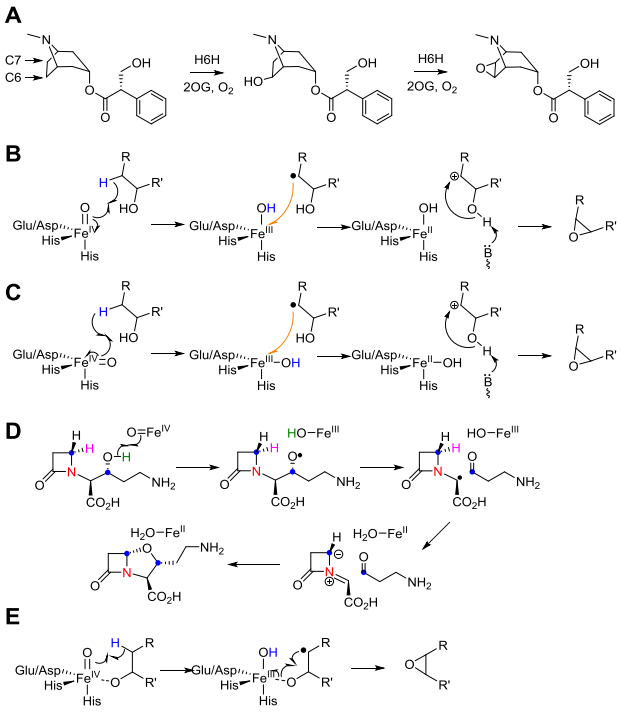

Scheme 1. Proposed mechanisms for oxacycle formation in Fe/2OG enzymes. **A**) H6H converts hyoscyamine to scopolamine in two turnovers, via a hydroxylated intermediate. **B**) Electron transfer, "ET," mechanism, initiated by H• abstraction from carbon by an in-line ferryl intermediate, followed by ET to the iron preceding or concomitant with attack of the hydroxo group. **C)** Electron transfer, "ET," mechanism, initiated by H• abstraction from carbon by an off-line ferryl intermediate. **D**) O-H abstraction mechanism proposed for CAS. **E**) Oxacyclization mechanism via "radical group transfer" mechanism, analogous to the Fe/2OG halogenases, dependent on transient coordination of the substrate hydroxyl group to iron.

Herein, we examine the mechanism of epoxide formation in H6H, in particular the structural factors which control its selectivity for oxacyclization over dihydroxylation in the

second turnover, using a combination of transient kinetic, structural, and spectroscopic approaches.

Results and Discussion

H6H produces scopolamine via a 6-hydroxy-hyoscyamine intermediate. In order to examine the key mechanistic questions in H6H, we first sought to unambiguously assign the regioselectivity of the first turnover, first reported to occur at C6 three decades ago.[37] When H6H is exposed to its substrate hyoscyamine in the presence of excess 2OG and O_2, a product with a mass of +14 Da relative to the substrate is detected by LC-MS, as expected for the epoxide product (Figure S1); furthermore, this product coelutes with authentic scopolamine (Figure S2). In the presence of limiting quantities of the co-substrate 2OG, a species with a mass shift of +16 Da is observed, consistent with a mono-hydroxylated intermediate (Figure 1A). Up to ~1 equivalent of 2OG, the intensity of the +16 Da species increases as substrate is consumed. Beyond ~1 equivalent, the +16 species decreases in intensity as the product peak (+14 Da) accumulates.

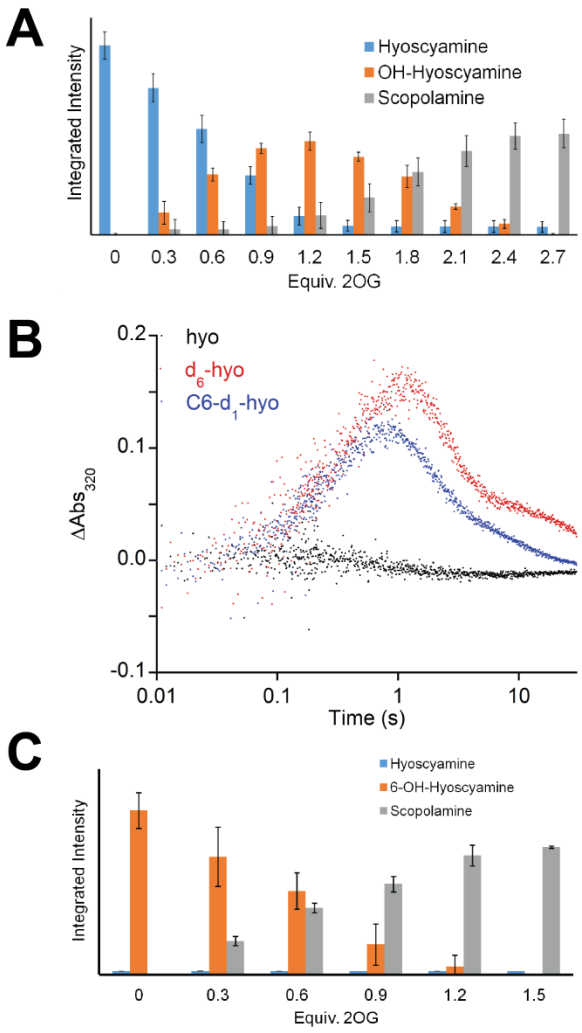

Figure 1. Conversion of hysoscyamine to scopolamine by hyoscyamine 6β-hydroxylase (H6H). **A**) H6H converts hysoscyamine (blue bars) to scopolamine (grey bars) via a mono-hydroxylated intermediate (orange bars). Concentrations of H6H, Fe(II), and hyoscyamine were 66, 60, and 60 μM, respectively. Equivalents of 2OG are reported with respect to Fe(II). **B**) Change in absorption at 320 nm when the H6H•Fe(II)•2OG•substrate complex is rapidly mixed with oxygen saturated buffer at 4°C when the complex is prepared with hyoscyamine (black), 1,5,6,6,7,7-[^{2}H]$_{6}$-hyoscyamine (red), and 6-^{2}H-hyoscyamine (6-*d*-Hyo, blue). Pre-mix concentrations of H6H, Fe(II), 2OG, and substrate were 750, 650, 2000, and 2000 μM, respectively. **C**) H6H converts synthetic 6-OH-Hyo (orange bars) to scopolamine (gray bars).

Concentrations of H6H, Fe(II), and hyoscyamine were 66, 60, and 60 μM, respectively. Error bars represent the standard deviation calculated from three independent experiments.

To examine the regiospecificity of the hydroxylation step, the enzyme was subjected to single-turnover kinetic experiments. When the H6H•Fe(II)•2OG•hyoscyamine is rapidly mixed with oxygen saturated buffer and monitored by stopped-flow absorption (SF-abs), no transient features are evident (Figure 1B, black). However, the reaction with oxygen of H6H•Fe(II)•2OG•1,5,6,6,7,7-[^{2}H]$_6$-hyoscyamine, in which all putative H• abstraction sites are labeled with deuterium, gives rise to a transient absorption feature at 320 nm with maximum accumulation at ~1 second (Figure 1B, red). As has been established in a large number of Fe/2OG enzymes, such features are associated with the accumulation of a ferryl intermediate.[1,19,21,27–29] The appearance of the feature only in the presence of the ^{2}H-labeled substrate is consistent with a large ^{2}H kinetic isotope effect on decay of the ferryl intermediate. Reaction with the substrate 6-^{2}H-hyoscyamine (6-*d*-Hyo) gives rise to a very similar kinetic trace (Figure 1B, blue), indicating that the first turnover reaction is initiated by H• abstraction from C6. The accumulation of the putative ferryl intermediate is modestly diminished in the presence of 6-*d*-Hyo, suggesting that a small percentage of ferryl decay events proceed by reaction with other tropane positions.

LC-MS analysis of the mono-hydroxylated intermediate in the reaction shows co-elution with synthetically prepared 6-hydroxy-hyoscyamine (6-OH-Hyo) (Figure S2). In addition, reaction with 6-^{2}H-hyoscyamine gives rise to a species with a mass shift of +15, indicating loss of the deuterium label, whereas reaction with 7-^{2}H-hyoscyamine gives rise to an intermediate

with a mass shift of +16, indicating retention of the label (Figure S3). Finally, reaction of the enzyme with synthetically prepared 6-OH-Hyo gives rise to the expected scopolamine product (Figure 1C); thus, 6-OH-Hyo is a chemically-competent intermediate. Together, these results definitively show that H6H catalyzes formation of scopolamine via a 6-OH-Hyo intermediate.

Epoxidation turnover is initiated by H• abstraction from C7. In order to probe the mechanism of epoxide formation in the second turnover of the H6H reaction, we examined single turnover kinetics of the reaction of H6H with 6-OH-Hyo. Some transient absorbance is observed with the unlabeled substrate, but the accumulation of a 320 nm feature is dramatically increased in the presence of 1,5,6,7,7-[^{2}H]$_5$-6-hydroxy-hyoscyamine (Figure 2). Notably, the maximum accumulation of the intermediate occurs over 10 seconds after mixing, substantially slower than the hydroxylation turnover. In addition, a nearly identical feature is observed in the presence of 7-^{2}H-6-hydroxy-hyoscyamine (7-*d*-6-OH-Hyo). The observation of a large kinetic isotope effect on decay of the ferryl intermediate in the presence of 7-*d*-6-OH-Hyo strongly suggests that the ferryl decays via H• abstraction from C7 of 6-OH-Hyo. Such an observation is consistent with a C-H H• abstraction mechanism, but not an O-H H• abstraction mechanism analogous to that proposed for CAS (Scheme 1).

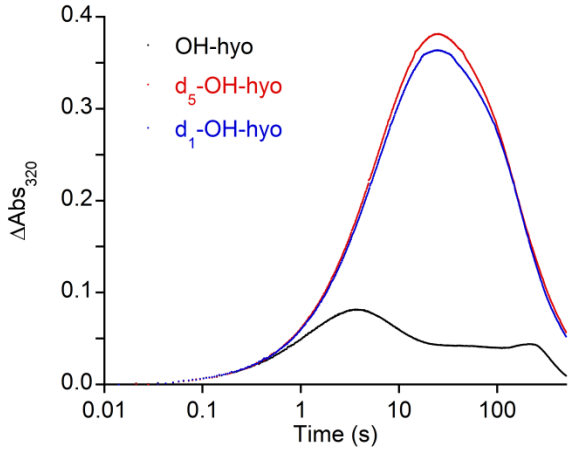

Figure 2. Change in absorption at 320 nm when the H6H•Fe(II)•2OG•substrate complex is rapidly mixed with oxygen saturated buffer at 4°C when the complex is prepared with 6-hydroxy-hyoscyamine (black), 1,5,6,7,7-[^{2}H]$_5$-6-hydroxy-hyoscyamine (red), and 7-^{2}H-6-hydroxy-hyoscyamine (blue). Pre-mix concentrations of H6H, Fe(II), 2OG, and substrate were 750, 650, 2000, and 2000 μM, respectively.

Structural factors controlling epoxidation selectivity in H6H. The observation that formation of the epoxide occurs via H• abstraction from C7 raises the question of how chemoselectivity favoring epoxidation over hydroxylation of C7 (to form a 6,7-dihydroxy-hyoscyamine product) is enforced in H6H. Previous studies in the Fe/2OG halogenases have suggested that structural factors, in particular substrate positioning, may be key to understanding this chemoselectivity.[31,32,34] In order to examine these structural factors, we solved a crystal structure of H6H to 2.5 Å resolution in complex with Fe(II) and hyoscyamine in the absence of O_2 (Figure 3 and Table S1). H6H possesses an overall cupin-type fold consistent with other structures of Fe/2OG enzymes (Figure 3A). Malate from the crystallization solution occupies the putative 2OG binding site in the structure; attempts to obtain high-quality crystals with the

cosubstrate bound were unsuccessful. However, electron density consistent with binding of the hyoscyamine substrate is clear (Figure 3B). The positions which undergo epoxidation, C6 and C7 of the tropane ring, are poised above the iron center (3.7 and 3.4 Å, respectively, for hydrons modeled based on expected bond distances and angles, Figure 3C) in good position for H• abstraction by the ferryl intermediate. Given that the C6, not C7, hydron is abstracted from hyoscyamine by the enzyme, the observation of a shorter distance to C7 is somewhat surprising. However, the angle of the Fe-H_{C6} vector relative to Fe-N_{His274} axis (and thus the expected Fe-O_{oxo} axis of a ferryl intermediate in the typical, "in-line" position) is ~10°, compared to ~40° for the Fe-H_{C7} vector. These angles suggest that a H• abstraction from C6 would proceed via σ-channel reactivity, whereas a C7 hydron would likely react via a π channel. A σ-channel reaction would be expected to proceed at a much greater rate,[46] presumably obviating the increased distance.

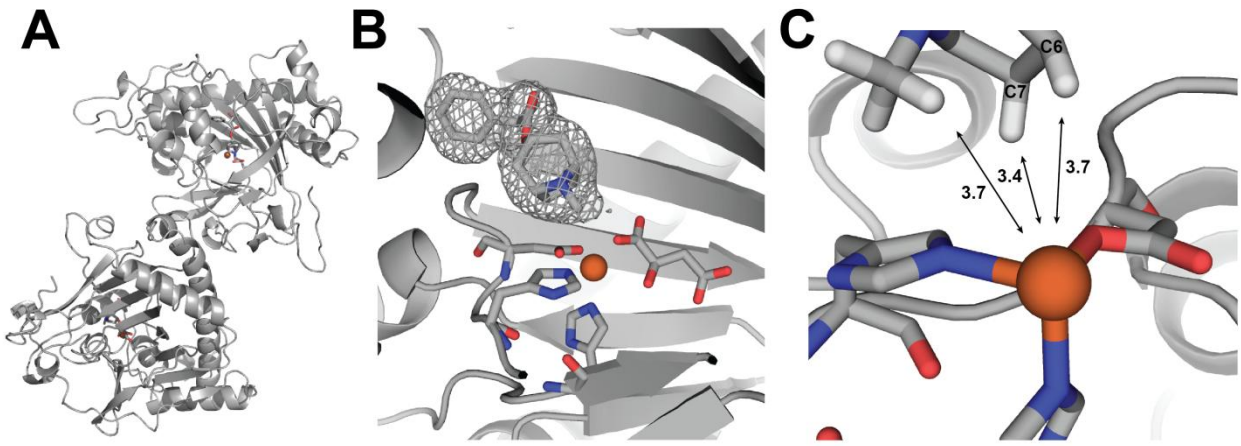

Figure 3. Structure of H6H. **A**) H6H forms a cupin fold, consistent with other Fe/2OG enzymes. **B**) Hyoscyamine is present in the active site, with the tropane ring above the iron center poised for reactivity. The omit map depicted was generated by substrate deletion followed by

refinement, contoured to 3.0 σ. **C**) Distances to hyoscyamine hydrons (modeled based on expected bond lengths and angles).

In addition, we solved a second crystal structure of H6H in complex with Fe(II) and 6-OH-Hyo to 2.1 Å resolution (Figure S4 and Table S1); once again, malate is bound in place of 2OG. No major structural changes accompany the enzyme being poised for the second (epoxide-forming) turnover compared to the first (hydroxylating) turnover (Figure S5). The hydroxo group at C6 lies above the iron center, ~2.6 Å away; examination of the electron density map reveals continuous electron density between iron and oxygen (Figure S4), suggesting the hydroxide may be weakly coordinating. Although it is tempting to speculate that such coordination could allow a "radical group transfer mechanism" similar to that proposed for the Fe/2OG halogenases and the related mononuclear iron-dependent enzyme isopenicillin-N-synthase (Scheme 1E),[1,28,47] coordination by the substrate after binding of 2OG would leave the iron center coordinatively saturated and unable to react with O_2. More likely, the hydroxylated product remains coordinated following the first turnover (as has recently been observed in the Fe/2OG hydroxylase VioC),[48] but formation of the full enzyme•Fe(II)•2OG•substrate complex is accompanied by dissociation of the weak substrate coordination, in analogy to the loss of the water ligand in other Fe/2OG enzymes.[2] Together, these structures provide a detailed picture of the overall structure of H6H and the general positioning of hyoscyamine and 6-OH-Hyo in the active site; however, given the lack of 2OG and the possibility of substrate and active site rearrangements in the reactive ferryl state compared to the reactant complex,[48] precise conclusions concerning the disposition of the substrate are difficult to draw.

Examination of hyoscyamine binding to H6H in the presence of a ferryl-mimicking vanadyl complex. Given the incomplete nature of the enzyme complexes observed in our x-ray

crystal structures, we investigated the structure of an H6H•vanadyl•succinate•hyoscyamine complex. Vanadyl [V(IV)-oxo] has recently been shown to serve as a remarkably faithful structural mimic of ferryl [Fe(IV)-oxo] intermediates in Fe/2OG enzymes.[49] In addition to forming a distorted octahedral complex with enzyme and succinate analogous to that proposed for the ferryl intermediate:[48–50] i) DFT calculations based on the x-ray crystal structure of the vanadyl complex in the L-arginine 3-hydroxylase, VioC correctly predict the ferryl Mössbauer parameters obtained in rapid-freeze-quench experiments;[48] ii) the disposition of the substrate analog, L-homoarginine, relative to the vanadyl center in VioC is consistent with its altered reactivity (mixture of H• abstraction from C3 and C4), whereas its disposition in the corresponding x-ray crystal structure of the Fe(II) reactant complex is not;[51] and iii) vanadyl induces formation of a stable complex between the Fe/2OG halogenase SyrB2 and its protein substrate SyrB1, an effect previously observed only for the ferryl intermediate.[49] Because vanadyl is electron paramagnetic resonance (EPR) active (Figure S6), structural information in vanadyl complexes can be obtained by measuring hyperfine (HF) couplings between vanadyl and specifically-^{2}H-labeled substrates using hyperfine sublevel correlation (HYSCORE) spectroscopy. H6H•vanadyl•succinate•substrate complexes were prepared with 6-*d*-Hyo, 7-^{2}H-hyoscyamine (7-*d*-Hyo), methyl-[^{2}H]$_3$-hyoscyamine (methyl-d_3-Hyo), and unlabeled hyoscyamine; the presence of ^{2}H-associated signals in the labeled complexes indicates that, as expected, the labeled positions are in relative proximity to the vanadium (Figure 4).

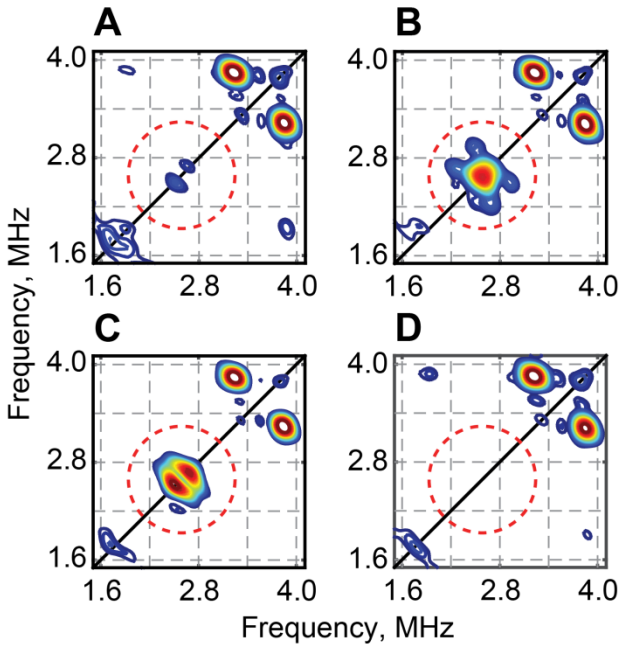

Figure 4. HYSCORE spectra of H6H•vanadyl•succinate•substrate complexes in the presence of 6-*d*-Hyo (**A**), 7-*d*-Hyo (**B**), methyl-d_3-Hyo (**C**), and unlabelled hyoscyamine (**D**). The region of the spectrum associated with deuterium is denoted by the red-dashed circle. Spectra were collected at 396 mT and 35 K with microwave frequency 9.434 GHz.

The field-dependent HYSCORE spectra can be related to the position of the deuteron relative to the V-O_{oxo} vector. The corresponding distances for C6, C7, and the N8-methyl group are 3.8 ± 0.3, 3.3 ± 0.1, and 3.3 ± 0.1 Å, respectively (Figures S7-S10). Consistent with the crystal structure, C7 is somewhat closer to the metal than C6 (Figure 3C). In addition, the O-V-^{2}H angle observed for 7-*d*-Hyo is 40 ± 5°, in good agreement with the crystal structure, assuming an in-line ferryl arrangement (Figure S11). Since the ^{2}H-associated signals for 6-*d*-Hyo are relatively weak (Figure 4A and S10), an O-V-^{2}H angle cannot be determined with certainty, though the data are consistent with the ~10-20° angle expected from the crystal structure.

Overall, these data support the structural insight obtained from the crystal structure and indicate that both C6 and C7 are in position to react by H• abstraction in a state mimicking the structure of the ferryl intermediate.

Does H6H stabilize an offline M(IV)-oxo to avoid hydroxylation in its second turnover? It has been suggested that the Fe/2OG halogenases stabilize an offline ferryl oxo in order to minimize adventitious hydroxylation activity and promote halogenation selectivity.[32–34] Moreover, it has been hypothesized that this may be a general mechanism in non-hydroxylating Fe/2OG enzymes.[1] H6H provides an ideal system to test this hypothesis; since the first turnover is a hydroxylation and the second is a dehydrogenation/oxacyclization, the enzyme would be expected to stabilize an inline ferryl in the presence of hyoscyamine (first turnover, hydroxylation) and an offline ferryl in the presence of 6-OH-Hyo (second turnover, oxacyclization, Scheme 1C). Using vanadyl as a ferryl surrogate in the presence of 7-*d*-Hyo and 7-*d*-6-OH-Hyo, the O-V-^{2}H angle can be measured via field-dependent HYSCORE (*vide supra*). In the H6H•vanadyl•succinate•7-*d*-Hyo complex, this angle is 40 ± 5° (Figure S8), similar to the angles observed in vanadyl complexes of Fe/2OG hydroxylases TauD and VioC,[48,49] and consistent with an inline oxo geometry and the crystallographic data (Figure S11). In addition, an angle of 25 ± 5° is observed between the C-H and V-O_{oxo} vectors (Figure 5). If the offline ferryl hypothesis is correct, one would expect both of these angles to become significantly less acute (~50 and ~65° for the O-V-^{2}H and C-H/V-O angles, respectively; Figure 5) in the presence of 7-*d*-6-OH-Hyo, barring significant rearrangement of the substrate. Since no such rearrangement is observed in the crystal structures with hyoscyamine and 6-hydroxy-hyoscyamine (Figure S5), such a rearrangement seems unlikely. Thus, these angles can be used to report the disposition of the oxo relative to the C7-^{2}H bond.

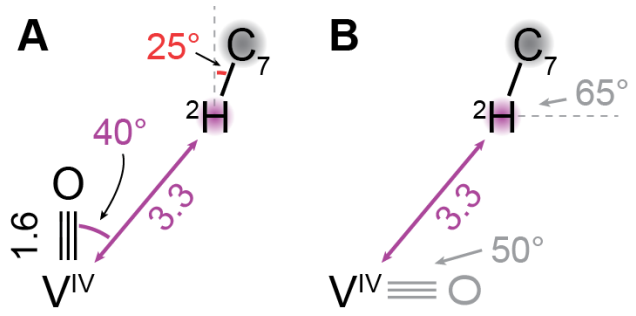

Figure 5. Simplified, two-dimensional representation of the disposition of the C_7-H bond of hyoscyamine/6-OH-Hyo relative to vanadyl, including the O-V-^{2}H angle (blue) and C-H/V-O angle (red). **A**) Distances and angles derived from simulation of field-dependent ^{2}H-HYSCORE of the H6H•vanadyl•succinate•7-*d*-Hyo complex. V-O distance is derived from previous EXAFS experiments.[49] **B**) Approximate expected angles for an offline vanadyl conformation, assuming no substrate rearrangement (grey).

Contrary to this expectation of a significant change in angle, the field-dependent ^{2}H-HYSCORE patterns observed for the H6H•vanadyl•succinate•7-*d*-6-OH-Hyo complex are nearly identical to those observed for H6H•vanadyl•succinate•7-*d*-Hyo (Figure 6). Indeed, simulation of the data from 7-*d*-6-OH-Hyo yields O-V-^{2}H and C-H/V-O angles of 37 ± 5° and 25 ± 5°, respectively, and a V-^{2}H distance of 3.4 ± 0.1 Å (Figures S12 and S13).

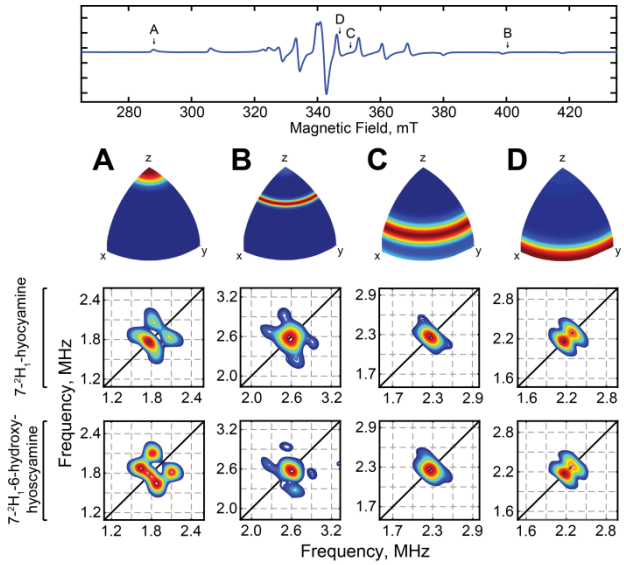

Figure 6. Comparison of ^{2}H-HYSCORE patterns observed for vanadyl complexes of H6H in the presence of 7-*d*-Hyo (above) 7-*d*-6-OH-Hyo (below) at 280 mT (**A**), 396 mT (**B**), 344 mT (**C**), and 340 mT (**D**). Orientation selectivities probed by each magnetic field position (shown above) are color coded (red - fully excited; blue, not excited). Magnetic field positions are indicated by black arrows on the one-dimensional EPR spectrum (top)

Given the sensitivity of these measurements to changes in the disposition of the C-H bond relative to V-O_{oxo} (or in this case, *vice versa*), these data are seemingly inconsistent with the stabilization of an offline M(IV)-oxo in the presence of 6-hydroxy-hyoscyamine. However, the two-dimensional representation in Figure 5 and the assumption of a perfect 90° shift in oxo position from in-line to offline are relatively simplistic. To more robustly examine the disposition of the vanadyl oxo in three dimensions, we calculated V-O_{oxo} vectors consistent with these EPR data and the position of the substrate as determined in the crystal structures (Figure 7). This calculation was performed taking into account i) the V-^{2}H distance from EPR, ii) the

O_{oxo}-V-^{2}H angle from EPR, iii) the C-H/V-O angle from EPR, and iv) the C-H-Fe angle from the crystal structure, taking into account the associated experimental uncertainty from each method. This visualization was performed with the hyoscyamine crystal structure, but due to the similarity of the ^{2}H hyperfine parameters, an analogous visualization with 6-OH-Hyo is nearly identical. The center of the distribution lies very nearly trans to the distal histidine, as expected for an in-line ferryl. The "wings" of the distribution are less compatible with the observed EPR parameters; moreover, these positions would likely be sterically occluded by the aspartate and succinate ligands. Overall, the visualization reinforces the conclusion that H6H stabilizes an in-line vanadyl conformation in the presense of both hyoscyamine and 6-OH-Hyo. It is, of course, possible that the vanadyl does not accurately mimic the structure of the ferryl intermediate in this case, though the excellent structural mimicry observed previously in multiple Fe/2OG enzymes weighs against this possibility.[48,49,51] Moreover, these conclusions are dependent on the assumption that the substrate position does not undergo significant rearrangement in the vanadyl complex relative to our crystal structures (as stated above). Given the rigidity of the tropane ring and the observation that minimal rearrangement occurs in the presence of 6-OH-Hyo compared to hyoscyamine, any such perturbations would be expected to be modest and therefore to be fully consistent with an in-line vanadyl configuration. Nevertheless, such subtle perturbations could be relevant to the control of reactivity in the epoxide-forming step, and further structural characterization of H6H could be of significant interest.

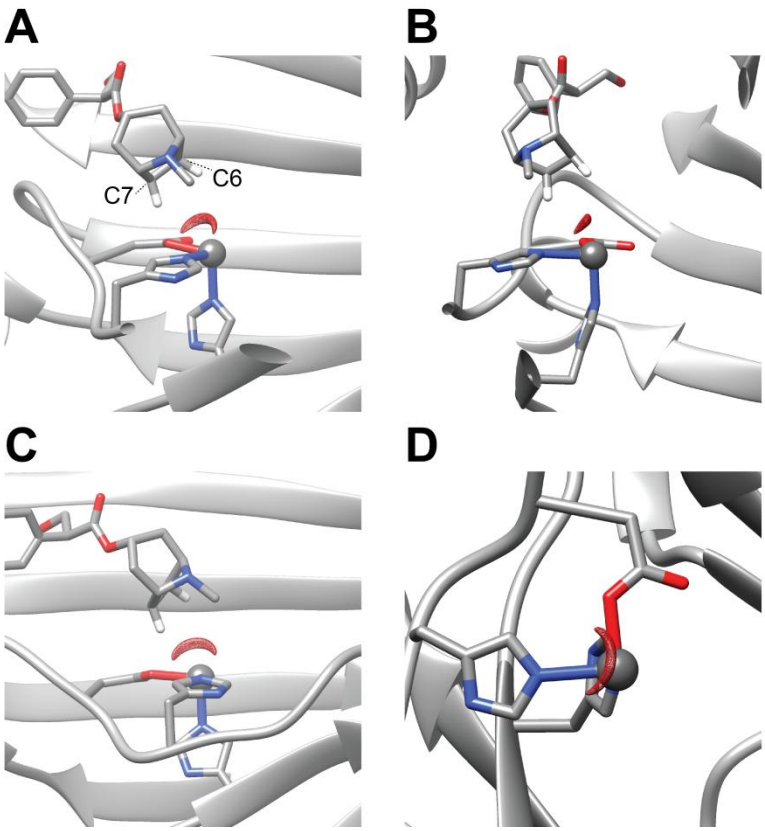

Figure 7. Vanadyl oxo positions compatible with the ^{2}H-HYSCORE data superimposed on the H6H•Fe(II)•hyoscyamine crystal structure. Compatible positions are displayed as a red mesh surface, contoured at 50% of maximum agreement with the observed EPR parameters.

Structural factors that promote second turnover hydroxylation in L290F H6H. Since H6H seemingly does not stabilize an offline M(IV)-oxo in the presence of 6-OH-Hyo, we sought to examine other factors that might affect reaction selectivity in the second turnover. To do this, we examined an L290F variant of H6H; unlike WT H6H, this mutant catalyzes appreciable 6,7-dihydroxylation of hyoscyamine, along with diminution of the epoxidized product (Figure S14). L290 is located in the substrate binding pocket of H6H (Figure S15); substitution of this residue with the bulkier phenylalanine might be expected to alter the substrate position, leading to

hydroxylation in the second turnover. To examine the structural factors which might promote a C7 hydroxylation, rather than cyclization in the second turnover, we collected field-dependent HYSCORE for the L290F-H6H•vanadyl•succinate•7-*d*-6-OH-Hyo complex. Simulation of these data (Figures S16 and S17) yields a marginally stronger HF coupling, corresponding to a distance of 3.26 ± 0.1 Å (compared to 3.41 ± 0.1 Å for WT); although this distance is close to the limit of precision in these measurements, the data suggest that the C7 hydron is modestly closer to vanadium, consistent with the added steric bulk of the phenylalanine substitution. The O-V-^{2}H and C-H/V-O angles are similar to those observed in WT (35° vs. 37° and 20° vs. 25°, respectively). This observation suggests that the precise M-^{2}H distance is critical for efficient cyclization activity, and potentially other non-hydroxylation outcomes as well.

Conclusions

Herein, we have examined the mechanism of epoxide formation in H6H. H6H activates C6 of hyoscyamine for hydroxylation in its first turnover; the second turnover converts 6-hydroxy-hyoscyamine to scopolamine in a dehydrogenation/oxacyclization reaction initiated by H• abstraction from C7. This rules out the class of oxacyclization mechanisms proposed to begin with O-H cleavage. Further, we have examined the structural factors that contribute to oxacyclization selectivity using x-ray crystallography and pulse EPR methods. Both C6 and C7 of hyoscyamine are poised for H• abstraction, with C6 more directly above the metal center. Minimal substrate movement is observed in crystal structures containing 6-hydroxy-hyoscyamine relative to hyoscyamine. Using vanadyl as a structural mimic of the ferryl intermediate, we examined whether H6H is able to preferentially stabilize an "offline" M(IV)-

oxo in the presence of its epoxidation substrate 6-OH-Hyo. The EPR data provide no evidence for such stabilization; the disposition of the C7-^{2}H bond is remarkably consistent in the first and second turnovers, suggesting that an offline ferryl is not required for H6H to achieve selectivity for oxacyclization in preference to a second hydroxylation. In an L290F variant of H6H that does catalyze dihydroxylation of hyoscyamine, we observe a modest decrease in M-^{2}H distance compared to WT, suggesting that precise control over this distance is a key factor in the reaction control.

Materials and Methods

Expression and purification of H6H

H6H gene *Hyoscyamus niger* was expressed in *E. coli* with a C-terminal His_8 tag. After cell lysis, H6H was purified by immobilized metal-ion affinity chromatography. The tag was then removed by cleavage with the protease from tobacco etch virus, followed by a second application to the metal-ion affinity chromatography column; untagged H6H was then collected from the flow-through. Protein was then subjected to size exclusion chromatography using a Superdex 200 pg column and anion exchange chromatography with a HiPrep DEAE FF column (GE Healthcare). For further details, see Supporting Information.

Activity assays of H6H.

In a typical assay, anaerobic enzyme was mixed with ferrous ammonium sulfate, 2OG, and substrate in an anoxic chamber (MBRAUN). The resulting solution was removed from the chamber, and two volumes of air-saturated buffer were added. This mixture was allowed to react

at 4 °C, and the reaction was terminated by removal of the enzyme via spin filtration. The solution was then examined using a Agilent 1200 series LC system coupled to an Agilent 6410 QQQ mass spectrometer. Chromatography was carried out using an Agilent 1.8 μm extended C-18 (4.6 x 50 mm) column, with detection by electrospray ionization MS in positive ion mode. For further details, see Supporting Information.

Stopped-flow UV-visible absorption spectroscopy

Stopped-flow absorption experiments were performed on an Applied Photophysics Ltd. (Leatherhead, UK) SX-20 stopped-flow spectrophotometer housed in an MBraun (Stratham, NH) anoxic chamber. Reactions were carried out at 5 °C in a single-mixing configuration with a 1 cm path length and a photodiode-array (PDA) detector. Additional details are provided in the appropriate figure legends.

Crystallization and structure solution of H6H

*Hn*H6H lacking an affinity tag was purified from *E. coli* (for details, see Supporting Information) and prepared for crystallization by deoxygenating the apo-enzyme with argon gas prior to crystallization. The protein (10 mg/mL in 20 mM Tris-HCl pH 7.5, 80 mM KCl buffer) was equilibrated for 10 minutes at RT in an N_2 (3% hydrogen) atmosphere glove box (Coy Laboratory Products) with 1 molar equivalent of iron(II)ammonium sulfate, 5 equivalents of 2-OG, and 5 equivalents substrate solubilized in buffer, before crystal drop set-up. Crystals were obtained by mixing 1 μL of protein solution with 1 μL of a pre-made crystallization solution from the 96 well JCSG+ sparse matrix screen (well F8) purchased from Qiagen (NeXtal Suites). The crystals were soaked in cryoprotectant containing 20% (v/v) PEG 400, 0.1 M Tris-HCl pH

7.5, and 16% (v/v) ethylene glycol prior to mounting on rayon loops and flash freezing in liquid N_2.

All crystallographic datasets were collected at either the Life Sciences Collaborative Access Team (LS-CAT) or the National Institute of General Medical Science and National Cancer Institute Collaborative Access Team (GM/CA-CAT) beamlines at the Advanced Photon Source (Argonne National Laboratory). Phases were determined using the online molecular replacement server BALBES,[52] which identified the coordinates of anthocyanidin synthase from *Abrabidopsis thaliana* (PDB accession code 1GP6),[53] an Fe/2-OG enzyme that shares ~28% sequence identity to *Hn*H6H, as the initial search model. For additional details, see Supporting Information.

EPR sample preparation

H6H-vanadyl complexes were prepared in a manner analogous to that previously described.[49] H6H, vanadyl sulfate, succinate, and substrate were mixed anaerobically, transferred to EPR tubes (4.0 mm O.D., 3.0 mm I.D.), and frozen in liquid nitrogen. For WT samples in complex with 7-*d*-Hyo, 6-*d*-Hyo, hyoscyamine, 7-*d*-6-OH-Hyo, and 6-OH-Hyo; H6H, vanadyl sulfate, succinate, and substrate were mixed to concentrations of 2.9 mM, 2.6 mM, 10 mM, and 10 mM, respectively. For WT samples in complex with methyl-d_3-Hyo and H6H L290F samples in complex with 7-*d*-6-OH-Hyo, and 6-OH-Hyo, H6H, vanadyl sulfate, succinate, and substrate were mixed to concentrations of 1.4 mM, 1.3 mM, 7.0 mM, and 4.4 mM, respectively.

EPR measurements

X-band continuous wave (CW) measurements were performed on a Bruker ESP 300 spectrometer with an ER 041 MR microwave bridge and an ER 4116DM resonator.

Measurements were performed at 80 K, with a microwave power 200 μW, 10 Gauss modulation amplitude, and 80 ms conversion time. Pulse EPR measurements were performed on a Bruker Elexsys E580 X-band spectrometer equipped with a SuperX-FT microwave bridge. A Bruker ER 4118X-MS5 resonator was used in combination with an Oxford CF935 helium flow cryostat. Microwave pulses generated by the microwave bridge were amplified by a 1 kW traveling wave tube (TWT) amplifier (Applied Systems Engineering, model 117x).

EPR analysis

Data processing and spectral simulations were performed using Kazan Viewer, a home-written suite of utilities in MATLAB (MATLAB r2015a, The Mathworks Inc.). One-dimensional EPR simulations were performed using the "pepper" utility from the EasySpin software package.[54] HYSCORE data were analyzed by simultaneous frequency-domain simulation of all field-dependent spectra until a satisfactory solution was achieved. Euler angles are reported with respect to the ^{51}V hyperfine coupling tensor, which is colinear with the g matrix in our simulations. Geometric information was calculated using a point-dipole model, according to the formula $T_{VD}(MHz) = 12.1362 r_{VD}^{-3}$. Deviations from this idealized model could result from significant delocalization of spin density onto the vanadyl-oxo ligand. However, available experimental and theoretical results suggest that this delocalization is likely to be 5-20%.[55,56] At these levels of spin density on oxygen, deviations from the point dipole model are calculated using a geometric model to be within the stated experimental errors.

Literature Cited

(1) Bollinger, J. M., Jr.; Chang, W.-c.; Matthews, M. L.; Martinie, R. J.; Boal, A. K.; Krebs, C. Mechanisms of 2-Oxoglutarate-Dependent Oxygenases: The Hydroxylation Paradigm and Beyond. In *2-Oxoglutarate-Dependent Oxygenases*; Hausinger, R. P., Schofield, C. J., Eds.; RSC Metallobiology; Royal Society of Chemistry, 2015.

(2) Solomon, E. I.; Brunold, T. C.; Davis, M. I.; Kemsley, J. N.; Lee, S.-K.; Lehnert, N.; Neese, F.; Skulan, A. J.; Yang, Y.-S.; Zhou, J. Geometric and Electronic Structure/Function Correlations in Non-Heme Iron Enzymes. *Chem. Rev.* **2000**, *100*, 235–350.

(3) Hausinger, R. P. Fe(II)/α-Ketoglutarate-Dependent Hydroxylases and Related Enzymes. *Crit. Rev. Biochem. Mol. Biol.* **2004**, *39*, 21–68.

(4) Costas, M.; Mehn, M. P.; Jensen, M. P.; Que, L., Jr. Dioxygen Activation at Mononuclear Nonheme Iron Active Sites: Enzymes, Models, and Intermediates. *Chem. Rev.* **2004**, *104*, 939–986.

(5) Kivirikko, K. I.; Myllyharju, J. Prolyl 4-Hydroxylases and Their Protein Disulfide Isomerase Subunit. *Matrix Biol.* **1998**, *16*, 357–368.

(6) Donovan, A.; Lima, C. A.; Pinkus, J. L.; Pinkus, G. S.; Zon, L. I.; Robine, S.; Andrews, N. C. The Iron Exporter Ferroportin/Slc40a1 Is Essential for Iron Homeostasis. *Cell Metab.* **2005**, *1*, 191–200.

(7) Ivan, M.; Kondo, K.; Yang, H.; Kim, W.; Valiando, J.; Ohh, M.; Salic, A.; Asara, J. M.; Lane, W. S.; Jr, W. G. K. HIFα Targeted for VHL-Mediated Destruction by Proline Hydroxylation: Implications for O2 Sensing. *Science* **2001**, *292*, 464–468.

(8) Jaakkola, P.; Mole, D. R.; Tian, Y.-M.; Wilson, M. I.; Gielbert, J.; Gaskell, S. J.; Kriegsheim, A. von; Hebestreit, H. F.; Mukherji, M.; Schofield, C. J.; Maxwell, P. H.; Pugh, C. W.; Ratcliffe, P. J. Targeting of HIF-α to the von Hippel-Lindau Ubiquitylation Complex by O_2-Regulated Prolyl Hydroxylation. *Science* **2001**, *292*, 468–472.

(9) Epstein, A. C. R.; Gleadle, J. M.; McNeill, L. A.; Hewitson, K. S.; O'Rourke, J.; Mole, D. R.; Mukherji, M.; Metzen, E.; Wilson, M. I.; Dhanda, A.; Tian, Y; Masson, N.; Hamilton, D. L.; Jaakkola, P.; Barstead, R.; Hodgkin, J.; Maxwell, P. H.; Pugh, C. W.; Schofield, C. J.; Ratcliffe, P. J. *C. Elegans* EGL-9 and Mammalian Homologs Define a Family of Dioxygenases That Regulate HIF by Prolyl Hydroxylation. *Cell* **2001**, *107*, 43–54.

(10) Gerken, T.; Girard, C. A.; Tung, Y.-C. L.; Webby, C. J.; Saudek, V.; Hewitson, K. S.; Yeo, G. S. H.; McDonough, M. A.; Cunliffe, S.; McNeill, L. A.; Galvanovkis, J.; Rorsman, P.; Robins, P.; Prieur, X.; Coll, A. P.; Ma, M.; Jovanovic, Z.; Farooqui, I. S.; Dedgwick, B.; Barroso, I.; Lindahl, T.; Ponting, C. P.; Ashcroft, F. M.; O'Rahilly, S.; Schofield, C. J. The Obesity-Associated FTO Gene Encodes a 2-Oxoglutarate-Dependent Nucleic Acid Demethylase. *Science* **2007**, *318*, 1469–1472.

(11) Trewick, S. C.; Henshaw, T. F.; Hausinger, R. P.; Lindahl, T.; Sedgwick, B. Oxidative Demethylation by *Escherichia Coli* AlkB Directly Reverts DNA Base Damage. *Nature* **2002**, *419*, 174–178.

(12) Falnes, P. Ø.; Johansen, R. F.; Seeberg, E. AlkB-Mediated Oxidative Demethylation Reverses DNA Damage in *Escherichia Coli*. *Nature* **2002**, *419*, 178–182.

(13) Yi, C.; Jia, G.; Hou, G.; Dai, Q.; Zhang, W.; Zheng, G.; Jian, X.; Yang, C.-G.; Cui, Q.; He, C. Iron-Catalysed Oxidation Intermediates Captured in a DNA Repair Dioxygenase. *Nature* **2010**, *468*, 330–333.

(14) Tsukada, Y.; Fang, J.; Erdjument-Bromage, H.; Warren, M. E.; Borchers, C. H.; Tempst, P.; Zhang, Y. Histone Demethylation by a Family of JmjC Domain-Containing Proteins. *Nature* **2006**, *439*, 811–816.
(15) Klose, R. J.; Yamane, K.; Bae, Y.; Zhang, D.; Erdjument-Bromage, H.; Tempst, P.; Wong, J.; Zhang, Y. The Transcriptional Repressor JHDM3A Demethylates Trimethyl Histone H3 Lysine 9 and Lysine 36. *Nature* **2006**, *442*, 312–316.
(16) Cloos, P. A. C.; Christensen, J.; Agger, K.; Maiolica, A.; Rappsilber, J.; Antal, T.; Hansen, K. H.; Helin, K. The Putative Oncogene GASC1 Demethylates Tri- and Dimethylated Lysine 9 on Histone H3. *Nature* **2006**, *442*, 307–311.
(17) Ito, S.; Shen, L.; Dai, Q.; Wu, S. C.; Collins, L. B.; Swenberg, J. A.; He, C.; Zhang, Y. Tet Proteins Can Convert 5-Methylcytosine to 5-Formylcytosine and 5-Carboxylcytosine. *Science* **2011**, *333*, 1300–1303.
(18) He, Y.-F.; Li, B.-Z.; Li, Z.; Liu, P.; Wang, Y.; Tang, Q.; Ding, J.; Jia, Y.; Chen, Z.; Li, L.; et al. Tet-Mediated Formation of 5-Carboxylcytosine and Its Excision by TDG in Mammalian DNA. *Science* **2011**, *333*, 1303–1307.
(19) Krebs, C.; Galonić Fujimori, D.; Walsh, C. T.; Bollinger, J. M., Jr. Non-Heme Fe(IV)–Oxo Intermediates. *Acc. Chem. Res.* **2007**, *40*, 484–492.
(20) Koehntop, K. D.; Emerson, J. P.; Que, L., Jr. The 2-His-1-Carboxylate Facial Triad: A Versatile Platform for Dioxygen Activation by Mononuclear Non-Heme iron(II) Enzymes. *J. Biol. Inorg. Chem.* **2005**, *10*, 87–93.
(21) Price, J. C.; Barr, E. W.; Tirupati, B.; Bollinger, J.Martin; Krebs, C. The First Direct Characterization of a High-Valent Iron Intermediate in the Reaction of an α-Ketoglutarate-Dependent Dioxygenase: A High-Spin Fe(IV) Complex in Taurine/α-Ketoglutarate Dioxygenase (TauD) from *Escherichia Coli*. *Biochemistry* **2003**, *42*, 7497–7508.
(22) Riggs-Gelasco, P. J.; Price, J. C.; Guyer, R. B.; Brehm, J. H.; Barr, E. W.; Bollinger, J. M., Jr.; Krebs, C. EXAFS Spectroscopic Evidence for an FeO Unit in the Fe(IV) Intermediate Observed during Oxygen Activation by Taurine:α-Ketoglutarate Dioxygenase. *J. Am. Chem. Soc.* **2004**, *126*, 8108–8109.
(23) Proshlyakov, D. A.; Henshaw, T. F.; Monterosso, G. R.; Ryle, M. J.; Hausinger, R. P. Direct Detection of Oxygen Intermediates in the Non-Heme Fe Enzyme Taurine/α-Ketoglutarate Dioxygenase. *J. Am. Chem. Soc.* **2004**, *126*, 1022–1023.
(24) Hoffart, L. M.; Barr, E. W.; Guyer, R. B.; Bollinger, J. M., Jr.; Krebs, C. Direct Spectroscopic Detection of a C-H-Cleaving High-Spin Fe(IV) Complex in a Prolyl-4-Hydroxylase. *Proc. Natl. Acad. Sci. U. S. A.* **2006**, *103*, 14738–14743.
(25) Price, J. C.; Barr, E. W.; Glass, T. E.; Krebs, C.; Bollinger, J. M., Jr. Evidence for Hydrogen Abstraction from C1 of Taurine by the High-Spin Fe(IV) Intermediate Detected during Oxygen Activation by Taurine:α-Ketoglutarate Dioxygenase (TauD). *J. Am. Chem. Soc.* **2003**, *125*, 13008–13009.
(26) Price, J. C.; Barr, E. W.; Hoffart, L. M.; Krebs, C.; Bollinger, J. M., Jr. Kinetic Dissection of the Catalytic Mechanism of Taurine:α-Ketoglutarate Dioxygenase (TauD) from *Escherichia Coli*. *Biochemistry* **2005**, *44*, 8138–8147.
(27) Galonić, D. P.; Barr, E. W.; Walsh, C. T.; Bollinger, J. M., Jr.; Krebs, C. Two Interconverting Fe(IV) Intermediates in Aliphatic Chlorination by the Halogenase CytC3. *Nat. Chem. Biol.* **2007**, *3*, 113–116.
(28) Matthews, M. L.; Krest, C. M.; Barr, E. W.; Vaillancourt, F. H.; Walsh, C. T.; Green, M. T.; Krebs, C.; Bollinger, J. M., Jr. Substrate-Triggered Formation and Remarkable

Stability of the C−H Bond-Cleaving Chloroferryl Intermediate in the Aliphatic Halogenase, SyrB2. *Biochemistry* **2009**, *48*, 4331–4343.
(29) Chang, W.-c.; Guo, Y.; Wang, C.; Butch, S. E.; Rosenzweig, A. C.; Boal, A. K.; Krebs, C.; Bollinger, J. M., Jr. Mechanism of the C5 Stereoinversion Reaction in the Biosynthesis of Carbapenem Antibiotics. *Science* **2014**, *343*, 1140–1144.
(30) Blasiak, L. C.; Vaillancourt, F. H.; Walsh, C. T.; Drennan, C. L. Crystal Structure of the Non-Haem Iron Halogenase SyrB2 in Syringomycin Biosynthesis. *Nature* **2006**, *440*, 368–371.
(31) Matthews, M. L.; Neumann, C. S.; Miles, L. A.; Grove, T. L.; Booker, S. J.; Krebs, C.; Walsh, C. T.; Bollinger, J. M., Jr. Substrate Positioning Controls the Partition between Halogenation and Hydroxylation in the Aliphatic Halogenase, SyrB2. *Proc. Natl. Acad. Sci. U. S. A.* **2009**, *106*, 17723–17728.
(32) Martinie, R. J.; Livada, J.; Chang, W.-c.; Green, M. T.; Krebs, C.; Bollinger, J. M., Jr.; Silakov, A. Experimental Correlation of Substrate Position with Reaction Outcome in the Aliphatic Halogenase, SyrB2. *J. Am. Chem. Soc.* **2015**, *137*, 6912–6919.
(33) Wong, S. D.; Srnec, M.; Matthews, M. L.; Liu, L. V.; Kwak, Y.; Park, K.; Bell, C. B. I.; Alp, E. E.; Zhao, J.; Yoda, Y.; Kitao, S.; Seto, M.; Krebs, C.; Bollinger, J. M., Jr.; Solomon, E. I. Elucidation of the Fe(IV)=O Intermediate in the Catalytic Cycle of the Halogenase SyrB2. *Nature* **2013**, *499*, 320–323.
(34) Mitchell, A. J.; Zhu, Q.; Maggiolo, A. O.; Ananth, N. R.; Hillwig, M. L.; Liu, X.; Boal, A. K. Structural Basis for Halogenation by Iron- and 2-Oxo-Glutarate-Dependent Enzyme WelO5. *Nat. Chem. Biol.* **2016**, *12*, 636–640.
(35) Srnec, M.; Wong, S. D.; Matthews, M. L.; Krebs, C.; Bollinger, J. M., Jr.; Solomon, E. I. Electronic Structure of the Ferryl Intermediate in the α-Ketoglutarate Dependent Non-Heme Iron Halogenase SyrB2: Contributions to H Atom Abstraction Reactivity. *J. Am. Chem. Soc.* **2016**, *138*, 5110–5122.
(36) Borowski, T.; Noack, H.; Radoń, M.; Zych, K.; Siegbahn, P. E. M. Mechanism of Selective Halogenation by SyrB2: A Computational Study. *J. Am. Chem. Soc.* **2010**, *132*, 12887–12898.
(37) Hashimoto, T.; Yamada, Y. Hyoscyamine 6β-Hydroxylase, a 2-Oxoglutarate-Dependent Dioxygenase, in Alkaloid-Producing Root Cultures. *Plant Physiol.* **1986**, *81*, 619–625.
(38) Hashimoto, T.; Matsuda, J.; Yamada, Y. Two-Step Epoxidation of Hyoscyamine to Scopolamine Is Catalyzed by Bifunctional Hyoscyamine 6β-Hydroxylase. *FEBS Lett.* **1993**, *329*, 35–39.
(39) Salowe, S. P.; Marsh, E. N.; Townsend, C. A. Purification and Characterization of Clavaminate Synthase from Streptomyces Clavuligerus: An Unusual Oxidative Enzyme in Natural Product Biosynthesis. *Biochemistry* **1990**, *29*, 6499–6508.
(40) Salowe, S. P.; Krol, W. J.; Iwata-Reuyl, D.; Townsend, C. A. Elucidation of the Order of Oxidations and Identification of an Intermediate in the Multistep Clavaminate Synthase Reaction. *Biochemistry* **1991**, *30*, 2281–2292.
(41) Schardl, C. L.; Grossman, R. B.; Nagabhyru, P.; Faulkner, J. R.; Mallik, U. P. Loline Alkaloids: Currencies of Mutualism. *Phytochemistry* **2007**, *68*, 980–996.
(42) Pan, J.; Bhardwaj, M.; Faulkner, J. R.; Nagabhyru, P.; Charlton, N. D.; Higashi, R. M.; Miller, A.-F.; Young, C. A.; Grossman, R. B.; Schardl, C. L. Ether Bridge Formation in Loline Alkaloid Biosynthesis. *Phytochemistry* **2014**, *98*, 60–68.

(43) Pan, J.; Bhardwaj, M.; Zhang, B.; Chang, W.; Schardl, C. L.; Krebs, C.; Grossman, R. B.; Bollinger, J. M., Jr. Installation of the Ether Bridge of Lolines by the Iron- and 2-Oxoglutarate-Dependent Oxygenase, LolO: Regio- and Stereochemistry of Sequential Hydroxylation and Oxacyclization Reactions. *Biochemistry* **2018**, *57*, 2074–2083.
(44) Zhang, Z.; Ren, J.; Stammers, D. K.; Baldwin, J. E.; Harlos, K.; Schofield, C. J. Structural Origins of the Selectivity of the Trifunctional Oxygenase Clavaminic Acid Synthase. *Nat. Struct. Biol.* **2000**, *7*, 127–133.
(45) Borowski, T.; de Marothy, S.; Broclawik, E.; Schofield, C. J.; Siegbahn, P. E. M. Mechanism for Cyclization Reaction by Clavaminic Acid Synthase. Insights from Modeling Studies. *Biochemistry* **2007**, *46*, 3682–3691.
(46) Ye, S.; Neese, F. Nonheme Oxo-iron(IV) Intermediates Form an Oxyl Radical upon Approaching the C–H Bond Activation Transition State. *Proc. Natl. Acad. Sci. U. S. A.* **2011**, *108*, 1228–1233.
(47) Tamanaha, E.; Zhang, B.; Guo, Y.; Chang, W.-c.; Barr, E. W.; Xing, G.; St. Clair, J.; Ye, S.; Neese, F.; Bollinger, J. M., Jr.; Krebs, C. Spectroscopic Evidence for the Two C–H-Cleaving Intermediates of *Aspergillus Nidulans* Isopenicillin N Synthase. *J. Am. Chem. Soc.* **2016**, *138*, 8862–8874.
(48) Mitchell, A. J.; Dunham, N. P.; Martinie, R. J.; Bergman, J. A.; Pollock, C. J.; Hu, K.; Allen, B. D.; Chang, W.-c.; Silakov, A.; Bollinger, J. M., Jr.; Krebs, C.; Boal, A. K. Visualizing the Reaction Cycle in an Iron(II)- and 2-(Oxo)-Glutarate-Dependent Hydroxylase. *J. Am. Chem. Soc.* **2017**, *139*, 13830–13836.
(49) Martinie, R. J.; Pollock, C. J.; Matthews, M. L.; Bollinger, J. M., Jr.; Krebs, C.; Silakov, A. Vanadyl as a Stable Structural Mimic of Reactive Ferryl Intermediates in Mononuclear Nonheme-Iron Enzymes. *Inorg. Chem.* **2017**, *56*, 13382–13389.
(50) Sinnecker, S.; Svensen, N.; Barr, E. W.; Ye, S.; Bollinger, J. M., Jr.; Neese, F.; Krebs, C. Spectroscopic and Computational Evaluation of the Structure of the High-Spin Fe(IV)-Oxo Intermediates in Taurine: α-Ketoglutarate Dioxygenase from *Escherichia Coli* and Its His99Ala Ligand Variant. *J. Am. Chem. Soc.* **2007**, *129*, 6168–6179.
(51) Dunham, N. P.; Chang, W.-c.; Mitchell, A. J.; Martinie, R. J.; Zhang, B.; Bergman, J. A.; Rajakovich, L. J.; Wang, B.; Silakov, A.; Krebs, C.; Boal, A. K.; Bollinger, J. M., Jr. Two Distinct Mechanisms for C–C Desaturation by Iron(II)- and 2-(Oxo)glutarate-Dependent Oxygenases: Importance of α-Heteroatom Assistance. *J. Am. Chem. Soc.* **2018**, *140*, 7116–7126.
(52) Long, F.; Vagin, A. A.; Young, P.; Murshudov, G. N. BALBES: A Molecular-Replacement Pipeline. *Acta Crystallogr. Sect. D* **2008**, *64*, 125–132.
(53) Wilmouth, R. C.; Turnbull, J. J.; Welford, R. W. D.; Clifton, I. J.; Prescott, A. G.; Schofield, C. J. Structure and Mechanism of Anthocyanidin Synthase from Arabidopsis Thaliana. *Struct. Lond. Engl. 1993* **2002**, *10*, 93–103.
(54) Stoll, S.; Schweiger, A. EasySpin, a Comprehensive Software Package for Spectral Simulation and Analysis in EPR. *J. Magn. Reson.* **2006**, *178*, 42–55.
(55) Baute, D.; Goldfarb, D. The 17O Hyperfine Interaction in $V^{17}O(H_2{}^{17}O)_5{}^{2+}$ and $Mn(H_2{}^{17}O)_6{}^{2+}$ Determined by High Field ENDOR Aided by DFT Calculations. *J. Phys. Chem. A* **2005**, *109*, 7865–7871.
(56) Matsuoka, N.; Tsuchimoto, M.; Yoshioka, N. Theoretical Study of Magnetic Properties of Oxovanadium(IV) Complex Self-Assemblies with Tetradentate Schiff Base Ligands. *J. Phys. Chem. B* **2011**, *115*, 8465–8473.

Supporting Information

Materials and Methods

Construction of H6H expression vector.

The H6H gene from *Hyoscyamus niger* was codon-optimized for expression in *Escherichia coli*, with expression under control of the T7 promoter; this construct included a C-terminal His_8 metal ion affinity tag along with an 18-residue linker and a tobacco etch virus (TEV) protease recognition site to allow for tag cleavage.

Expression and purification of H6H.

The plasmid was transformed into BL21 (DE3) cells and grown at 37 °C in rich Luria-Bertani (LB) media supplemented with 50 µg/mL kanamycin. At an OD_{600} of ~0.7, the cultures were chilled to 18 °C and induced by addition of isopropyl β-D-1-thiogalactopyranoside (IPTG) to a final concentration of 0.25 mM. The cultures were shaken overnight at 18 °C before being harvested by centrifugation.

All purification steps were performed at 4 °C. Cell paste was resuspended in 3 volumes of buffer A (20 mM Tris pH 7.5, 80 mM KCl, 20 mM imidazole, and 10% glycerol). Cell lysis was achieved by approximately two cycles of passage through a microfluidizer (M110EH-30, Microfluidics, Newton, MA) at ~20,000 psi. Cell debris was removed by centrifugation and the supernatant was loaded onto a Ni-NTA agarose column (approximately one mL of Ni-NTA per gram of cell paste). The column was washed twice with five column volumes of the buffer A, and the protein was eluted by application of buffer A with the addition of 300 mM imidazole. Elution fractions containing H6H were pooled and concentrated with a centrifugal concentrator with a 30 kDa molecular weight cutoff filter (Pall Corp., Port Washington, NY). TEV Protease was added at a 1:50 molar ratio (concentration determined by assuming an extinction coefficient of 47,500 $M^{-1}cm^{-1}$, based on the method of Gill and von Hippel[1]) and cleavage proceeded during an overnight dialysis against buffer B (20 mM Tris pH 7.5, 80 mM KCl, and 10% glycerol) with the addition of 1 mM DTT. After removal of DTT by repeated spin concentration and dilution with buffer B, the protein was reloaded onto the Ni-NTA agarose column. The flowthrough was

concentrated before being dialyzed against buffer B also containing 10 mM EDTA. Two additional rounds of dialysis with buffer B removed the metal chelator. The enzyme was then concentrated for further purification.

H6H was further purified using size exclusion chromatography with a Superdex 200 pg column equilibrated in buffer B using an ÄKTA Pure FPLC (GE Healthcare Life Sciences). Fractions containing the target enzyme were pooled, concentrated, and buffer exchanged using a Sephadex G-25 PD-10 destalting column into a low-salt buffer (50mM HEPES, 50mM KCl, 10% glycerol, pH 7.0) for anion exchange chromatography. A HiPrep DEAE FF column was used for anion exchange with a gradient of 0-100% 1M KCl over 10 column volumes. Fractions containing the target enzyme were pooled, buffer exchanged into buffer B using a PD-10 column, and concentrated to the desired concentration.

Activity assays of H6H.

Activity assays were carried out in buffer B, with component concentrations given in the appropriate figure legend. Products were identified by LC-MS. In a typical assay, anaerobic enzyme was combined with ferrous ammonium sulfate, 2-oxo glutarate (2OG), and substrate in an anoxic chamber (MBRAUN LabMaster 130 Glovebox). The resulting solution was removed from the chamber, and two volumes of air-saturated buffer B were added. This mixture was allowed to react at 4 °C for 0.5-8 hr. The reaction was terminated by removal of the enzyme via spin filtration. 2 µL aliquots of each sample were injected onto the LC-MS (Agilent 1200 series LC system coupled to an Agilent 6410 QQQ mass spectrometer) and compounds were examined by electrospray ionization MS in positive ion mode. Chromatography was carried out using an Agilent 1.8 µm extended C-18 (4.6 x 50 mm) column. The flow rate was 0.3 mL/min, the aqueous phase A was 2% formic acid, 7% methanol, and 91% water, and the mobile phase B was pure methanol with 2% formic acid. The elution program was: 100% A for 1 min, from 100% A to 32.5% A from 1 to 9 min, then from 32.5% A to 100% A from 9 min to 17 mins. Substrates for LCMS assays were purchased from TCI or were provided by Prof. Hung-wen Liu.

Protein preparation for x-ray crystallography.

A tag-free version of the H6H enzyme from *Hyoscyamus niger* was cloned into the pET-24b(+) *Escherichia coli* overexpression vector by standard recombinant DNA methods and transformed into BL21 (DE3) *E. coli* cells for large-scale growth. The plasmid was transformed into BL21 (DE3) cells and grown at 37 °C in rich Luria-Bertani (LB) media supplemented with 50 μg/mL kanamycin. At an OD_{600} of ~0.7, the cultures were chilled to 18 °C and induced by addition of isopropyl β-D-1-thiogalactopyranoside (IPTG) to a final concentration of 0.25 mM. The cultures were shaken overnight at 18 °C before being harvested by centrifugation. Cell paste was resuspended in lysis buffer containing 20 mM Tris-HCl pH 7.5 at 4 °C, 80 mM KCl, 10mM EDTA, and 1 mM DTT. The cells were lysed via sonication (QSonica Q500, 3 min total pulse time, 8 s on/30 s off, 50% amplitude) and centrifuged at 10,000 rpm for 30 minutes in an F14-6x250y rotor (Thermo Scientific). The crude lysate was vacuum filtered through a 20 μm filter prior to loading onto a DEAE-sepharose weak anion exchange column using an ÄKTA Pure FPLC (GE Healthcare Life Sciences). *Hn*H6H was eluted using an increasing linear gradient of 0-500 mM KCl in buffer containing 10 mM EDTA and 1 mM DTT. This procedure was repeated using a strong anion exchange Q-sepharose column and subsequently concentrated for size exclusion chromatography (HiLoad Superdex 200) with 20 mM Tris-HCl pH 7.5 at 4 °C, 80 mM KCl, 10mM EDTA, and 1 mM DTT buffer.

General crystallographic methods.

All crystallographic datasets were collected at either the Life Sciences Collaborative Access Team (LS-CAT) or the National Institute of General Medical Science and National Cancer Institute Collaborative Access Team (GM/CA-CAT) beamlines at the Advanced Photon Source (Argonne National Laboratory). Diffraction images were processed and scaled with the HKL2000 software package.[2] Phases were determined using the online molecular replacement server BALBES,[3] which identified the coordinates of anthocyanidin synthase from *Abrabidopsis thaliana* (PDB accession code 1GP6),[4] which is also an Fe/2-OG enzyme that shares ~28% sequence identity to *Hn*H6H, as the initial search model. REFMAC5,[5] implemented within the CCP4 package suite,[6] and Coot[7] were used for model building and refinement. Electron density maps for figures were calculated using the FFT program[8] in the CCP4. Figures were generated using the PyMol molecular graphic systems (Schrödinger, LLC).

Crystallization of HnH6H with hyoscyamine and hydroxyhysocyamine.

Purified *Hn*H6H was prepared for crystallization by deoxygenating the apo-enzyme with argon gas prior to crystallization. The protein (10 mg/mL in 20 mM Tris-HCl pH 7.5, 80 mM KCl buffer) was equilibrated for 10 minutes at RT in an N_2 (3% hydrogen) atmosphere glove box (Coy Laboratory Products) with 1 molar equivalent of iron(II)ammonium sulfate, 5 equivalents of 2-OG, and 5 equivalents hyoscyamine solubilized in buffer, before crystal drop set-up. Crystals were obtained by mixing 1 μL of protein solution with 1 μL of a pre-made crystallization solution from the 96 well JCSG+ sparse matrix screen (well F8) purchased from Qiagen (NeXtal Suites). This screen condition is reported by Qiagen to contain 2.1 M DL-Malic acid pH 7.0. Optimization around this primary condition would not yield crystals, leading us to believe there could a minor contaminant in our screen stock which mandated crystal formation; thus we optimized around this particular solution stock. We could reproducibly obtain diffraction quality crystals (0.1-0.3 mm in diameter) by mixing of 1 μL of this stock with 1 μL of our protein solution in the pedestal of 24-well sitting drop crystal tray, which contained 500 μL of 1.0 M $LiSO_4$ in the precipitant well. The crystals were soaked in cryoprotectant containing 20% (v/v) PEG 400, 0.1 M Tris-HCl pH 7.5, and 16% (v/v) ethylene glycol prior to mounting on rayon loops and flash freezing in liquid N_2.

Crystals with the hydroxhyscyamine substrate were prepared using the same procedure as previously described, except the protein stock was initially equilibrated with 5 molar equivalents of the hydroxylated substrate in place of hyoscyamine. The subsequent crystallization procedure was identical, except the crystals were cryoprotected in a solution of 1 M 2-OG, 0.1 M Tris-HCl pH 7.0, and 10% (v/v) ethylene glycol for 5-10 minutes prior to flash freezing.

Supporting Figures

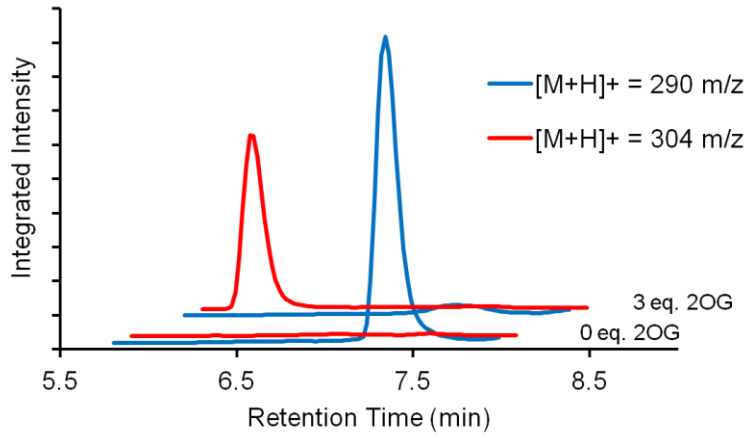

Figure S1. H6H produces scopolamine *in vitro*. In the presence of Fe(II), 2OG, and hyoscyamine, a new species is detected with a mass of +14 Da with respect to the substrate. Concentrations of H6H, Fe(II), and hyoscyamine were 66, 60, and 60 μM, respectively. Equivalents of 2OG are reported with respect to Fe(II).

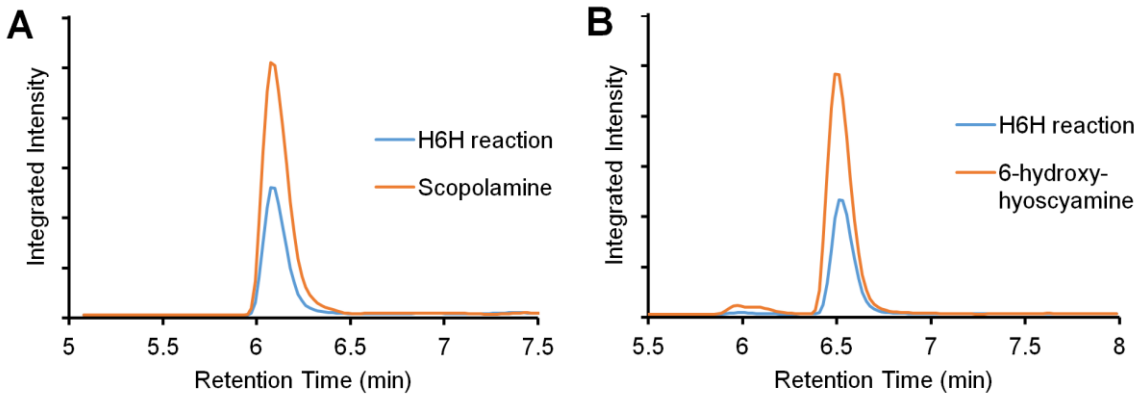

Figure S2. Single ion chromatograms at $[M+H]^+$ = 304 m/z (A) and 306 m/z (B). **A**) The product of the H6H reaction in the presence of excess 2OG (blue) co-elutes with an authentic scopolamine standard (orange). Reaction concentrations of H6H, Fe, 2OG and hyoscyamine were 66, 60, 180, and 60 μM, respectively. Concentration of scopolamine standard was 100 μM. **B**) The $[M+H]^+$ = 306 m/z intermediate (+16 Da relative to hyoscyamine) of the H6H reaction (blue) co-elutes with synthetically prepared 6-hydroxy-hyoscyamine (orange). Reaction concentrations of H6H, Fe, 2OG and hyoscyamine were 66, 60, 54, and 60 μM, respectively. Concentration of 6-hydroxy-hyoscyamine standard was 100 μM.

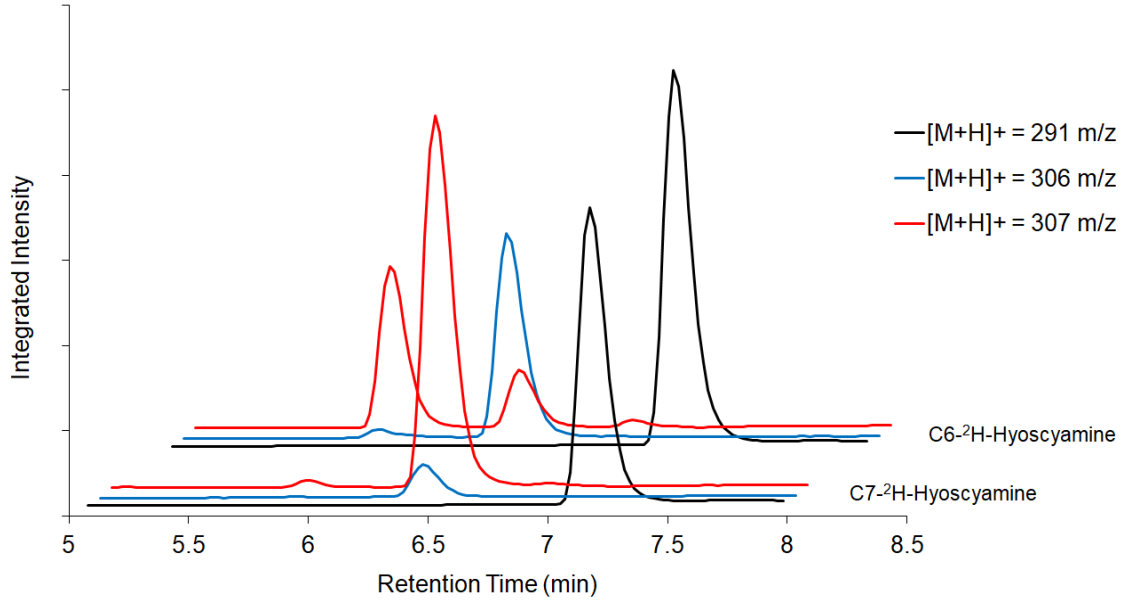

Figure S3. Regiospecificity of the first turnover hydroxylation reaction in H6H. When incubated with C7-^{2}H-hyoscyamine, the hydroxylated intermediate exhibits a mass shift of +16 Da (red traces) relative to the substrate (black traces). When incubated with C6-^{2}H-hyoscyamine, the co-eluting hydroxylated intermediate exhibits a mass shift of +15 Da (blue traces). Several +16 Da peaks are still observed in this reaction, consistent with retargeting to nearby positions when reactivity at the native C6 site is slowed by the kinetic isotope effect associated with deuterium incorporation. Concentrations of H6H, Fe, 2OG and hyoscyamine were 66, 60, 54, and 60 μM, respectively.

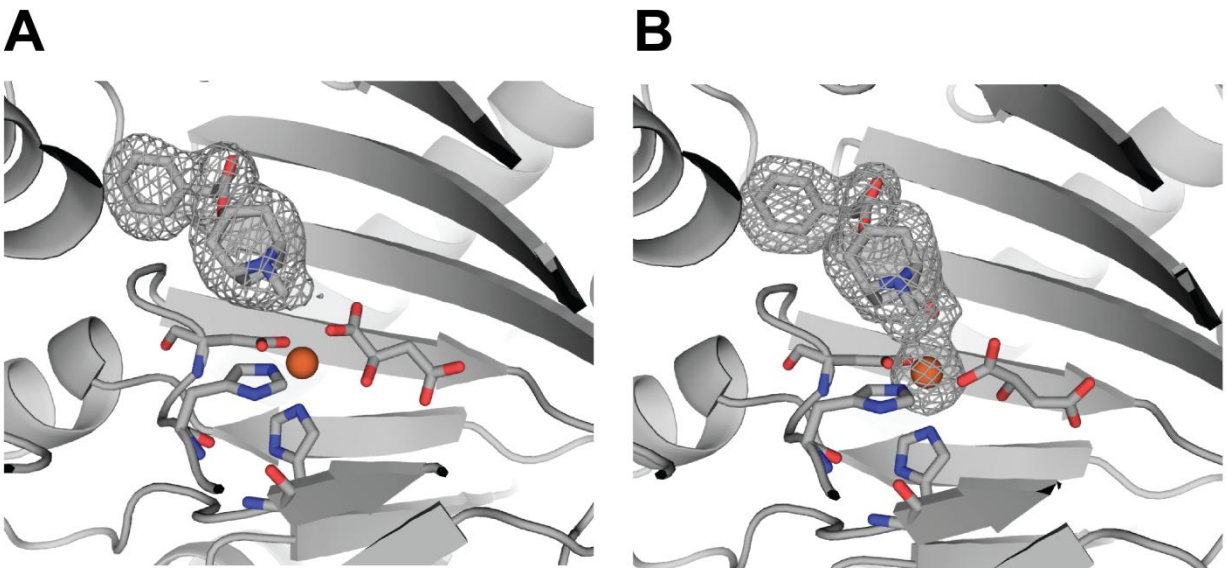

Figure S4. Structures of H6H, solved in the presence of Fe(II) and hyoscyamine (**A**) or 6-OH-Hyo (**B**). Cages represent omit density for the substrate (**A**) or substrate and iron (**B**), generated by deletion of the substrate or the substrate and iron, respectively, followed by refinement, contoured to 3.0 σ.

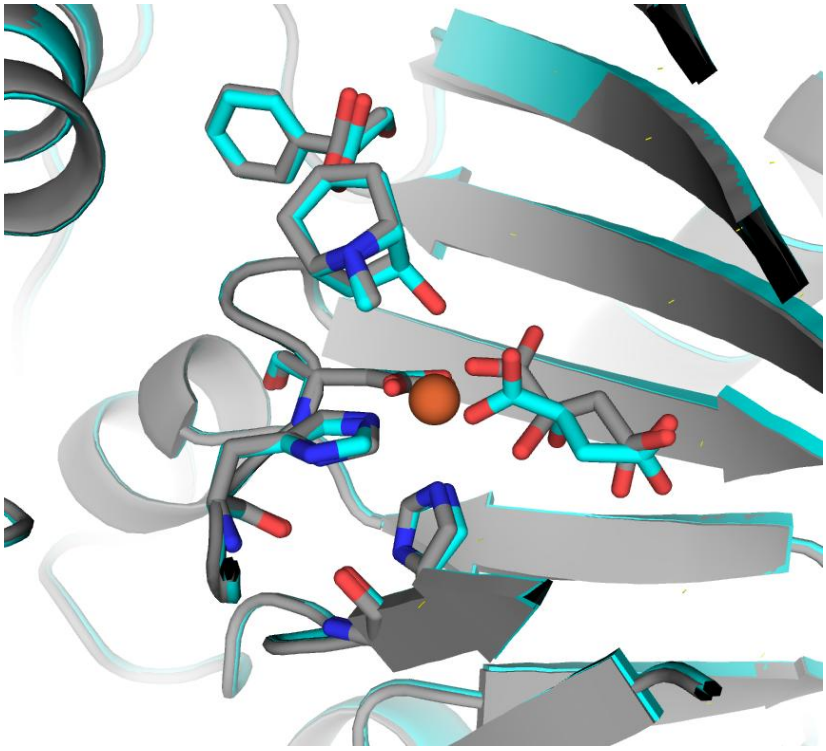

Figure S5. Structural overlay of the H6H•Fe(II)•hyoscyamine (gray) and H6H•Fe(II)•6-hydroxy-hyoscyamine (cyan) models.

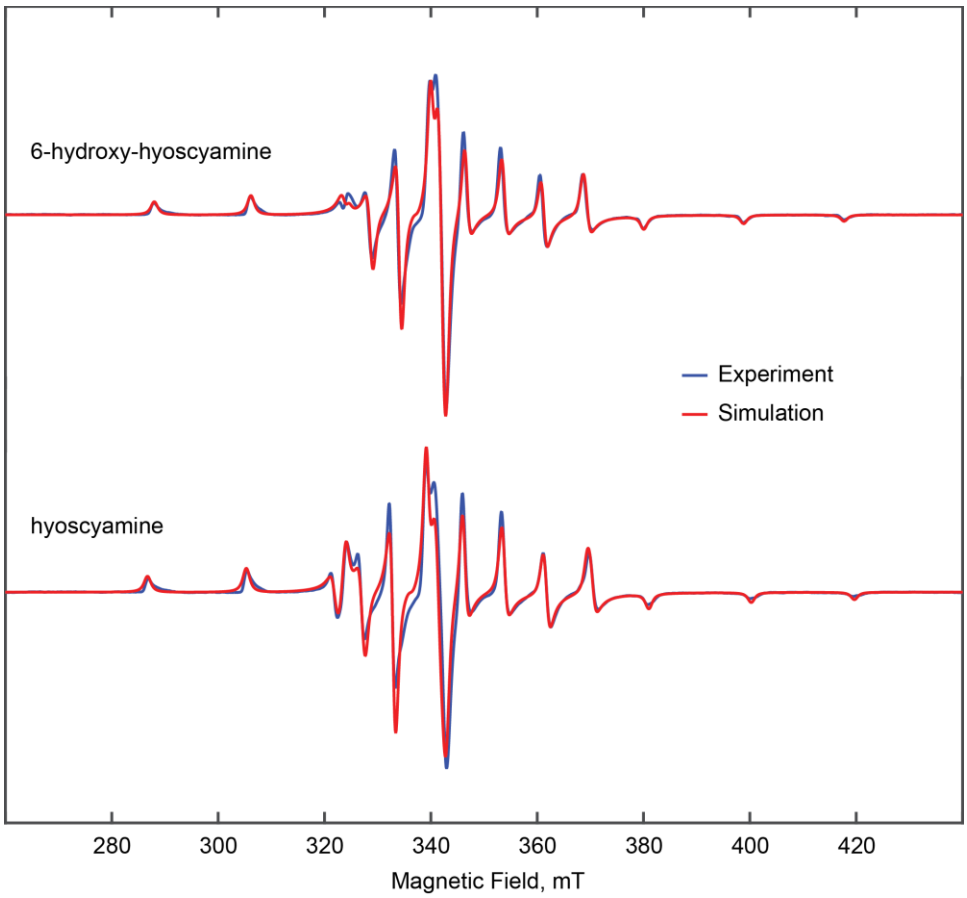

Figure S6. Continuous-wave, X-band EPR spectra of H6H•vanadyl•succinate•substrate complexes (blue) and simulations (red). Slight differences are observed for the spectrum in the presence of 6-hydroxy-hyoscyamine (top), compared to hyoscyamine (bottom), particularly in the 320-330 mT region. Measurements were performed at 80 K, with a microwave frequency of 9.622 GHz (top) and 9.623 GHz (bottom). Simulation parameters for 6-hydroxy-hyoscyamine are: g = [1.978, 1.978, 1.947] ± 0.002 and A_V = [174,180,505] ± 5 MHz. Simulation parameters for hyoscyamine are: g = [1.980, 1.980, 1.945] ± 0.002 and A_V = [192,184,517] ± 5 MHz.

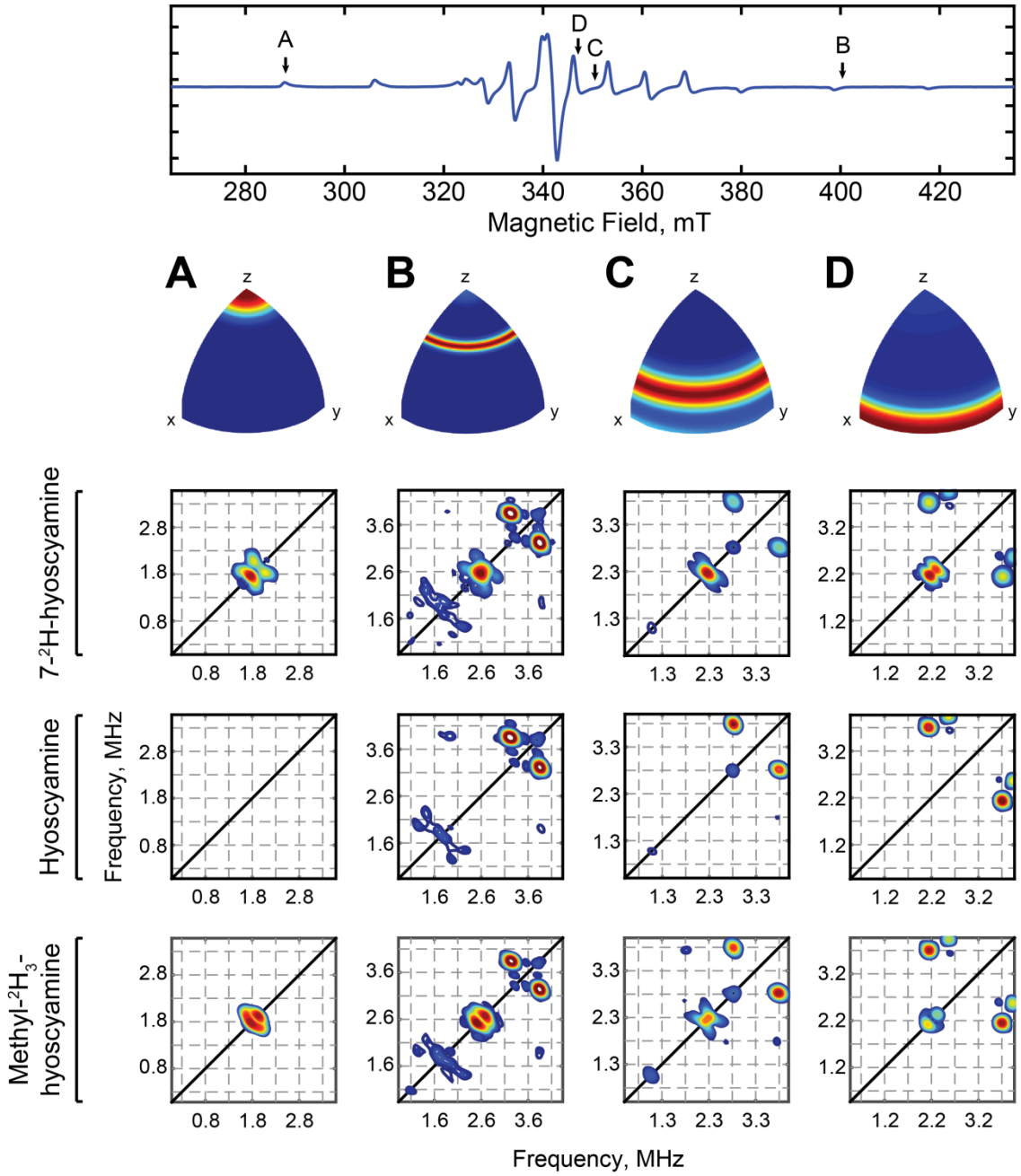

Figure S7. Comparison of field-dependent HYSCORE spectra of H6H•vanadyl•succinate•substrate complexes in the presence of 7-^{2}H-hyoscyamine (above), hyoscyamine (middle), and Methyl-$^{2}H_3$-hyoscyamine (below), collected at 280.5 mT (**A**), 396 mT (**B**), 344.5 mT (**C**), and 339.5 mT (**D**). Orientation selectivities probed by each magnetic field position (shown above the spectra) are color coded using an RGB color scheme (red - fully excited; blue, not excited). Magnetic field positions are indicated by black arrows on the one-dimensional EPR spectrum (top). Contour minima are set to 20% (top) or 30% (bottom) of maximum. Spectra were collected at 35 K with microwave frequency 9.433 GHz, $\pi/2$ pulse length 8 ns, and τ of 228 (**A**), 184 (**B**), 208 (**C**), and 212 (**D**) ns.

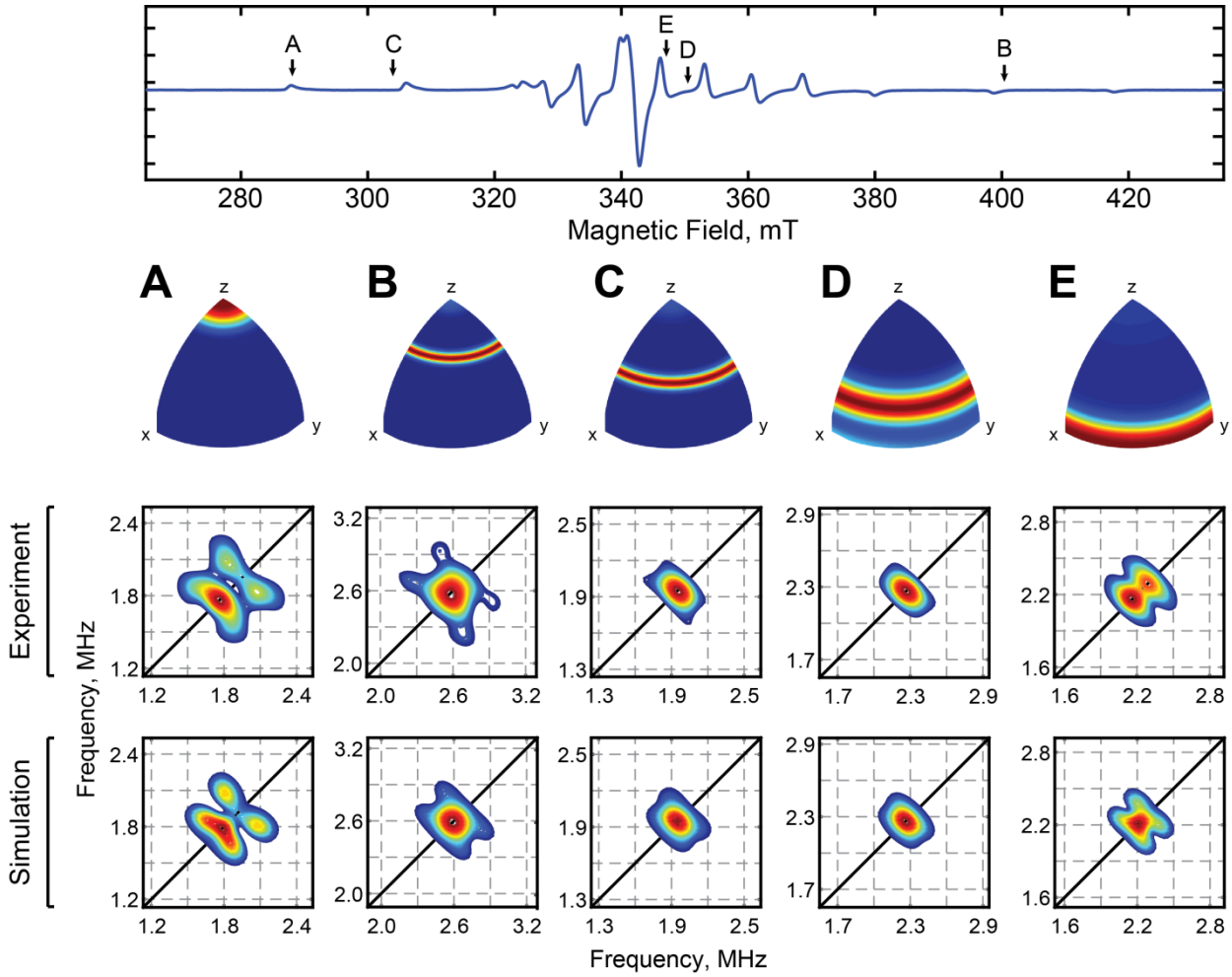

Figure S8. Comparison of field-dependent ^{2}H-HYSCORE spectra of H6H•vanadyl•succinate•substrate complexes in the presence of 7-^{2}H-hyoscyamine (above) and simulations (below), collected at 280.5 mT (**A**), 396 mT (**B**), 296.5 mT (**C**), 344.5 mT (**D**), and 339.5 mT (**E**). Orientation selectivities probed by each magnetic field position (shown above the spectra) are color coded using an RGB color scheme (red - fully excited; blue, not excited). Magnetic field positions are indicated by black arrows on the one-dimensional EPR spectrum (top). Contour maxima are normalized to the ^{2}H signals; contour minima are set to 30% of maximum. Spectra were collected at 35 K with microwave frequency 9.433 GHz, $\pi/2$ pulse length 8 ns, and τ of 228 (**A**), 184 (**B**), 240 (**C**), 208 (**D**), and 212 (**E**) ns. Features can be simulated with a single axial ^{2}H hyperfine tensor with magnitude A = 0.33 ± 0.05 MHz (Euler angles [0,40±5,45±10]°) and quadrupole coupling [-0.04, -0.04, 0.08] ± 0.01 MHz (Euler angles [0, 25±5, 45±15]°).

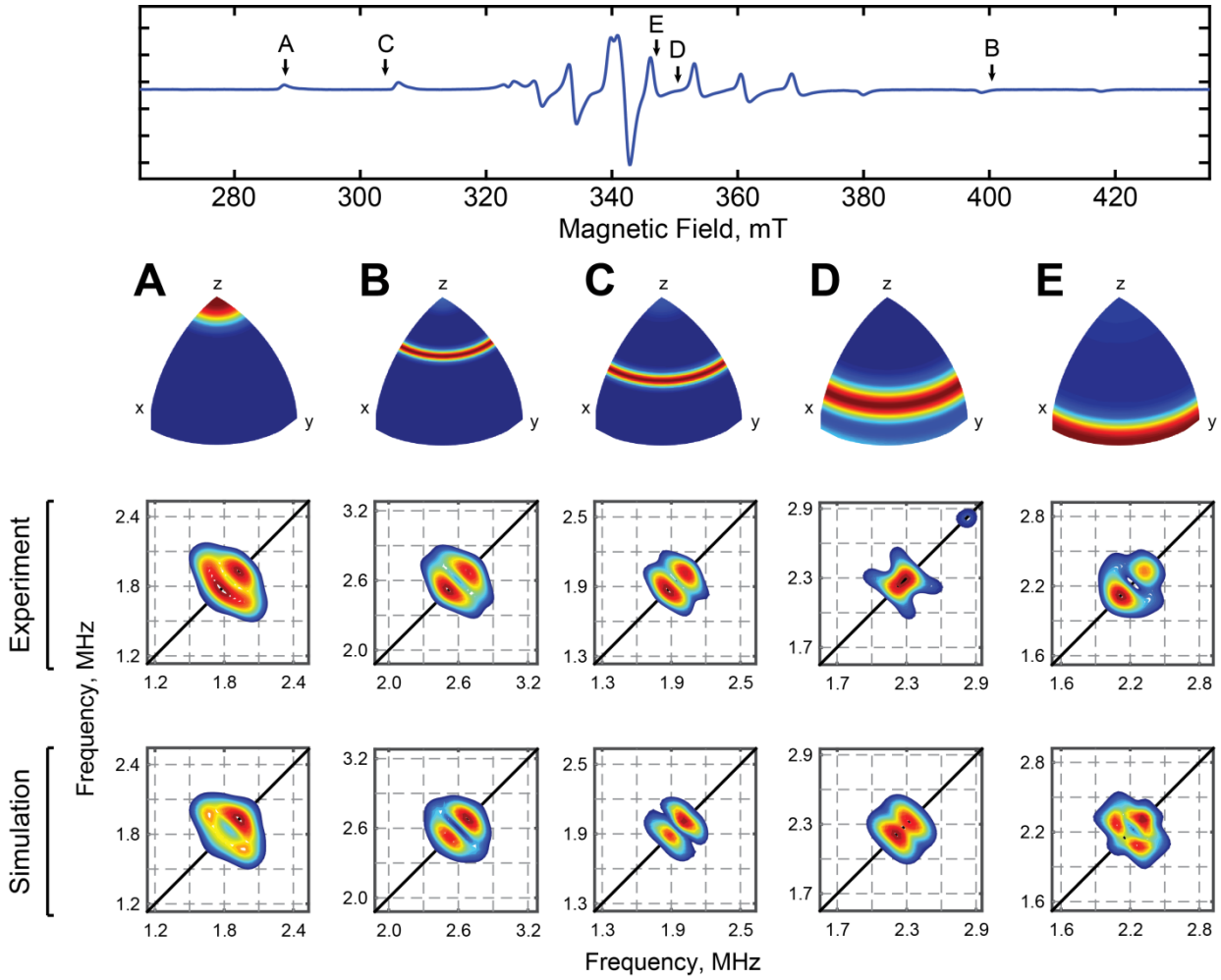

Figure S9. Comparison of field-dependent ^{2}H-HYSCORE spectra of H6H•vanadyl•succinate•substrate complexes in the presence of methyl-$^{2}H_3$-hyoscyamine (above) and simulations (below), collected at 280.5 mT (**A**), 396 mT (**B**), 296 mT (**C**), 344.5 mT (**D**), and 339.5 mT (**E**). Orientation selectivities probed by each magnetic field position (shown above the spectra) are color coded using an RGB color scheme (red - fully excited; blue, not excited). Magnetic field positions are indicated by black arrows on the one-dimensional EPR spectrum (top). Contour maxima are normalized to the ^{2}H signals; contour minima are set to 35% of maximum. Spectra were collected at 35 K with microwave frequency 9.433 GHz, $\pi/2$ pulse length 8 ns, and τ of 228 (**A**), 184 (**B**), 240 (**C**), 208 (**D**), and 212 (**E**) ns. Features can be simulated with a single axial ^{2}H hyperfine tensor with magnitude A = 0.37 ± 0.05 MHz (Euler angles [0,39±5,25±10]°) and quadrupole coupling [-0.05, -0.05, 0.10] ± 0.01 MHz (Euler angles [0, 65±5, 20±10]°).

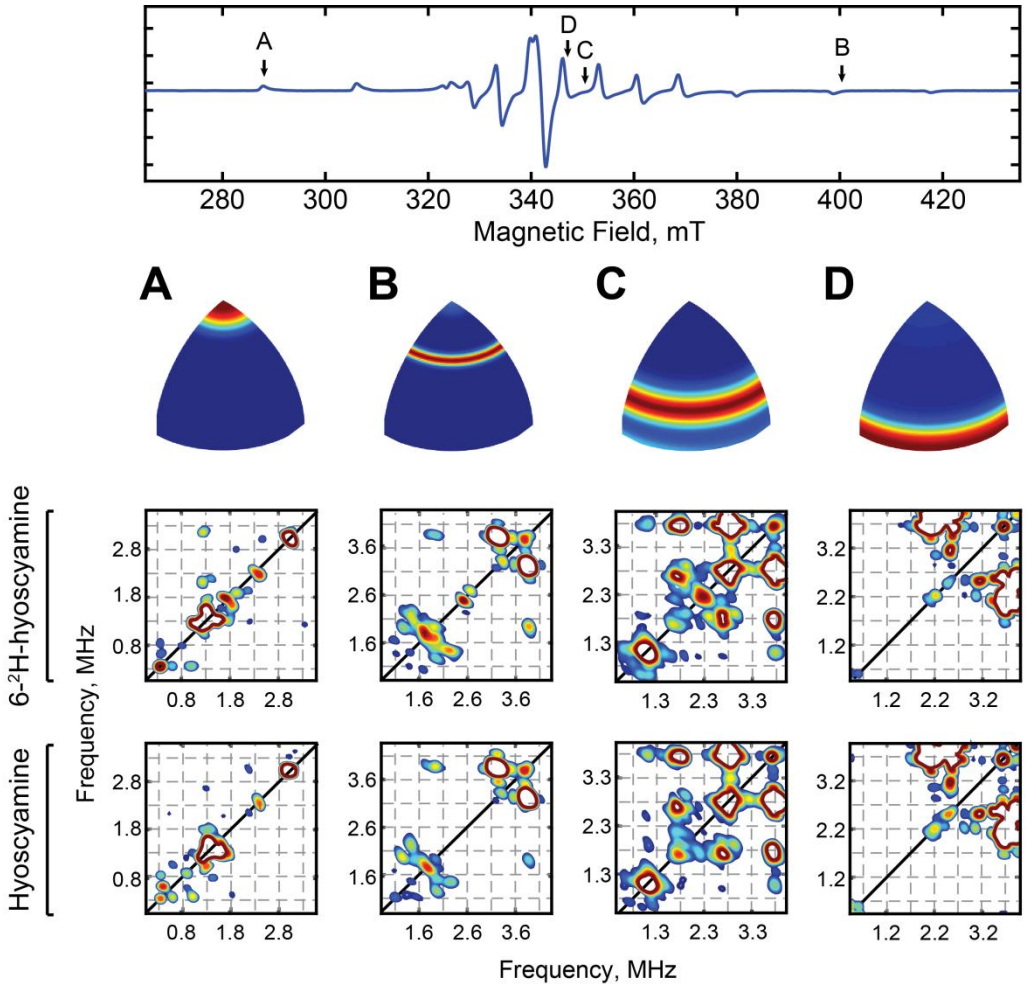

Figure S10. Comparison of field-dependent HYSCORE spectra of H6H•vanadyl•succinate•substrate complexes in the presence of 6-*d*-Hyo (above) and hyoscyamine (below), collected at 280.5 mT (**A**), 396 mT (**B**), 344.5 mT (**C**), and 339.5 mT (**D**). Orientation selectivities probed by each magnetic field position (shown above the spectra) are color coded using an RGB color scheme (red - fully excited; blue, not excited). Magnetic field positions are indicated by black arrows on the one-dimensional EPR spectrum (top). Contour maxima are normalized to the ^{2}H signals, if present; contour minima are set to 50% of maximum. Spectra were collected at 35 K with microwave frequency 9.433 GHz, $\pi/2$ pulse length 8 ns, and τ of 228 (**A**), 184 (**B**), 208 (**C**), and 212 (**D**) ns. Given the relatively poor signal to noise of the ^{2}H-associated signals and the interference of nearby ^{14}N signals, a full simulation of the ^{2}H hyperfine and quadrupole couplings is inappropriate. However, we can assign a lower limit for the hyperfine coupling of 0.37 MHz, assuming an axial, through-space coupling.

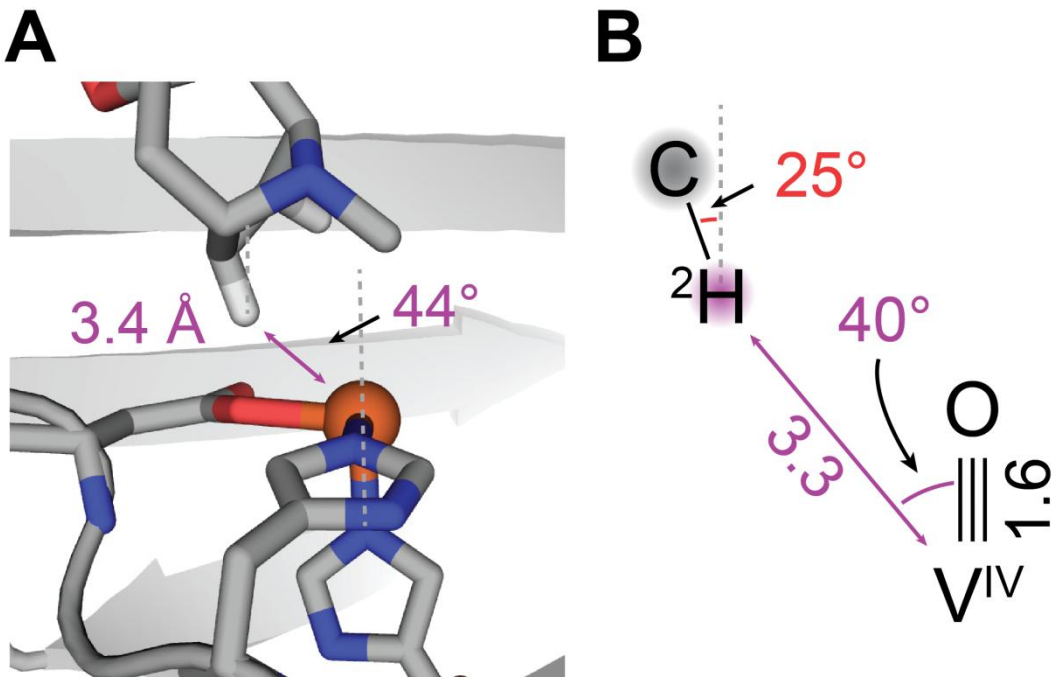

Figure S11. Comparison of structural metrics for C_7-H derived from the H6H•Fe(II)•hyoscyamine crystal structure (**A**) and ^{2}H-HYSCORE (**B**). The M-H distance are similar: 3.4 Å vs 3.3 Å, respectively; as are the O-M-H angles: 44° vs 40°, respectively.

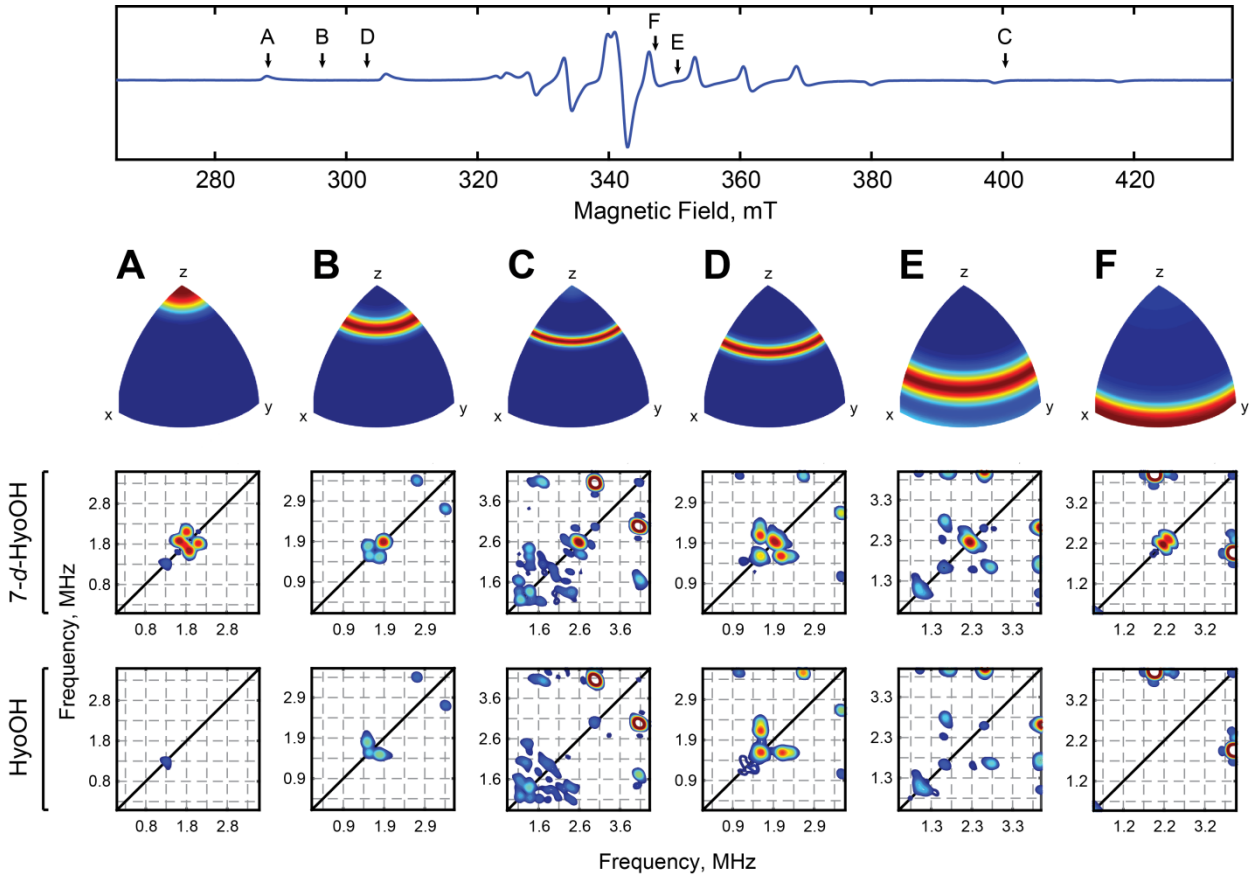

Figure S12. Comparison of field-dependent HYSCORE spectra of H6H•vanadyl•succinate•substrate complexes in the presence of 7-*d*-6-OH-Hyo (above) and 6-OH-Hyo (below), collected at 281.5 mT (**A**), 287 mT (**B**), 395 mT (**C**), 293 mT (**D**), 344.5 mT (**E**), and 340 mT (**F**). Orientation selectivities probed by each magnetic field position (shown above the spectra) are color coded using an RGB color scheme (red - fully excited; blue, not excited). Magnetic field positions are indicated by black arrows on the one-dimensional EPR spectrum (top). Contour maxima are normalized to the ^{2}H signals, if present; contour minima are set to 30% of maximum. Spectra were collected at 35 K with microwave frequency 9.443 GHz, $\pi/2$ pulse length 8 ns, and τ of 232 (**A**), 224 (**B**), 188 (**C**), 244 (**D**), 208 (**E**), and 212 (**F**) ns.

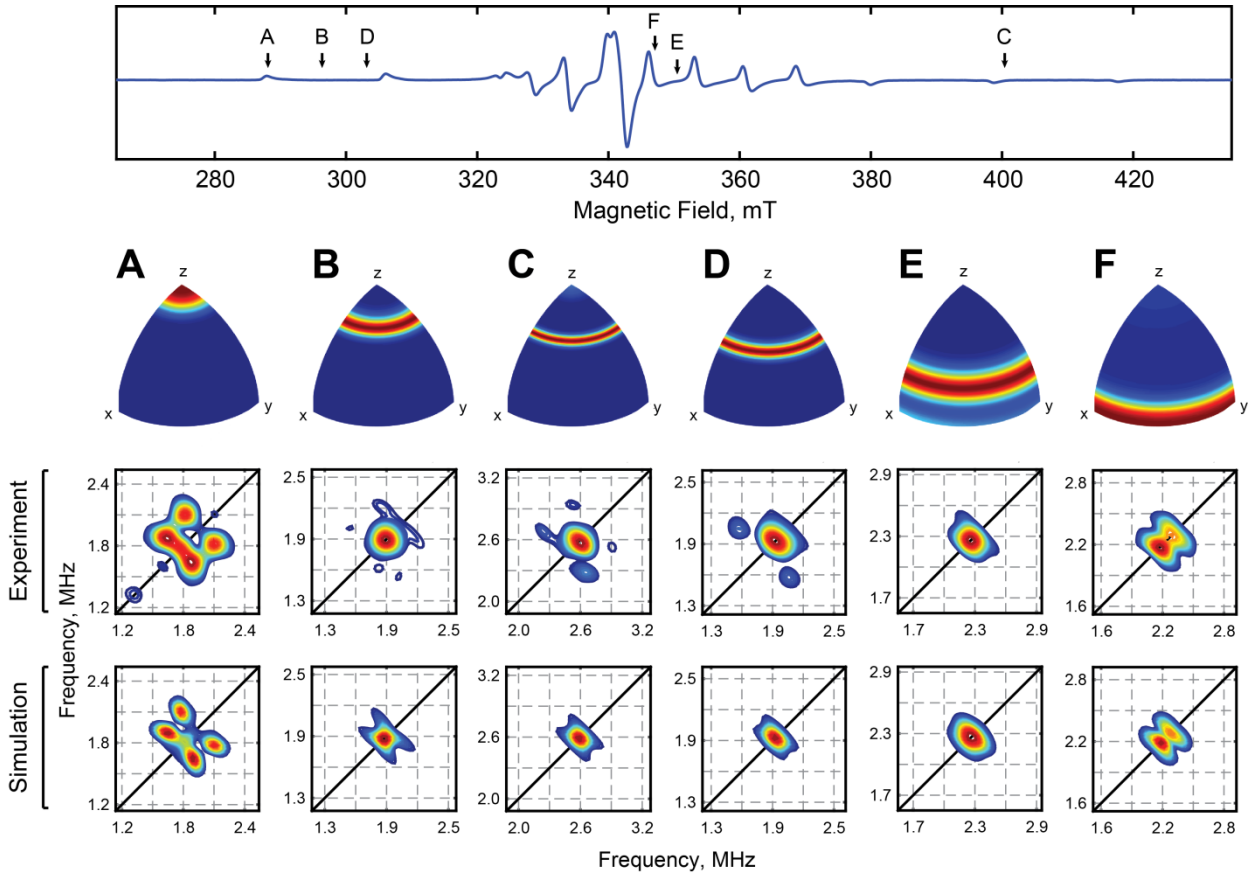

Figure S13. Comparison of field-dependent ^{2}H-HYSCORE spectra (above) of H6H•vanadyl•succinate•substrate complexes in the presence of 7-*d*-6-OH-Hyo and simulations (below), collected at 281.5 mT (**A**), 287 mT (**B**), 395 mT (**C**), 293 mT (**D**), 344.5 mT (**E**), and 340 mT (**F**). Orientation selectivities probed by each magnetic field position (shown above the spectra) are color coded using an RGB color scheme (red - fully excited; blue, not excited). Magnetic field positions are indicated by black arrows on the one-dimensional EPR spectrum (top). Contour maxima are normalized to the ^{2}H signals; contour minima are set to 30% of maximum. Spectra were collected at 35 K with microwave frequency 9.433 GHz, $\pi/2$ pulse length 8 ns, and τ of 232 (**A**), 224 (**B**), 188 (**C**), 244 (**D**), 208 (**E**), and 212 (**F**) ns. Features can be simulated with a single axial ^{2}H hyperfine tensor with magnitude A = 0.31 ± 0.04 MHz (Euler angles [0, 37±5 ,55±10]°) and quadrupole coupling [-0.04, -0.04, 0.08] ± 0.01 MHz (Euler angles [0, 25±5, 45±15]°).

A

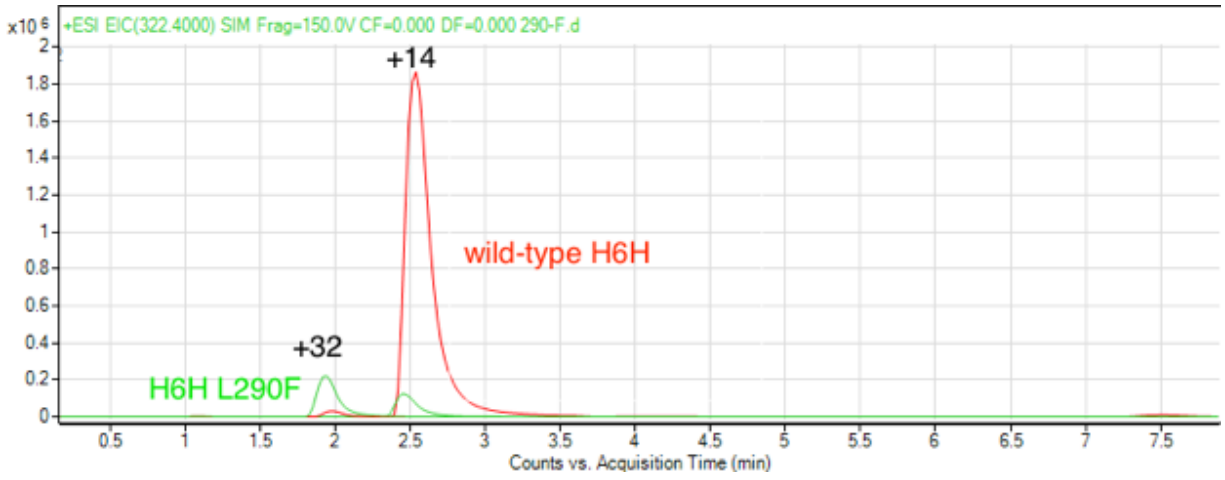

B

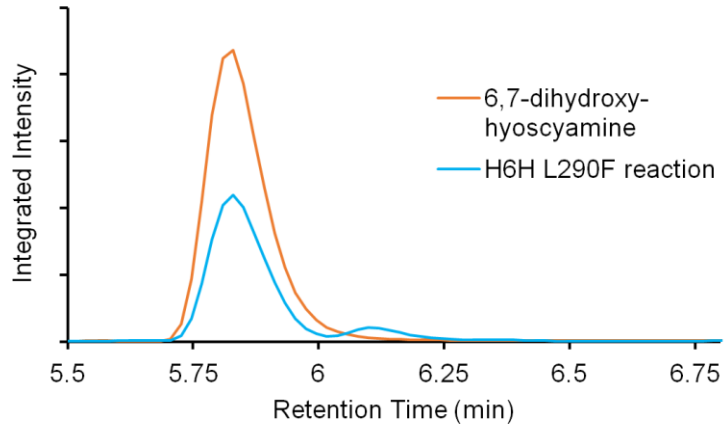

Figure S14. H6H L290F catalyzes formation of 6,7-dihydroxy-hyoscyamine. **A**) H6H L290F (green) catalyzes appreciable dihydroxylation (+32) of hyoscyamine, along with diminution of epoxidation (+14) compared to WT (red). **B**) Single ion chromatograms at $[M+H]^+$ = 322 m/z (+32 Da with respect to hyoscyamine); the product of the H6H L290F reaction (blue) co-elutes with synthetically-prepared 6,7-dihydroxy-hyoscyamine (orange). Reaction concentrations of H6H, Fe, 2OG and hyoscyamine were 100, 90, 1660, and 1660 μM, respectively. Concentration of 6,7-dihydroxy-hyoscyamine standard was 100 μM.

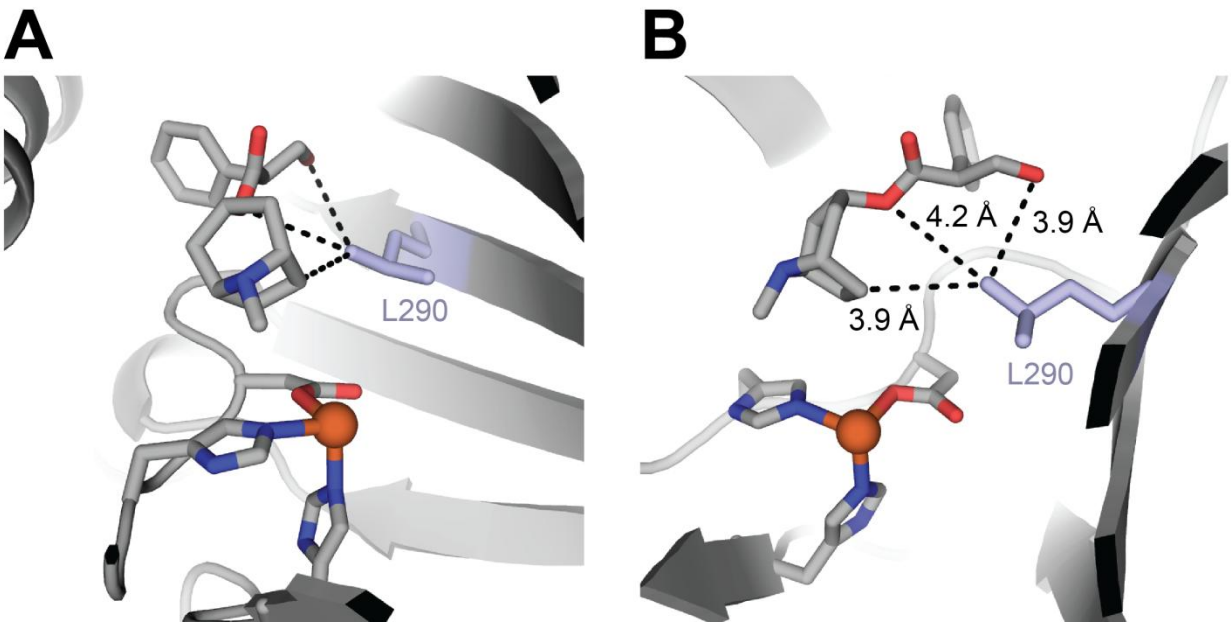

Figure S15. Location of residue L290 (light purple) in the active site of H6H (**A**) and contacts between L290 and the hyoscyamine substrate (**B**).

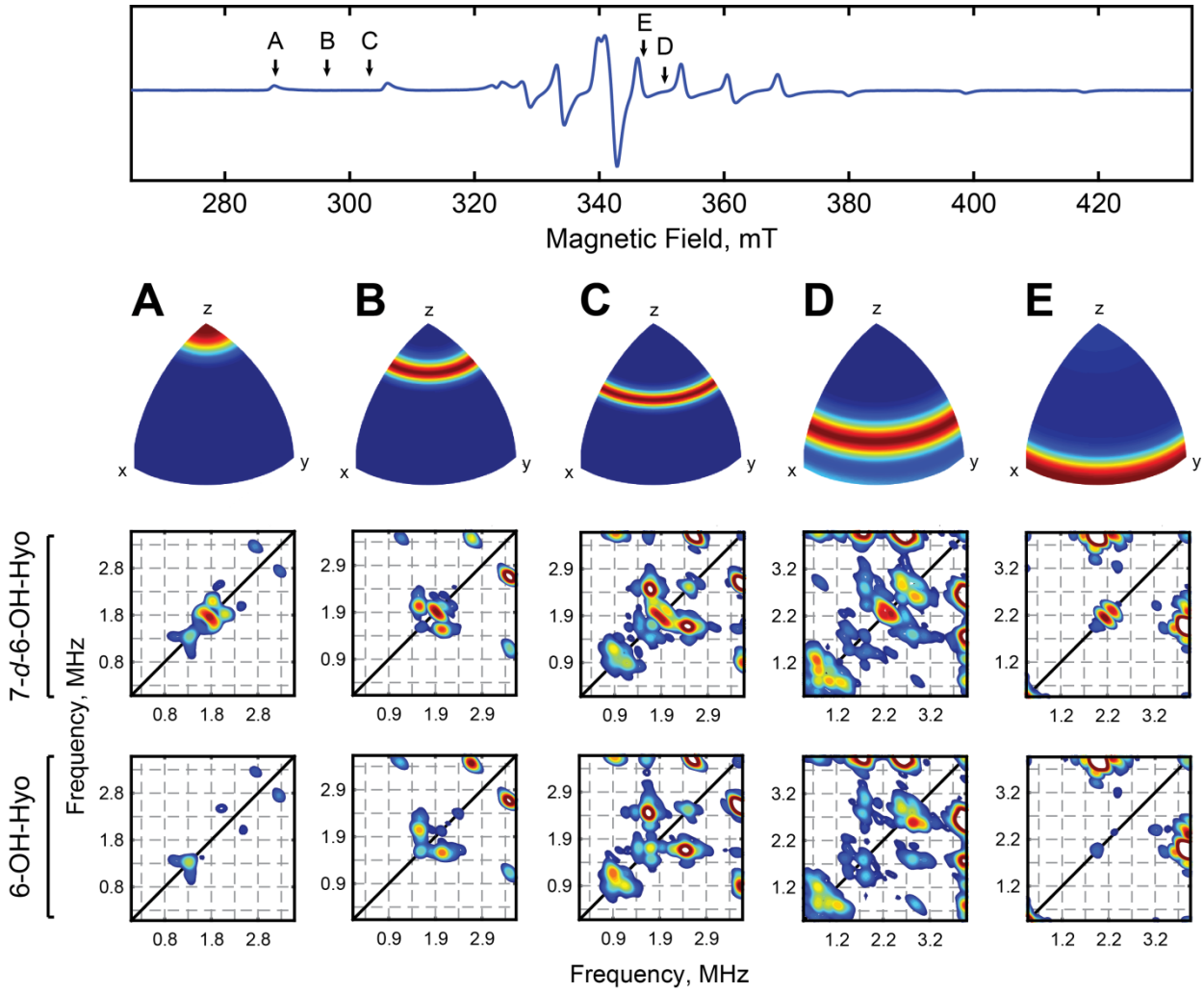

Figure S16. Comparison of field-dependent HYSCORE spectra of H6H-L290F•vanadyl•succinate•substrate complexes in the presence of 7-*d*-6-OH-Hyo (above) and 6-OH-Hyo (below), collected at 280.5 mT (**A**), 288 mT (**B**), 295 mT (**C**), 343 mT (**D**), and 338.5 mT (**E**). Orientation selectivities probed by each magnetic field position (shown above the spectra) are color coded using an RGB color scheme (red - fully excited; blue, not excited). Magnetic field positions are indicated by black arrows on the one-dimensional EPR spectrum (top). Contour maxima are normalized to the ^{2}H signals, if present; contour minima are set to 30% of maximum. Spectra were collected at 35 K with microwave frequency 9.403 GHz, π/2 pulse length 8 ns, and τ of 228 (**A**), 248 (**B**), 240 (**C**), 208 (**D**), and 216 (**E**) ns.

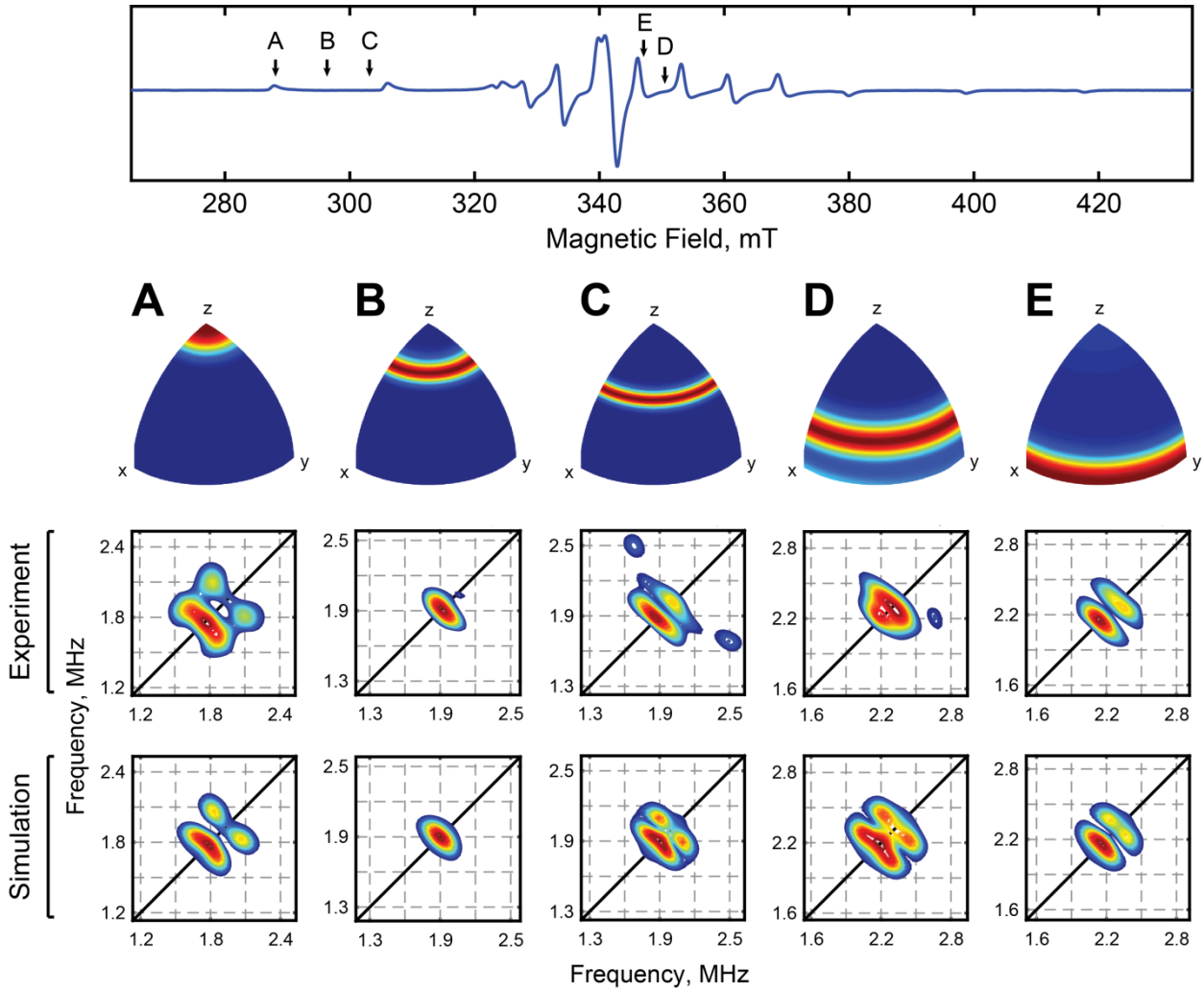

Figure S17. Comparison of field-dependent ^{2}H-HYSCORE spectra (above) of H6H-L290F•vanadyl•succinate•substrate complexes in the presence of 7-*d*-6-OH-Hyo and simulations (below), collected at 280.5 mT (**A**), 288 mT (**B**), 295 mT (**C**), 343 mT (**D**), and 338.5 mT (**E**). Orientation selectivities probed by each magnetic field position (shown above the spectra) are color coded using an RGB color scheme (red - fully excited; blue, not excited). Magnetic field positions are indicated by black arrows on the one-dimensional EPR spectrum (top). Contour maxima are normalized to the ^{2}H signals; contour minima are set to 40% of maximum. Spectra were collected at 35 K with microwave frequency 9.403 GHz, $\pi/2$ pulse length 8 ns, and τ of 228 (**A**), 248 (**B**), 240 (**C**), 208 (**D**), and 216 (**E**) ns. Features can be simulated with a single axial ^{2}H hyperfine tensor with magnitude A = 0.35 ± 0.04 MHz (Euler angles [0, 35±5 ,0±15]°) and quadrupole coupling [-0.045, -0.045, 0.09] ± 0.01 MHz (Euler angles [0, 20±5, -60±20]°).

Supplementary Tables

Table S1. Data collection and refinement statistics for crystal structures of *Hn*H6H.

	*Hn*H6H-hyoscyamine	*Hn*H6H-hydroxyhyoscyamine
Data collection		
Space group	*P* 32 2 1	*P* 32 2 1
Cell dimensions		
a, *b*, *c* (Å)	81.8, 81.8, 260.6	82.2, 82.2, 262.3
α, β, γ (°)	90.0, 90.0, 120.0	90.0, 90.0, 120.0
Resolution (Å)	50.0-2.53 (2.57-2.53)	50.0-2.10 (2.14-2.10)
R_{merge}	0.166 (0.795)	0.123 (0.998)
R_{pim}	0.058 (0.327)	0.061 (0.490)
$I / \sigma I$	13.5 (1.8)	11.3 (1.6)
$CC_{1/2}$	0.837	0.700
Completeness (%)	94.5 (56.6)	98.7 (93.2)
Redundancy	7.9 (5.0)	3.9 (3.9)
Refinement		
Resolution (Å)	86.8-2.53	87.44-2.10
No. reflections	32850	60306
R_{work} / R_{free}	0.219/0.246	0.233/0.256
No. atoms	5586	5835
Protein	5478	5467
Ligand/ion	44	64
Water/solvent	64	304
B-factors		
Protein	39.10	29.49
Ligand/ion	30.10	25.11
Water/solvent	28.29	27.71
R.m.s. deviations		
Bond lengths (Å)	0.006	0.006
Bond angles (°)	1.140	1.115
Molprobity clashscore	0.66 (100^{th} percentile)	0.60 (100^{th} percentile)
Rotamer outliers (%)	0.16	0
Ramachandran favored (%)	98.53	98.97

Literature Cited

(1) Gill, S. C.; von Hippel, P. H. Calculation of Protein Extinction Coefficients from Amino Acid Sequence Data. *Anal. Biochem.* **1989**, *182*, 319–326.

(2) Otwinowski, Z.; Minor, W. [20] Processing of X-Ray Diffraction Data Collected in Oscillation Mode. In *Methods in enzymology*; Elsevier, 1997; Vol. 276, pp 307–326.

(3) Long, F.; Vagin, A. A.; Young, P.; Murshudov, G. N. BALBES: A Molecular-Replacement Pipeline. *Acta Crystallogr. D Biol. Crystallogr.* **2008**, *64*, 125–132.

(4) Wilmouth, R. C.; Turnbull, J. J.; Welford, R. W. D.; Clifton, I. J.; Prescott, A. G.; Schofield, C. J. Structure and Mechanism of Anthocyanidin Synthase from Arabidopsis Thaliana. *Struct. Lond. Engl. 1993* **2002**, *10*, 93–103.

(5) Murshudov, G. N.; Vagin, A. A.; Dodson, E. J. Refinement of Macromolecular Structures by the Maximum-Likelihood Method. *Acta Crystallogr. D Biol. Crystallogr.* **1997**, *53*, 240–255.

(6) Winn, M. D.; Ballard, C. C.; Cowtan, K. D.; Dodson, E. J.; Emsley, P.; Evans, P. R.; Keegan, R. M.; Krissinel, E. B.; Leslie, A. G.; McCoy, A. Overview of the CCP4 Suite and Current Developments. *Acta Crystallogr. D Biol. Crystallogr.* **2011**, *67*, 235–242.

(7) Emsley, P.; Cowtan, K. Coot: Model-Building Tools for Molecular Graphics. *Acta Crystallogr. D Biol. Crystallogr.* **2004**, *60*, 2126–2132.

(8) Ten Eyck, L. F. Fast Fourier Transform Calculation of Electron Density Maps. In *Methods in enzymology*; Elsevier, 1985; Vol. 115, pp 324–337.

Appendix A

Experimental Correlation of Substrate Position and Reaction Outcome in the Aliphatic Halogenase, SyrB2.

Reprinted with permission from

Martinie, R. J.; Livada, J.; Chang, W-c.; Green, M. T.; Krebs, C.; Bollinger, J. M., Jr.; Silakov, A. *J. Am. Chem. Soc.* **2015**, *137*, 6912–6919.

Acknowledgements

I thank Dr. Wei-chen Chang for training me in how to work with SyrB1 and SyrB2, and for answering so many of my questions, especially though not exclusively, when I was just starting in the lab. I also thank Jovan Livada for his help in collecting some of the HYSCORE data. Prof. Carsten Krebs and Prof. J. Martin Bollinger, Jr. provided critical feedback on the manuscript in preparation for publication. Above all, I thank Prof. Alexey Silakov, who contributed to this work in countless and invaluable ways. He trained me in the use of the pulse EPR spectrometer, we collected many of the data together, and he was a constant, very critical, source of feedback when analyzing the data.

JACS
JOURNAL OF THE AMERICAN CHEMICAL SOCIETY
Article
pubs.acs.org/JACS

Experimental Correlation of Substrate Position with Reaction Outcome in the Aliphatic Halogenase, SyrB2

Ryan J. Martinie,[†] Jovan Livada,[†] Wei-chen Chang,[†] Michael T. Green,[†] Carsten Krebs,[†,‡] J. Martin Bollinger, Jr.,[†,‡] and Alexey Silakov*[,†]

Departments of [†]Chemistry and of [‡]Biochemistry and Molecular Biology, The Pennsylvania State University, University Park, Pennsylvania 16802, United States

Supporting Information

ABSTRACT: The iron(II)- and 2-(oxo)glutarate-dependent (Fe/2OG) oxygenases catalyze an array of challenging transformations, but how individual members of the enzyme family direct different outcomes is poorly understood. The Fe/2OG halogenase, SyrB2, chlorinates C4 of its native substrate, L-threonine appended to the carrier protein, SyrB1, but hydroxylates C5 of L-norvaline and, to a lesser extent, C4 of L-aminobutyric acid when SyrB1 presents these non-native amino acids. To test the hypothesis that positioning of the targeted carbon dictates the outcome, we defined the positions of these three substrates by measuring hyperfine couplings between substrate deuterium atoms and the stable, EPR-active iron−nitrosyl adduct, a surrogate for reaction intermediates. The Fe−^{2}H distances and N−Fe−^{2}H angles, which vary from 4.2 Å and 85° for threonine to 3.4 Å and 65° for norvaline, rationalize the trends in reactivity. This experimental correlation of position to outcome should aid in judging from structural data on other Fe/2OG enzymes whether they suppress hydroxylation or form hydroxylated intermediates on the pathways to other outcomes.

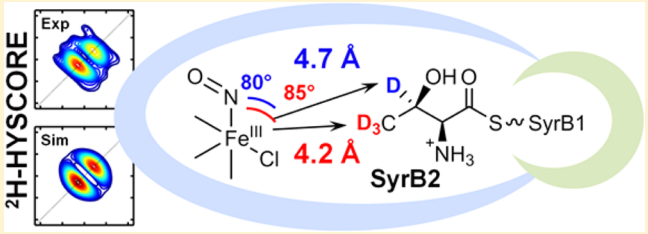

INTRODUCTION

Mononuclear[1−4] and dinuclear[1,5,6] nonheme iron enzymes, cytochromes P450,[7] and radical SAM enzymes[8,9] activate and functionalize inert C−H bonds with a remarkable degree of specificity and selectivity. Members of the iron- and 2-(oxo)glutarate-dependent (Fe/2OG) oxygenase family catalyze a variety of transformations at unactivated carbon centers, including hydroxylation, desaturation, cyclization, stereoinversion, and halogenation; these reactions play crucial roles in microbial metabolism and biosynthesis,[2] as well as oxygen and body mass homeostasis,[10−12] DNA repair,[13−15] epigenetic inheritance, and control of transcription in humans.[16−18] The mechanistic strategy employed by this family was first elucidated for the hydroxylases.[4] These enzymes activate oxygen at their common Fe(II) cofactor, which is coordinated by a $(His)_2(Glu/Asp)_1$ "facial triad" ligand set,[19,20] to form a high-spin (S = 2) Fe(IV)−oxo (ferryl) intermediate.[21−24] This ferryl unit abstracts a hydrogen atom (H$^\bullet$) from the substrate,[25] yielding an Fe(III)−hydroxo/substrate−radical intermediate; this radical then couples with the hydroxo ligand (formally HO$^\bullet$), producing the hydroxylated product and an Fe(II) complex.[4,26,27] Current understanding of the mechanisms employed by other Fe/2OG oxygenases to direct this potent reactivity to only one of several alternative reaction outcomes (e.g., halogenation, stereoinversion, etc.) is incomplete. A robust understanding of this control is a major unmet challenge and will be required for these systems to be exploited for potential biotechnological applications, including production of new drug compounds.

The Fe/2OG aliphatic halogenases provide an ideal system to study enzymatic discrimination between accessible reactivities. SyrB2 from *Pseudomonas syringae* B301D is the founding member of the Fe/2OG aliphatic halogenases.[28−31] It catalyzes chlorination of the C4 position of L-threonine appended via a thioester linkage to the phosphopantetheine arm of the companion aminoacyl carrier protein, SyrB1 (hereafter, all L-aminoacyl-*S*-SyrB1 substrates are abbreviated by designating only the appended amino acid in boldface type, e.g., **Thr**; Figure 1). In SyrB2, the sequence position that normally provides the carboxylate of the canonical facial triad of protein ligands is occupied by an alanine (Ala118), and the cosubstrate, chloride (Cl^-), occupies the vacated site in the iron coordination sphere.[32] Fe/2OG halogenases mechanistically parallel the hydroxylases in that both employ ferryl intermediates as the H$^\bullet$-abstracting species.[33−35] However, following this step, the reactivities diverge: in the halogenases it is the Cl$^\bullet$ ligand, rather than the HO$^\bullet$, that couples with the substrate radical. Thus, halogenases generate the substrate radical in a manner similar to the hydroxylases but are faced with the more difficult challenge of directing it to chlorination rather than hydroxylation. Efficient H$^\bullet$ transfer to the ferryl would seemingly imply proximity to the hydroxo ligand in the subsequent step, and HO$^\bullet$/substrate radical coupling occurs readily in the hydroxylases. Yet, the native substrate of SyrB2, **Thr**, is almost exclusively chlorinated (Figure 1),[36] although

Received: March 31, 2015
Published: May 12, 2015

DOI: 10.1021/jacs.5b03370
J. Am. Chem. Soc. 2015, 137, 6912−6919

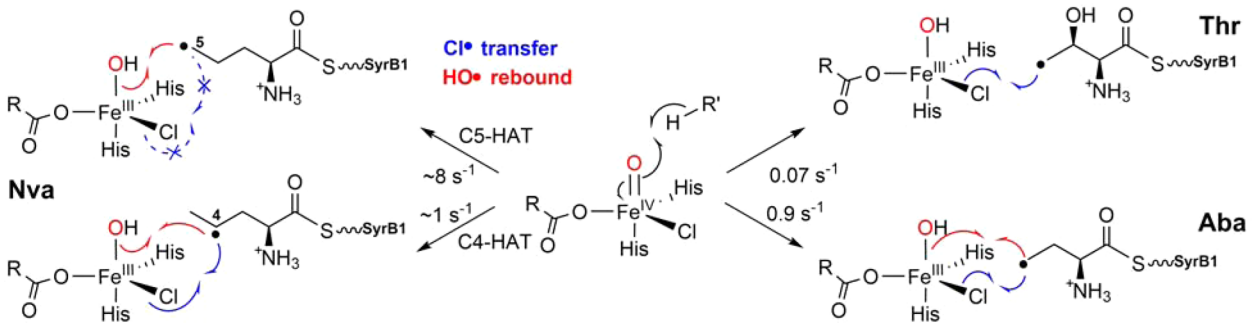

Figure 1. Divergent reactivity of the SyrB2 ferryl intermediate upon SyrB1 presenting different amino acids: threonine (**Thr**; top right), aminobutyric acid (**Aba**; bottom right), norvaline (**Nva**; left). Red arrows depict hydroxylation, whereas blue arrows depict halogenation. R = CH_2CH_2COOH.

non-native substrates undergo hydroxylation as well as chlorination. Therefore, SyrB2 represents an intriguing case in which two different reaction outcomes catalyzed by this enzyme family (hydroxylation and halogenation) are observed, making it an ideal system for investigating how the enzymes discriminate between reactivities.

Our previous work showed that the *cis*-chloroferryl complex in SyrB2 reacts more rapidly with SyrB1 presenting L-aminobutyric acid (**Aba**) or L-norvaline (**Nva**) than with **Thr**, suggesting a programmed inefficiency in H• abstraction from the native substrate. Formed with **Nva**, the complex decays 130-fold more rapidly (9.5 s^{-1} at 5 °C) than with **Thr** (0.07 s^{-1}); with **Aba**, the rate is intermediate (0.9 s^{-1}) (Figure 1).[36] Selectivity for chlorination is also strongly modulated: **Thr** is almost exclusively chlorinated, **Aba** is chlorinated and hydroxylated at C4 to similar extents, and **Nva** is predominately hydroxylated at the C5 position.[36] It was reasoned that the decrease in ferryl decay rates could most simply arise from an increase in the distance between the H• donor and acceptor. Positioning the substrate away from the ferryl oxygen would also likely diminish the efficiency of HO• rebound and could thereby enable the competing Cl• transfer in the subsequent step. These observations led to the hypothesis that substrate positioning controls the outcome in SyrB2, with the native **Thr** being held farther away from the ferryl oxygen and closer to the halogen to trade proficiency in H• abstraction for selectivity in ligand–radical transfer.[36] This hypothesis was supported by the nearly complete reversal of the outcome for **Nva** from hydroxylation of C5 to chlorination of C4 by deuterium (D) substitution at C5. With neither or both positions deuterium labeled, the chloroferryl complex abstracts H(D) more rapidly from C5, but with only C5 labeled, the C4 position is targeted more rapidly, due to the large kinetic isotope effect disfavoring D• abstraction. Redirection to C4 results in more chlorination than hydroxylation (~4:1), as rationalized by the positioning hypothesis.[36]

To date, no experimental structural data to evaluate the substrate-positioning hypothesis have been reported. The nature and magnitude of repositioning that might be required to explain the observed effects on reactivity are thus unknown. Moreover, recent theoretical work has suggested that interchange of the oxygen and chloride ligands relative to their positions in the crystal structure could also contribute to the control of outcome.[37,38] According to these studies, the substrate dictates both the chloro/oxo disposition and the frontier orbitals involved in the H•-abstraction step, with the engagement of π- or σ-type ferryl orbitals favoring Cl• or HO• transfer, respectively.[38] Although not incompatible with the positioning hypothesis, this idea would imply that the differential reactivity observed for the different substrates might arise primarily from substrate–protein interactions that impact the partition between the axial and the equatorial coordination isomers of the ferryl complex rather than from substrate positioning per se.

Given the possibility that these other factors might be involved in directing the halogenation outcome and the likelihood that proper substrate positioning is also essential to avoidance of hydroxylation in the other types of Fe/2OG-oxygenase reactivity, we sought to directly probe the positions of the various target C–H bonds relative to the iron center. Electron paramagnetic resonance (EPR) spectroscopy can resolve relatively weak interactions between unpaired electrons (e.g., centered on a metallocofactor) and nearby magnetic nuclei (e.g., $^{1,2}H$, ^{14}N). Unfortunately, all of the species in the catalytic cycle of SyrB2 that have been characterized to date have integer spin states [several high-spin (S = 2) Fe(II) forms and the high-spin (S = 2) haloferryl complex] and therefore cannot be addressed by conventional, perpendicular-mode EPR methods. Therefore, in order to obtain an EPR-active probe in the active site, an Fe–NO complex was generated (Figure 2A).[39−41] Nitric oxide (NO•) has been employed as an analog of O_2 that binds to Fe(II) complexes to form an S = 3/2 iron–nitrosyl complex (denoted $\{Fe\text{-}NO\}^7$)[42] best described as a high-spin Fe(III) center (S = 5/2) antiferromagnetically coupled to NO^- (S = 1).[43−45] This complex is thought to be analogous to the putative $\{Fe–OO\}^8$ intermediate in the catalytic cycle,[43,46] and previous studies on taurine:2OG dioxygenase (TauD) have employed such complexes in combination with pulse EPR methods to determine the position of substrate C–H bonds.[40,41] In this work, we employed hyperfine sublevel correlation (HYSCORE) spectroscopy to obtain geometric information about the active site of SyrB2 by measuring hyperfine couplings to specifically ^2H-labeled **Thr**, **Aba**, and **Nva** substrates. The magnitude and orientation dependence of these hyperfine parameters provide spatial information about the labeled position relative to the metallocofactor; these data represent the first experimental structural data on the SyrB2:aminoacyl-SyrB1 complex and reveal the nature and extent of repositioning in the SyrB2 substrates exhibiting such widely divergent reactivities.

■ RESULTS

When the complex of SyrB2 with its substrates is exposed to gaseous NO, a dark yellow complex characterized by an almost

DOI: 10.1021/jacs.5b03370
J. Am. Chem. Soc. 2015, 137, 6912–6919

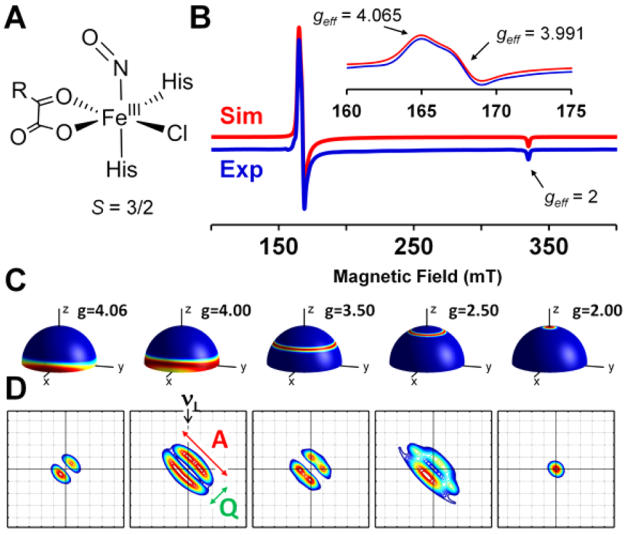

Figure 2. Chemical structural representation (A) and continuous-wave, X-band EPR spectrum (B) of the $\{Fe\text{-}NO\}^7$ form of SyrB2 in complex with aminoacyl-SyrB1. R = CH_2CH_2COOH. Experimental spectrum (blue) and simulation (red, shifted upward for clarity). (Inset) Expanded view of the g_{eff} = 4 region of the spectrum. (C) Orientation selectivity pattern calculated for various magnetic fields using "RGB" color coding (red, fully excited; blue, not excited). Corresponding effective g values are shown to the right of each hemisphere. (D) HYSCORE spectra calculated using orientation selectivity patterns from panel C and spin Hamiltonian parameters for **NO-4,5-d_5-Nva** from Table S1, Supporting Information. Splitting due to hyperfine coupling (A) and quadrupole coupling (Q) is indicated in the g = 4 spectrum.

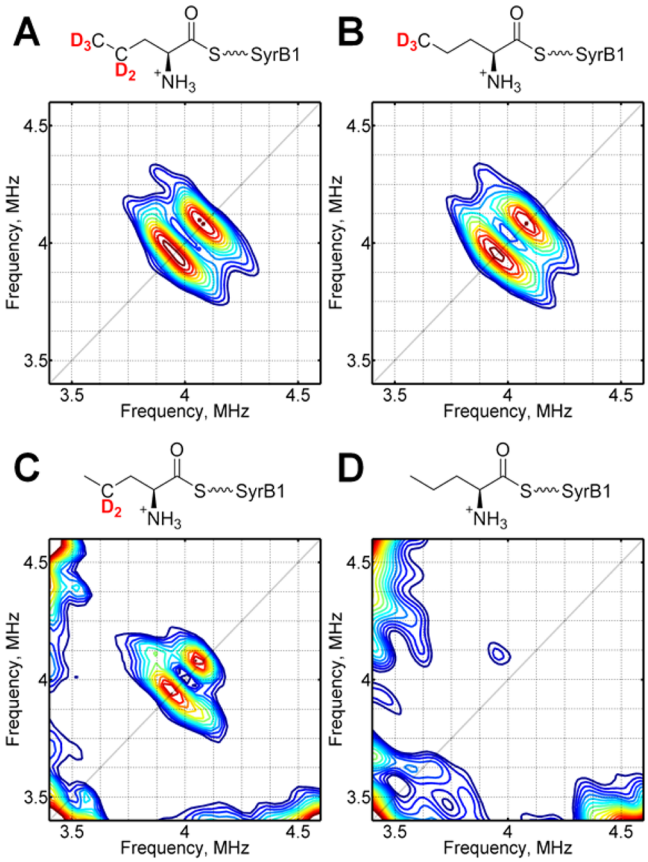

Figure 3. HYSCORE spectra and substrate chemical structures for (A) **NO-4,5-d_5-Nva**, (B) **NO-5-d_3-Nva**, (C) **NO-4-d_2-Nva**, and (D) **NO-Nva**, collected at g_{eff} = 3.98. Experimental conditions: magnetic field = 613.5 (A, B) and 613 mT (C, D); microwave frequency = 34.201 (A, D), 34.199 (B), and 34.202 (C) GHz; temperature = 4.5 (A) and 4.0 K (B, C, D). Contour levels are adjusted to the maximum of the ^2H signal with minimum at 50% of maximum.

axial EPR signal (Figure 2B) with principal g_{eff} values of 4.06, 3.99, and 2.00 is produced. These parameters are typical of $\{Fe{-}NO\}^7$ complexes with S = 3/2 ground states and minor rhombicity in the zero-field splitting.[40,41,43] Figure 3A shows a Q-band HYSCORE spectrum collected for the $\{Fe\text{-}NO\}^7$ form of SyrB2 in complex with SyrB1 presenting 4,4,5,5,5-[$^2H_5$]-L-norvaline (hereafter abbreviated **NO-4,5-d_5-Nva**). In ^2H-HYSCORE spectra, hyperfine coupling is manifest as splitting along the antidiagonal, centered on the deuterium Larmor frequency; in addition, further splitting along the diagonal is observed due to the nuclear quadrupole interaction (Figure 2D). At g_{eff} = 3.98 (~613 mT), the observed HYSCORE spectrum exhibits such a signal, centered at the deuterium Larmor frequency (4.0 MHz; Figure 3A). Comparison with the same spectrum collected for a sample prepared with all-protium norvaline (**NO-Nva**) confirms that this feature is attributable to deuterium (Figure 3D). Additional features are observed in all measured spectra (Figure S1, Supporting Information) and attributed to matrix protons and ^{14}N nuclei (e.g., from the histidine ligands and/or from NO), consistent with previous observations on similar systems.[40] For the **NO-4,5-d_5-Nva** complex, it is ambiguous whether the ^2H-HYSCORE signals arise from interactions with deuterium nuclei at C4, C5, or both positions. However, the spectrum of the complex prepared with **5,5,5-[$^2H_3$]-Nva** (**NO-5-d_3-Nva**) at g_{eff} = 3.98 (Figure 3B) reveals features that are essentially identical to those of **NO-4,5-d_5-Nva**. Moreover, spectra of the **NO-4-d_2-Nva** complex have features with visibly reduced width and intensity compared to either **NO-4,5-d_5-Nva** or **NO-5-d_3-Nva** (Figure 3C). Therefore, the signals observed for **NO-4,5-d_5-Nva** are attributed to deuterons at the C5 position.

Because the deuterium nuclei of interest lie along a particular vector in the active site, the hyperfine interaction will have an angular dependence with respect to the electronic **g** tensor (Figure 2C and 2D). In order to ascertain this angular dependence, HYSCORE spectra for **NO-4,5-d_5-Nva** were collected at multiple magnetic fields (Figure S2, Supporting Information), corresponding to excitation of different orientational subpopulations of spins (Figure 2C). For all spectra collected, signals for **NO-4,5-d_5-Nva** and **NO-5-d_3-Nva** were essentially identical (Figure S3, Supporting Information) and simulated by a single axial hyperfine coupling with magnitude T = 0.40 ± 0.05 MHz and quadrupole coupling constant K = 0.035 ± 0.005 MHz (Table S1, Figures S2 and S3, Supporting Information). The ability of a single deuterium hyperfine coupling (rather than three) to adequately account for the observed spectra likely reflects rotational averaging of the three C5 deuterons. In a similar fashion, field-dependent spectra of **NO-4-d_2-Nva** were simulated with parameters T = 0.28 ± 0.05 MHz and K = 0.025 ± 0.005 MHz (Table S1, Figure S4, Supporting Information).

Field-dependent HYSCORE spectra of the NO complex formed with the substrate **2,3,3,4,4,4-[$^2H_6$]-Aba** (**NO-*per*-d_6-Aba**) reveal deuterium features that are visibly less broad than those arising from **NO-4,5-d_5-Nva**, suggesting that, in this sample, the hyperfine interactions are weaker and the

DOI: 10.1021/jacs.5b03370
J. Am. Chem. Soc. 2015, 137, 6912–6919

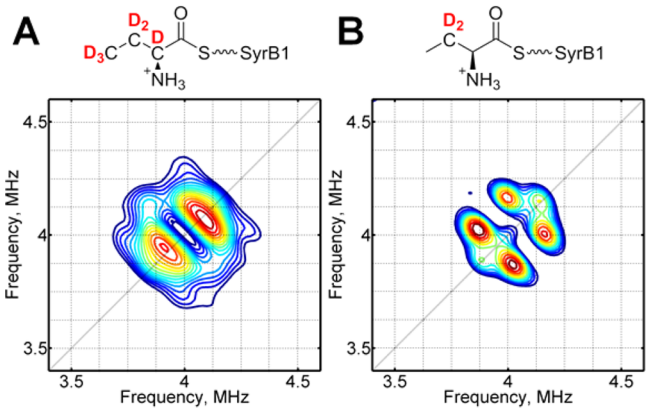

Figure 4. HYSCORE spectra and substrate chemical structures for (A) **NO-*per*-d_6-Aba** and (B) **NO-3-d_2-Aba**, collected at g_{eff} = 3.98. Experimental conditions: magnetic field = 611.9 (A) and 613.5 mT (B); microwave frequency = 34.148 (A) and 34.200 GHz (B); temperature = 4.65 (A) and 4.0 K (B). Contour levels are set as in Figure 3.

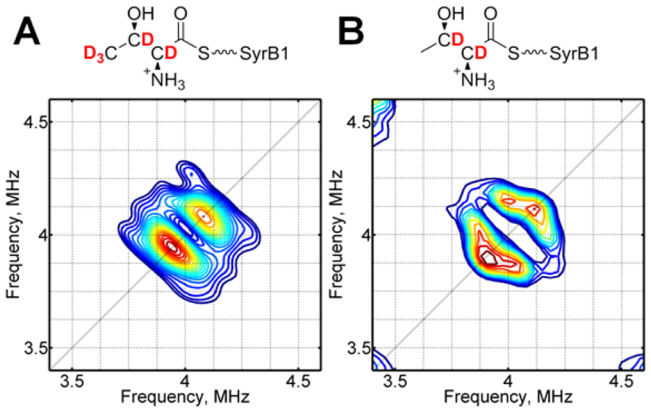

Figure 5. HYSCORE spectra and substrate chemical structures for (A) **NO-*per*-d_5-Thr** and (B) **NO-2,3-d_2-Thr**, collected at g_{eff} = 3.98. Experimental conditions: magnetic field = 613.6 (A) and 613.5 mT (B); microwave frequency = 34.206 (A) and 34.201 GHz (B); temperature = 4.6 (A) and 4.0 K (B). Contour levels are set as in Figure 3.

deuterium nuclei more distant from the {Fe−NO}^{7} moiety (Figures 4A and S5, Supporting Information). As in the case of **Nva**, the spectral features of the **NO-*per*-d_6-Aba** complex arise primarily from the methyl deuterons. This fact, established by the weaker and narrower signals from the **NO-3-d_2-Aba** complex (Figure 4B), shows that the deuterium nuclei at C4 are the closest to the {Fe−NO}^{7} unit, consistent with the known ability of C4 but not C3 to donate H$^\bullet$ to the ferryl intermediate.[35] Although, in principle, the spectrum of **NO-*per*-d_6-Aba** may also contain some contribution from the single deuteron at C2, the complete inactivity of C2 for H$^\bullet$ donation to the ferryl in multiple different non-native substrates suggests that this contribution should be negligible. The spectra for **NO-*per*-d_6-Aba** were simulated with axial hyperfine and quadrupole coupling tensors with magnitude T = 0.29 ± 0.04 MHz and K = 0.050 ± 0.005 MHz, respectively (Table S1, Figure S5, Supporting Information). Spectra collected for **NO-3-d_2-Aba** were simulated with T = 0.14 ± 0.02 MHz and K = 0.043 ± 0.005 MHz (Table S1, Figure S6, Supporting Information).

The native substrate of SyrB2, **Thr**, is almost exclusively chlorinated, and determination of the position of this substrate relative to the cofactor is of particular interest. Therefore, field-dependent HYSCORE spectra of the NO complex formed with the substrate **2,3,4,4,4-[$^2H_5$]-Thr** (**NO-*per*-d_5-Thr**) were recorded. These spectra are similar to the spectra of **NO-*per*-d_6-Aba**, although the ^{2}H signals are discernibly less broad (Figure 5A). Spectra were also collected for the complex prepared with **2,3-d_2-Thr** (Figure 5B). As in the case of **Aba** and **Nva**, the absence of deuteria on the terminal methyl group results in diminished width and intensity of the ^{2}H HYSCORE cross peaks (Figure 5), thus allowing assignment of the majority of the ^{2}H signals in the **NO-*per*-d_5-Thr** spectrum to deuterons on C4. The field-dependent spectra of **NO-*per*-d_5-Thr** were simulated with T = 0.20 ± 0.03 MHz and K = 0.040 ± 0.005 MHz (Table S1, Figure S7, Supporting Information). Signals for **NO-2,3-d_2-Thr**, which we attribute primarily to the single deuteron at the C3 position, were simulated with T = 0.15 ± 0.03 MHz and K = 0.043 ± 0.005 MHz (Figure S8, Supporting Information).

In previous studies on {Fe−NO}^{7} complexes in enzymes, the point-dipole approximation has been used to relate the magnitude of the hyperfine coupling to an Fe−^{2}H distance, with the second hyperfine Euler angle (θ) roughly corresponding to the (O)N−Fe−^{2}H angle.[39−41] To provide more accurate Fe−^{2}H distance and N−Fe−^{2}H angle estimates, we instead developed a geometric model that accounts for spin-density distribution across the Fe−NO unit, with explicit dipolar contributions from both the ferric and the NO$^-$ species (see Materials and Methods). Analyzed by this model, the observed hyperfine parameters correspond to Fe−^{2}H distances of 4.2 ± 0.3, 3.7 ± 0.2, 3.7 ± 0.3, and 3.4 ± 0.3 Å and N−Fe−^{2}H angles of 85° ± 10°, 85° ± 10°, 81° ± 15°, and 64° ± 7° for **NO-*per*-d_5-Thr**, **NO-*per*-d_6-Aba**, **NO-4-d_2-Nva**, and **NO-4,5-d_5-Nva**, respectively (Table S2, Supporting Information, Figure 6B).

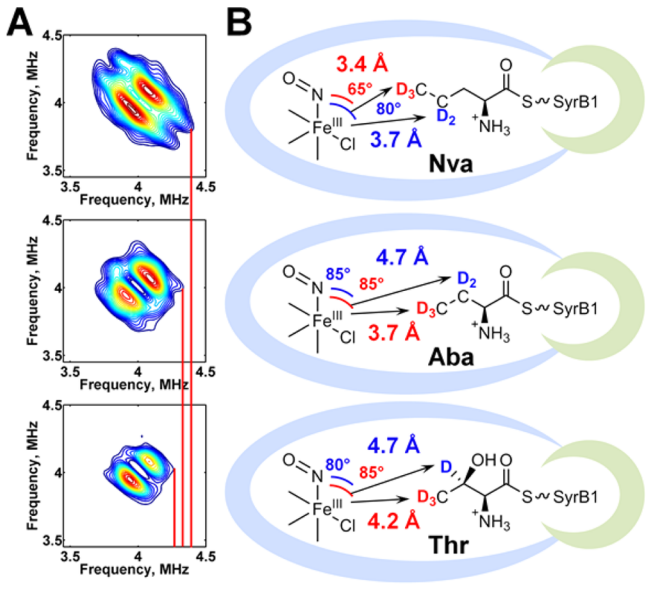

Figure 6. (A) Comparison of the ^{2}H-HYSCORE signals for **NO-4,5-d_5-Nva** (top), **NO-*per*-d_6-Aba** (center), and **NO-*per*-d_5-Thr** (bottom). Red, vertical bars have been added for ease of comparison. Spectra depicted were collected at g_{eff} = 3.98; experimental details are provided in the legends of Figures 3−5. (B) SyrB2 active site models for substrates **Thr**, **Aba**, and **Nva**. Red labels indicate parameters for the methyl deuterons, whereas blue labels indicate the C3 deuterons in Aba and Thr and the C4 deuterons in Nva.

DOI: 10.1021/jacs.5b03370
J. Am. Chem. Soc. 2015, 137, 6912−6919

DISCUSSION

Comparison of the hyperfine coupling constants for the methyl groups of the three substrates investigated reveals a striking trend (Figure 6A). The magnitude of the hyperfine coupling increases significantly through the series: **NO-*per*-d_5-Thr** (0.20 MHz), **NO-*per*-d_6-Aba** (0.29 MHz), **NO-4,5-d_5-Nva** (0.40 MHz), corresponding to distances of 4.2, 3.7, and 3.4 Å, respectively. The observed deuterium positions are fully consistent with the trends in H•-abstraction rate constants and chlorination selectivity previously reported for these substrates. **Nva** is the most efficient H• donor to the ferryl complex and closest to the metallocofactor (3.4 Å). H• transfer from **Thr**, 0.8 Å farther away, is markedly (130-fold) slower. The observed distances for **NO-4-d_2-Nva** and **NO-*per*-d_6-Aba** are very similar, just as the reactivities of C4 of **Aba** and **Nva** are similar. Finally, the hyperfine couplings observed for **NO-3-d_2-Aba** and **NO-2,3-d_2-Thr** correspond to distances of 4.7 ± 0.3 and 4.7 ± 0.4 Å, respectively, consistent with published observations that the chloroferryl complex in SyrB2 does not target the C3 position (e.g., of **Ala**).[35]

The N−Fe−D angle of 85° implies that the target deuterons of **Thr** lie nearly in the plane perpendicular to the Fe−N bond (Figure 6B). Under the simplest assumption, the oxo group of the ferryl complex and hydroxo ligand of the Fe(III)−OH/substrate−radical state would reside in approximately the same location as the nitrosyl ligand (Figure 1). This disposition of substrate and cofactor would also help to rationalize the reactivity data. As shown by computational studies, the nearly orthogonal Fe═O/C−H orientation would result in poor orbital overlap and thus be expected to afford relatively inefficient H• abstraction, as observed for **Thr**. The large angle would then also place the substrate radical relatively far from the hydroxo ligand and potentially much closer to the chloro ligand, which is also expected to lie in the plane perpendicular to the Fe−N bond (Figure 6B). The predominant chlorination observed for **Thr** would thus be rationalized. It should be noted that the position of the Cl^- ligand *within* the plane perpendicular to the Fe−N bond cannot be determined from these data; however, based on the observation of Cl• transfer, it is likely that the target ^2H is close to the Cl^- (i.e., that the Cl−Fe−N−^2H dihedral angle is small). Intriguingly, the relatively modest structural perturbations observed for **Nva**, including a ∼0.8 Å closer approach and ∼20° tilt toward the Fe−N(O) bond, are sufficient to largely unleash both the H•-abstraction potency of the ferryl and the default hydroxylation outcome. Although **NO-*per*-d_5-Thr**, **NO-*per*-d_6-Aba**, and **NO-4-d_2-Nva** all exhibit similar angles (80−85°), the C4 carbons of both **Nva** and **Aba** nevertheless exhibit a partial loss of selectivity, undergoing a mixture of hydroxylation and chlorination. As previously suggested, this difference is potentially attributable to the shorter average distance of the C4 carbon in the non-native substrates from the cofactor (shown here to be the ∼0.5 Å), to greater flexibility of the non-native side chains for dynamic approach, or to both. As the only structural distinction between **Thr** and **Aba**, the *β*-hydroxyl group of **Thr** seemingly must serve to anchor the native side chain (e.g., via hydrogen bonding) either to enforce the greater distance or to restrict its dynamics (or both). Elucidation of this interaction could provide avenues for rational design to promote halogenation of alternative substrates.

Overall, the striking correlation between the observed distances and angles and the reactivity patterns of **Thr**, **Aba**, and **Nva** strongly corroborates the assertion that substrate positioning controls chemoselectivity in SyrB2. These data do not rule out the possibility that coordination isomerism also contributes to selectivity, but the magnitude of the differences in positioning observed in this study strongly suggests that substrate positioning exerts a major influence. In addition, our measurements define this differential positioning; the native substrate is held close to the chloride in the plane perpendicular to the Fe−N(O) bond but at a greater distance from the iron center compared to the non-native substrates. The result of this careful positioning of the native substrate is relatively sluggish H• abstraction by the ferryl intermediate but high chlorination selectivity in the ligand-transfer step.

Although these experiments define the position of the substrate, the interactions which dictate this positioning remain unknown. The large angle observed for **NO-*per*-d_5-Thr** is not obviously consistent with previous docking models together with the simplest assumption that NO would replace the water ligand in the published X-ray crystal structure[32] (Figure S9A, Supporting Information).[37] However, NO coordination at one of the two sites occupied in the crystal structure by the chloride ion and by C1 of 2OG could result in the observed angle (Figure S9B and S9C, Supporting Information). The latter of these two NO binding modes has been observed in clavaminate synthase.[47] Our results thus imply that for the docking model to be correct, a shift of the Cl^- ligand or the 2OG carboxylate must accompany addition of NO and, by analogy, possibly also O_2 to the Fe(II) cofactor. Alternatively, it is also possible that SyrB1 may bind in a different manner that places the substrate at the observed angle when NO adds at the position of the water. This question emphasizes the importance of further structural characterization of the SyrB1:SyrB2 complex.

Finally, the measurement of substrate placement for carbon centers undergoing different outcomes maps the transition from hydroxylation to halogenation; these parameters potentially provide a geometric map for the promotion or suppression of hydroxylation in the Fe/2OG reaction manifold. The striking conclusion is that relatively stringent control of substrate position is required to suppress the hydroxylation outcome. We suggest that these parameters establish guiding metrics for analyzing other alternative reactions catalyzed by members of the Fe/2OG oxygenase family. By comparison of substrate positions in other enzymes with the parameters reported here, cases (e.g., olefin-installing 1,2-dehydrogenations in biosyntheses of antibiotics) in which hydroxylation might or might not be part of the mechanistic pathway can now be analyzed to ascertain whether these poorly understood alternative outcomes arise from avoiding HO• rebound (as in the SyrB2 reaction) or from further processing of a hydroxylated intermediate in a "cryptic hydroxylation" mechanism.

CONCLUSION

Hyperfine couplings have been measured between a series of deuterium-labeled substrates and an active-site {Fe−NO}^{7} complex of the Fe/2OG aliphatic halogenase, SyrB2. Analysis of these parameters provides the first experimental structural data on the complex of an Fe/2OG halogenase with its substrate. The methyl groups of the substrates **Thr**, **Aba**, and **Nva** lie 4.2, 3.7, and 3.4 Å from the metallocofactor (Fe−D distance), explaining the previously observed trend in rates of H• abstraction and chlorination versus hydroxylation selectivity. In addition, the distances observed for adjacent positions (C3

DOI: 10.1021/jacs.5b03370
J. Am. Chem. Soc. 2015, 137, 6912−6919

of **Thr** and **Aba** and C4 of **Nva**) are also consistent with expectations from reactivity studies. The results, along with the analogy of the iron−nitrosyl complex to oxygen-bound intermediates in the catalytic cycle, substantiate the hypothesis that substrate positioning controls reaction outcome in SyrB2 catalysis. Both a relatively long Fe−D distance and an almost perpendicular N−Fe−D angle conspire to promote chlorination of the native substrate, **Thr**. Moreover, the structural parameters for targets spanning the continuum of SyrB2 reactivity, from almost pure halogenation to predominant hydroxylation, lay a foundation for the investigation of how other Fe/2OG enzymes are able to direct other reactions in the diverse array catalyzed by this important enzyme family.

MATERIALS AND METHODS

Materials. Commercially available materials were used without further purification. 2,3,4,4,4-[$^2H_5$]-L-Threonine was purchased from Cambridge Isotope Laboratories. 4,4,5,5,5-[$^2H_5$]-L-Norvaline, 2,3,3,4,4,4-[$^2H_6$]-L-2-aminobutyric acid, 3,3-[$^2H_2$]-L-2-aminobutyric acid, and 2,3-[$^2H_2$]-L-threonine were purchased from C/D/N isotopes. 5,5,5-[$^2H_3$]-L-Norvaline and 4,4-[$^2H_2$]-L-norvaline were synthesized as described elsewhere.[36]

Generation of the Substrate-Bound {Fe−NO}^{7} Complexes. SyrB2 and SyrB1 were prepared, and SyrB1 was charged with the desired amino acid, as previously described.[35] Aminoacyl-*S*-SyrB1 and SyrB2 were deoxygenated separately as previously described.[21] After deoxygenation, SyrB2, Fe(II), Cl^-, 2OG, and aminoacyl-*S*-SyrB1 were mixed in a MBraun (Stratham, NH) anoxic chamber to final concentrations of 1.25, 1.15, 10, 5, and 1.6 mM, respectively. The resulting solution was returned to the Schlenk line; the flask was briefly evacuated to ∼100 Torr and slowly refilled with nitric oxide gas (Messer) to >900 Torr. Under this atmosphere, the protein was incubated on ice with brisk stirring for 10 min, as the dark yellow color developed. The resulting complex was concentrated anaerobically by spin filtration to approximately one-half its original volume (∼15 min), transferred to an EPR tube, and frozen in liquid nitrogen.

Electron Paramagnetic Resonance Measurements. Continuous wave (CW) and pulse EPR spectra were acquired on a Bruker Elexsys E580 spectrometer equipped with a SuperX-FT microwave bridge. CW spectra were acquired at X-band frequencies using a Bruker SHQE resonator. A temperature of 7 K was maintained with an ER 4112-HV Oxford Instruments liquid helium flow cryostat.

Field-swept pulse EPR and HYSCORE spectra were acquired at Q-band frequencies by using a home-built intermediate-frequency extension of the SuperX-FT X-band bridge that has a Millitech 5 W pulse power amplifier. All experiments were conducted on a home-built TE_{011} resonator utilizing the open resonator concept developed by Annino et al.[48] and mechanical construction of the probehead similar to that presented by Reijerse et al.[49] This setup allows $t(\pi/2)$ = 12−16 ns at maximum input power with a spectrometer dead time (including the resonator ring time) of 100−120 ns. Data acquisition and control of experimental parameters were performed by using Bruker XEPR software.

HYSCORE Spectra. HYSCORE spectra were obtained using the standard HYSCORE program available in the XEPR software, with the exception of HYSCORE spectra collected at 950 mT. For standard HYSCORE measurements, the parameters $t(\pi/2)$ = 8 ns and τ = 140 ns (variables defined in Figure S10, Supporting Information) were used. HYSCORE spectra at 950 mT were collected using the matched HYSCORE technique utilizing a PulseSpel program in XEPR.[50] In the latter case, the length of the second and fourth $\pi/2$ pulses was adjusted to match the ^2H Larmor frequency of 6.2 MHz, $t_m \cong 40$ ns (Figure S10, Supporting Information). For this purpose the pulses were generated by the secondary pulse forming unit (i.e, using the $\pm\langle x\rangle$ channels) and attenuated to allow for $t(\pi/2)$ = 40 ns. Unless otherwise noted, spectra were collected with a 28 ns step size and 300 (602, 613, and 700 mT) or 200 points (950 mT) in the *x* and *y* dimensions. Shot repetition time was set to 50 μs, with 100 shots per point. The typical number of scans averaged was 6 (602 mT), 3 (613 mT), 12 (700 mT), and 45 (950 mT). A standard four-step phase cycle was used in all cases. Additional experimental parameters are reported in the figure legends.

Data Analysis. Data processing and spectral simulations were performed using Kazan viewer, a home-written suite of utilities in MATLAB.[51] One-dimensional EPR simulations were performed using the "pepper" utility from the EasySpin software package.[52] HYSCORE data were analyzed by simultaneous frequency domain simulation of all field-dependent spectra until a satisfactory solution was achieved. To reduce the number of fitting variables, a purely axial point-dipolar model of the ^2H hyperfine interaction was used

$$\mathbf{A} = [-1, -1, 2]\mathbf{T} \tag{1}$$

where **T** is the magnitude of the interaction. In addition, the quadrupole coupling was assumed to be purely axial; thus, the following principal values of the quadrupole coupling were used

$$\mathbf{Q} = [-1, -1, 2]\mathbf{K} \tag{2}$$

where $\mathbf{K} = eqQ/[4I(2I + 1)h]$, eqQ is the strength of the electric field gradient, and *I* is the nuclear spin quantum number (I = 1 for ^2H). In the case of **NO-*per*-d_6-Aba** and **NO-4-d_2-Nva**, the axial quadrupole interaction was found to be insufficient and an additional fitting variable η was introduced such that

$$\mathbf{Q}_{x,y,z} = [-1 - \eta, -1 + \eta, 2]\mathbf{K} \tag{3}$$

Details of the parameters used to simulate the experimental data are provided in Table S1, Supporting Information. The orientation of a given tensor is defined by the Euler angles (*y* convention) ϕ, θ, and ψ. In axial tensors, the ϕ angle is meaningless and was not included in any simulations. Uncertainty analysis was performed by stepwise alteration of a given parameter until the fit quality was unacceptable by visual inspection. Both fits and uncertainty analysis were confirmed by construction of one-dimensional "skyline" plots. These plots were constructed with the skyline along the antidiagonal of the HYSCORE plot in order to remove width contributions arising from quadrupolar interactions (Figure S11, Supporting Information).

Distance and angle information was obtained by constructing a model which accounts for hyperfine coupling of the deuterium nucleus with the S = 1 NO^- species and the S = 5/2 ferric species. Distances and angles fixed on the basis of studies on model complexes were Fe−N = 1.75 Å and N−O = 1.14 Å.[53] Varying the Fe−N−O angle from 120° to 180° and the O−N−Fe−^2H dihedral from 0° to 180° produced small deviations relative to the uncertainty in simulation of the hyperfine parameters. The reported parameters are for Fe−N−O = 150° and O−N−Fe−^2H = 180° (Figure S12, Supporting Information). The *z* component of the ground state **g** tensor was assumed to lie along the Fe−N bond.[43] For a given deuterium position, dipolar coupling tensors A_{FeD}, A_{OD}, and A_{ND} were computed using eq 1 to calculate the principal components of the tensors with magnitude, T_{XD}, according to the formula

$$T_{XD}(\text{MHz}) = 12.1362 r_{XD}^{-3} \tag{4}$$

Then the individual tensors were oriented along the corresponding X−D vectors and combined, accounting for the appropriate spin-projection factors and assuming equal spin density on nitrogen and oxygen

$$\mathbf{A}_{tot} = 7/5\mathbf{A}_{FeD} - 2/5(0.5\mathbf{A}_{OD} + 0.5\mathbf{A}_{ND}) \tag{5}$$

where 7/5 and −2/5 are the spin-projection factors for iron and NO, respectively.[54] In addition, the $\mathbf{A}_{tot}$ tensor was rotated according to the third Euler angle (ψ) in the orientation of the experimentally derived hyperfine tensors. The Fe−^2H distance and N−Fe−^2H angle were then varied to match the experimentally observed hyperfine tensor (see Tables S1 and S2, Supporting Information).

DOI: 10.1021/jacs.5b03370
J. Am. Chem. Soc. 2015, 137, 6912−6919

■ ASSOCIATED CONTENT

Supporting Information

Field-dependent HYSCORE spectra, simulations, skyline plots, tables of simulation parameters, and descriptive diagrams. The Supporting Information is available free of charge on the ACS Publications website at DOI: 10.1021/jacs.5b03370.

■ AUTHOR INFORMATION

Corresponding Author

*alexey.silakov@gmail.com

Notes

The authors declare no competing financial interest.

■ ACKNOWLEDGMENTS

R.J.M. gratefully acknowledges the support of the Schriesheim Distinguished Graduate Fellowship (Pennsylvania State University). This work was supported by the National Institutes of Health (GM-69657 to C.K. and J.M.B.) and the National Science Foundation (MCB-642058 and CHE-724084 to C.K. and J.M.B.).

■ REFERENCES

(1) Solomon, E. I.; Brunold, T. C.; Davis, M. I.; Kemsley, J. N.; Lee, S.-K.; Lehnert, N.; Neese, F.; Skulan, A. J.; Yang, Y.-S.; Zhou, J. *Chem. Rev.* **2000**, *100*, 235−350.

(2) Hausinger, R. P. *Crit. Rev. Biochem. Mol. Biol.* **2004**, *39*, 21−68.

(3) Costas, M.; Mehn, M. P.; Jensen, M. P.; Que, L., Jr. *Chem. Rev.* **2004**, *104*, 939−986.

(4) Krebs, C.; Galonić Fujimori, D.; Walsh, C. T.; Bollinger, J. M., Jr. *Acc. Chem. Res.* **2007**, *40*, 484−492.

(5) Wallar, B. J.; Lipscomb, J. D. *Chem. Rev.* **1996**, *96*, 2625−2658.

(6) Krebs, C.; Bollinger, J. M., Jr.; Booker, S. J. *Curr. Opin. Chem. Biol.* **2011**, *15*, 291−303.

(7) Green, M. T. *Curr. Opin. Chem. Biol.* **2009**, *13*, 84−88.

(8) Frey, P. A.; Hegeman, A. D.; Ruzicka, F. J. *Crit. Rev. Biochem. Mol. Biol.* **2008**, *43*, 63−88.

(9) Booker, S. J. *Curr. Opin. Chem. Biol.* **2009**, *13*, 58−73.

(10) Ivan, M.; Kondo, K.; Yang, H.; Kim, W.; Valiando, J.; Ohh, M.; Salic, A.; Asara, J. M.; Lane, W. S.; W, G. K., Jr. *Science* **2001**, *292*, 464−468.

(11) Jaakkola, P.; Mole, D. R.; Tian, Y.-M.; Wilson, M. I.; Gielbert, J.; Gaskell, S. J.; Kriegsheim, A. von; Hebestreit, H. F.; Mukherji, M.; Schofield, C. J.; Maxwell, P. H.; Pugh, C. W.; Ratcliffe, P. J. *Science* **2001**, *292*, 468−472.

(12) Gerken, T.; Girard, C. A.; Tung, Y.-C. L.; Webby, C. J.; Saudek, V.; Hewitson, K. S.; Yeo, G. S. H.; McDonough, M. A.; Cunliffe, S.; McNeill, L. A.; Galvanovskis, J.; Rorsman, P.; Robins, P.; Prieur, X.; Coll, A. P.; Ma, M.; Jovanovic, Z.; Farooqi, I. S.; Sedgwick, B.; Barroso, I.; Lindahl, T.; Ponting, C. P.; Ashcroft, F. M.; O'Rahilly, S.; Schofield, C. J. *Science* **2007**, *318*, 1469−1472.

(13) Trewick, S. C.; Henshaw, T. F.; Hausinger, R. P.; Lindahl, T.; Sedgwick, B. *Nature* **2002**, *419*, 174−178.

(14) Falnes, P. Ø.; Johansen, R. F.; Seeberg, E. *Nature* **2002**, *419*, 178−182.

(15) Yi, C.; Jia, G.; Hou, G.; Dai, Q.; Zhang, W.; Zheng, G.; Jian, X.; Yang, C.-G.; Cui, Q.; He, C. *Nature* **2010**, *468*, 330−333.

(16) Tsukada, Y.; Fang, J.; Erdjument-Bromage, H.; Warren, M. E.; Borchers, C. H.; Tempst, P.; Zhang, Y. *Nature* **2006**, *439*, 811−816.

(17) Klose, R. J.; Yamane, K.; Bae, Y.; Zhang, D.; Erdjument-Bromage, H.; Tempst, P.; Wong, J.; Zhang, Y. *Nature* **2006**, *442*, 312−316.

(18) Cloos, P. A. C.; Christensen, J.; Agger, K.; Maiolica, A.; Rappsilber, J.; Antal, T.; Hansen, K. H.; Helin, K. *Nature* **2006**, *442*, 307−311.

(19) Que, L., Jr. *Nat. Struct. Mol. Biol.* **2000**, *7*, 182−184.

(20) Koehntop, K. D.; Emerson, J. P.; Que, L., Jr. *J. Biol. Inorg. Chem.* **2005**, *10*, 87−93.

(21) Price, J. C.; Barr, E. W.; Tirupati, B.; Bollinger, J. M., Jr.; Krebs, C. *Biochemistry* **2003**, *42*, 7497−7508.

(22) Hoffart, L. M.; Barr, E. W.; Guyer, R. B.; Bollinger, J. M., Jr.; Krebs, C. *Proc. Natl. Acad. Sci. U.S.A.* **2006**, *103*, 14738−14743.

(23) Proshlyakov, D. A.; Henshaw, T. F.; Monterosso, G. R.; Ryle, M. J.; Hausinger, R. P. *J. Am. Chem. Soc.* **2004**, *126*, 1022−1023.

(24) Riggs-Gelasco, P. J.; Price, J. C.; Guyer, R. B.; Brehm, J. H.; Barr, E. W.; Bollinger, J. M., Jr.; Krebs, C. *J. Am. Chem. Soc.* **2004**, *126*, 8108−8109.

(25) Price, J. C.; Barr, E. W.; Glass, T. E.; Krebs, C.; Bollinger, J. M., Jr. *J. Am. Chem. Soc.* **2003**, *125*, 13008−13009.

(26) Hanauske-Abel, H. M.; Günzler, V. *J. Theor. Biol.* **1982**, *94*, 421−455.

(27) Groves, J. T. *J. Chem. Educ.* **1985**, *62*, 928−931.

(28) Vaillancourt, F. H.; Yin, J.; Walsh, C. T. *Proc. Natl. Acad. Sci. U.S.A.* **2005**, *102*, 10111−10116.

(29) Vaillancourt, F. H.; Vosburg, D. A.; Walsh, C. T. *ChemBioChem* **2006**, *7*, 748−752.

(30) Galonić, D. P.; Vaillancourt, F. H.; Walsh, C. T. *J. Am. Chem. Soc.* **2006**, *128*, 3900−3901.

(31) Vaillancourt, F. H.; Yeh, E.; Vosburg, D. A.; O'Connor, S. E.; Walsh, C. T. *Nature* **2005**, *436*, 1191−1194.

(32) Blasiak, L. C.; Vaillancourt, F. H.; Walsh, C. T.; Drennan, C. L. *Nature* **2006**, *440*, 368−371.

(33) Galonić, D. P.; Barr, E. W.; Walsh, C. T.; Bollinger, J. M., Jr.; Krebs, C. *Nat. Chem. Biol.* **2007**, *3*, 113−116.

(34) Galonić Fujimori, D.; Barr, E. W.; Matthews, M. L.; Koch, G. M.; Yonce, J. R.; Walsh, C. T.; Bollinger, J. M., Jr.; Krebs, C.; Riggs-Gelasco, P. J. *J. Am. Chem. Soc.* **2007**, *129*, 13408−13409.

(35) Matthews, M. L.; Krest, C. M.; Barr, E. W.; Vaillancourt, F. H.; Walsh, C. T.; Green, M. T.; Krebs, C.; Bollinger, J. M., Jr. *Biochemistry* **2009**, *48*, 4331−4343.

(36) Matthews, M. L.; Neumann, C. S.; Miles, L. A.; Grove, T. L.; Booker, S. J.; Krebs, C.; Walsh, C. T.; Bollinger, J. M., Jr. *Proc. Natl. Acad. Sci. U.S.A.* **2009**, *106*, 17723−17728.

(37) Borowski, T.; Noack, H.; Radoń, M.; Zych, K.; Siegbahn, P. E. M. *J. Am. Chem. Soc.* **2010**, *132*, 12887−12898.

(38) Wong, S. D.; Srnec, M.; Matthews, M. L.; Liu, L. V.; Kwak, Y.; Park, K.; Bell, C. B. I.; Alp, E. E.; Zhao, J.; Yoda, Y.; Kitao, S.; Seto, M.; Krebs, C.; Bollinger, J. M., Jr.; Solomon, E. I. *Nature* **2013**, *499*, 320−323.

(39) Yang, T. C.; Wolfe, M. D.; Neibergall, M. B.; Mekmouche, Y.; Lipscomb, J. D.; Hoffman, B. M. *J. Am. Chem. Soc.* **2003**, *125*, 7056−7066.

(40) Muthukumaran, R. B.; Grzyska, P. K.; Hausinger, R. P.; McCracken, J. *Biochemistry* **2007**, *46*, 5951−5959.

(41) Casey, T. M.; Grzyska, P. K.; Hausinger, R. P.; McCracken, J. *J. Phys. Chem. B* **2013**, *117*, 10384−10394.

(42) Enemark, J. H.; Feltham, R. D. *Coord. Chem. Rev.* **1974**, *13*, 339−406.

(43) Brown, C. A.; Pavlosky, M. A.; Westre, T. E.; Zhang, Y.; Hedman, B.; Hodgson, K. O.; Solomon, E. I. *J. Am. Chem. Soc.* **1995**, *117*, 715−732.

(44) Hauser, C.; Glaser, T.; Bill, E.; Weyhermüller, T.; Wieghardt, K. *J. Am. Chem. Soc.* **2000**, *122*, 4352−4365.

(45) Ye, S.; Price, J. C.; Barr, E. W.; Green, M. T.; Bollinger, J. M., Jr.; Krebs, C.; Neese, F. *J. Am. Chem. Soc.* **2010**, *132*, 4739−4751.

(46) Ye, S.; Riplinger, C.; Hansen, A.; Krebs, C.; Bollinger, J. M., Jr.; Neese, F. *Chem.—Eur. J.* **2012**, *18*, 6555−6567.

(47) Zhang, Z.; Ren, J.; Harlos, K.; McKinnon, C. H.; Clifton, I. J.; Schofield, C. J. *FEBS Lett.* **2002**, *517*, 7−12.

(48) Annino, G.; Cassettari, M.; Martinelli, M. *IEEE Trans. Microwave Theory Tech.* **2009**, *57*, 775−783.

(49) Reijerse, E.; Lendzian, F.; Isaacson, R.; Lubitz, W. *J. Magn. Reson.* **2012**, *214*, 237−243.

(50) Jeschke, G.; Rakhmatullin, R.; Schweiger, A. *J. Magn. Reson.* **1998**, *131*, 261−271.

DOI: 10.1021/jacs.5b03370
J. Am. Chem. Soc. 2015, 137, 6912−6919

(51) Kazan Viewer-Homepage Alexey Silakov: https://sites.google.com/site/silakovalexey/kazan-viewer; accessed May 7, 2015.
(52) Stoll, S.; Schweiger, A. *J. Magn. Reson.* **2006**, *178*, 42−55.
(53) Westre, T. E.; Di Cicco, A.; Filipponi, A.; Natoli, C. R.; Hedman, B.; Solomon, E. I.; Hodgson, K. O. *J. Am. Chem. Soc.* **1994**, *116*, 6757−6768.
(54) Bencini, A.; Gatteschi, D. *EPR of Exchange Coupled Systems*; Springer-Verlag: Berlin, 1990.

DOI: 10.1021/jacs.5b03370
J. Am. Chem. Soc. 2015, 137, 6912−6919

Supporting Information for:

Experimental Correlation of Substrate Position with Reaction Outcome in the Aliphatic Halogenase, SyrB2

Ryan J. Martinie,[a] Jovan Livada,[a] Wei-chen Chang,[a] Michael T. Green,[a] Carsten Krebs,[a,b] J. Martin Bollinger Jr.,[a,b] and Alexey Silakov[a*]

Departments of [a]Chemistry and [b]Biochemistry and Molecular Biology, The Pennsylvania State University, University Park, PA, USA.

SI Figures

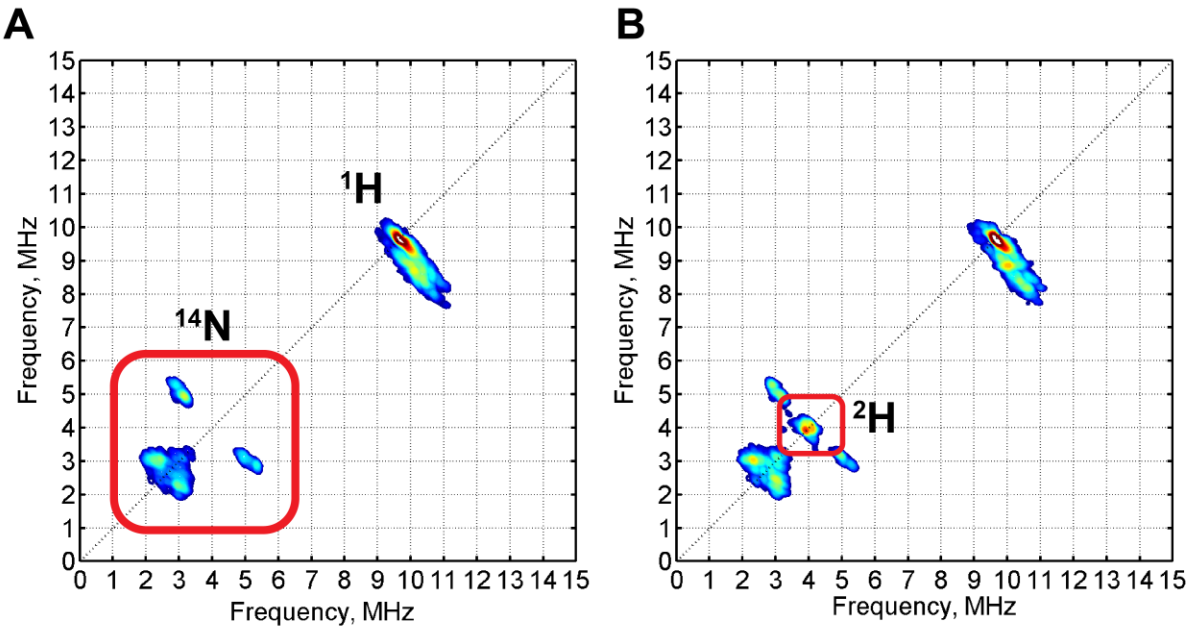

Figure S1. Representative HYSCORE spectra of **NO-Aba** (A) and **NO-*per*-d_6-Aba** (B). Signals arising from ^{14}N, ^{1}H, and ^{2}H nuclei are indicated. Experimental conditions given in Figure 4 of the main text.

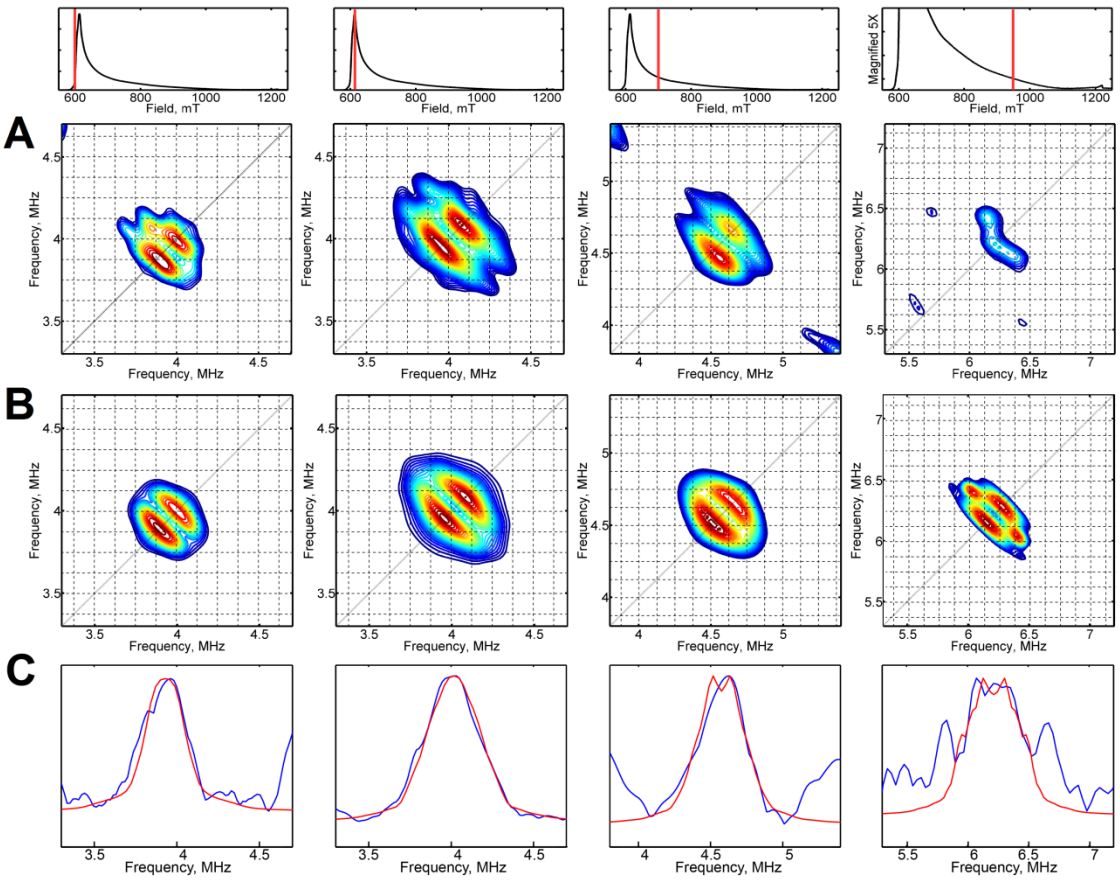

Figure S2. Experimental (A) and simulated (B) HYSCORE spectra for **NO-4,5-d_5-Nva**. C) Anti-diagonal skyline plots with experimental (blue) and simulated (red) spectra overlaid. Red lines in one-dimensional, absorptive EPR spectra (top) indicate magnetic field at which corresponding HYSCORE were collected/simulated. Experimental Conditions (listed from left to right): Magnetic Field: 602.2 mT, 613.5 mT, 700.0 mT, 950.0 mT; Microwave Frequency: 34.209 GHz (602.2 mT), 34.201 GHz (613.5 and 950.0 mT), 34.207 GHz (700.0 mT); 700.0 mT spectrum collected with 200 points in x and y dimensions. Temperature: 4.2, 4.5, 4.2, and 4.0 K.

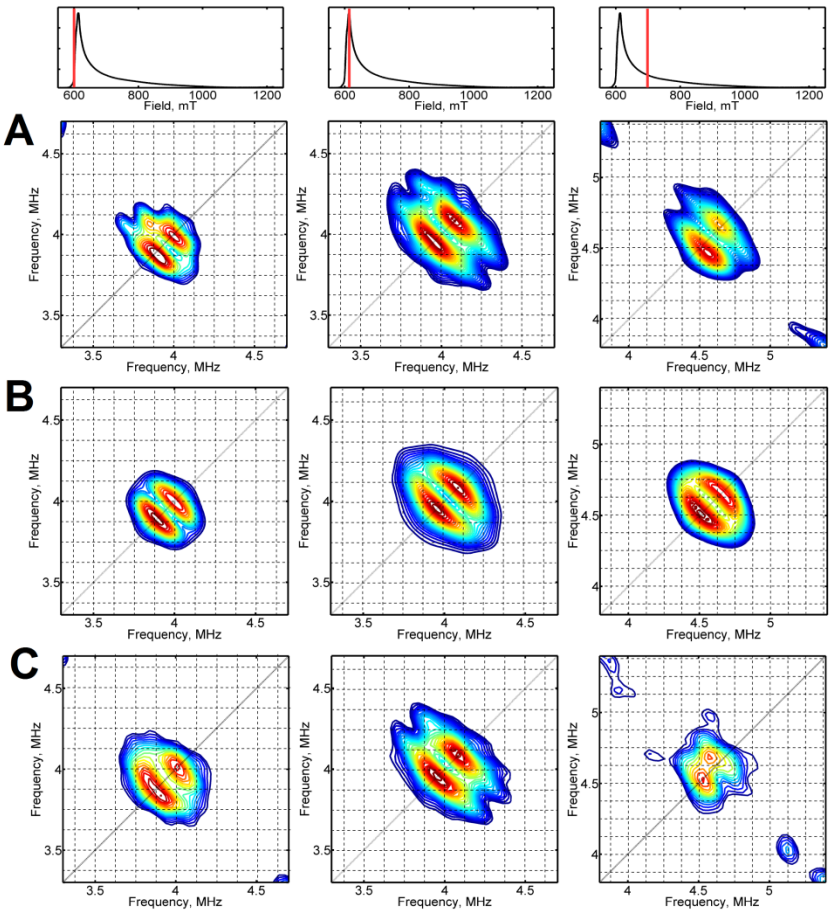

Figure S3. Comparison of HYSCORE spectra obtained for A) **NO-4,5-*d*$_5$-Nva** and C) **NO-5-*d*$_3$-Nva**. B) Simulated spectra. Red lines in one-dimensional, absorptive EPR spectra (top) indicate magnetic field at which corresponding HYSCORE were collected/simulated. Experimental parameters. **NO-4,5-*d*$_5$-Nva** (see legend, Figure S4); **NO-5-*d*$_3$-Nva**: Magnetic Field: 602.2 mT, 613.5 mT, 700.0 mT; Microwave Frequency: 34.198 GHz (602.2 mT), 34.199 GHz (613.5 and 700.0 mT); Temperature: 4.0 K.

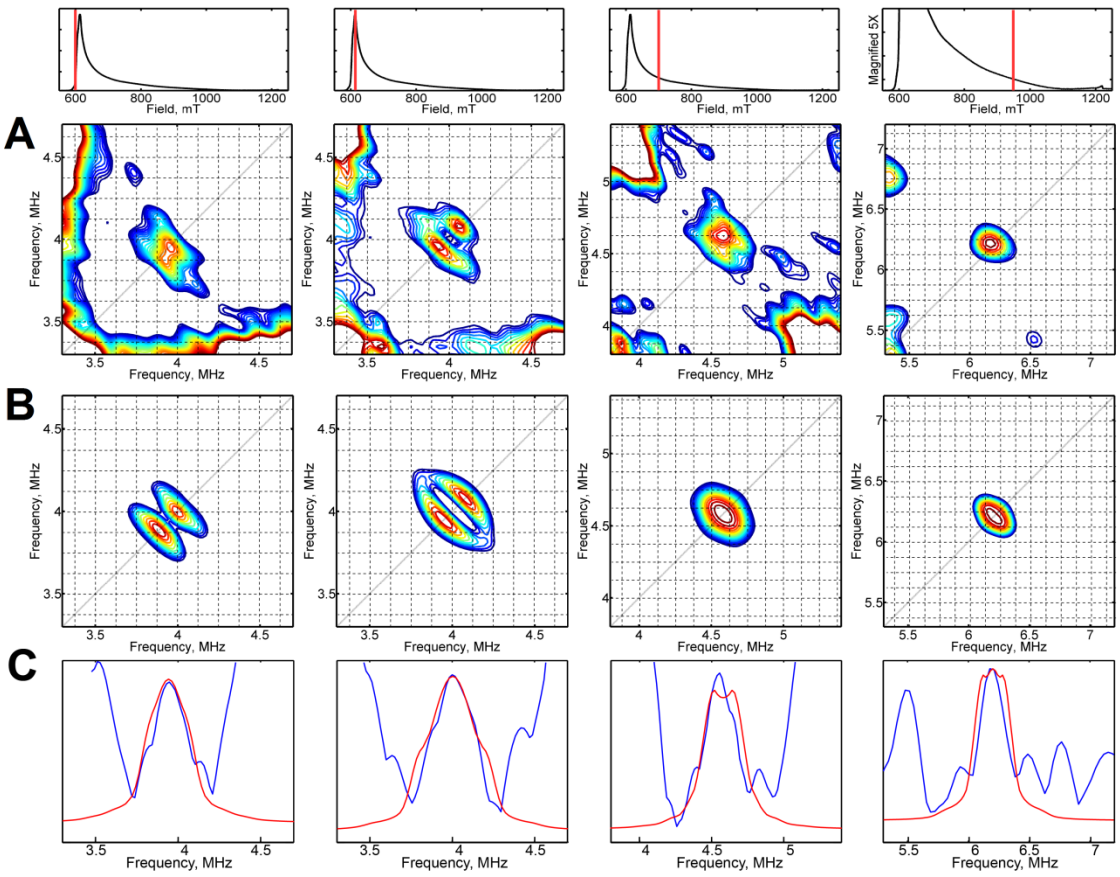

Figure S4. Experimental (A) and simulated (B) HYSCORE spectra for **NO-4-d_2-Nva**. C) Anti-diagonal skyline plots with experimental (blue) and simulated (red) spectra overlaid. Red lines in one-dimensional, absorptive EPR spectra (top) indicate magnetic field at which corresponding HYSCORE were collected/simulated. Experimental Conditions (listed from left to right): Magnetic Field: 602.2 mT, 613.0 mT, 700.0 mT, 950.0 mT; Microwave Frequency: 34.203 GHz (602.2 and 700.0 mT), 34.202 GHz (613.5 mT), 34.189 GHz (950.0 mT); 950.0 mT spectrum collected with 128 points in x and y dimensions. Temperature: 4.0 K.

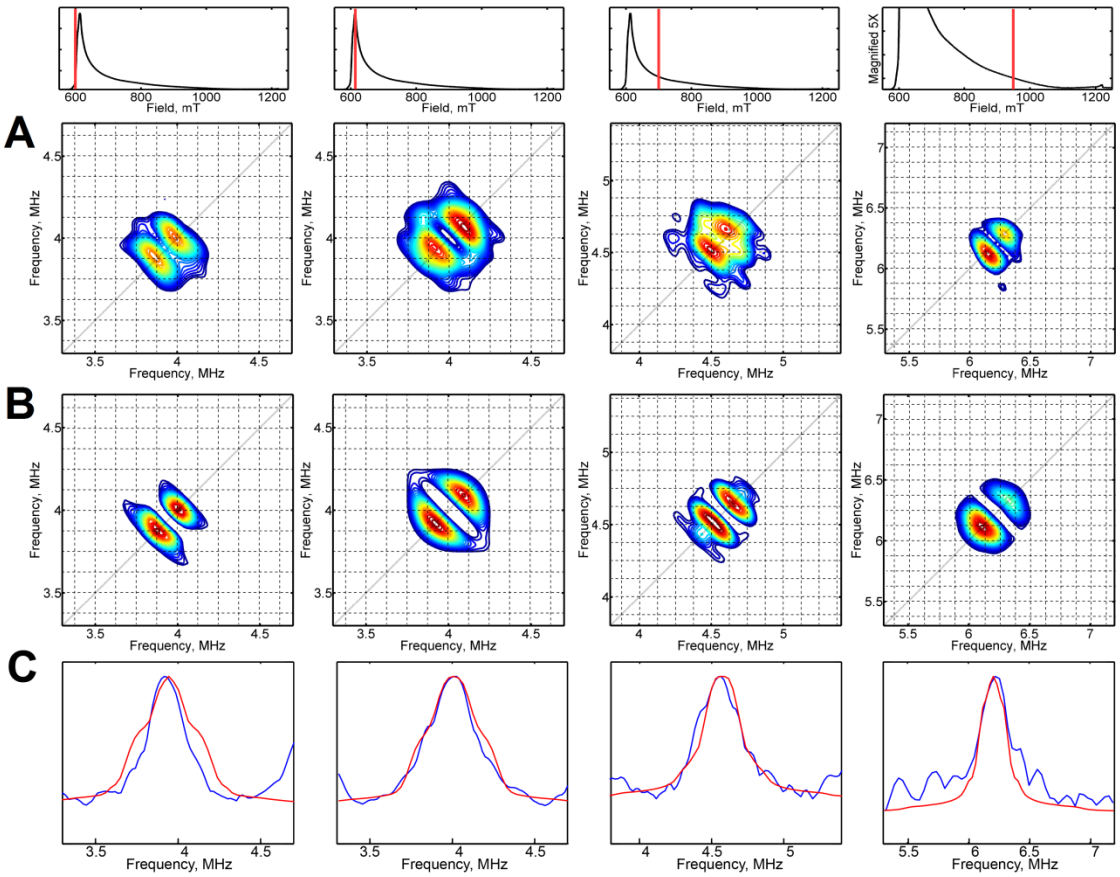

Figure S5. Experimental (A) and simulated (B) HYSCORE spectra for **NO-*per*-d_6-Aba**. C) Anti-diagonal skyline plots with experimental (blue) and simulated (red) spectra overlaid. Red lines in one-dimensional, absorptive EPR spectra (top) indicate magnetic field at which corresponding HYSCORE were collected/simulated. Experimental Conditions (listed from left to right): Magnetic Field: 602.2 mT, 611.9 mT, 700.0 mT, 950.0 mT; Microwave Frequency: 34.148 GHz (602.2, 611.9, and 700.0 mT) 34.192 GHz (950.0 mT); 700.0 mT spectrum collected with 350 points in the x and y dimension with 24 ns step. Temperature: 4.65 K (602.2, 611.9, and 700.0 mT), 4.2 K (950.0 mT).

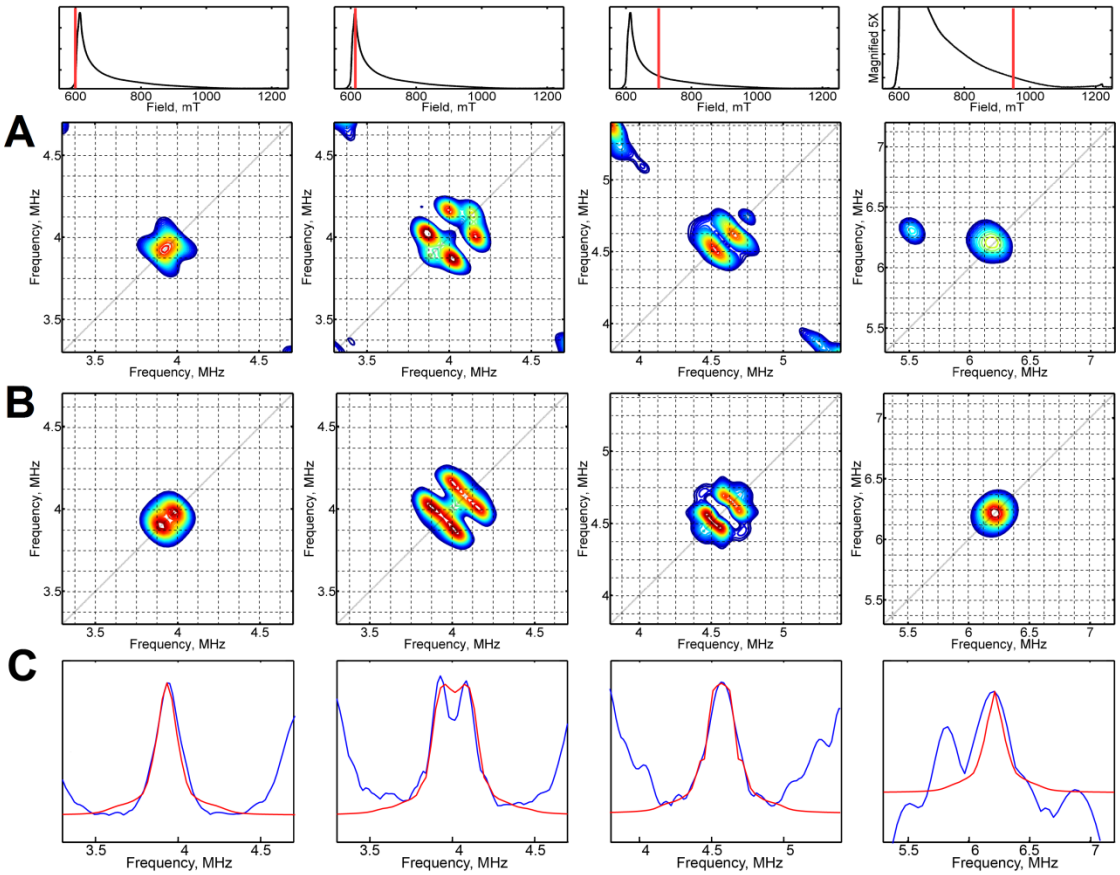

Figure S6. Experimental (A) and simulated (B) HYSCORE spectra for **NO-3-d_2-Aba**. C) Anti-diagonal skyline plots with experimental (blue) and simulated (red) spectra overlaid. Red lines in one-dimensional, absorptive EPR spectra (top) indicate magnetic field at which corresponding HYSCORE were collected/simulated. Experimental Conditions (listed from left to right): Magnetic Field: 602.2 mT, 613.5 mT, 700.0 mT, 950.0 mT; Microwave Frequency: 34.204 GHz (602.2 and 950.0 mT), 34.200 GHz (613.5 and 700.0 mT); Temperature: 4.0 K.

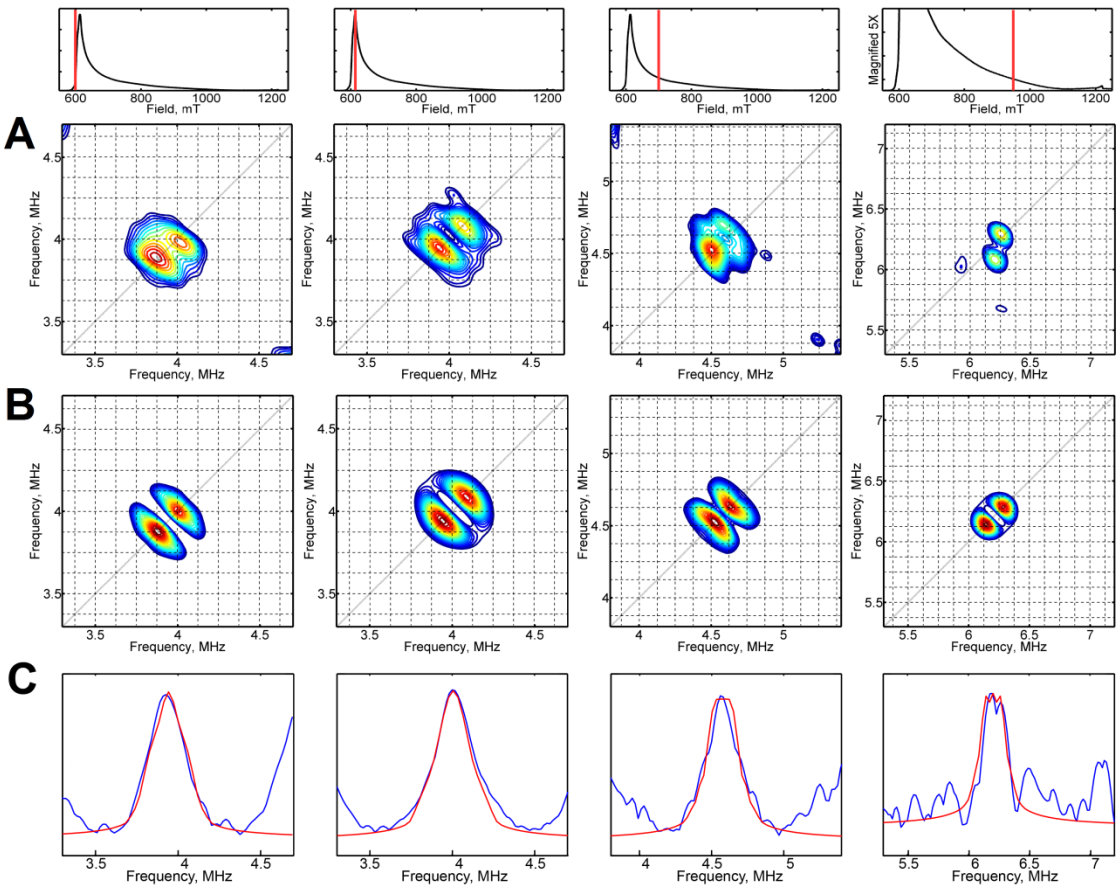

Figure S7. Experimental (A) and simulated (B) HYSCORE spectra for **NO-*per*-d_5-Thr**. C) Anti-diagonal skyline plots with experimental (blue) and simulated (red) spectra overlaid. Red lines in one-dimensional, absorptive EPR spectra (top) indicate magnetic field at which corresponding HYSCORE were collected/simulated. Experimental Conditions (listed from left to right): Magnetic Field: 602.2 mT, 613.6 mT, 700.0 mT, 950.0 mT; Microwave Frequency: 34.206 GHz (602.2, 613.6, and 700.0 mT) 34.202 GHz (950.0 mT); 700.0 mT spectrum collected with 350 points in the x and y dimensions with 24 ns step; Temperature: 4.6 K (602.2, 613.6, and 700.0 mT), 4.2 K (950.0 mT).

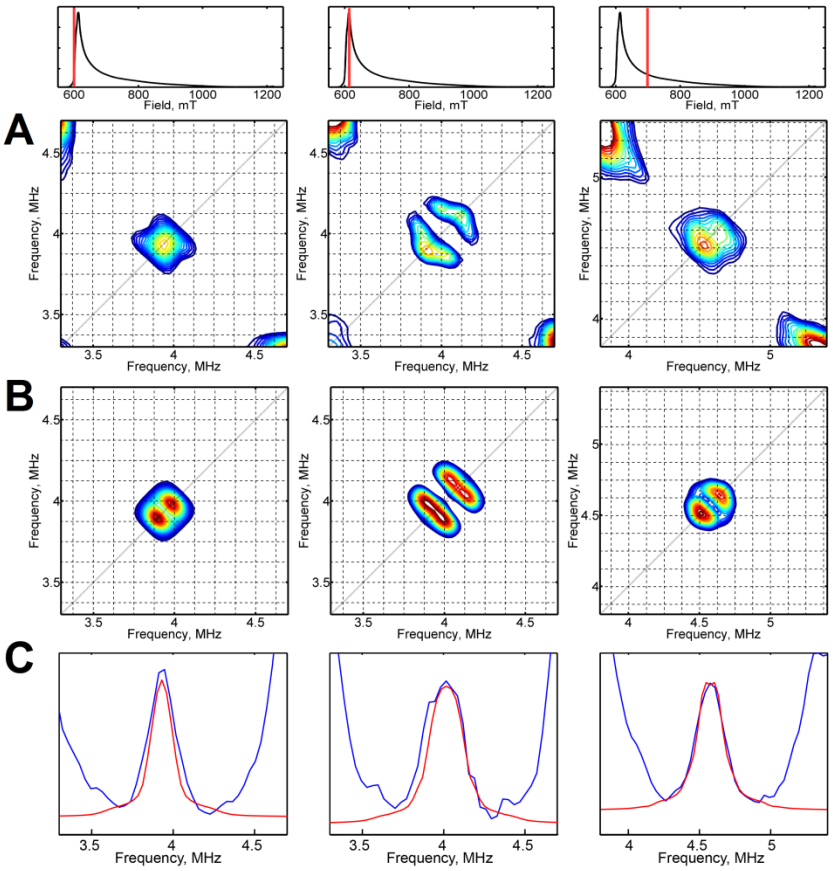

Figure S8. Experimental (A) and simulated (B) HYSCORE spectra for **NO-2,3-*d*$_2$-Thr**. C) Anti-diagonal skyline plots with experimental (blue) and simulated (red) spectra overlaid. Red lines in one-dimensional, absorptive EPR spectra (top) indicate magnetic field at which corresponding HYSCORE were collected/simulated. Experimental Conditions (listed from left to right): Magnetic Field: 602.2 mT, 613.5 mT, 700.0 mT; Microwave Frequency: 34.201 GHz; Temperature: 4.0 K.

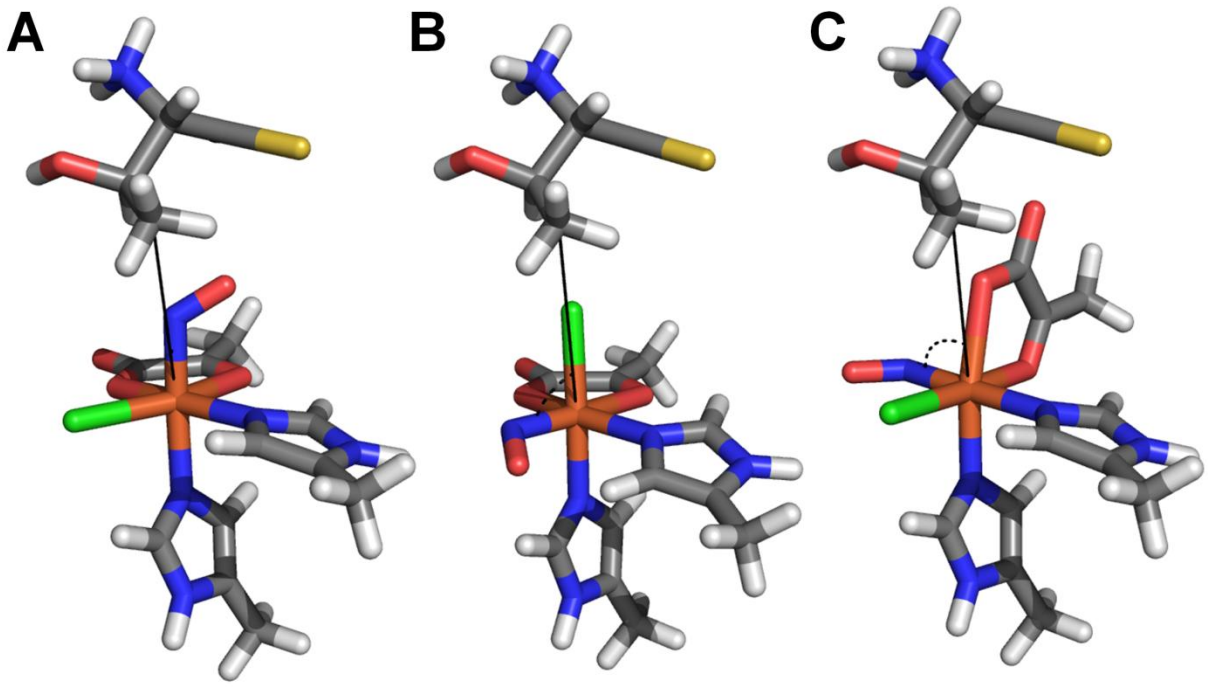

Figure S9. Comparison of substrate docking models for **Thr** with NO displacing the following ligands (relative to the crystal structure): the water ligand (A), the chloride ligand (B), and C1 of 2OG (C). Adapted from ref. 37 in the main text by replacement of the ferryl O-atom with NO, and of acetate with 2-oxo-propionic acid

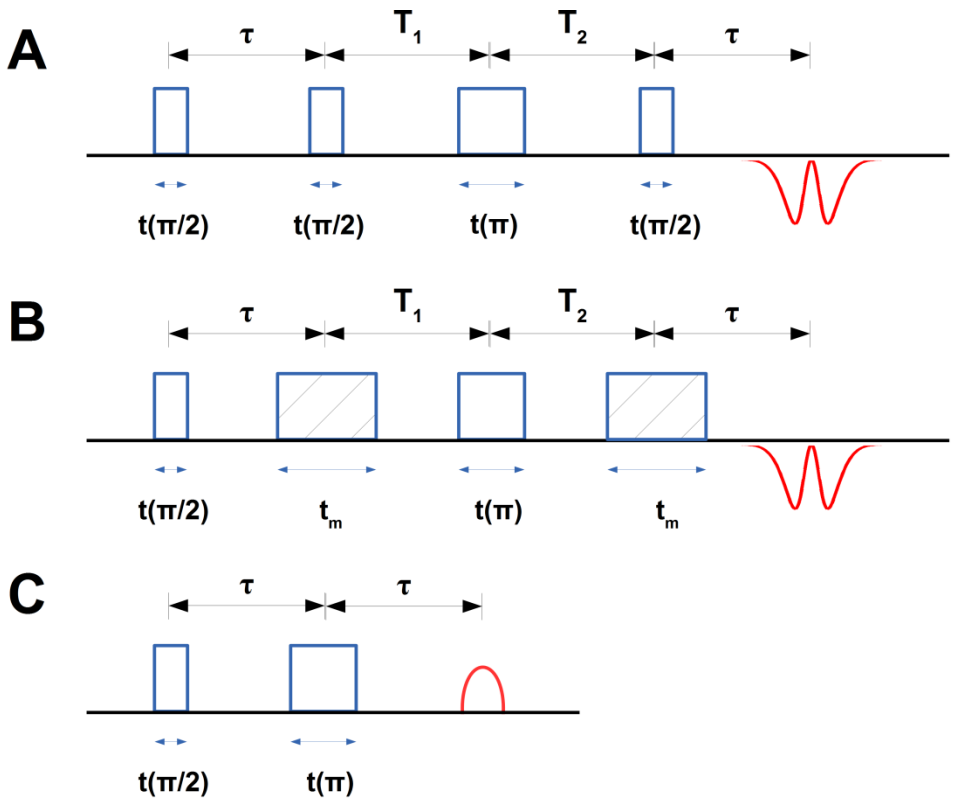

Figure S10. EPR pulse sequences employed: A) HYSCORE, B) Matched HYSCORE, C) Spin-echo detected EPR (one-dimensional).

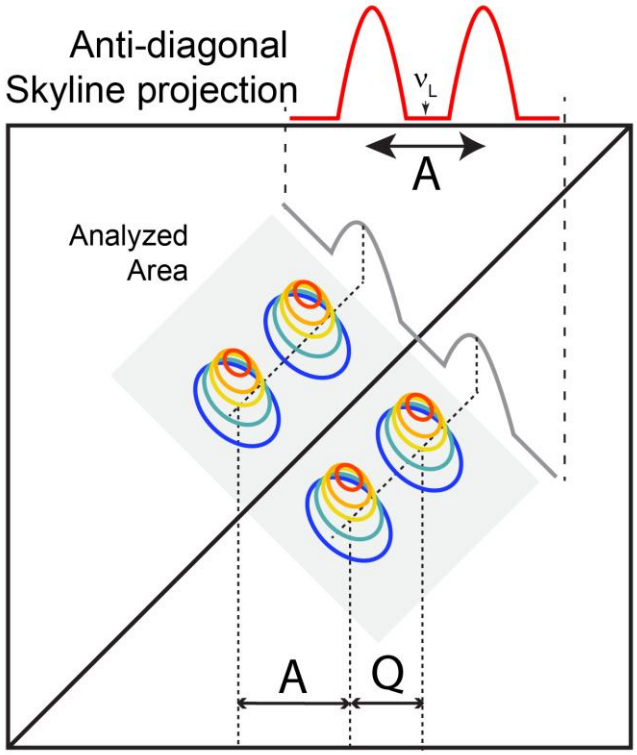

Figure S11. Cartoon representation of anti-diagonal skyline plot construction. A hypothetical HYSCORE spectrum, consisting of four peaks which are split by both hyperfine (A) and quadrupole (Q) interactions. The grey spectrum represents a skyline plot of the analyzed area (shaded grey), which is projected onto the frequency axis (red) to give the final result. For convenience, the projected result is shifted so as to be centered on the Larmor frequency.

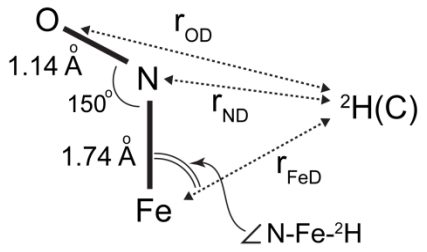

Figure S12. Schematic representation of the model used to determine Fe-^{2}H distances from a given hyperfine coupling tensor.

SI Tables

Table S1. Spin Hamiltonian parameters used to simulate HYSCORE spectra. Parentheses indicate uncertainty in the last reported digit, determined by altering the parameter until the fit was deemed unacceptable by visual inspection. Variables are defined in the Materials and Methods.

	Hyperfine Coupling				Quadrupole Coupling				
	T (MHz)	ϕ (°)	θ (°)	ψ (°)	K (MHz)	ϕ (°)	θ (°)	ψ (°)	η
d5-Nva	0.40(5)	-	58(5)	47(10)	0.035(5)	-	51(10)	0(10)	-
d3-Nva	0.40(5)	-	58(5)	47(10)	0.035(5)	-	51(10)	0(10)	-
d2-Nva	0.28(5)	-	75(15)	50(20)	0.025(5)	-	65(20)	17(20)	-0.5
d6-Aba	0.29(4)	-	80(10)	40(10)	0.050(5)	-	55(10)	7(10)	0.2
d2-Aba	0.14(2)	-	80(10)	75(10)	0.043(5)	-	45(10)	10(10)	-
d5-Thr	0.20(3)	-	80(10)	42(10)	0.040(5)	-	53(10)	0(10)	-
d2-Thr	0.14(3)	-	75(10)	57(10)	0.043(5)	-	30(20)	30(20)	-

Table S2. Geometric parameters obtained based on the hyperfine coupling tensors reported in Table S1. r_{eff} represents the distance obtained from a simple point-dipole approximation, whereas r_{model} represents that obtained from fitting of the hyperfine tensor using multiple dipolar coupling contriburions in an antiferromagnetic coupling model (see Materials and Methods). Parentheses indicate uncertainty in the last reported digit.

	Hyperfine Coupling		
	r_{eff} (Å)	r_{model} (Å)	N-Fe-D (°)
d5-Nva	3.1(2)	3.4(3)	64(7)
d3-Nva	3.1(2)	3.4(3)	64(7)
d2-Nva	3.5(3)	3.7(3)	81(15)
d6-Aba	3.5(2)	3.7(2)	85(10)
d2-Aba	4.4(3)	4.7(3)	85(10)
d5-Thr	3.9(3)	4.2(3)	85(10)
d2-Thr	4.4(4)	4.7(4)	81(10)

Appendix B

Evidence for a Di-μ-oxo Diamond Core in the Mn(IV)/Fe(IV) Activation Intermediate of Ribonucleotide Reductase from *Chlamydia trachomatis*.

Reprinted with permission from

Martinie, R. J.; Blaesi, E. J.; Krebs, C.; Bollinger, J. M., Jr.; Silakov, A.; Pollock, C. J. *J. Am. Chem. Soc.* **2017**, 139, 1950-1957.

Acknowledgements

I gratefully acknowledge Dr. Beth Blasei, who helped to collect the EXAFS data at SSRL and provided many valuable discussions. Prof. Carsten Krebs and Prof. J. Martin Bollinger, Jr. provided critical feedback on the manuscript in preparation for publication. In particular, Carsten's dissatisfaction with the "eyebrow" figure improved it greatly. Once again, I profusely thank Prof. Alexey Silakov, who was involved in all aspects of the EPR data collection, analysis, and presentation. Finally, not enough can be said about the contributions of Dr. Chris Pollock to this work. It was with Chris that the idea for this study was hatched at CHESS C-line in a fit of frustration with the samples we were measuring. Furthermore, Chris was intimately involved in the collection of the EXAFS data, took the lead in analyzing the same, and, in short, taught me everything I know about x-ray spectroscopy.

JACS
JOURNAL OF THE AMERICAN CHEMICAL SOCIETY

Article

pubs.acs.org/JACS

Evidence for a Di-μ-oxo Diamond Core in the Mn(IV)/Fe(IV) Activation Intermediate of Ribonucleotide Reductase from *Chlamydia trachomatis*

Ryan J. Martinie,[†] Elizabeth J. Blaesi,[†] Carsten Krebs,[†,‡] J. Martin Bollinger, Jr.,[†,‡] Alexey Silakov,*[,†] and Christopher J. Pollock*[,†]

[†]Department of Chemistry and [‡]Department of Biochemistry and Molecular Biology, The Pennsylvania State University, University Park, Pennsylvania 16802, United States

Supporting Information

ABSTRACT: High-valent iron and manganese complexes effect some of the most challenging biochemical reactions known, including hydrocarbon and water oxidations associated with the global carbon cycle and oxygenic photosynthesis, respectively. Their extreme reactivity presents an impediment to structural characterization, but their biological importance and potential chemical utility have, nevertheless, motivated extensive efforts toward that end. Several such intermediates accumulate during activation of class I ribonucleotide reductase (RNR) β subunits, which self-assemble dimetal cofactors with stable one-electron oxidants that serve to initiate the enzyme's free-radical mechanism. In the class I-c β subunit from *Chlamydia trachomatis*, a heterodinuclear Mn(II)/Fe(II) complex reacts with dioxygen to form a Mn(IV)/Fe(IV) intermediate, which undergoes reduction of the iron site to produce the active Mn(IV)/Fe(III) cofactor. Herein, we assess the structure of the Mn(IV)/Fe(IV) activation intermediate using Fe- and Mn-edge extended X-ray absorption fine structure (EXAFS) analysis and multifrequency pulse electron paramagnetic resonance (EPR) spectroscopy. The EXAFS results reveal a metal−metal vector of 2.74−2.75 Å and an intense light-atom (C/N/O) scattering interaction 1.8 Å from the Fe. Pulse EPR data reveal an exchangeable deuterium hyperfine coupling of strength |T| = 0.7 MHz, but no stronger couplings. The results suggest that the intermediate possesses a di-μ-oxo diamond core structure with a terminal hydroxide ligand to the Mn(IV).

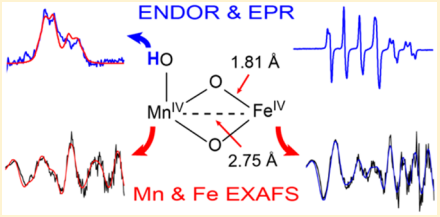

INTRODUCTION

Metalloenzymes catalyze a diverse array of biochemical reactions in metabolism and regulation; some of the most chemically challenging of these reactions are effected by high-valent iron and manganese complexes. Among a myriad of other examples,[1−7] the oxidation of methane to methanol by the soluble form of methane monooxygenase (sMMO),[8−11] the production of deoxyribonucleotides for DNA synthesis and repair,[12−15] water oxidation by the oxygen evolving complex of photosystem II,[16−18] and metabolism of the majority of prodrugs in humans[19,20] all involve such complexes at key steps. A robust understanding of the structures of these potent intermediates and how enzymes generate and control them is central to efforts to develop bioinspired catalysts for water oxidation, C−H-bond activation, and other processes not yet mastered by synthetic chemists.[7,21]

The ferritin-like dimetal-carboxylate (FDC) oxidases and oxygenases are a particularly illustrative example of how structurally similar proteins can direct different pathways for formation and decay of high-valent transition metal intermediates and thereby specify different outcomes. Members of this important enzyme superfamily utilize a largely conserved protein structure and ligand sphere to bind nonheme dimetal cofactors that interact with dioxygen or reduced forms thereof to generate an array of distinct intermediates and carry out diverse biological functions.[22] One of the most extensively studied FDC proteins, the hydroxylase component of soluble methane monooxygenase (sMMOH), effects the conversion of methane to methanol. sMMOH activates oxygen at its diiron(II/II) cluster to form a μ-peroxodiiron(III/III) complex, P (or H_{peroxo}), which subsequently decays to the high-valent intermediate, Q, a diiron(IV/IV) complex.[9,23] The potently oxidizing Q overcomes the high homolytic C−H bond-dissociation energy (104 kcal/mol) of methane to initiate its hydroxylation. An analogous mechanism has been proposed for the related fatty acid desaturases.[24] Another FDC protein, aldehyde deformylating oxygenase (ADO), converts C_n fatty aldehydes to the corresponding C_{n-1} alk(a/e)nes and formate, a formally redox-neutral conversion.[25−27] ADO activates oxygen, purportedly via a diiron(III/III)-peroxyhemiacetal complex,[28,29] which undergoes univalent reduction to initiate a radical-scission reaction that cleaves the C−C bond.[29] Thus, different members of the FDC family utilize divergent mechanistic strategies to achieve chemically diverse outcomes.

Additional distinct outcomes occur in the β subunits of class I ribonucleotide reductases (RNRs). RNRs catalyze the reduction of ribonucleotides to deoxyribonucleotides via a

Received: November 7, 2016
Published: January 11, 2017

DOI: 10.1021/jacs.6b11563
J. Am. Chem. Soc. 2017, 139, 1950−1957

largely conserved free-radical mechanism,[13,30] initiated by a transient cysteine-thiyl radical.[31,32] In class I RNRs, present in eukaryotes as well as some bacteria and archaea, this thiyl radical is generated by a long-range electron transfer from the cysteine in the α subunit to a stable, one-electron oxidant in the β subunit.[31,33] The β subunit is an FDC protein, and the dimetal cofactor serves either directly as the catalytically required oxidant or to generate this oxidant. In a class I-a RNR, the diiron(II/II) form of the β subunit reacts with oxygen to form a μ-peroxodiiron(III/III) complex akin to P in sMMOH,[34−36] but instead of undergoing a redox-neutral conversion to a Q-like diiron(IV/IV) complex, it (or its nonaccumulating successor) instead undergoes one-electron reduction to produce the diiron(III/IV) complex, X.[12,37] X oxidizes a nearby tyrosine to form a stable tyrosyl radical cofactor,[38−42] which serves as the initiating one-electron oxidant of the cysteine in α. Class I-b enzymes employ a structurally similar dimanganese cluster to install the tyrosyl radical;[43−45] rather than reacting directly with dioxygen, the dimanganese(II/II) cofactor reacts with superoxide (generated from O_2 by a flavin-containing activator protein, NrdI, that forms a complex with the RNR β subunit) to form a dimanganese(III/IV) intermediate that oxidizes the tyrosine.[15,43,46] In contrast, the β subunits of class I-c RNRs, exemplified by the protein from *Chlamydia trachomatis* (*Ct*), have a phenylalanine at the sequence position occupied by the radical-harboring tyrosine in the class I-a/b subunits.[47] The stable one-electron oxidant is instead harbored directly on the metallocofactor, a Mn(IV)/Fe(III) complex.[14,48−51] In the *Ct* RNR β subunit, the Mn(II)/Fe(II) complex reacts with dioxygen to generate a Mn(IV)/Fe(IV) intermediate (hereafter denoted **4**/**4**; Scheme 1),[52] which is reduced by one electron to form the active Mn(IV)/Fe(III) cofactor.[53]

Scheme 1. Activation Pathway of the Class I-c Ribonucleotide Reductase[a]

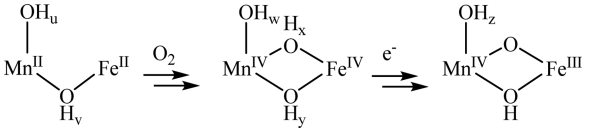

[a]Subscripted letters u−z are intended to designate protonation states that are not known; each term thus has an integer value ranging from 0 to 2.[51,52,54]

The FDC proteins thus constitute a remarkably flexible scaffold that can use iron or manganese in diverse O_2-activation chemistry that enables multiple essential biological functions. This functional flexibility depends on the capacity of the individual proteins to direct formation of intermediate states with appropriate reactivity, to avoid formation of alternative high-valent complexes, and, thereby, to suppress undesired outcomes (e.g., self-hydroxylations) for which the FDC scaffold is competent. To understand the structural basis for this control of reaction pathway, it is necessary to define the manifold of structures represented among these high-valent intermediates. Historically, structural characterization of these complexes has been fraught with controversy. Indeed, despite the more than two decades of scrutiny, Q and X continue to be subjects of structural studies. Nearly 20 years ago, an examination of Q by extended X-ray absorption fine structure (EXAFS) suggested an Fe−Fe distance of only 2.46 Å, leading to the proposal of a di-μ-oxo diamond core structure for the intermediate.[10] However, for the ensuing 19 years, this structural assignment has remained controversial, as such a short distance could not readily be reproduced in either computational models or small molecule mimics,[55−58] and other studies suggested that an "open core" might, in fact, be significantly more reactive for the H·-abstraction step needed to initiate methane hydroxylation.[55] More recent continuous-flow resonance Raman experiments were interpreted in favor of the originally proposed diamond-core geometry,[11] but it remains unclear whether a structure with a 2.46 Å Fe−Fe separation is possible. Similar controversy has surrounded the structure of X. An early EXAFS study concluded that it also has an unusually short Fe−Fe distance of only 2.5 Å,[59] but a more recent study on more concentrated samples gave an Fe−Fe distance of 2.8 Å,[60] compatible with the distance expected of a di-μ-oxo core. Potentially at odds with the conclusions of the second EXAFS study, magnetic circular dichroism (MCD) experiments were interpreted as necessitating that one of the two single-atom (presumably oxygen) bridges, required to give the short Fe−Fe distance determined by EXAFS, be protonated (i.e., a μ-oxo/μ-hydroxo core).[61,62] However, distances longer than the measured 2.8 Å are predicted for such a core,[60] and electron nuclear double resonance (ENDOR) experiments on X carried out over 20 years have consistently shown no evidence for the required proton of a hydroxo bridge.[37,63−65] Compounding the uncertainty, the most recent ENDOR work suggested that it might have only a single nonprotein oxygen bridge, a conclusion that is potentially incompatible with the short Fe−Fe distance.[66] Clearly, whereas the structures of these intermediates are of significant interest, the history of attempts to define them has been rife with controversy.

The Mn(IV)/Fe(IV) activation intermediate in the class I-c RNR β subunit (**4**/**4**) is directly analogous to sMMOH Q_t in that both metals have a formally +IV oxidation state following direct reaction of the dimetal(II/II) cluster with dioxygen. On this basis, it was suggested that **4**/**4** might also have a di-μ-oxo diamond core geometry,[52] although no dispositive evidence for or against this hypothesis has been reported. Investigation of the structure of **4**/**4** has the potential to illuminate mechanisms of oxygen activation at heterodinuclear Mn/Fe sites, for which the range of chemical capabilities remains underexplored relative to that of their diiron counterparts. The potential of this manifold for difficult oxidation outcomes has been underscored recently by the discovery of the "R2lox" family of proteins, in which a heterodinuclear Mn/Fe site has been shown to activate an aliphatic C−H bond and an aryl O−H bond in formation of an intraprotein Val-Tyr cross-link.[67,68] This reactivity contrasts with the one-electron chemistry performed by **4**/**4**, reminiscent of the divergent functions of the diiron complexes, Q and X. Moreover, **4**/**4** remains, to our knowledge, the only known example of a Mn(IV)/Fe(IV) complex, and its structure is therefore of fundamental interest in inorganic chemistry.

The heterodinuclear nature of **4**/**4** confers a number of distinct advantages in investigating its structure. First, it leads to a ground state with total electron spin, S_{tot}, of 1/2 (by contrast to the integer-spin ground state of Q), enabling application of electron paramagnetic resonance (EPR) methods.[52] Second, it allows the structure of the cofactor to be probed in site-selective fashion by X-ray absorption spectroscopy (XAS), as was previously done for the active Mn(IV)/Fe(III) state.[54] A third advantage, conferred by the size and solubility of the *Ct*

DOI: 10.1021/jacs.6b11563
J. Am. Chem. Soc. 2017, 139, 1950−1957

RNR β subunit and the favorable formation and decay kinetics of the intermediate, is that **4**/**4** can be prepared in relatively high concentration and purity,[52] a factor that has proven relevant in the structural investigation of X.[60] Capitalizing on these advantages, we interrogated **4**/**4** by a combination of XAS and EPR spectroscopy to deduce the structure of its inorganic core.

RESULTS AND DISCUSSION

Samples containing high concentrations of **4**/**4** were prepared by using the previously reported method of *in situ* generation of oxygen from chlorite with the enzyme chlorite dismutase (for details, see the Supporting Information).[69] Because EXAFS probes all absorbers in a sample, knowledge of the sample composition was critical for proper data analysis; detailed speciation information was obtained by analysis of the Mössbauer spectra of the samples ([Fe] = 2.6 mM; [Mn] = 2.6 mM; 65% **4**/**4**; for details, see the Supporting Information).[52,69]

The Fe *K*-edge EXAFS data and fits (Figure 1 top and Table 1) reveal a first coordination sphere composed of a shell of

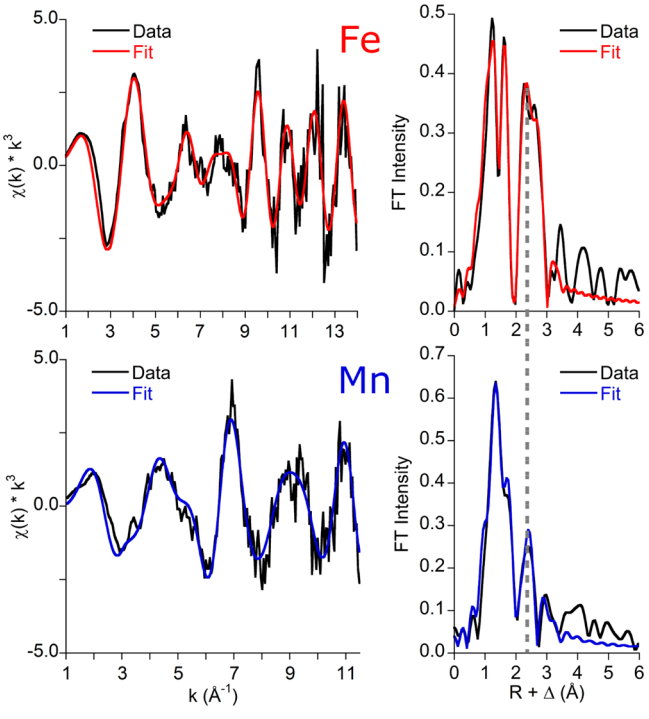

Figure 1. EXAFS traces (left) and corresponding Fourier transformed data (right) of **4**/**4**-containing samples at the iron (top) and manganese (bottom) edges. Experimental traces are black, and fits using parameters presented in Table 1 are red (Fe) and blue (Mn). A putative metal−metal interaction (dashed line) is observed in both Fourier transforms at ∼2.75 Å. Experimental data were acquired and fit for k = 1−14 Å^{-1} for Fe and 1−11.5 Å^{-1} for Mn.

light-atom scatterers at an average distance of 1.81 Å and another shell at an average of 2.01 Å. Both fit best with a coordination number of two. At longer distances, an Fe−Mn interaction is seen at 2.74 Å, and light-atom scatterers are observed at 2.97 and 3.33 Å. A contribution at 2.5 Å is also present, reminiscent of the early EXAFS data on Q and X, but this intensity could not be acceptably fit with a metal scatterer (see tables in the Supporting Information).

The Mn *K*-edge EXAFS data and fits (Figure 1 bottom and Table 1) provide a picture that is complementary to that afforded by the Fe data. A first shell of scatterers can be fit at a distance of 1.86 Å. This distance, significantly less than the ∼2.0 Å expected for protein-derived ligands to Mn(IV), suggests that the first shell is made up of both protein ligands and nonprotein oxygen (e.g., oxo or hydroxo) ligands at an *average* distance of 1.86 Å from the Mn(IV). The lack of resolution of protein and nonprotein constituents of this first shell can be rationalized by the lower resolution in the Mn EXAFS data (∼0.15 Å), which results from the limited k-range that can be interrogated before the Fe edge interferes (at k = 12). A smaller contribution at 2.19 Å, likely a result of the ∼30% Mn(II) contaminant in the sample, is also present. As with the fits to the Fe K-edge data, a metal scatterer is observed at 2.75 Å, and metal-light atom interactions are seen at longer distances. These distances are quantitatively consistent with those obtained in a density functional theory (DFT) optimized model for **4**/**4** with a di-μ-oxo core.[58] Importantly, no interaction is observed at 2.5 Å, confirming that the intensity observed at that distance in the Fe data does not arise from a metal scatterer. For both metal edges, the sum of the coordination numbers for the first coordination spheres is less than the expected value of six. We attribute this discrepancy to static disorder within the samples, which coalesces multiple shells of scatterers in a manner that cannot adequately be modeled by the assumption of a Gaussian distribution of distances embodied by the Debye−Waller parameter.[70] Similar observations have been noted in previous studies on high-valent dimetal complexes.[10,71]

These EXAFS data provide structural metrics that drastically limit the range of possible core structures for **4**/**4**. The first coordination sphere of the Fe contains two shells: one at 1.81 Å and the other at 2.01 Å. The latter is consistent with the expected distances between Fe(IV) and protein ligands. The 1.81 Å distance is too short for protein (∼2.0 Å) or hydroxide ligands (1.85−1.95 Å) and too long for a terminal oxo (∼1.65−1.70 Å), but it is entirely consistent the distance expected for a bridging oxo ligand (∼1.80 Å).[55,72,73] Although the observed number of scatterers in the best fit to the data (two) is not a reliable quantitative measure, the intensity of this feature in the FT is notably high, particularly by comparison to those for complexes known to have a single oxo scatterer. Moreover, the intensity of this feature is very similar to that reported for a di-μ-oxo-diiron(IV) diamond core complex; in fact, the entire Fourier transform for the Fe-edge in the data for **4**/**4** is similar to that for the diiron(IV) complex.[55] Because the iron in its binding site should have only two open coordination sites,[74−76] the presence of two oxo scatterers would preclude the presence of a μ-hydroxo ligand; the analysis would therefore suggest that **4**/**4** could have a di-μ-oxo diamond core geometry.

The metal−metal (M-M) scattering interaction at 2.74−2.75 Å, observed in both the Mn and Fe edge data, is markedly short. While no structurally characterized high-valent Mn−Fe model compounds that might serve as direct precedents have been reported, Mn(IV)/Mn(IV),[71,77−79] Fe(IV)/Fe(IV),[55,73] and Fe(IV)/Fe(III)[72,80] models are known. Among those complexes with two oxo bridges, the range of M−M distances is 2.67−2.78 Å. By contrast, the known inorganic complexes with one oxo and one hydroxo bridge have M-M distances in the range of 2.79−2.91 Å, and a di-μ-hydroxo complex has a M−M distance of ∼2.93 Å (Figures S1 and S2). The observed distance of 2.74−2.75 Å for **4**/**4** is thus uniquely consistent with those of the di-μ-oxo-dimetal models. This distance also

DOI: 10.1021/jacs.6b11563
J. Am. Chem. Soc. 2017, 139, 1950−1957

Table 1. Numerical Results from Fits to the Fe and Mn EXAFS[a]

Fe				Mn			
scatterer	N	R (Å)	σ^2 (Å^2)	scatterer	N	R (Å)	σ^2 (Å^2)
Fe−C/N/O	2	1.81	0.00978	Mn−C/N/O	2	1.86	0.00722
Fe−C/N/O	2	2.01	0.00636	Mn−C/N/O	1	2.19	0.00422
Fe−C/N/O	2	2.50	0.00400	Mn−Fe	0.7	2.75	0.00472
Fe−Mn	1	2.74	0.00384	Mn−C/N/O	2	2.99	0.00315
Fe−C/N/O	4	2.97	0.00542	Mn−C/N/O	2	3.28	0.00620
Fe−C/N/O	1	3.33	0.00271				
F		0.467		F		0.401	
E_0		−2.05 eV		E_0		2.77 eV	

[a]Uncertainty in distance determinations are ±0.02 Å.

precludes monobridged, "open-core" structures, which exhibit even longer M-M distances (~3.4 Å).[73] Such structures would also not be expected to yield the unusually intense 1.81-Å interaction observed in the Fe EXAFS (vide supra), because a single μ-oxo would be expected at ~1.8 Å, and an additional terminally coordinated oxo (if present), would be closer to the metal ion (1.65−1.70 Å), likely unresolved, and therefore anticipated to shift the peak arising from the μ-oxo to a value less than 1.8 Å.

Although high-valent heterodinuclear models are unavailable, the Mn(IV)/Fe(III) form of *Ct* RNR β offers a valuable point of comparison. On the basis of EXAFS analysis, this form of the cofactor was assigned as having a μ-oxo/μ-hydroxo diamond core structure;[54] this conclusion was corroborated by results from nuclear resonance vibrational spectroscopy (NRVS) and MCD spectroscopy.[81] The EXAFS investigation indicated a Mn−Fe distance of 2.92 Å, ~0.17 Å longer than the distance observed for **4**/**4** (vide supra). This elongation would be expected to occur following one-electron reduction of the iron site and protonation of one of the oxo bridges.[71]

The conclusion that the two presumptive bridging oxygen ligands are unprotonated emerges only indirectly from the EXAFS data, on the basis of comparisons of measured distances to those found in a limited set of well-characterized homodinuclear model complexes. Moreover, the data provide no information concerning the protonation state of the expected terminal oxygen ligand to the Mn(IV) site (Scheme 1), due in part to the low resolution of the Mn EXAFS data. In order to address these questions, we examined **4**/**4** by multifrequency pulse EPR techniques. In **4**/**4**, the Mn(IV) has an electron-spin quantum number, S, of 3/2 and couples antiferromagnetically to the Fe(IV) ion (S = 2), resulting in an overall S_{tot} = 1/2 ground state, which makes the complex amenable to EPR characterization.[52] The continuous-wave (CW) X-band spectrum of **4**/**4** reflects strong hyperfine (HF) coupling of the unpaired electron with the ^{55}Mn nucleus (with nuclear-spin quantum number, I, of 5/2), which splits the resonance into six discrete packets (Figure 2A). Using simultaneous, multifrequency simulation, both X- and Q-band spectra can be simulated with parameters g = [2.028, 2.021, 2.013] ± 0.001 and A_{Mn} = [221, 243, 246] ± 5 MHz, in reasonable agreement with previously published parameters (Figure S3).[52] EPR can afford useful structural information by revealing HF couplings to nearby magnetic nuclei, including hydrons that are invisible to EXAFS analysis. In particular, observation of HF couplings to exchangeable hydrons might reveal the ligand protonation states and provide a more direct assessment of the nature of the bridging and terminal nonprotein oxygen ligands. To probe exchangeable hydrons,

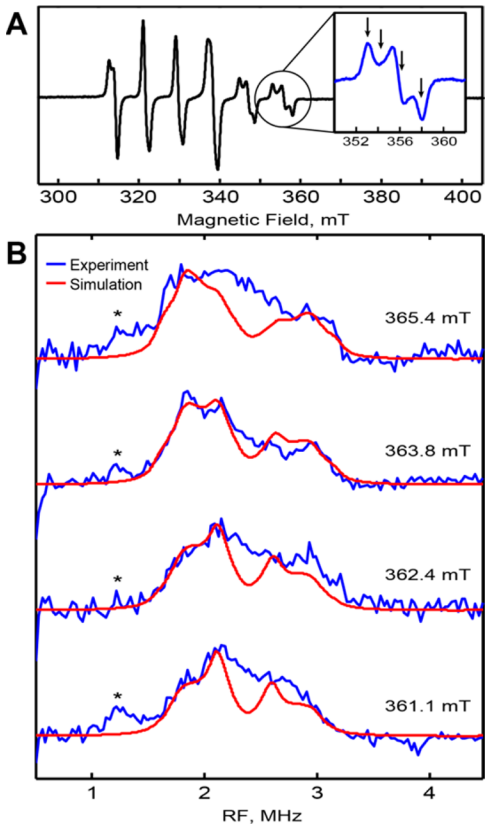

Figure 2. Interrogation of **4**/**4** by electron paramagnetic resonance methods. (A) Continuous-wave, X-band spectrum with expanded view of the packet at the highest magnetic field (inset). (B) X-band, field-dependent, ^{2}H-ENDOR spectra (blue) and simulations (red) of **4**/**4** prepared in D_2O. The field positions for the ENDOR spectra are indicated by the arrows in the inset of panel (A) . The peaks marked with an asterisk are artifacts due to experimental setup. The deviations between the experimental and simulated spectra near the Larmor frequency (ν_L = 2.36, 2.37, 2.38, and 2.39 MHz at 361.1, 362.4, 363.8, and 365.4 mT, respectively) are attributable to matrix deuterons. All measurements were performed at 15 K. CW and ENDOR measurements were performed with microwave frequencies of 9.628 and 9.702 GHz, respectively.

field-dependent deuterium electron−nuclear double resonance (^{2}H-ENDOR) spectra were recorded at X-band on a sample of **4**/**4** prepared in ^2H_2O (D_2O) buffer (Figure 2B). Comparison to spectra recorded under identical conditions on a sample prepared in H_2O buffer indicates that the observed signals are attributable to deuterium and that there is no observable interference from other nuclei (e.g., ^{14}N) in this frequency

DOI: 10.1021/jacs.6b11563
J. Am. Chem. Soc. 2017, 139, 1950−1957

regime (Figure S4). The ^{2}H-ENDOR spectra can be simulated with a single predominantly anisotropic hyperfine coupling (Figure 2B) A_{2H} = [-0.90, −0.43, 1.41] ± 0.1 MHz with Euler angles [0, 25, 0] ± 15° (see the Supporting Information for additional details). The deuterium nuclear quadrupole interaction was simulated with the tensor [-0.07, −0.07, 0.14] ± 0.03 MHz and Euler angles [0, 110, 0] ± 20°.

To verify the absence of stronger couplings (which might, in theory, be obscured by the periodic blindspots inherent in the Mims ENDOR pulse sequence utilized above), we performed additional X- and Q-band ENDOR measurements of the ^{1}H region (Figure S5). The overall breadth of the field-dependent ^{1}H-ENDOR spectra are compatible with the ^{2}H hyperfine coupling detailed above; no stronger couplings were observed.

The magnitude of the observed anisotropic HF coupling (|T| = 0.7 MHz) and the rhombicity parameter (ε = 0.3), extracted from the observed ^{2}H HF coupling, can be related to geometric information via a model that accounts for dipolar coupling of the deuterium nucleus to the S = 3/2 Mn(IV) center and the S = 2 Fe(IV) center, weighted according to their spin-projection factors (Figure S6; for details, see Supporting Information). HF parameters calculated according to this model for ^{2}H nuclei located at different positions relative to the Mn(IV)/Fe(IV) cluster were compared to the measured values. The resulting compatible positions are shaded black in Figure 3, with lighter shading indicating less good agreement; the shaded region constitutes a "geometric confidence interval."

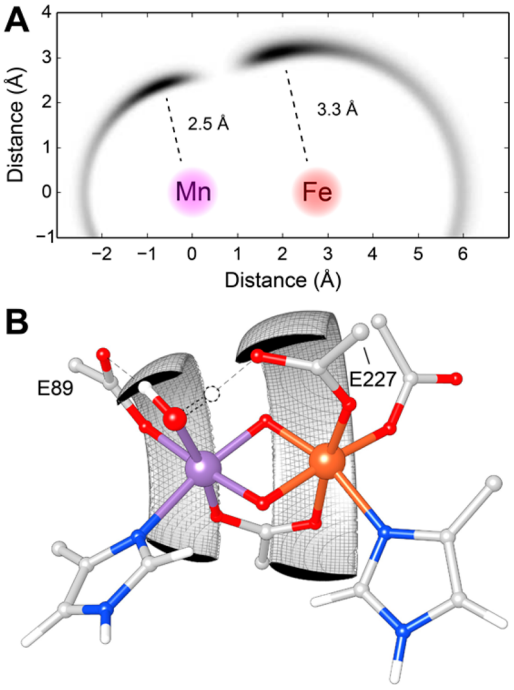

Figure 3. Assessment of the geometric disposition of the detected exchangeable deuterium in **4**/**4** with respect to the Mn(IV)/Fe(IV) cluster. (A) Positions compatible with the observed ^{2}H-hyperfine coupling (black shading), relative to the Mn−Fe. The plane of the paper represents an arbitrary plane containing Fe, Mn, and the deuteron of interest. (B) Compatible positions (isosurface at 50% of the maximum according to eq S4) represented in three dimensions, superimposed on a three-dimensional model of **4**/**4**, based on data from Noodleman and co-workers.[58] Atoms are color-coded as follows: manganese (magenta), iron (rust), carbon (gray), nitrogen (blue), oxygen (red), and hydrogen (white).

The resulting metal-^{2}H distances are most compatible with a terminal hydroxide/water ligand to the Mn(IV). The analysis gives two mathematically compatible regions: one ∼2.45 Å from Mn and the other ∼3.25 Å from Fe (Figure 3A). In both cases, the observed coupling is too strong to be compatible with exchangeable hydrons on first- and second-sphere residues (e.g., coordinating histidines), as the closest exchangeable hydrons are expected to be >5.0 Å from both the Mn site and the Fe site, giving rise to couplings with magnitude less than or equal to 0.1 MHz.[58,74−76] Furthermore, the observed coupling is both too weak and insufficiently rhombic to be assigned to the ^{2}H nucleus of a bridging hydroxide (|T| ∼ 1.7−2.3 MHz, ε ∼ 0.8−1.0).[65,68,82−84] The ∼2.45 Å possibility is compatible with a hydroxide/water ligand to Mn(IV), on the basis of typical bond lengths/angles (2.4 ± 0.1 Å).[54,58,78,79] In contrast, the ∼3.25-Å possibility does not correspond to any ^{2}H that could be bonded to one of the known heteroatoms in a chemically reasonable geometry, being too far away for a hydroxide/water ligand to Fe(IV).

The structural assignment of a terminally coordinated hydroxide/water ligand to Mn(IV) can be further refined by consideration of the coordination sphere and the local hydrogen bonding network (Figure 3B). The open coordination site for Mn(IV) is approximately perpendicular to the Mn−Fe vector. Moreover, the Fe−Mn−O-H dihedral angle is, theoretically and in the absence of restrictive hydrogen-bonding interaction, subject to change by free rotation about the Mn−O bond. However, the many available structures of RNR β subunits suggest that hydrogen bonding interactions to either Glu 89 or Glu 227 (or both) could very well restrict this rotation and bias or fix the dihedral angle. Thus, there are two likely positions for the exchangeable hydron, one in which the O−H bond is oriented generally toward the Fe ion, allowing the hydroxo ligand to donate an H-bond to Glu 227, and another oriented away from the Fe, allowing H-bond donation to Glu 89 (Figure 3B). Intriguingly, a deuteron oriented toward Glu 227 is expected to exhibit a coupling that is significantly more rhombic (ε = 0.8−1.0) and somewhat larger (|T| ∼ 0.8) than the observed coupling (hydrogen with dashed outline in Figure 3B). In contrast, the position oriented away from the iron is completely compatible with the observed hyperfine coupling, as the expected position (Figure 3B) shows significant overlap with the region indicated by the EPR data (black shading/isosurface). These data cannot definitively assign the observed signals as arising from a single deuteron (i.e., on a hydroxide ligand), rather than two (i.e., on a water ligand); it is possible that the observed signal arises from the superposition of two nonidentical HF couplings or from two indistinguishable HF couplings. However, we favor the hydroxide possibility because (i) a single HF coupling is sufficient to simulate the data, and (ii) a second ^{2}H nucleus would likely lie in the position hydrogen bonded to Glu 227, which would, due to the greater rhombicity predicted by the model, exhibit a significantly larger coupling in one orientation than that observed (rather than being indistinguishable).

The EXAFS and ENDOR data represent orthogonal probes of the structure of **4**/**4** and together suggest a di-μ-oxo diamond core structure with a terminally coordinated hydroxide ligand to Mn(IV) (Figure 3B). The short Mn−Fe distance (2.74−2.75 Å) observed in both Mn- and Fe-edge EXAFS data requires at least two bridging atoms and precludes monobridged or "open-core" structures. Among di-μ-(hydr)oxo diamond core structures, a di-μ-oxo is most compatible with

DOI: 10.1021/jacs.6b11563
J. Am. Chem. Soc. 2017, 139, 1950−1957

both the M−M distance (by comparison to well-characterized models) and the intense 1.81 Å first shell of scatterers around Fe. Moreover, the presence of a μ-hydroxo ligand would give rise to a large, rhombic HF coupling from an exchangable hydron, which is not present. An exchangeable hydron is observed by ^{2}H-ENDOR, with parameters consistent with a terminal hydroxide/water ligand to Mn(IV). This signal is most compatible with a terminally coordinated hydroxide ligand to Mn(IV), hydrogen bonded to Glu 89, though water cannot be explicitly ruled out on the basis of the available data. This comprehensive assignment represents the first structural characterization of any Mn(IV)/Fe(IV) complex and adds to the very few reported for other types of biological high-valent transition metal complexes.

MATERIALS AND METHODS

Preparation of 4/4 Samples for XAS and EPR Analysis. The β subunit of *Chlamydia trachomatis* (*Ct*) ribonucleotide reductase was overexpressed and purified to homogeneity as previously described.[14] Following removal of oxygen,[2] *Ct* β_2, Mn(II), Fe(II), and chlorite dismutase were mixed to final concentrations of 2.2 mM, 3.3 mM, 3.3 mM, and 25 μM, respectively.[69] This mixture was rapidly mixed in a 4:1 volume ratio with a 50 mM solution of sodium chlorite, and the reaction solution was rapidly frozen after 0.23 s in liquid ethane (XAS) or isopentane (EPR).

XAS Data Collection and Processing. X-ray absorption spectra were collected on beamline 7-3 at the Stanford Synchrotron Radiation Lightsource under ring conditions of 3 GeV and 500 mA. A Si(220) monochromator (φ = 90°) was used for energy selection of the incident beam; harmonic rejection was achieved using a Rh-coated mirror (9 keV) and by detuning the monochromator by 25%. The energy of the incident beam was calibrated using metal foils upstream of the sample (7111.3 eV for Fe, 6539.0 eV for Mn). Scans were carried out over the energy ranges of 6880−7930 eV (Fe) and 6310−7110 eV (Mn) for 685 and 800 s durations, respectively. Sample temperature was maintained at 10 K in an Oxford liquid helium cryostat.

Data processing was performed using the EXAFSPAK software package.[85] Three-segment splines (of orders 2, 3, and 3) were removed from the EXAFS using PySpline[86] and the EXAFS data were then fit using OPT. Scattering paths for EXAFS fits were generated from appropriate structural models using FEFF 9.0 (additional details can be found in the Supporting Information).[87]

XAS Damage Assessment. Due to the presence of two different high-valent metal ions in **4**/**4**, care was required to ensure that both metals remained stable during both Fe and Mn scans. Initially, fresh sample spots and highly attenuated beam were used to collect rapid edge scans (60−100 s exposure) for both Fe and Mn; given the short exposure time and low incident intensity, these spectra were taken to be undamaged. Then, to assess the stability of a metal during its own scan (e.g., Fe), a new spot was used to collect a full EXAFS scan at the Fe edge, followed on the same spot by a rapid Fe edge scan; only when the rapid edge scan overlaid with the initial, undamaged edge spectrum was the EXAFS scan deemed to have a safe level of exposure. This process was then repeated on a new sample spot, except that, instead of rescanning the Fe edge afterward, a rapid Mn edge scan was collected and compared to the undamaged Mn edge spectrum to ensure that the Mn was also stable during the Fe scan. When the Fe scan was established, this entire process was repeated for Mn. The process of performing a full EXAFS scan in order to assess damage was found to be critically important due to the energy dependence of the X-ray flux; simply performing repeated rapid edge scans until damage became apparent was found to overestimate safe exposure times by a significant margin (~10%). Edge overlays and additional details can be found in Figures S7 and S8.

EPR Measurements. X-band CW measurements were performed on a Bruker ESP 300 spectrometer with an ER 041 MR microwave bridge and an ER 4116DM resonator. All other EPR measurements were performed on a Bruker Elexsys E580 X-band spectrometer equipped with a SuperX-FT microwave bridge. For pulse EPR measurements at X-band, a Bruker EN 4118X-MD4 dielectric ENDOR resonator was used in concert with an Oxford CF935 helium flow cryostat. Pulse EPR spectra at Q-band frequencies were acquired using a home-built intermediate-frequency extension of the SuperX-FT X-band bridge equipped with a Millitech 5W pulse power amplifier.

EPR Analysis. Data processing and spectral simulations were performed using Kazan viewer, a home-written suite of utilities in MATLAB.[88] One-dimensional EPR simulations were performed using the "pepper" utility from the EasySpin software package.[89] ENDOR data were analyzed by simultaneous frequency domain simulation of all field-dependent spectra until a satisfactory solution was achieved. Euler angles are reported with respect to the ^{55}Mn hyperfine coupling tensor, which is colinear with the *g* matrix in our simulations.

ASSOCIATED CONTENT

Supporting Information

The Supporting Information is available free of charge on the ACS Publications website at DOI: 10.1021/jacs.6b11563.

Additional details concerning sample preparation, data collection, and analysis; additional EPR spectra; Mössbauer analysis of sample composition; X-ray damage assessment; X-ray analysis of Fe-only and Mn-only control samples; tables of EXAFS fits (PDF)

AUTHOR INFORMATION

Corresponding Authors

*aus40@psu.edu
*cjp27@psu.edu

ORCID

Carsten Krebs: 0000-0002-3302-7053
Christopher J. Pollock: 0000-0001-5736-513X

Notes

The authors declare no competing financial interest.

ACKNOWLEDGMENTS

This material is based upon work supported by the National Science Foundation Graduate Research Fellowship Program under Grant No. DGE1255832. C.J.P. and E.J.B. thank the NIH for National Research Service Awards (GM113389-01 and GM116353-01). This work was supported by the National Institutes of Health (GM55365 to J.M.B. and C.K.). Portions of this work were conducted at the Stanford Synchrotron Radiation Lightsource, SLAC National Accelerator Laboratory, which is supported by the U.S. Department of Energy, Office of Science, Office of Basic Energy Sciences under Contract No. DE-AC02-76SF00515. The SSRL Structural Molecular Biology Program is supported by the DOE Office of Biological and Environmental Research, and by the National Institutes of Health, National Institute of General Medical Sciences (including P41GM103393).

REFERENCES

(1) Krebs, C.; Galonić Fujimori, D.; Walsh, C. T.; Bollinger, J. M., Jr. *Acc. Chem. Res.* **2007**, *40*, 484−492.
(2) Price, J. C.; Barr, E. W.; Tirupati, B.; Bollinger, J. M., Jr.; Krebs, C. *Biochemistry* **2003**, *42*, 7497−7508.
(3) Hoffart, L. M.; Barr, E. W.; Guyer, R. B.; Bollinger, J. M., Jr.; Krebs, C. *Proc. Natl. Acad. Sci. U. S. A.* **2006**, *103*, 14738−14743.
(4) Galonić, D. P.; Barr, E. W.; Walsh, C. T.; Bollinger, J. M., Jr.; Krebs, C. *Nat. Chem. Biol.* **2007**, *3*, 113−116.

DOI: 10.1021/jacs.6b11563
J. Am. Chem. Soc. 2017, 139, 1950−1957

(5) Wang, C.; Chang, W.-c.; Guo, Y.; Huang, H.; Peck, S. C.; Pandelia, M.-E.; Lin, G.; Liu, H.; Krebs, C.; Bollinger, J. M., Jr. *Science* **2013**, *342*, 991−995.
(6) Chang, W.-c.; Guo, Y.; Wang, C.; Butch, S. E.; Rosenzweig, A. C.; Boal, A. K.; Krebs, C.; Bollinger, J. M., Jr. *Science* **2014**, *343*, 1140−1144.
(7) Bollinger, J. M., Jr.; Chang, W.-c.; Matthews, M. L.; Martinie, R. J.; Boal, A. K.; Krebs, C. In *2-Oxoglutarate-Dependent Oxygenases*; Hausinger, R. P., Schofield, C. J., Eds.; Royal Society of Chemistry: London, 2015.
(8) Kovaleva, E. G.; Neibergall, M. B.; Chakrabarty, S.; Lipscomb, J. D. *Acc. Chem. Res.* **2007**, *40*, 475−483.
(9) Lee, S. K.; Fox, B. G.; Froland, W. A.; Lipscomb, J. D.; Münck, E. *J. Am. Chem. Soc.* **1993**, *115*, 6450−6451.
(10) Shu, L.; Nesheim, J. C.; Kauffmann, K.; Münck, E.; Lipscomb, J. D.; Que, L., Jr. *Science* **1997**, *275*, 515−518.
(11) Banerjee, R.; Proshlyakov, Y.; Lipscomb, J. D.; Proshlyakov, D. A. *Nature* **2015**, *518*, 431−434.
(12) Sturgeon, B. E.; Burdi, D.; Chen, S.; Huynh, B. H.; Edmondson, D. E.; Stubbe, J.; Hoffman, B. M. *J. Am. Chem. Soc.* **1996**, *118*, 7551−7557.
(13) Stubbe, J.; van der Donk, W. A. *Chem. Rev.* **1998**, *98*, 705−762.
(14) Jiang, W.; Yun, D.; Saleh, L.; Barr, E. W.; Xing, G.; Hoffart, L. M.; Maslak, M.-A.; Krebs, C.; Bollinger, J. M., Jr. *Science* **2007**, *316*, 1188−1191.
(15) Cotruvo, J. A., Jr.; Stich, T. A.; Britt, R. D.; Stubbe, J. *J. Am. Chem. Soc.* **2013**, *135*, 4027−4039.
(16) Umena, Y.; Kawakami, K.; Shen, J.-R.; Kamiya, N. *Nature* **2011**, *473*, 55−60.
(17) Cox, N.; Pantazis, D. A.; Neese, F.; Lubitz, W. *Acc. Chem. Res.* **2013**, *46*, 1588−1596.
(18) Cox, N.; Retegan, M.; Neese, F.; Pantazis, D. A.; Boussac, A.; Lubitz, W. *Science* **2014**, *345*, 804−808.
(19) Rittle, J.; Green, M. T. *Science* **2010**, *330*, 933−937.
(20) Yosca, T. H.; Rittle, J.; Krest, C. M.; Onderko, E. L.; Silakov, A.; Calixto, J. C.; Behan, R. K.; Green, M. T. *Science* **2013**, *342*, 825−829.
(21) Bollinger, J. M., Jr.; Broderick, J. B. *Curr. Opin. Chem. Biol.* **2009**, *13*, 51−57.
(22) Krebs, C.; Bollinger, J. M., Jr.; Booker, S. J. *Curr. Opin. Chem. Biol.* **2011**, *15*, 291−303.
(23) Lee, S. K.; Nesheim, J. C.; Lipscomb, J. D. *J. Biol. Chem.* **1993**, *268*, 21569−21577.
(24) Fox, B. G.; Lyle, K. S.; Rogge, C. E. *Acc. Chem. Res.* **2004**, *37*, 421−429.
(25) Warui, D. M.; Li, N.; Nørgaard, H.; Krebs, C.; Bollinger, J. M., Jr.; Booker, S. J. *J. Am. Chem. Soc.* **2011**, *133*, 3316−3319.
(26) Li, N.; Nørgaard, H.; Warui, D. M.; Booker, S. J.; Krebs, C.; Bollinger, J. M., Jr. *J. Am. Chem. Soc.* **2011**, *133*, 6158−6161.
(27) Li, N.; Chang, W.-c.; Warui, D. M.; Booker, S. J.; Krebs, C.; Bollinger, J. M., Jr. *Biochemistry* **2012**, *51*, 7908−7916.
(28) Pandelia, M.-E.; Li, N.; Nørgaard, H.; Warui, D. M.; Rajakovich, L. J.; Chang, W.-c.; Booker, S. J.; Krebs, C.; Bollinger, J. M., Jr. *J. Am. Chem. Soc.* **2013**, *135*, 15801−15812.
(29) Rajakovich, L. J.; Nørgaard, H.; Warui, D. M.; Chang, W.-c.; Li, N.; Booker, S. J.; Krebs, C.; Bollinger, J. M., Jr.; Pandelia, M.-E. *J. Am. Chem. Soc.* **2015**, *137*, 11695−11709.
(30) Nordlund, P.; Reichard, P. *Annu. Rev. Biochem.* **2006**, *75*, 681−706.
(31) Stubbe, J.; Nocera, D. G.; Yee, C. S.; Chang, M. C. Y. *Chem. Rev.* **2003**, *103*, 2167−2202.
(32) Licht, S.; Gerfen, G. J.; Stubbe, J. *Science* **1996**, *271*, 477−481.
(33) Tomter, A. B.; Zoppellaro, G.; Andersen, N. H.; Hersleth, H.-P.; Hammerstad, M.; Røhr, Å. K.; Sandvik, G. K.; Strand, K. R.; Nilsson, G. E.; Bell, C. B., III; Barra, A.-L.; Blasco, E.; Le Pape, L.; Solomon, E. I.; Andersson, K. K. *Coord. Chem. Rev.* **2013**, *257*, 3−26.
(34) Bollinger, J. M., Jr.; Krebs, C.; Vicol, A.; Chen, S.; Ley, B. A.; Edmondson, D. E.; Huynh, B. H. *J. Am. Chem. Soc.* **1998**, *120*, 1094−1095.
(35) Moënne-Loccoz, P.; Baldwin, J.; Ley, B. A.; Loehr, T. M.; Bollinger, J. M., Jr. *Biochemistry* **1998**, *37*, 14659−14663.
(36) Skulan, A. J.; Brunold, T. C.; Baldwin, J.; Saleh, L.; Bollinger, J. M., Jr.; Solomon, E. I. *J. Am. Chem. Soc.* **2004**, *126*, 8842−8855.
(37) Burdi, D.; Sturgeon, B. E.; Tong, W. H.; Stubbe, J.; Hoffman, B. M. *J. Am. Chem. Soc.* **1996**, *118*, 281−282.
(38) Ehrenberg, A.; Reichard, P. *J. Biol. Chem.* **1972**, *247*, 3485−3488.
(39) Atkin, C. L.; Thelander, L.; Reichard, P.; Lang, G. *J. Biol. Chem.* **1973**, *248*, 7464−7472.
(40) Sjöberg, B.-M.; Reichard, P. *J. Biol. Chem.* **1977**, *252*, 536−541.
(41) Sjöberg, B.-M.; Reichard, P.; Gräslund, A.; Ehrenberg, A. *J. Biol. Chem.* **1978**, *253*, 6863−6865.
(42) Larsson, A.; Sjöberg, B.-M. *EMBO J.* **1986**, *5*, 2037−2040.
(43) Cotruvo, J. A., Jr.; Stubbe, J. *Biochemistry* **2010**, *49*, 1297−1309.
(44) Cox, N.; Ogata, H.; Stolle, P.; Reijerse, E.; Auling, G.; Lubitz, W. *J. Am. Chem. Soc.* **2010**, *132*, 11197−11213.
(45) Cotruvo, J. A., Jr.; Stubbe, J. *Biochemistry* **2011**, *50*, 1672−1681.
(46) Boal, A. K.; Cotruvo, J. A., Jr.; Stubbe, J.; Rosenzweig, A. C. *Science* **2010**, *329*, 1526−1530.
(47) Högbom, M.; Stenmark, P.; Voevodskaya, N.; McClarty, G.; Gräslund, A.; Nordlund, P. *Science* **2004**, *305*, 245−248.
(48) Jiang, W.; Bollinger, J. M., Jr.; Krebs, C. *J. Am. Chem. Soc.* **2007**, *129*, 7504−7505.
(49) Voevodskaya, N.; Lendzian, F.; Ehrenberg, A.; Gräslund, A. *FEBS Lett.* **2007**, *581*, 3351−3355.
(50) Bollinger, J. M., Jr.; Jiang, W.; Green, M. T.; Krebs, C. *Curr. Opin. Struct. Biol.* **2008**, *18*, 650−657.
(51) Jiang, W.; Yun, D.; Saleh, L.; Bollinger, J. M., Jr.; Krebs, C. *Biochemistry* **2008**, *47*, 13736−13744.
(52) Jiang, W.; Hoffart, L. M.; Krebs, C.; Bollinger, J. M., Jr. *Biochemistry* **2007**, *46*, 8709−8716.
(53) Jiang, W.; Saleh, L.; Barr, E. W.; Xie, J.; Gardner, M. M.; Krebs, C.; Bollinger, J. M., Jr. *Biochemistry* **2008**, *47*, 8477−8484.
(54) Younker, J. M.; Krest, C. M.; Jiang, W.; Krebs, C.; Bollinger, J. M., Jr.; Green, M. T. *J. Am. Chem. Soc.* **2008**, *130*, 15022−15027.
(55) Xue, G.; Wang, D.; De Hont, R.; Fiedler, A. T.; Shan, X.; Münck, E.; Que, L., Jr. *Proc. Natl. Acad. Sci. U. S. A.* **2007**, *104*, 20713−20718.
(56) Rinaldo, D.; Philipp, D. M.; Lippard, S. J.; Friesner, R. A. *J. Am. Chem. Soc.* **2007**, *129*, 3135−3147.
(57) Han, W.-G.; Noodleman, L. *Inorg. Chim. Acta* **2008**, *361*, 973−986.
(58) Han, W.-G.; Giammona, D. A.; Bashford, D.; Noodleman, L. *Inorg. Chem.* **2010**, *49*, 7266−7281.
(59) Riggs-Gelasco, P. J.; Shu, L.; Chen, S.; Burdi, D.; Huynh, B. H.; Que, L., Jr.; Stubbe, J. *J. Am. Chem. Soc.* **1998**, *120*, 849−860.
(60) Dassama, L. M. K.; Silakov, A.; Krest, C. M.; Calixto, J. C.; Krebs, C.; Bollinger, J. M., Jr.; Green, M. T. *J. Am. Chem. Soc.* **2013**, *135*, 16758−16761.
(61) Mitić, N.; Saleh, L.; Schenk, G.; Bollinger, J. M., Jr.; Solomon, E. I. *J. Am. Chem. Soc.* **2003**, *125*, 11200−11201.
(62) Mitić, N.; Clay, M. D.; Saleh, L.; Bollinger, J. M., Jr.; Solomon, E. I. *J. Am. Chem. Soc.* **2007**, *129*, 9049−9065.
(63) Willems, J.-P.; Lee, H.-I.; Burdi, D.; Doan, P. E.; Stubbe, J.; Hoffman, B. M. *J. Am. Chem. Soc.* **1997**, *119*, 9816−9824.
(64) Burdi, D.; Willems, J.-P.; Riggs-Gelasco, P. J.; Antholine, W. E.; Stubbe, J.; Hoffman, B. M. *J. Am. Chem. Soc.* **1998**, *120*, 12910−12919.
(65) Shanmugam, M.; Doan, P. E.; Lees, N. S.; Stubbe, J.; Hoffman, B. M. *J. Am. Chem. Soc.* **2009**, *131*, 3370−3376.
(66) Doan, P. E.; Shanmugam, M.; Stubbe, J.; Hoffman, B. M. *J. Am. Chem. Soc.* **2015**, *137*, 15558−15566.
(67) Andersson, C. S.; Högbom, M. *Proc. Natl. Acad. Sci. U. S. A.* **2009**, *106*, 5633−5638.
(68) Shafaat, H. S.; Griese, J. J.; Pantazis, D. A.; Roos, K.; Andersson, C. S.; Popović-Bijelić, A.; Gräslund, A.; Siegbahn, P. E. M.; Neese, F.; Lubitz, W.; Högbom, M.; Cox, N. *J. Am. Chem. Soc.* **2014**, *136*, 13399−13409.

DOI: 10.1021/jacs.6b11563
J. Am. Chem. Soc. 2017, 139, 1950−1957

(69) Dassama, L. M. K.; Yosca, T. H.; Conner, D. A.; Lee, M. H.; Blanc, B.; Streit, B. R.; Green, M. T.; DuBois, J. L.; Krebs, C.; Bollinger, J. M., Jr. *Biochemistry* **2012**, *51*, 1607−1616.
(70) Beckwith, M. A.; Ames, W.; Vila, F. D.; Krewald, V.; Pantazis, D. A.; Mantel, C.; Pécaut, J.; Gennari, M.; Duboc, C.; Collomb, M.-N.; Yano, J.; Rehr, J. J.; Neese, F.; DeBeer, S. *J. Am. Chem. Soc.* **2015**, *137*, 12815−12834.
(71) Baldwin, M. J.; Stemmler, T. L.; Riggs-Gelasco, P. J.; Kirk, M. L.; Penner-Hahn, J. E.; Pecoraro, V. L. *J. Am. Chem. Soc.* **1994**, *116*, 11349−11356.
(72) Hsu, H.-F.; Dong, Y.; Shu, L.; Young, V. G., Jr.; Que, L., Jr. *J. Am. Chem. Soc.* **1999**, *121*, 5230−5237.
(73) Xue, G.; Fiedler, A. T.; Martinho, M.; Münck, E.; Que, L., Jr. *Proc. Natl. Acad. Sci. U. S. A.* **2008**, *105*, 20615−20620.
(74) Andersson, C. S.; Öhrström, M.; Popović-Bijelić, A.; Gräslund, A.; Stenmark, P.; Högbom, M. *J. Am. Chem. Soc.* **2012**, *134*, 123−125.
(75) Dassama, L. M. K.; Boal, A. K.; Krebs, C.; Rosenzweig, A. C.; Bollinger, J. M., Jr. *J. Am. Chem. Soc.* **2012**, *134*, 2520−2523.
(76) Dassama, L. M. K.; Krebs, C.; Bollinger, J. M., Jr.; Rosenzweig, A. C.; Boal, A. K. *Biochemistry* **2013**, *52*, 6424−6436.
(77) Larson, E.; Lah, M. S.; Li, X.; Bonadies, J. A.; Pecoraro, V. L. *Inorg. Chem.* **1992**, *31*, 373−378.
(78) Schäfer, K.-O.; Bittl, R.; Zweygart, W.; Lendzian, F.; Haselhorst, G.; Weyhermüller, T.; Wieghardt, K.; Lubitz, W. *J. Am. Chem. Soc.* **1998**, *120*, 13104−13120.
(79) Jensen, A. F.; Su, Z.; Hansen, N. K.; Larsen, F. K. *Inorg. Chem.* **1995**, *34*, 4244−4252.
(80) Wang, D.; Farquhar, E. R.; Stubna, A.; Münck, E.; Que, L., Jr. *Nat. Chem.* **2009**, *1*, 145−150.
(81) Kwak, Y.; Jiang, W.; Dassama, L. M. K.; Park, K.; Bell, C. B., III.; Liu, L. V.; Wong, S. D.; Saito, M.; Kobayashi, Y.; Kitao, S.; Seto, M.; Yoda, Y.; Alp, E. E.; Zhao, J.; Bollinger, J. M., Jr.; Krebs, C.; Solomon, E. I. *J. Am. Chem. Soc.* **2013**, *135*, 17573−17584.
(82) Thomann, H.; Bernardo, M.; McCormick, J. M.; Pulver, S.; Andersson, K. K.; Lipscomb, J. D.; Solomon, E. I. *J. Am. Chem. Soc.* **1993**, *115*, 8881−8882.
(83) DeRose, V. J.; Liu, K. E.; Lippard, S. J.; Hoffman, B. M. *J. Am. Chem. Soc.* **1996**, *118*, 121−134.
(84) DeRose, V. J.; Liu, K. E.; Kurtz, D. M., Jr.; Hoffman, B. M.; Lippard, S. J. *J. Am. Chem. Soc.* **1993**, *115*, 6440−6441.
(85) George, G. N. *EXAFSPAK*, EXAFSPAK, SSRL, SLAC; Stanford University: Stanford, CA.
(86) Tenderholt, A.; Hedman, B.; Hodgson, K. O. *AIP Conf. Proc.* **2006**, *882*, 105−107.
(87) Rehr, J. J.; Kas, J. J.; Vila, F. D.; Prange, M. P.; Jorissen, K. *Phys. Chem. Chem. Phys.* **2010**, *12*, 5503−5513.
(88) Kazan Viewer - Homepage Alexey Silakov, https://sites.google.com/site/silakovalexey/kazan-viewer (accessed October 14, 2016).
(89) Stoll, S.; Schweiger, A. *J. Magn. Reson.* **2006**, *178*, 42−55.

DOI: 10.1021/jacs.6b11563
J. Am. Chem. Soc. 2017, 139, 1950−1957

Supporting Information for:

Evidence for a Di-μ-oxo "Diamond Core" in the Mn(IV)/Fe(IV) Activation Intermediate of Ribonucleotide Reductase from *Chlamydia trachomatis*

Ryan J. Martinie,[a] Elizabeth J. Blaesi,[a] Carsten Krebs,[a,b] J. Martin Bollinger Jr.,[a,b] Alexey Silakov,[a*] and Christopher J. Pollock[a*]

Departments of [a]Chemistry and of [b]Biochemistry and Molecular Biology, The Pennsylvania State University, University Park, PA 16802, USA.

Materials and Methods

Preparation of Mn(IV)/Fe(IV) Samples for XAS Analysis

The β subunit of *Chlamydia trachomatis* (*Ct*) ribonucleotide reductase was overexpressed and purified to homogeneity as previously described.[1,2] Protein from multiple purifications was combined prior to deoxygenation. The protein was deoxygenated by repeated, brief application of vacuum (150-200 torr), followed by backfilling with argon. This process was repeated eight times, followed by 5 min. under argon; this entire cycle was repeated seven times, and the protein left under argon for 30 min.[3] Following deoxygenation, protein concentration was determined by the absorbance at 280 nm (ε_0 = 57750 $M^{-1}cm^{-1}$ per monomer).[1] Protein was reconstituted in a nitrogen-atmosphere MBraun anaerobic chamber with 1.5 equivalents of Mn(II) and 1.5 equivalents of ^{57}Fe(II) on a per dimer basis. Following addition of the metals, the mixture was allowed to equilibrate anaerobically for at least 30 min. at 4 °C. *Ct* β2, Mn(II), Fe(II), and chlorite dismutase were mixed to final concentrations of 2.2 mM, 3.3 mM, 3.3 mM, and 25 μM, respectively.

The above mixture was rapidly mixed at 5 °C in a 4:1 volumetric ratio with a 50 mM solution of sodium chlorite in 100 mM HEPES pH 7.6 (at 4 °C), 10% (v/v) glycerol (the same buffer used for *Ct* β). The mixing produces a 20% dilution of the protein sample, resulting in a post-mix metal concentration of 2.6 mM = [Fe] = [Mn]. Chlorite dismutase reacts very rapidly with chlorite to produce O_2 in high concentrations.[2] Mixing was performed using an Update Instruments (Madison, WI) rapid-freeze quench apparatus, with a ram velocity of 2.5 cm/s. Following mixing, the sample was cryogenically quenched in liquid ethane after 230 ms. Because the volume of reconstituted protein was too large for a single quench (~4.2 mL), this process was performed in two consecutive runs, each run containing approximately half of the volume of reconstituted protein. Following the quench, sample from both runs was combined prior to packing the EXAFS samples in order to ensure homogeneity between samples. Samples were packed in modified Mössbauer cells, in which the bottom was removed and replaced with a window of 38 μm Kapton tape. All manipulations were performed at 77 K. Following packing, samples were stored in liquid nitrogen.

Preparation of Control Samples for XAS Analysis

All control samples were derived from the same combined batch of purified, deoxygenated protein used for the experimental samples. The manganese control was made by addition of 3 equivalents of Mn(II) on a per dimer basis, transferred to an EXAFS cell, and frozen in liquid nitrogen. The iron control was made by reconstituting with 3 equivalents of ^{57}Fe(II) on a per dimer basis, followed by quenching and packing in an identical manner to that described for the Mn(IV)/Fe(IV) samples.

Mössbauer Characterization of XAS Samples

Mössbauer spectra were recorded using a spectrometer that has been described previously.[3,4] All spectra were recorded with a field of 53 mT applied parallel to the gamma beam. Spectra were recorded for an experimental Mn(IV)/Fe(IV) sample and for an iron-only control. The iron-only spectrum was recorded using a packed XAS sample. However, this method was found to result in a poor signal-to-noise ratio for the Mn(IV)/Fe(IV) sample due to the lower concentration of ^{57}Fe; therefore, a sample was packed with a greater sample volume in a conventional Mössbauer cell, and the measurement performed on this sample.

The spectrum of the Fe-only control is dominated by features attributable to the Fe(III)/Fe(IV) form of the protein, which we refer to as *Ct* X (Figure S9). By subtraction of a reference spectrum for *Ct* X,[4] it is clear that this species constitutes ~75% of Mössbauer intensity and, by extension, the iron in the sample. The difference spectrum resulting from this subtraction can be simulated as a single quadrupole doublet with isomer shift δ = 1.3 mm/s and ΔE_q = 3.1 mm/s, parameters consistent with a N/O coordinated high-spin ferrous species. The Mössbauer spectrum of the Mn(IV)/Fe(IV) sample is dominated by features consistent with **4/4** (Figure S10). In order to estimate the contribution of protein molecules which have bound two iron atoms, rather than one manganese and one iron, the spectrum of the iron-only control can be subtracted from the experimental spectrum. This procedure indicates that ~30% of the iron is in this diiron form. After subtraction of the diiron contaminants, subtraction of a reference spectrum for **4/4** (65% of the iron) leaves very little residual intensity (<10%). This residual intensity can be simulated as a quadrupole doublet with δ = 0.5 mm/s and ΔE_q = 1.5 mm/s; these parameters are consistent with a high-spin ferric site, presumably resulting from **4/4** that has decayed to

Mn(IV)/Fe(III). Overall, the Mössbauer data indicate the following iron-containing species present in the experimental samples: **4/4** (65%), *Ct* X (24%), Fe(II) (6%), Mn(IV)/Fe(III) (5%). Of these species, *Ct* X and Fe(II) are accounted for in the iron-only control samples, and the Mn(IV)/Fe(III) contaminant is present in too small a proportion to make a detectable contribution in EXAFS analysis.

Although Mössbauer can only detect ^{57}Fe-containing species, we can also infer the distribution of manganese species from the Mössbauer data. Because [Fe] = [Mn] and each heterodinuclear species contains an equal number of manganese and iron ions, we can infer that **4/4** contains 65% of the manganese (and, by extension, Mn(IV)/Fe(III) contains ~5%) in the sample. Moreover, because Mn(II) is unreactive towards oxygen, the remaining 30% of the manganese is expected to remain in the Mn(II) form. This unreacted manganese is accounted for in the manganese-only control. Thus, by inference, the Mössbauer data indicate the following distribution of manganese-containing species in the experimental samples: **4/4** (65%), Mn(II) (30%), Mn(IV)/Fe(III) (5%).

XAS Data Collection

X-ray absorption spectra were collected on beamline 7-3 at the Stanford Synchrotron Radiation Lightsource under ring conditions of 3 GeV and 500 mA. A Si(220) monochromator (φ=90°) was used for energy selection of the incident beam; harmonic rejection was achieved using a Rh-coated mirror (9 keV) and by detuning the monochromator by 25%. The energy of the incident beam was calibrated using metal foils upstream of the sample (7111.3 eV for Fe, 6539.0 eV for Mn). Scans were carried out over the energy ranges of 6880 – 7930 eV (Fe) and 6310 – 7110 eV (Mn) and lasted for 685 and 800 seconds, respectively. The beam intensity was measured using N_2-filled ion chambers before the sample and aluminum Reynolds filters were placed in the beam path to attenuate the intensity when necessary. The sample was placed at 45° relative to the incident beam and the Kα fluorescence was monitored using a 30 element germanium detector. Sample temperature was maintained at 10 K in an Oxford liquid helium cryostat.

The edge and pre-edge regions of the XAS spectra for the **4/4**-containing samples and the controls are consistent with the expected oxidation states (Figure S11-S12). The EXAFS traces

and Fourier transformed data for the Fe-only and Mn-only controls are presented in Figure S13; best fit parameters are listed in Table S2.

Data Processing

Data processing was done using the EXAFSPAK software package.[5] The pre-edge background was removed by fitting a Gaussian function to the low energy data and subtracting this function from the entire spectrum. Three-segment splines (of orders 2, 3, and 3) were removed from the EXAFS using PySpline[6] and the EXAFS were then fit using OPT. Scattering paths for EXAFS fitting were generated with FEFF 9.0[7] using a DFT optimized model of the **4/4** intermediate,[8] an optimized model of intermediate X from *E. coli*,[9] and the crystal structure of the Mn(II)/Fe(II) form of the enzyme (PDB code 4D8F, modified by replacing the Fe with a second Mn).[10] During EXAFS fitting, the distances, Debye-Waller factors, and E_0 parameter were all allowed to float while coordination numbers were systematically varied; for all fits the passive electron reduction factor (S_0^2) was fixed at 1. For XANES analysis, the pre-edge region was fit using BlueprintXAS[11] and the edge jump obtained from the fits was normalized to 1; reported areas and intensity-weighted average energies are the average of at least 22 physically reasonable fits.

Preparation of Mn(IV)/Fe(IV) Samples for EPR Analysis

Samples for EPR were prepared in the manner described for the XAS samples, with the following exceptions: 1) natural abundance Fe(II) was used for reconstitution, in order to avoid the loss of orientation selectivity caused by the ^{57}Fe hyperfine splitting,[4] 2) cryogenic isopentane (-150 °C) was used instead of liquid ethane, and 3) samples were packed in EPR tubes, rather than EXAFS cells. Quartz EPR tubes (QSIL Corp.) were used for X-band (3.8 mm O.D./2.8 mm I.D.) and Q-band (2.8 mm O.D./1.8 mm I.D.) measurements. For the samples prepared in D_2O buffer, purified protein was exchanged into 100 mM HEPES ($pH_{apparent}$ = 7.2, pD = 7.6 at 4 °C), 5% glycerol by 10-fold dilution of concentrated protein, followed by reconcentration to the original volume; this was repeated twice. D_2O was obtained from Cambridge Isotope Laboratories (Cambridge, MA).

EPR Measurements

X-band continuous wave (CW) measurements were performed on a Bruker ESP 300 spectrometer with an ER 041 MR microwave bridge and an ER 4116DM resonator. All other EPR measurements were performed on a Bruker Elexsys E580 X-band spectrometer equipped with a SuperX-FT microwave bridge. For pulse EPR measurements at X-band, a Bruker EN 4118X-MD4 dielectric ENDOR resonator was used in concert with an Oxford CF935 helium flow cryostat. Microwave pulses generated by the microwave bridge were amplified by a 1 kW traveling wave tube (TWT) amplifier (Applied Systems Engineering, model 117x). Pulse EPR spectra at Q-band frequencies were acquired using a home-built intermediate-frequency extension of the SuperX-FT X-band bridge that has a Millitech 5W pulse power amplifier. All experiments were conducted on a home-built TE_{011} resonator utilizing the open resonator concept developed by Annino et al.[12] and mechanical construction of the probehead similar to that presented by Reijerse et al.[13] This setup allows $t(\pi/2)$ = 12-16 ns at maximum input power with spectrometer dead time (including the resonator ring time) of 100-120 ns. Data acquisition and control of experimental parameters were performed by using Bruker XEPR software.

The field-swept EPR spectra were obtained using a 2-pulse Hahn echo sequence. X-band ^{2}H-ENDOR spectra were acquired using the sequence developed by Mims. X- and Q-band ^{1}H-ENDOR spectra were acquired using a refocused Mims sequence.[14]

Spectra were acquired using the following parameters:

X-band CW
- Temperature: 15 K
- Microwave attenuation: 40 dB
- Modulation amplitude: 5 Gauss

X-band ^{2}H-ENDOR (Mims)
- π pulse: 16 ns
- τ : 248 ns
- T_{RF}: 15 μs
- Shots/loop: 10
- Shot repetition time: 640 μs

X-band ^{1}H-ENDOR (refocused Mims)
- π pulse: 16 ns
- τ : 48 ns
- T_{RF}: 4 μs
- Shots/loop: 10
- Shot repetition time: 640 μs

Q-band field-swept 2-pulse Hahn echo
π pulse: 12 ns
τ : 380 ns
Shots/loop: 100
Shot repetition time: 1000 μs
Q-band ^{1}H-ENDOR (refocused Mims)
π pulse: 16 ns
τ : 48 ns
T_{RF}: 15 μs
Shots/loop: 3
Shot repetition time: 1000 μs

EPR Analysis

Data processing and spectral simulations were performed using Kazan viewer, a home-written suite of utilities in MATLAB.[15] One-dimensional EPR simulations were performed using the "pepper" utility from the EasySpin software package.[16] ENDOR data were analyzed by simultaneous frequency domain simulation of all field-dependent spectra until a satisfactory solution was achieved. The rhombicity of the hyperfine coupling, ε, was defined as

$$[A_x, A_y, A_z] = [-1-\varepsilon, -1+\varepsilon, 2]*T + A_{iso} \quad (1)$$

In this construction, positive and negative values of T can yield identical simulations of ENDOR spectra; because the structural analysis below relies only on |T|, it was sufficient to take into account only one of the two possibilities; A_x, A_y, and A_z are reported using $T \geq 0$.

Geometric information was obtained by constructing a model which accounts for hyperfine coupling of the deuterium nucleus with the S = 3/2 Mn(IV) and the S = 2 Fe(IV) species (Figure S6). The Mn-Fe distance was fixed at 2.75 Å, on the basis of the EXAFS data. For a given deuterium position, dipolar coupling tensors A_{FeD} and A_{MnD} were computed with magnitude, T_{XD}, according to the formula

$$T_{XD}(\text{MHz}) = 12.1362 r_{XD}^{-3} \quad (2)$$

Then the individual tensors were oriented along the corresponding X−D vectors and combined, accounting for the appropriate spin projection factors

$$\mathbf{A_{tot}} = 2\mathbf{A_{FeD}} - 1\mathbf{A_{MnD}} \quad (3)$$

where 2 and −1 are the spin-projection factors for iron and manganese, respectively.[17]

The extent of agreement between the resulting calculated hyperfine coupling for a given position and the experimental hyperfine coupling was determined using the formula

$$D = \exp(-(|T_{calc}|-|T_{exp}|)^2/2\sigma_T^2)\cdot\exp(-(\varepsilon_{calc}-\varepsilon_{exp})^2/2\sigma_\varepsilon^2) \quad (4)$$

where $|T_{calc}|$ and $|T_{exp}|$ represent the calculated and experimental hyperfine coupling magnitude, respectively; ε_{calc} and ε_{exp} represent the calculated and experimental rhombicity of the hyperfine coupling, respectively; and $\sigma_T = 0.1$ MHz and $\sigma_\varepsilon = 0.2$ represent the estimated uncertainty in the experimental hyperfine coupling magnitude and rhombicity, respectively. Greater extent of agreement, D, is depicted with darker shading in Figure 3A of the main text; the isosurface in Figure 3B is depicted at D = 0.5.

Supplementary Figures

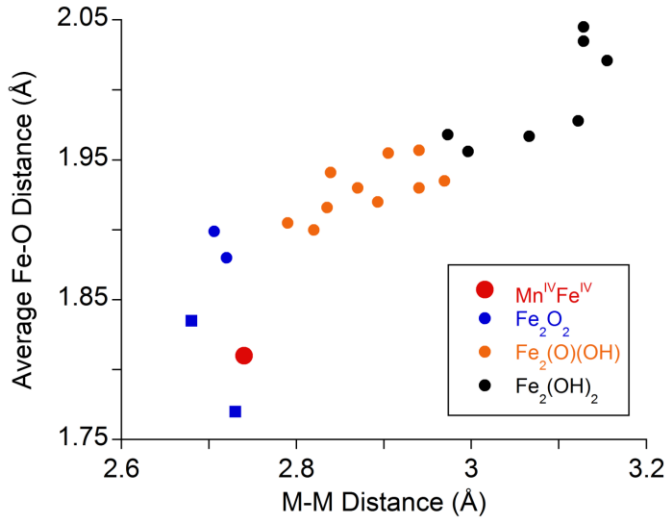

Figure S1. Comparison of Fe-O and M-M distances in crystallographically (circles) or EXAFS (squares) characterized diiron model complexes with the distances obtained by EXAFS herein.[18–25] **4/4** clearly clusters with the di-μ-oxo diamond core models.

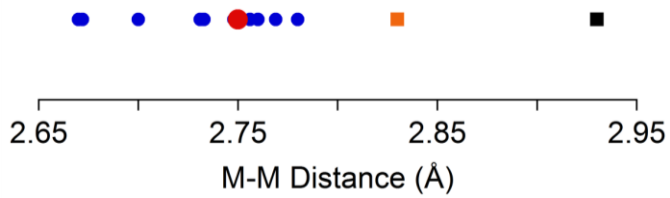

Figure S2. Comparison of M-M distances in crystallographically (circles) or EXAFS (squares) characterized dimanganese model complexes with the distance obtained by EXAFS herein.[26–29] **4/4** clearly clusters with the di-μ-oxo diamond core models. Markers are color coded as in Figure S1.

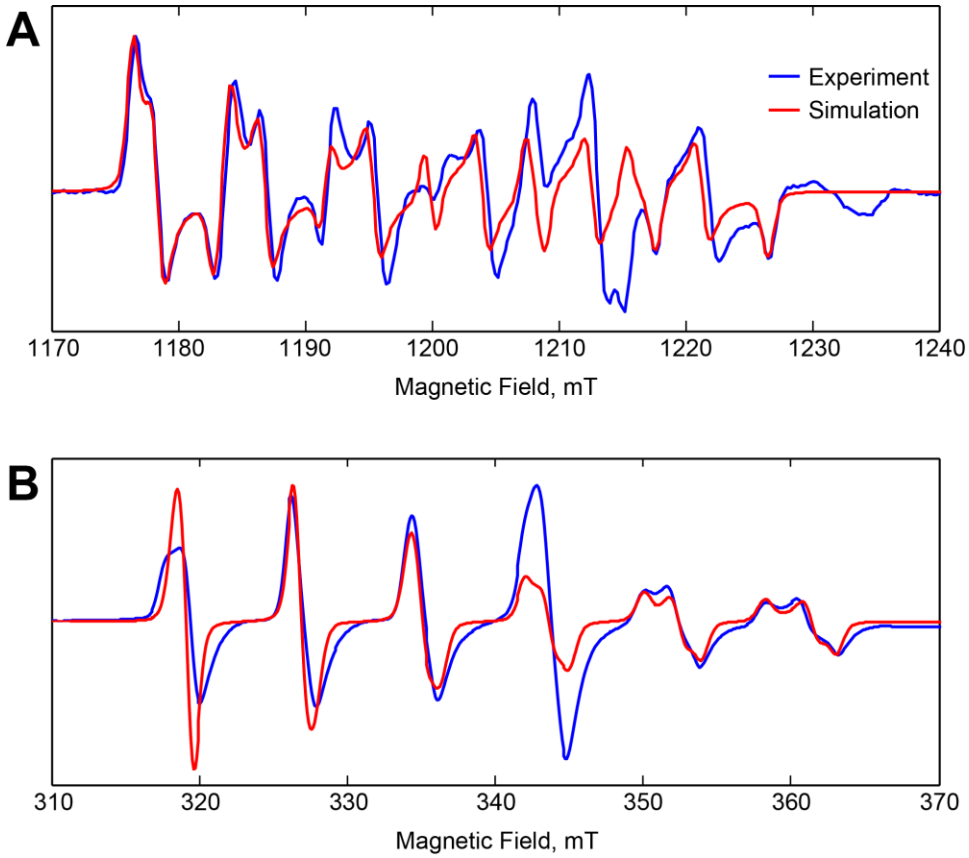

Figure S3: Multifrequency analysis of the **4/4** EPR spectrum. Spectra were recorded at Q-band (A) and X-band (B); experimental results are depicted in blue, whereas simulations are shown in red. Note that the deviations observed at $g \sim 2$ are due to the *Ct* X contaminant. The X-band spectrum was recorded using a standard continuous-wave (CW) experiment; however, Q-band CW spectra were found to exhibit considerable contamination from free Mn(II) present in the sample. Therefore, we acquired the Q-band spectrum using a field-swept 2-pulse Hahn echo experiment, with τ = 380 ns and $t_{\pi/2}$ = 12 ns; the derivative of the experimental spectrum is displayed. We attribute the decreased prominence of the Mn(II) signals to discrepancies in the relaxation properties and total spin between **4/4** and the contaminant. Spectra were acquired using microwave frequencies of 33.948 GHz and 9.624 GHz at 25 K and 15 K for Q- and X-band spectra, respectively.

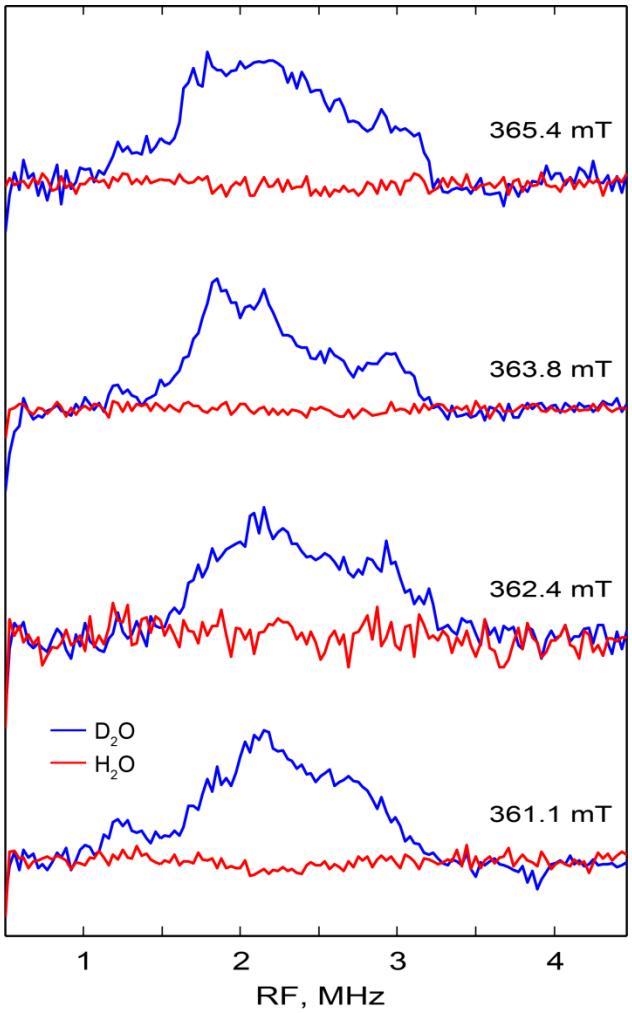

Figure S4: Comparison of field-dependent ^{2}H-ENDOR traces for **4/4** samples prepared in H_2O (red) and D_2O (blue) buffer. Spectra were collected at 15 K with a microwave frequency of 9.702 (D_2O) and 9.717 (H_2O) GHz.

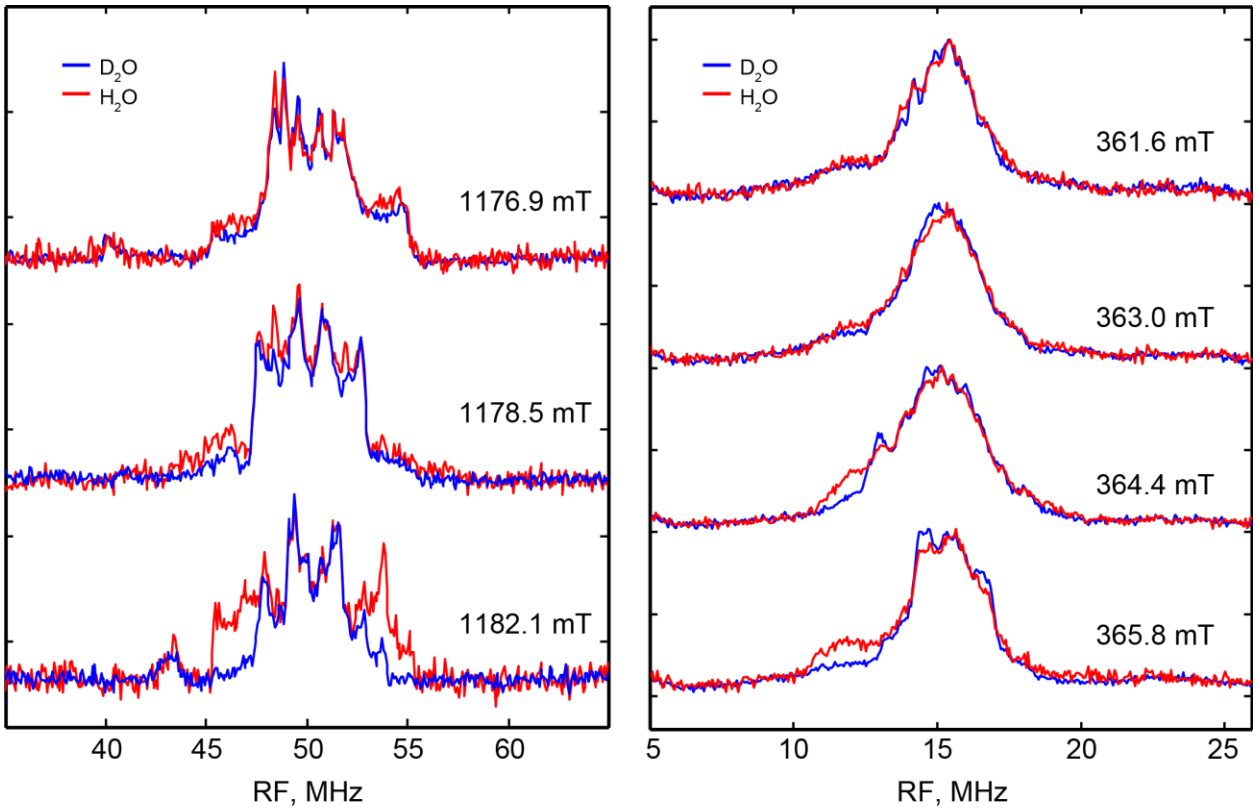

Figure S5: Comparison of field-dependent, Q-band (left) and X-band (right) ^{1}H-ENDOR spectra, obtained using the refocused Mims sequence with a tau of 48 ns.[14] Traces for **4/4** samples prepared in H_2O (red) and D_2O (blue) buffer. X-band spectra were collected at 15 K with a microwave frequency of 9.702 (D_2O) and 9.717 (H_2O) GHz. Q-band spectra were collected at 25 K with a microwave frequency of 33.946 GHz.

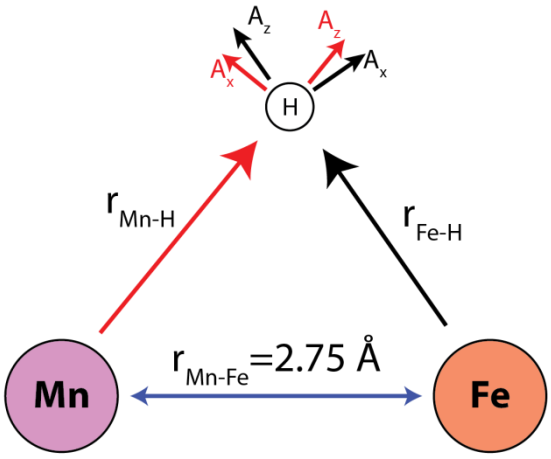

Figure S6. Geometric model for dipolar coupling of ^{2}H to Mn and Fe.

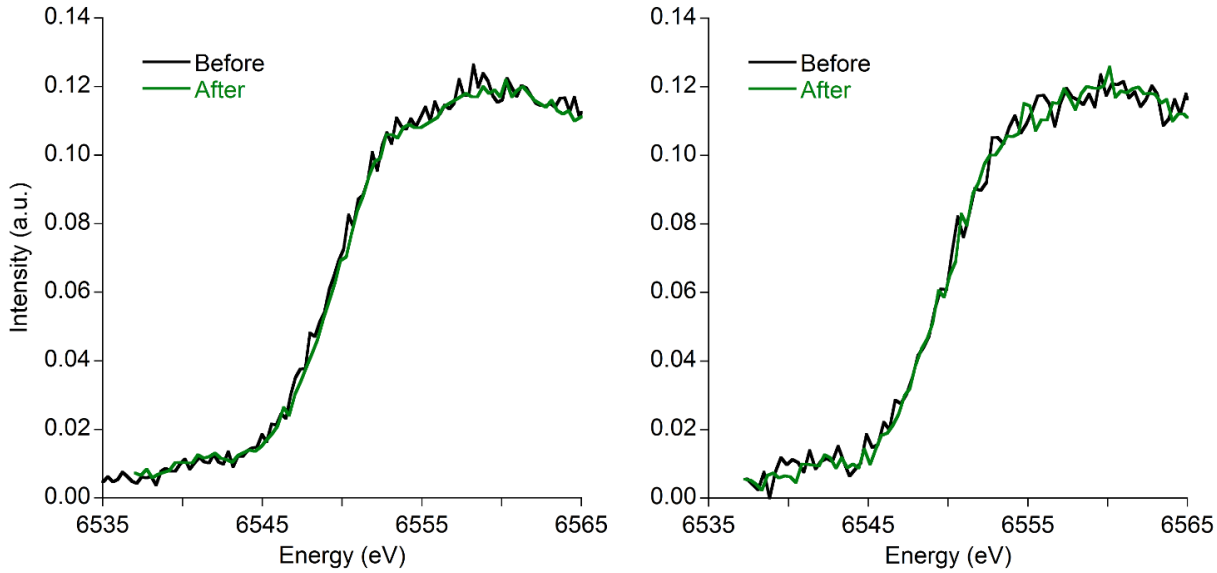

Figure S7: Damage assessment at the manganese edge was carried out after both Mn EXAFS scans (left) and Fe EXAFS scans (right). In order to observe no damage, during Mn EXAFS measurements five aluminum foil attenuators were placed in the beam path upstream of the sample, reducing the beam intensity to 11% of its initial value at 7.1 keV, while six filters were used during Fe EXAFS scans (reducing the intensity at 7.1 keV to 7%). EXAFS scans were 800 s and 685 s long for Mn and Fe, respectively.

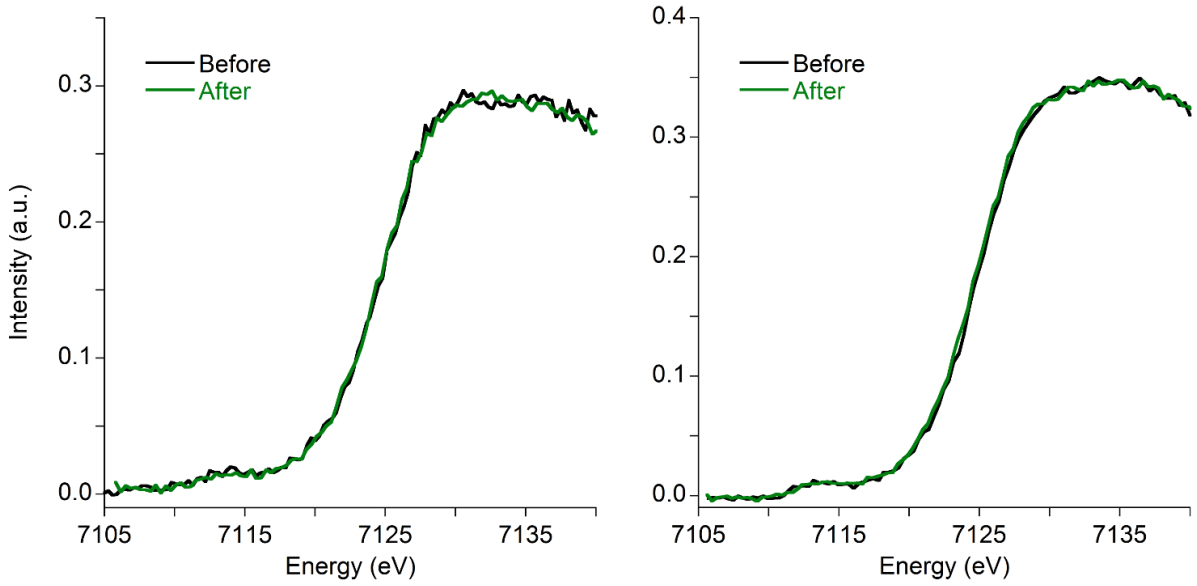

Figure S8: Damage assessment at the iron edge was carried out after both Fe EXAFS scans (left) and Mn EXAFS scans (right). In order to observe no damage, during Fe EXAFS measurements six aluminum foil attenuators were placed in the beam path upstream of the sample, reducing the beam intensity to 14% of its initial value at 8 keV, while five filters were used during Mn EXAFS scans (reducing the intensity at 8 keV to 20%).

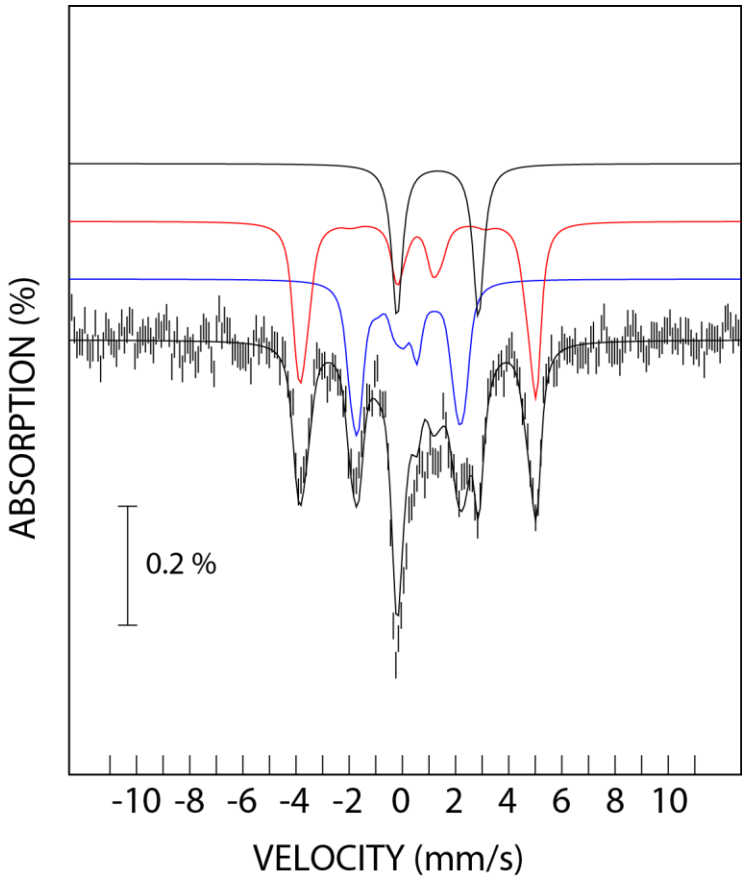

Figure S9: Mössbauer characterization of the iron-only control sample (preparation conditions described above). The experimental data is displayed by the black vertical bars, whereas the simulation is overlaid as a black solid line. Contributions to the simulation include: the Fe(IV) site (37%, blue solid line), Fe(III) site (37%, red solid line), and the Fe(II) site (21%, black solid line). The Fe(III)/Fe(IV) site was simulated on the basis of published spin Hamiltonian parameters,[2,30] which were allowed to float within ~20%.

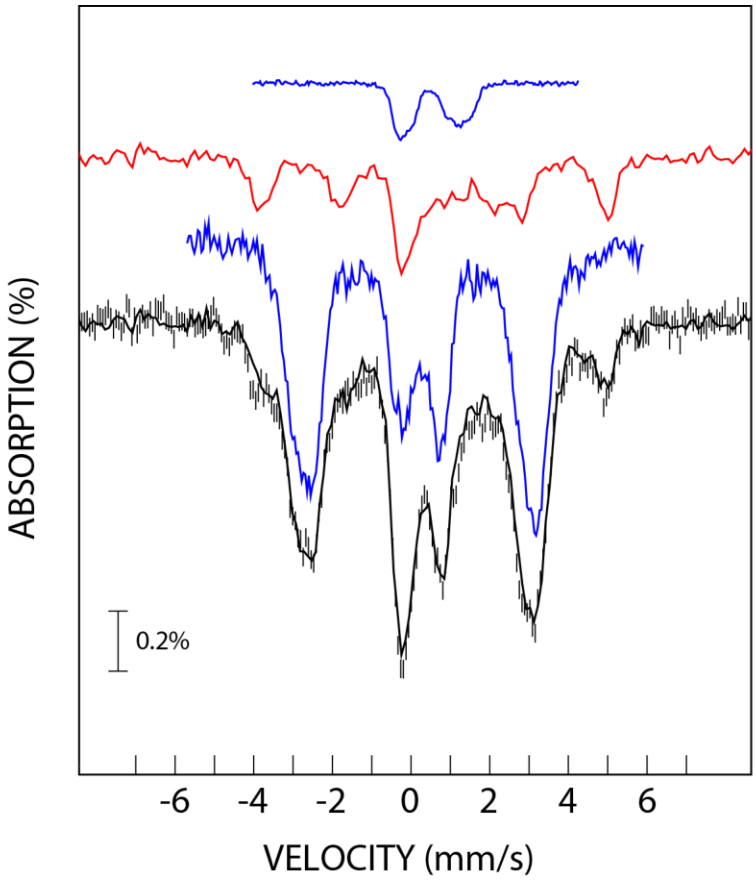

Figure S10: Mössbauer characterization of the Mn/Fe sample (preparation conditions described above). The experimental data is displayed by the black vertical bars, whereas the simulation is overlaid as a black solid line. Contributions to the simulation include: an experimental reference spectrum for the Mn(IV)/Fe(IV) intermedate (65%, blue solid line), the Fe-only control spectrum (30%, red solid line), and an experimental reference spectrum for the Mn(IV)/Fe(III) cofactor. Reference spectra for the Mn(IV)/Fe(IV) and Mn(IV)/Fe(III) forms are taken from reference (4) and (31), respectively.

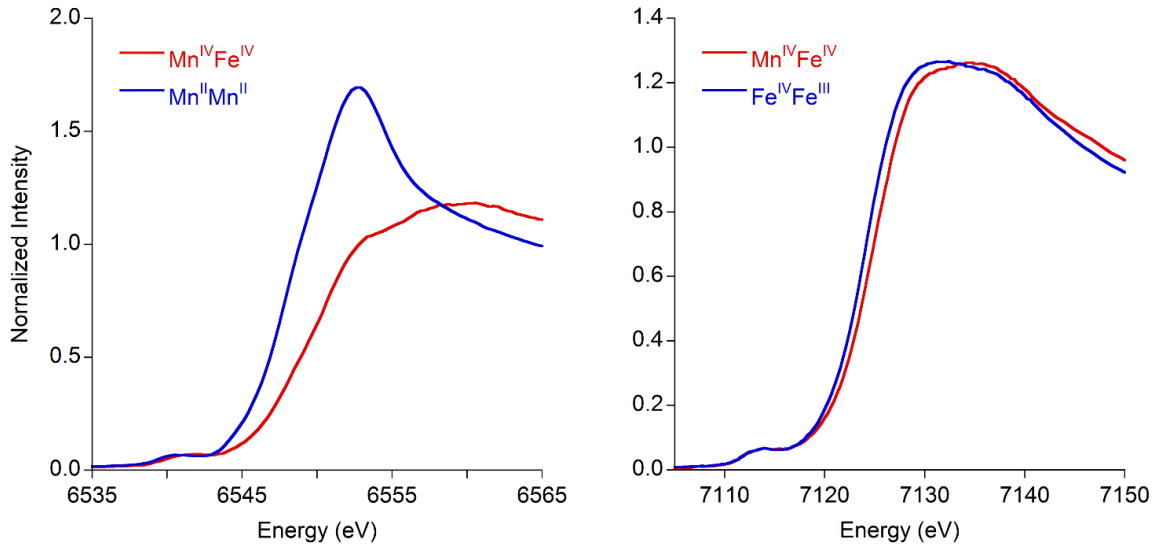

Figure S11: Overlays of the Mn (left) and Fe (right) edges for the **4/4** intermediate and the Mn-only and Fe-only controls. The expected shifts to higher energies for the higher valent intermediate are seen in both cases.

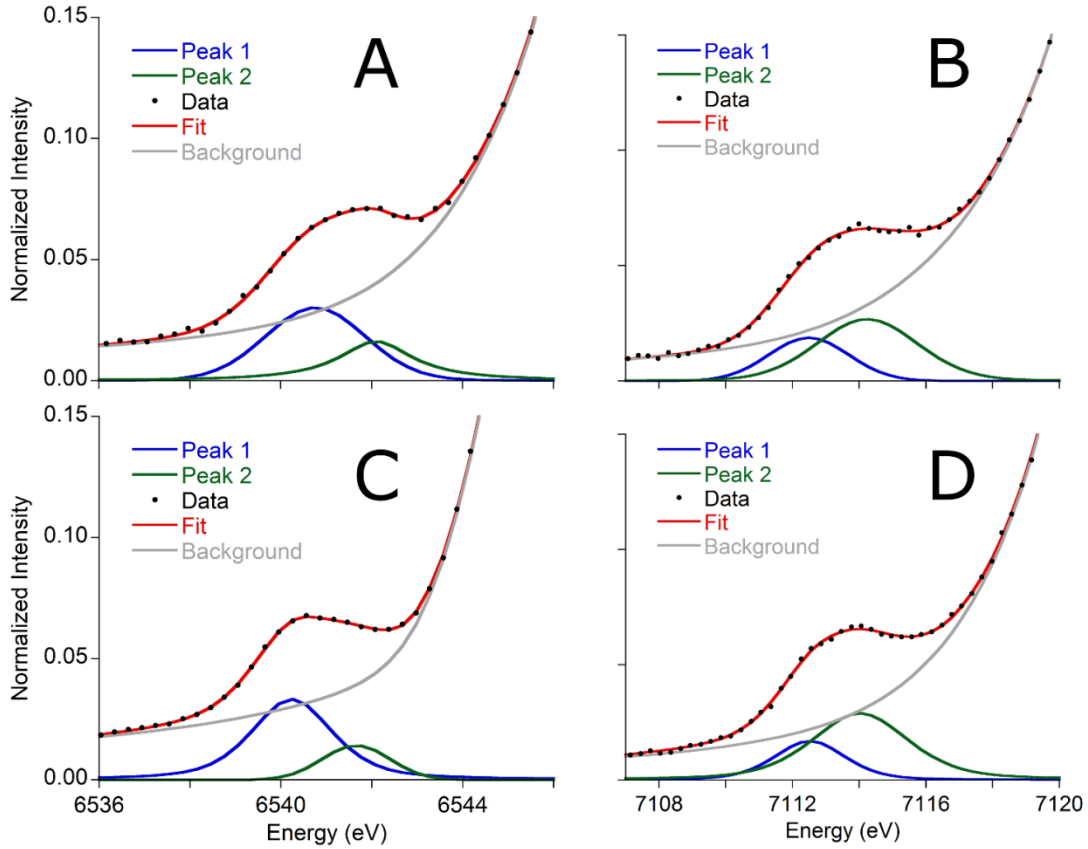

Figure S12: Representative pre-edge fits for the **4/4** intermediate (A / B) and the Mn-only (C) and Fe-only (D) controls.

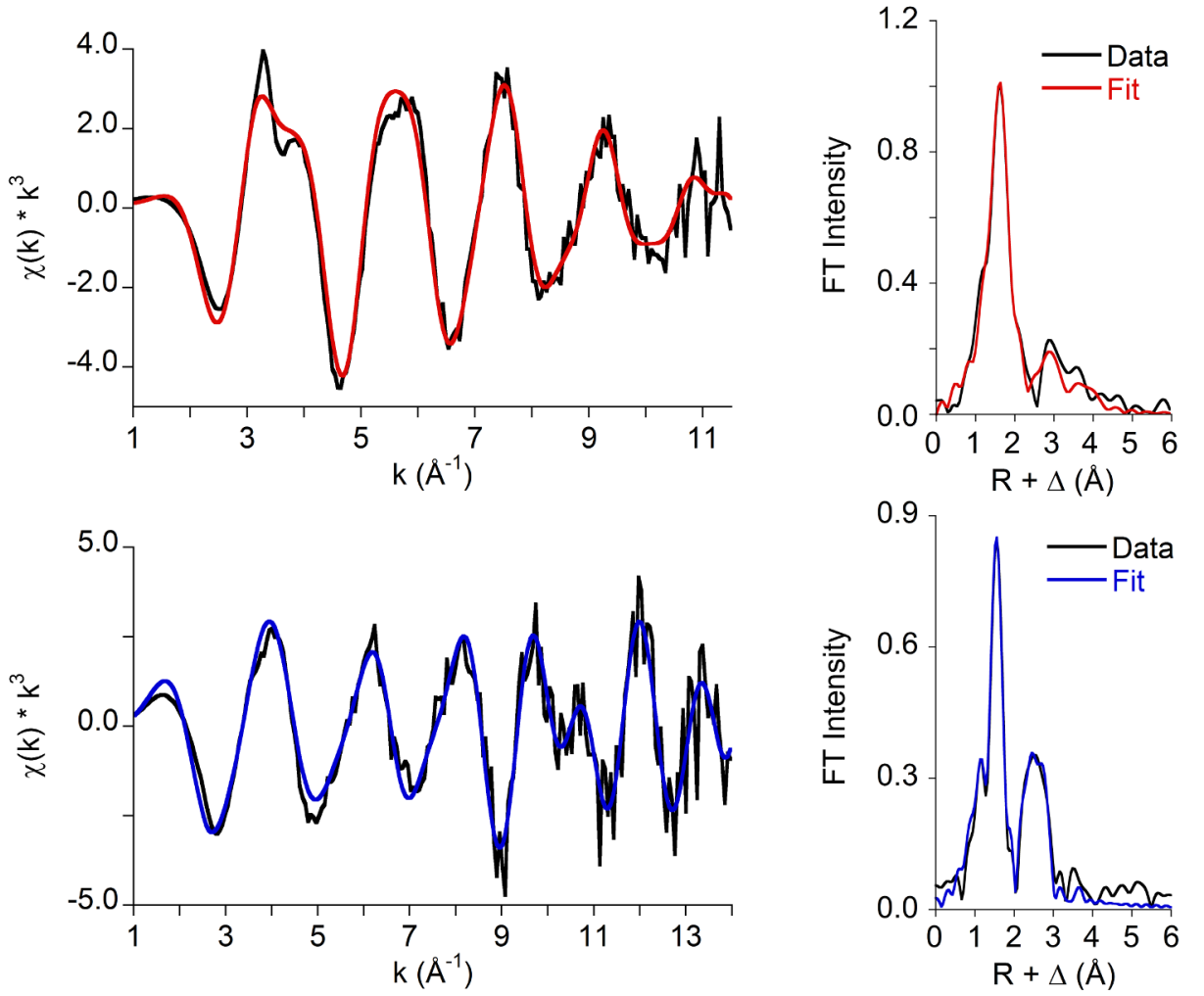

Figure S13: Fits to the k^3-weighted EXAFS and Fourier transforms for the Mn-only (top) and Fe-only (bottom) control samples. The Mn-only control has a dominant shell of scatterers at 2.14 Å, a shoulder at 2.56 Å, additional light atom contributions around 3.8 and 4.0 Å, and a Mn-Mn interaction at 4.2 Å. These results are entirely consistent with protein-bound Mn(II) and, of the interactions observed, only the first shell would be expected to contribute significantly to the EXAFS of the **4/4**. Indeed, a shell at 2.19 Å is needed to adequately fit those data, possibly as a result of the ~30% Mn(II) contaminant present. The scatterers at longer distances would not be expected to be visible above the noise of **4/4**, so they were not included in fits to **4/4**. Fits to the Fe-only control revealed interactions at 1.72 and 1.99 Å, a metal-metal vector at 2.79 Å, and additional light atom scatterers at 3.0 and 3.4 Å. These data are in near quantitative agreement with those obtained on an isoelectronic intermediate (intermediate **X**) from the *E. coli* class Ia RNR,[9] suggesting that *Ct* X has a very similar structure to **X**. Moreover, the contributions to these EXAFS occur at very similar distances to the main features in the **4/4** (e.g. 1.72 vs. 1.81 Å, 1.99 vs. 2.01 Å, 2.79 vs. 2.75 Å). Given the similarity, no explicit effort was made to account for these contributions during the fitting of the **4/4**.

Supplementary Tables

Table S1: Pre-edge fit parameters

	Area[a]	IWAE[b] (eV)	N[c]
4/4 (Mn)	13.9 (2.5)	6541.2 (2)	30
Mn(II)	13.1 (1.9)	6540.5 (1)	33
4/4 (Fe)	18.5 (2.4)	7113.7 (1)	28
Fe(III)/Fe(IV)	19.4 (3.2)	7113.8 (2)	22

[a] Area calculated by multiplying integral of pre-edge peaks by 100; [b] Intensity weighted average energies; [c] Number of physically reasonable fits used to generate parameters.

The Fe pre-edge areas measured for the **4/4** are consistent with those observed for other di-μ-oxo species (18 – 22 units for MMO intermediate Q,[32] 19.0 – 19.7 units for TPA dimers[24]) and are lower than those reported for species possessing terminal oxo coordination (≥25 units).[33] Likewise, the Mn pre-edge area is similar to that from the putative di-μ-oxo in superoxidized catalase (14.5 units),[34] though it is smaller than what has been observed in a model system.[35]

Table S2: EXAFS fit parameters for the Mn(II) and Fe(III)/Fe(IV) controls

Mn				Fe			
Scatterer	**N**	**R (Å)**	**σ^2 (Å^2)**	**Scatterer**	**N**	**R (Å)**	**σ^2 (Å^2)**
Mn-C/N/O	4.5	2.14	0.00858	Fe-C/N/O	0.5	1.72	0.00157
Mn-C/N/O	1	2.56	0.00717	Fe-C/N/O	3.5	1.99	0.00801
Mn-C/N/O	4	3.81	0.00347	Fe-Fe	1	2.79	0.00602
Mn-C/N/O	4	3.98	0.00103	Fe-C/N/O	4	3.04	0.00216
Mn-Mn	1	4.19	0.00437	Fe-C/N/O	2	3.41	0.00584
F		0.237		F		0.380	
E_0		3.89 eV		E_0		4.71 eV	

Table S3: Summary of the best EXAFS fits for Mn(II) control

		Component 1			Component 2			Component 3			Mn-Mn			Component 5		
F	E_0	N	R	σ^2	N	R	σ^2	N	R	σ^2	N	R	σ^2	N	R	σ^2
0.3591	3.76	4	2.14	7.34												
0.3402	3.98	4.5	2.14	8.62	1	2.56	6.85									
0.3029	3.38	4	2.14	7.32	0.5	2.59	1.03	3	3.87	9.80						
0.2619	3.87	4.5	2.14	8.62	1	2.57	6.60	3.5	3.91	9.29	1	4.17	7.92			
0.2374	3.89	4.5	2.14	8.58	1	2.56	7.17	4	3.81	3.47	1	4.19	4.37	4	3.98	1.03
0.2322[a]	3.56	4.5	2.14	8.60	1	2.57	6.62	4	3.83	5.58	4	4.50	5.77	4	4.01	6.26

[a] Replacing the Mn scatterer at ~4.2 Å with light atoms results in a very small improvement in the F factor, though the distance increases substantially. Given the low intensity and long distances involved, it is difficult to discern whether a metal-metal scattering interaction is indeed present; in any case, no signals in this range are expected to interfere with interpretation of the data for the **4/4** intermediate so the details are of limited importance for this study.

Table S4: Summary of the best EXAFS fits for Fe(III)/Fe(IV) control

		Component 1			Component 2			Fe-Fe			Component 4			Component 5		
F	E0	N	R	σ^2	N	R	σ^2	N	R	σ^2	N	R	σ^2	N	R	σ^2
0.6199	-0.39	2	2.01	3.26												
0.5912	-2.04	1	1.75	9.33	3	1.99	5.19									
0.5473	-1.87	1	1.74	7.31	3.5	1.99	6.48	1	2.75	6.06						
0.3955	0.35	0.5	1.72	1.48	3.5	1.99	7.98	1	2.79	6.20	4	3.05	2.11			
0.3798	0.47	0.5	1.72	1.58	3.5	1.99	8.00	1	2.79	6.02	4	3.04	2.16	2	3.41	5.79
0.3913[a]	-1.01	0.5	1.72	1.35	3.5	1.99	8.15	1	3.03	4.79	3	2.81	2.16	2	3.25	6.74
0.3748[b]	-0.45	0.5	1.72	1.31	3.5	1.99	8.17	1	3.39	12.15	2	2.79	1.28	2	3.06	0.92
0.3963[c]	-0.74	0.5	1.72	1.44	3.5	1.99	8.03	3	2.79	2.96	3	3.06	2.06	3	3.37	9.22

[a] Attempts to fit the data with the Fe scatterer at ~3.0 Å yielded statistically inferior fits compared to those having the metal at ~2.8 Å.
[b] A very slightly better fit could be obtained by placing the Fe scatterer at ~3.4 Å, though in no case could physically reasonable Debye-Waller factors be obtained.
[c] Replacing the Fe scatterer with light atoms gave worse fits than those obtained with the metal present.

Table S5: Summary of the best EXAFS fits for Mn site of 4/4 intermediate

		Component 1			Component 2			Mn-Fe			Component 4			Component 5		
F	**E_0**	**N**	**R**	**σ^2**	**N**	**R**	**σ^2**	**N**	**R**	**σ^2**	**N**	**R**	**σ^2**	**N**	**R**	**σ^2**
0.634	-3.31	2	1.83	6.51												
0.532	1.35	2	1.85	6.65	1	2.18	5.10									
0.4387	1.06	2	1.85	6.94	1	2.18	4.35	0.7	2.74	7.34						
0.4131	2.55	2	1.86	7.22	1	2.19	4.14	0.7	2.75	4.35	2	2.97	2.89			
0.4012	3.11	2	1.86	7.22	1	2.19	4.37	0.7	2.76	4.84	2	3.00	3.26	2	3.28	6.46
0.4037[a]	0.86	2	1.85	6.96	1	2.19	5.59	0.7	3.07	6.19	2	2.78	3.40	3	3.28	1.39
0.4097[b]	0.25	2	1.85	6.92	1	2.18	5.34	0.7	3.27	8.95	2	2.76	1.75	1	3.06	3.86
0.4116[c]	1.21	2	1.85	6.89	1	2.18	5.63	2	2.76	2.19	1	3.07	1.67	2	3.28	2.28

[a] Placing the Fe scatterer at ~3.0 Å results in a worse fit than when the metal is at 2.75 Å.
[b] Similarly, having the Fe scatterer at ~3.3 Å results in inferior fits compared to when the metal is at 2.75 Å.
[c] Replacing the Fe scatterer with light atoms also has a negative impact on the fits.

Table S6: Summary of the best EXAFS fits for Fe site of 4/4 intermediate

		Component 1			Component 2			Fe-Mn			Component 4			Component 5			Component 6		
F	E_0	N	R	σ^2	N	R	σ^2	N	R	σ^2	N	R	σ^2	N	R	σ^2	N	R	σ^2
0.8788	4.00	1	1.99	9.34															
0.7384	-0.30	2	1.80	8.68	3	2.02	8.67												
0.6696	-1.15	2	1.81	9.26	2	2.02	5.40	1	2.75	4.60									
0.5496	0.51	2	1.80	9.16	3	2.02	8.80	1	2.77	4.07	3	2.99	2.59						
0.5284	-0.14	2	1.79	8.89	3	2.01	8.75	1	2.76	3.90	3	2.98	2.40	2	3.35	4.72			
0.467	-2.05	2	1.81	9.78	2	2.01	6.36	1	2.74	3.84	4	2.97	5.42	1	3.33	2.71	2	2.50	4.00
0.4992[a]	-6.37	2	1.78	9.17	2	1.99	7.95	3	2.72	1.31	3	2.48	5.25	2	3.30	3.26			
0.4668[b]	-6.12	2	1.79	9.02	2	2.00	6.48	1	2.50	8.30	4	2.36	21.23	2	3.29	2.71	4	2.72	1.66
0.4851[c]	-5.54	2	1.78	9.01	2	1.99	7.32	1	3.02	5.60	3	2.74	3.73	3	3.18	9.88	2	2.46	2.39
0.4781[d]	-3.33	2	1.80	9.68	2	2.01	7.34	3	2.73	2.04	2	3.05	7.40	2	3.30	4.24	2	2.48	2.68

[a] For the 5 shell fits, replacing the Mn scatterer with light atoms does result in an improvement to the fit.
[b] Attempts to fit the Mn scatterer to 2.5 Å led in all cases to fits with physically unreasonable Debye-Waller factors.
[c] Fitting the Mn at ~3.0 Å yielded statistically worse fits than when the metal was at ~2.75 Å.
[d] The fit improvement seen when replacing the Mn with light atom scatterers was not retained in the 6 shell fit, where a statistically worse outcome was observed.

The following tables contain all attempted fits to the EXAFS data for all samples. Distances are reported in Å and all Debye-Waller factors are reported as $x10^3$. The color code for Debye-Waller factors is: blue = unreasonably large (>0.01), purple = unreasonably small (0 – 0.001), and red = negative; fits with unreasonable Debye-Waller factors were not considered when determining the best fit. The best fit for a given number of shells is highlighted in green.

Table S7: EXAFS fitting results for Mn(II) control

		Component 1			Component 2			Component 3			Mn-Mn			Component 5		
F	E_0	N	R	σ^2	N	R	σ^2	N	R	σ^2	N	R	σ^2	N	R	σ^2
0.3615	2.93	4	2.13	7.32												
0.3821	3.11	5	2.13	9.65												
0.3909	3.96	3	2.14	4.97												
0.3591	3.76	4	2.14	7.34												
0.3653	3.47	4.5	2.14	8.49												
0.3443	4.04	4	2.14	7.45	1	2.58	6.50									
0.3486	3.32	5	2.14	9.74	1	2.55	6.48									
0.3899	4.09	3	2.14	5.01	1	2.61	3.39									
0.3402	3.98	4.5	2.14	8.62	1	2.56	6.85									
0.3455	4.09	4.5	2.14	8.36	2	2.55	14.39									
0.3407	4.09	4.5	2.14	8.52	1.5	2.55	10.54									
0.3459	3.92	4.5	2.14	8.41	0.5	2.57	3.44									
0.3436	3.21	4	2.13	7.34	0.5	2.58	0.99									
0.3444	3.95	4	2.14	7.46	1	2.58	6.45									
0.3519	4.09	4	2.14	7.54	1.5	2.58	8.07									
0.3487	3.31	5	2.14	9.69	1	2.55	6.37									
0.358	3.11	5	2.14	9.73	0.5	2.55	3.38									
0.3431	3.95	5	2.14	9.67	1.5	2.55	9.29									
0.3438	4.09	5	2.14	9.74	2	2.55	11.16									
0.3001	3.65	4.5	2.14	8.62	1	2.56	6.53	3	3.87	10.60						
0.3107	3.59	4.5	2.14	8.61	1	2.56	6.45	2	3.86	7.40						
0.3052	3.59	4.5	2.14	8.63	1	2.57	6.43	2.5	3.87	9.04						
0.3088	3.94	4	2.14	7.45	1	2.58	6.36	2.5	3.88	9.61						
0.313	3.64	5	2.14	9.76	1	2.56	6.21	2.5	3.88	9.79						
0.308	4.09	5	2.14	9.81	2	2.56	11.73	2.5	3.88	6.88						
0.3099	4.09	5	2.14	9.39	2.5	2.54	15.22	2.5	3.87	9.66						
0.3063	4.09	5	2.14	9.54	2	2.55	12.19	2.5	3.88	9.75						
0.3137	4.09	5	2.14	9.54	2	2.54	12.12	2	3.84	6.95						
0.3269	4.09	4	2.14	7.72	2	2.56	15.71	2.5	3.83	6.64						
0.3142	4.09	4	2.14	7.40	1.5	2.57	11.19	2.5	3.88	9.93						
0.3076	3.41	4	2.14	7.34	0.5	2.59	1.04	2.5	3.87	8.66						

0.3029	3.38	4	2.14	7.32	0.5	2.59	1.03	3	3.87	9.80						
0.313	3.34	4	2.14	7.34	0.5	2.59	0.96	2	3.86	6.90						
0.316	3.22	4.5	2.14	8.48	0.5	2.57	1.94	2	3.86	7.84						
0.3106	3.24	4.5	2.14	8.58	0.5	2.57	1.86	2.5	3.86	8.39						
0.3061	3.19	4.5	2.13	8.57	0.5	2.57	1.84	3	3.86	9.84						
0.2694	3.51	4	2.14	7.32	0.5	2.59	0.74	3	3.90	7.74	1	4.17	7.79			
0.2714	3.99	4	2.14	7.47	1	2.58	6.13	3	3.91	8.25	1	4.17	7.76			
0.2781	4.09	4	2.14	7.50	1.5	2.57	10.81	3	3.91	8.52	1	4.18	7.59			
0.2716	4.09	4.5	2.15	8.34	1	2.57	7.18	3	3.93	7.26	1	4.18	6.09			
0.2738	3.15	4.5	2.13	8.57	0.5	2.57	1.51	3	3.89	7.86	1	4.16	8.00			
0.2689	3.14	4.5	2.13	8.57	0.5	2.57	1.53	3.5	3.89	8.85	1	4.16	7.94			
0.2619	3.87	4.5	2.14	8.62	1	2.57	6.60	3.5	3.91	9.29	1	4.17	7.92			
0.2673	3.73	4.5	2.14	8.65	1	2.57	6.40	3	3.90	8.27	1	4.17	7.95			
0.2613	4.09	4.5	2.14	8.60	1.5	2.56	10.38	3.5	3.91	9.53	1	4.18	7.66			
0.3071	4.09	4.5	2.14	8.62	1	2.57	6.83	3.5	3.90	3.10	1	3.74	8.28			
0.3014	4.09	4.5	2.14	8.62	1	2.57	3.28	4	3.90	3.28	1	3.74	7.97			
0.2812	3.48	4.5	2.14	8.63	1	2.56	6.45	4	3.82	12.80	1	3.52	18.43			
0.2716	3.61	5	2.14	9.74	1	2.55	6.20	3.5	3.89	9.42	1	4.17	8.22			
0.2645	4.09	5	2.14	9.72	1.5	2.55	9.29	3.5	3.91	9.48	1	4.17	7.84			
0.2639	4.09	5	2.14	9.57	2	2.55	12.18	3.5	3.90	9.70	1	4.18	7.95			
0.2802	4.09	5	2.15	9.47	2	2.55	13.05	3	3.84	10.32	1	4.14	11.30			
0.2828	4.09	5	2.14	9.56	2	2.55	12.18	2	3.90	6.54	1	4.17	8.25			
0.2885	3.66	5	2.14	9.81	1	2.55	6.14	2	3.89	6.18	1	4.17	8.31			
0.2768	3.54	5	2.14	9.74	1	2.55	6.11	3	3.89	8.44	1	4.17	8.16			
0.2675	3.47	5	2.14	9.80	1	2.56	6.05	4	3.89	10.13	1	4.17	8.03			
0.2614	3.97	4	2.14	7.48	1	2.58	6.16	4	3.91	10.18	1	4.18	7.61			
0.266	3.98	4	2.14	7.47	1	2.58	6.15	3.5	3.91	9.32	1	4.18	7.72			
0.2713	4.01	4	2.14	7.47	1	2.58	6.16	3	3.91	8.27	1	4.17	7.80			
0.2802	4.09	4	2.14	7.57	1.5	2.58	6.79	3	3.91	6.79	1	4.18	7.14			
0.2727	4.09	4	2.14	7.50	1.5	2.57	10.82	3.5	3.91	9.52	1	4.18	7.53			
0.2857	4.09	4	2.14	7.71	1.5	2.57	10.44	2.5	3.89	7.31	1	4.17	8.22			
0.2385	3.96	4.5	2.14	8.55	1	2.56	7.15	3.5	3.82	1.68	1	4.18	3.82	3	3.99	-1.60
0.2379	3.94	4.5	2.14	8.58	1	2.56	7.22	3.5	3.80	2.36	1	4.18	4.37	4	3.98	0.89
0.2391	3.92	4.5	2.14	8.59	1	2.57	7.18	3.5	3.79	2.82	1	4.19	4.76	5	3.97	2.99
0.242	3.88	4.5	2.14	8.58	1	2.57	7.12	3.5	3.77	3.65	1	4.19	5.28	6	3.96	5.28
0.2394	3.82	4.5	2.14	8.58	1	2.57	7.08	4	3.79	3.96	1	4.19	4.79	5	3.97	3.14

0.2374	3.89	4.5	2.14	8.58	1	2.56	7.17	4	3.81	3.47	1	4.19	4.37	4	3.98	1.03
0.2373	3.85	4.5	2.14	8.58	1	2.57	7.10	4.5	3.81	4.68	1	4.19	4.38	4	3.99	1.28
0.2377	3.89	4.5	2.14	8.56	1	2.57	7.18	5	3.82	5.46	1	4.19	4.14	4	4.00	1.14
0.2394	3.70	4.5	2.14	8.59	1	2.57	6.85	6	3.82	8.51	1	4.19	4.74	4	4.00	2.44
0.2436	3.63	4.5	2.14	8.60	1	2.57	6.66	6	3.80	9.62	1	4.19	5.46	5	3.99	5.02
0.2362	3.70	4.5	2.14	8.59	1	2.57	6.84	6	3.83	8.12	1	4.19	4.17	3	4.00	0.16
0.2377	3.70	4.5	2.14	8.59	1	2.57	6.88	6	3.83	8.30	1	4.19	4.46	3.5	4.00	1.34
0.2613	3.38	4.5	2.14	8.61	1	2.57	6.50	6	3.76	9.97	1	3.54	13.76	4	3.99	12.47
0.2616	3.39	4.5	2.14	8.61	1	2.57	6.48	6	3.78	10.34	1	3.54	14.37	3	4.01	9.62
0.2633	3.41	4.5	2.14	8.60	1	2.57	6.47	5	3.77	8.05	1	3.55	13.87	3	3.97	11.02
0.2657	3.47	4.5	2.14	8.61	1	2.56	6.51	5	3.78	8.86	1	3.55	15.26	2	4.00	7.44
0.2346	4.09	4.5	2.14	8.54	1.5	2.56	10.63	4	3.81	3.17	1	4.18	4.24	4	3.98	0.72
0.2366	4.09	4.5	2.14	8.50	1.5	2.56	11.52	4	3.80	2.95	1	4.19	4.47	5	3.98	2.17
0.2368	4.09	4.5	2.14	8.57	1.5	2.57	10.65	3	3.78	1.28	1	4.18	4.47	5	3.96	2.38
0.2388	4.09	4.5	2.14	8.62	1.5	2.56	10.82	2	3.76	-0.70	1	4.18	4.90	5	3.94	3.27
0.2419	4.09	4.5	2.14	8.70	1.5	2.56	10.06	2	3.78	-0.70	1	4.17	4.85	4	3.95	1.06
0.2392	4.09	4.5	2.14	8.61	1.5	2.56	11.09	2	3.75	0.20	1	4.18	5.35	6	3.93	5.58
0.2514	3.51	4.5	2.14	8.55	0.5	2.57	2.56	2	3.75	0.32	1	4.17	5.29	6	3.92	5.61
0.2519	3.29	4.5	2.14	8.55	0.5	2.58	2.21	3	3.75	3.24	1	4.17	5.54	6	3.93	5.67
0.2521	3.33	4.5	2.14	8.55	0.5	2.58	2.36	3.5	3.76	4.31	1	4.18	5.48	6	3.94	5.68
0.2492	3.40	4.5	2.14	8.55	0.5	2.57	2.46	3.5	3.78	3.24	1	4.18	5.01	5	3.95	3.36
0.2479	3.93	4.5	2.14	8.55	0.5	2.57	2.52	3.5	3.79	2.66	1	4.17	4.70	4	3.96	1.29
0.2357	3.83	4.5	2.14	8.56	1	2.57	7.09	5	3.83	5.71	1	4.19	3.96	3	4.00	-0.50
0.2377	3.78	4.5	2.14	8.59	1	2.57	7.01	5	3.81	5.95	1	4.19	4.50	4	3.99	1.64
Below are attempts to replace Mn scatterer with light atoms																
0.2485	4.02	4.5	2.14	8.59	1	2.56	7.18	4	3.83	3.71	1	4.49	-3.30	4	4.02	4.02
0.2398	3.86	4.5	2.14	8.60	1	2.56	6.98	4	3.90	4.47	2	4.49	0.71	4	4.02	4.90
0.2348	3.71	4.5	2.14	8.60	1	2.56	6.78	4	3.83	5.00	3	4.50	3.43	4	4.02	5.57
0.2326	3.76	4.5	2.14	8.59	1	2.56	6.92	4	4.03	7.28	3	4.50	3.72	4	3.82	6.69
0.2322	3.56	4.5	2.14	8.60	1	2.57	6.62	4	3.83	5.58	4	4.50	5.77	4	4.01	6.26

Table S8: EXAFS fitting results for Fe(III)/Fe(IV) control

		Component 1			Component 2			Component 3			Component 4			Component 5		
F	E_0	N	R	σ^2	N	R	σ^2	N	R	σ^2	N	R	σ^2	N	R	σ^2
0.6965	0.50	1	2.01	0.25												
0.6199	-0.39	2	2.01	3.26												
0.6253	-0.92	3	2.01	6.01												
0.6651	-1.27	4	2.01	9.27												
0.6161	2.53	1	2.06	4.29	1	1.99	1.30									
0.6044	3.30	1	2.18	19.06	2	2.01	3.54									
0.5912	-2.04	1	1.75	9.33	3	1.99	5.19									
0.5934	-2.49	1	1.73	5.70	4	1.99	7.72									
0.6161	-3.07	1	1.72	4.29	5	1.98	10.44									
0.6005	-4.86	2	1.74	12.39	4	1.99	6.60									
0.5949	-4.08	2	1.77	17.84	3	1.99	4.95									
0.5964	-3.89	1.5	1.74	8.78	4	1.98	6.92									
0.6042	-4.10	1.5	1.73	7.91	4.5	1.98	8.04									
0.6158	-4.23	1.5	1.72	7.22	5	1.98	9.18									
0.5933	-3.09	1.5	1.77	14.17	3	2.00	4.99									
0.5925	-3.61	1.5	1.75	11.00	3.5	1.99	5.89									
0.587	0.00	1	1.75	8.13	3	1.99	5.30	1	2.10	14.92						
0.5893	-0.52	1	1.75	7.23	2	2.02	3.69	1	1.93	2.86						
0.5875	1.07	1	1.74	7.95	2	1.99	4.19	2	2.02	15.34						
0.591	0.73	1	1.75	6.61	1	2.05	2.24	2	1.96	4.26						
0.5931	-0.15	1.5	1.77	11.59	1	2.05	3.00	2	1.97	3.77						
0.6016	1.13	1.5	1.87	25.82	1	2.05	3.23	1	1.98	1.71						
0.5886	2.66	1.5	1.77	11.39	1	2.14	23.93	3	2.00	5.20						
0.5668	0.47	1	1.89	28.90	2	2.01	3.57	1	2.76	6.07						
0.55	-1.59	1	1.75	9.78	3	1.99	5.28	1	2.76	6.16						
0.5473	-1.87	1	1.74	7.31	3.5	1.99	6.48	1	2.75	6.06						
0.5514	-2.22	1	1.73	5.91	4	1.99	7.76	1	2.75	5.96						
0.5761	-2.87	1	1.71	4.52	5	1.98	10.39	1	2.75	5.79						
0.5591	-4.32	2	1.74	12.80	4	1.99	6.66	1	2.75	6.14						
0.5537	-3.36	2	1.78	19.17	3	2.00	5.11	1	2.75	6.20						
0.5795	-4.96	2	1.72	10.21	5	1.98	8.57	1	2.75	6.06						

0.5544	-3.39	1.5	1.74	9.55	4	1.99	6.99	1	2.75	6.06			
0.5507	-3.09	1.5	1.75	11.54	3.5	1.99	5.98	1	2.75	6.13			
0.5519	-2.70	1.5	1.77	14.80	3	2.00	5.07	1	2.75	6.22			
0.5511	-1.74	1	1.75	9.27	3	1.99	5.19	1	3.04	4.61			
0.5502	-2.40	1	1.73	5.55	4	1.99	7.72	1	3.04	4.48			
0.5719	-3.08	1	1.71	4.24	5	1.98	10.38	1	3.04	4.36			
0.4244	-2.56	1	1.73	5.54	3.5	1.98	6.38	1	2.77	9.81	1	3.05	-2.50
0.4066	-1.94	1	1.73	5.99	3.5	1.99	6.46	1	2.78	8.46	2	3.05	-0.30
0.404	-1.48	1	1.73	6.34	3.5	1.99	6.52	1	2.78	7.30	3	3.04	1.12
0.423	-2.83	1	1.73	6.12	3.5	1.98	6.74	1	3.02	5.84	3	2.80	2.13
0.444	-3.01	1	1.73	5.79	3.5	1.98	6.78	1	3.02	5.15	4	2.80	3.39
0.4133	-2.47	1	1.73	6.26	3.5	1.98	6.83	1	3.02	6.74	2	2.79	0.47
0.4111	-1.16	1	1.73	6.62	3.5	1.99	6.56	1	2.78	6.38	4	3.04	2.35
0.4135	-1.61	1	1.72	5.23	4	1.99	7.84	1	2.78	6.33	4	3.04	2.28
0.406	-1.89	1	1.72	5.02	4	1.98	7.80	1	2.78	7.25	3	3.04	1.04
0.4084	-2.30	1	1.72	4.76	4	1.98	7.75	1	2.78	8.38	2	3.04	-0.40
0.4157	-2.91	1	1.72	5.00	4	1.98	8.11	1	3.02	6.73	2	2.79	0.36
0.4288	-3.28	1	1.72	4.88	4	1.98	8.05	1	3.02	5.93	3	2.80	1.93
0.4145	-1.54	1	1.74	8.37	3	1.99	5.21	1	2.78	8.53	2	3.05	-0.20
0.4116	-1.03	1	1.75	9.04	3	1.99	5.28	1	2.78	7.34	3	3.05	1.25
0.4179	-0.71	1	1.75	9.35	3	2.00	5.34	1	2.78	6.43	4	3.04	2.47
0.4308	-0.50	1	1.75	9.85	3	2.00	5.39	1	2.78	5.66	5	3.04	3.70
0.4206	-2.13	1	1.74	8.58	3	1.99	5.56	1	3.03	6.77	2	2.79	0.60
0.427	-2.44	1	1.74	8.25	3	1.99	5.51	1	3.02	5.92	3	2.80	2.23
0.4451	-2.63	1	1.74	7.90	3	1.99	5.45	1	3.02	5.23	4	2.80	3.77
0.4189	-3.14	1.5	1.74	10.51	3.5	1.99	5.85	1	2.77	8.56	2	3.04	-0.20
0.4171	-2.60	1.5	1.74	11.21	3.5	1.99	5.95	1	2.78	7.38	3	3.04	1.22
0.4241	-2.24	1.5	1.75	11.68	3.5	1.99	6.02	1	2.78	6.44	4	3.04	2.45
0.421	-2.03	1.5	1.76	15.22	3	2.00	5.11	1	2.78	7.35	3	3.04	1.31
0.4273	-1.59	1.5	1.77	16.09	3	2.00	5.20	1	2.78	6.33	4	3.04	2.57
0.4288	-2.94	1.5	1.76	14.68	3	1.99	5.36	1	3.02	6.79	2	2.79	0.66
0.4346	-3.26	1.5	1.76	13.90	3	1.99	5.24	1	3.02	5.90	3	2.79	2.35
0.4211	-3.57	1.5	1.73	8.56	4	1.98	6.87	1	2.77	8.49	2	3.04	-0.30
0.4192	-3.11	1.5	1.73	8.96	4	1.98	6.94	1	2.78	7.38	3	3.04	1.14
0.4265	-2.74	1.5	1.73	9.31	4	1.99	7.01	1	2.78	6.42	4	3.04	2.37
0.4284	-4.00	1.5	1.73	8.86	4	1.98	7.23	1	3.02	6.68	2	2.79	0.50

0.4381	-3.99	1.5	1.73	8.39	4	1.98	7.10	1	3.02	5.82	3	2.79	2.13			
0.4591	-4.23	1.5	1.73	8.27	4	1.98	7.03	1	3.01	4.99	4	2.79	3.57			
0.3878	0.16	0.5	1.72	1.32	3.5	1.99	7.97	1	2.79	7.10	3	3.05	0.89			
0.3955	0.35	0.5	1.72	1.48	3.5	1.99	7.98	1	2.79	6.20	4	3.05	2.11			
0.4113	0.41	0.5	1.72	1.64	3.5	1.99	7.97	1	2.79	5.49	5	3.04	3.26			
0.4225	-0.08	0.5	1.72	1.08	4	1.99	9.41	1	2.79	5.47	5	3.04	3.16			
0.4161	-0.14	0.5	1.72	0.91	4	1.99	9.44	1	2.79	6.17	4	3.04	1.99			
0.3975	-0.31	0.5	1.72	0.78	4	1.99	9.42	1	2.79	7.09	3	3.05	0.78			
0.391	0.58	0.5	1.72	2.15	3	1.99	6.51	1	2.79	7.15	3	3.05	0.99			
0.3975	0.78	0.5	1.72	2.35	3	2.00	6.52	1	2.79	6.23	4	3.05	2.24			
0.412	0.86	0.5	1.72	2.54	3	2.00	6.52	1	2.79	5.52	5	3.04	3.43			
0.4671	-1.99	0.5	1.72	2.43	3	1.98	6.46	1	3.02	4.50	5	2.80	5.01			
0.4377	-1.41	0.5	1.72	2.60	3	1.99	6.51	1	3.02	5.10	4	2.80	3.51			
0.4143	-1.00	0.5	1.72	2.40	3	1.99	6.64	1	3.02	5.97	3	2.80	1.93			
0.4032	-0.67	0.5	1.72	2.10	3	1.99	6.82	1	3.03	6.90	2	2.80	0.25			
0.3999	-1.06	0.5	1.71	1.32	3.5	1.99	8.28	1	3.03	6.96	2	2.80	0.10			
0.4147	-1.12	0.5	1.71	1.33	3.5	1.99	8.23	1	3.02	5.87	3	2.80	1.72			
0.4025	-1.82	1	1.74	8.31	3	1.99	5.25	1	2.77	8.14	2	3.05	-0.40	2	3.40	3.26
0.4089	-2.03	1	1.74	8.24	3	1.99	5.23	1	2.77	8.15	2	3.05	-0.30	3	3.41	6.17
0.4163	-2.28	1	1.74	7.90	3	1.99	5.19	1	2.77	8.32	2	3.05	-0.20	4	3.41	9.97
0.398	-1.04	1	1.75	9.18	3	1.99	5.34	1	2.78	7.00	3	3.04	0.96	1	3.40	0.90
0.3988	-1.24	1	1.74	9.05	3	1.99	5.31	1	2.78	7.10	3	3.04	1.17	2	3.40	4.43
0.4028	-1.31	1	1.74	8.87	3	1.99	5.29	1	2.78	7.12	3	3.04	1.29	3	3.40	7.58
0.408	-1.49	1	1.74	8.74	3	1.99	5.25	1	2.78	7.32	3	3.05	1.29	4	3.41	11.48
0.4045	-0.66	1	1.75	9.67	3	2.00	5.38	1	2.78	5.38	4	3.04	2.40	1	3.40	1.98
0.4025	-0.70	1	1.75	9.74	3	2.00	5.38	1	2.78	6.13	4	3.04	2.60	2	3.40	5.32
0.4038	-0.83	1	1.75	9.62	3	2.00	5.35	1	2.78	6.33	4	3.04	2.62	3	3.40	8.26
0.4071	-0.86	1	1.75	9.37	3	2.00	5.32	1	2.78	6.40	4	3.04	2.60	4	3.40	11.82
0.4165	-0.47	1	1.75	10.04	3	2.00	5.39	1	2.78	5.50	5	3.04	3.76	1	3.38	2.88
0.4117	-0.44	1	1.75	9.96	3	2.00	5.40	1	2.78	5.52	5	3.04	3.86	2	3.39	5.84
0.4107	-0.45	1	1.75	9.92	3	2.00	5.38	1	2.78	5.38	5	3.04	3.88	3	3.39	8.48
0.412	-0.49	1	1.75	9.98	3	2.00	5.39	1	2.78	5.66	5	3.04	3.84	4	3.40	11.13
0.3895	-1.49	1	1.73	6.51	3.5	1.99	6.57	1	2.78	6.99	3	3.04	0.82	1	3.40	0.78
0.3901	-1.63	1	1.73	6.44	3.5	1.99	6.55	1	2.78	7.00	3	3.04	1.06	2	3.40	4.34
0.3938	-1.73	1	1.73	6.41	3.5	1.99	6.52	1	2.78	6.52	3	3.04	1.17	3	3.40	7.38
0.3957	-1.32	1	1.73	6.67	3.5	1.99	6.56	1	2.78	6.27	4	3.04	2.48	3	3.40	8.30

0.3948	-1.16	1	1.73	6.78	3.5	1.99	6.58	1	2.78	6.18	4	3.04	2.41	2	3.40	5.37
0.4083	-2.79	1	1.73	6.07	3.5	1.98	6.68	1	3.03	5.59	3	2.80	2.60	1	3.29	2.38
0.401	-2.66	1	1.73	6.09	3.5	1.98	6.69	1	3.03	4.98	3	2.80	2.66	2	3.27	6.01
0.3969	-2.53	1	1.73	6.18	3.5	1.98	6.70	1	3.03	4.86	3	2.80	2.59	3	3.26	9.48
0.3967	-2.65	1	1.73	6.33	3.5	1.98	6.77	1	3.03	7.88	2	2.79	0.49	1	3.32	0.69
0.3922	-2.56	1	1.73	6.34	3.5	1.98	6.74	1	3.04	6.53	2	2.79	0.79	2	3.31	4.37
0.391	-2.59	1	1.73	6.28	3.5	1.98	6.75	1	3.04	5.99	2	2.79	0.85	3	3.30	7.29
0.392	-2.54	1	1.73	6.29	3.5	1.98	6.74	1	3.03	5.66	2	2.79	0.86	4	3.29	10.44
0.4256	-3.00	1	1.73	5.79	3.5	1.98	6.60	1	3.03	3.92	4	2.81	5.02	1	3.24	0.23
0.4161	-2.78	1	1.73	5.86	3.5	1.98	6.61	1	3.03	3.46	4	2.81	4.99	2	3.24	2.82
0.4106	-2.62	1	1.73	6.02	3.5	1.98	6.63	1	3.03	3.77	4	2.81	4.42	3	3.24	7.28
0.4068	-2.45	1	1.73	6.10	3.5	1.98	6.66	1	3.02	4.05	4	2.81	4.12	4	3.23	11.52
0.3884	-2.12	1	1.73	6.26	3.5	1.99	6.67	1	3.38	11.65	2	2.78	1.69	2	3.06	0.81
0.3971	-1.73	1	1.73	6.53	3.5	1.99	6.74	1	3.37	11.53	2	2.79	1.18	3	3.06	2.96
0.4104	-1.48	1	1.73	6.76	3.5	1.99	6.79	1	3.37	10.87	2	2.79	0.68	4	3.06	5.21
0.3959	-2.44	1	1.73	5.93	3.5	1.98	6.59	1	3.38	11.73	3	2.79	4.03	2	3.05	0.24
0.3998	-2.02	1	1.73	6.24	3.5	1.99	6.64	1	3.37	12.04	3	2.79	3.30	3	3.05	2.14
0.4099	-1.74	1	1.73	6.51	3.5	1.99	6.71	1	3.37	11.67	3	2.79	2.92	4	3.05	3.98
0.4105	-2.84	1	1.73	5.57	3.5	1.98	6.50	1	3.38	11.81	4	2.79	6.53	2	3.05	-0.20
0.4115	-2.42	1	1.73	5.92	3.5	1.98	6.56	1	3.37	12.41	4	2.79	5.41	3	3.05	1.45
0.4195	-2.12	1	1.73	6.19	3.5	1.99	6.61	1	3.37	12.26	4	2.79	4.54	4	3.05	3.00
0.4001	-2.67	1	1.72	4.77	4	1.98	7.74	1	2.77	8.04	2	3.04	-0.50	3	3.40	5.84
0.4073	-2.68	1	1.72	4.77	4	1.98	7.74	1	2.77	7.99	2	3.04	-0.30	4	3.41	9.51
0.3912	-2.02	1	1.72	5.07	4	1.98	7.82	1	2.78	7.01	3	3.04	0.97	2	3.40	4.29
0.3944	-2.06	1	1.72	5.04	4	1.98	7.80	1	2.78	7.05	3	3.04	1.10	3	3.40	7.41
0.3991	-2.30	1	1.72	4.90	4	1.98	7.77	1	2.78	7.20	3	3.04	1.12	4	4.03	11.11
0.3994	-1.57	1	1.72	5.33	4	1.99	7.86	1	2.78	6.14	4	3.04	2.10	1	3.40	1.80
0.3965	-1.62	1	1.72	5.32	4	1.99	7.85	1	2.78	6.18	4	3.04	2.30	2	3.39	5.38
0.3969	-1.71	1	1.72	5.27	4	1.99	7.83	1	2.78	6.27	4	3.04	2.38	3	3.39	8.34
0.3991	-1.80	1	1.72	5.24	4	1.99	7.82	1	2.78	6.34	4	3.04	2.38	4	3.39	11.63
0.4134	-1.40	1	1.72	5.50	4	1.99	7.88	1	2.78	5.47	5	3.04	3.40	1	3.39	3.03
0.4077	-1.41	1	1.72	5.45	4	1.99	7.86	1	2.78	5.56	5	3.04	3.52	2	3.84	6.11
0.4055	-1.45	1	1.72	5.40	4	1.99	7.84	1	2.78	5.69	5	3.04	3.51	3	3.83	8.67
0.4056	-1.51	1	1.72	5.43	4	1.99	7.84	1	2.78	5.67	5	3.04	3.54	4	3.39	11.29
0.4187	-1.33	1	1.72	5.58	4	1.99	7.87	1	2.78	5.12	6	3.04	4.72	3	3.38	8.39
0.393	-0.03	0.5	1.72	1.98	3	1.99	6.47	1	2.78	8.00	2	3.05	-0.50	3	3.42	6.69

0.4019	-0.18	0.5	1.72	1.98	3	1.99	6.44	1	2.78	8.10	2	3.05	-0.40	4	3.43	11.77
0.3775	0.66	0.5	1.72	2.18	3	2.00	6.58	1	2.79	6.84	3	3.05	0.71	1	3.42	0.95
0.3791	0.64	0.5	1.72	2.20	3	2.00	6.55	1	2.79	6.85	3	3.05	0.92	2	3.42	4.54
0.3841	0.57	0.5	1.72	2.23	3	1.99	6.51	1	2.79	6.92	3	3.05	1.07	3	3.42	8.05
0.3901	0.50	0.5	1.72	2.23	3	1.99	6.48	1	2.79	7.06	3	3.05	1.09	4	3.43	14.09
0.3844	0.92	0.5	1.72	2.49	3	2.00	6.54	1	2.79	6.04	4	3.05	2.12	1	3.41	2.19
0.3824	0.95	0.5	1.72	2.44	3	2.00	6.55	1	2.79	6.03	4	3.05	2.31	2	3.41	5.83
0.3841	0.95	0.5	1.72	2.44	3	2.00	6.53	1	2.79	6.11	4	3.05	2.37	3	3.41	9.18
0.3877	0.94	0.5	1.72	2.42	3	2.00	6.52	1	2.79	6.19	4	3.05	2.37	4	3.42	13.78
0.398	1.00	0.5	1.72	2.66	3	2.00	6.53	1	2.79	5.38	5	3.04	3.43	1	3.40	3.47
0.3927	1.06	0.5	1.72	2.68	3	2.00	6.52	1	2.79	5.43	5	3.04	3.55	2	3.40	6.65
0.3915	1.12	0.5	1.72	2.70	3	2.00	6.50	1	2.79	5.51	5	3.04	3.56	3	3.40	9.53
0.3927	1.17	0.5	1.72	2.63	3	2.00	6.52	1	2.79	5.51	5	3.05	3.57	4	3.41	12.76
0.374	-0.17	0.5	1.72	1.17	3.5	1.99	8.03	1	2.79	8.12	2	3.05	-1.10	1	3.41	0.50
0.3794	-0.29	0.5	1.72	1.17	3.5	1.99	7.98	1	2.78	7.93	2	3.05	-0.80	2	3.42	3.06
0.3876	-0.40	0.5	1.72	1.21	3.5	1.99	7.91	1	2.78	7.94	2	3.05	-0.60	3	3.42	6.32
0.3963	-0.57	0.5	1.72	1.15	3.5	1.99	7.89	1	2.78	8.04	2	3.05	-0.50	4	3.43	11.15
0.3749	0.18	0.5	1.72	1.39	3.5	1.99	8.00	1	2.79	6.81	3	3.05	0.81	2	3.42	4.44
0.3797	0.11	0.5	1.72	1.38	3.5	1.99	7.97	1	2.79	6.90	3	3.05	0.94	3	3.42	7.95
0.3854	0.03	0.5	1.72	1.36	3.5	1.99	7.95	1	2.79	7.03	3	3.05	0.96	4	3.42	13.98
0.3819	0.45	0.5	1.72	1.56	3.5	1.99	8.02	1	2.79	6.02	4	3.04	1.96	1	3.52	2.16
0.3798	0.47	0.5	1.72	1.58	3.5	1.99	8.00	1	2.79	6.02	4	3.04	2.16	2	3.41	5.79
0.3811	0.46	0.5	1.72	1.56	3.5	1.99	7.99	1	2.79	6.11	4	3.05	2.23	3	3.41	9.30
0.3842	0.42	0.5	1.72	1.54	3.5	1.99	8.00	1	2.79	6.17	4	3.05	2.25	4	3.41	14.09
0.3972	0.53	0.5	1.72	1.74	3.5	1.99	8.00	1	2.79	5.34	5	3.04	3.25	1	3.40	3.34
0.3916	0.61	0.5	1.72	1.73	3.5	1.99	7.99	1	2.79	5.41	5	3.04	3.38	2	3.40	6.82
0.3899	0.64	0.5	1.72	1.71	3.5	2.00	7.99	1	2.79	5.46	5	3.04	3.41	3	3.40	9.71
0.3907	0.65	0.5	1.72	1.69	3.5	2.00	7.99	1	2.79	5.55	5	3.04	3.37	4	3.40	12.96
0.4169	0.51	0.5	1.72	1.87	3.5	1.99	7.96	1	2.78	4.88	6	3.04	4.52	1	3.39	4.37
0.4085	0.63	0.5	1.72	1.87	3.5	2.00	7.97	1	2.78	4.91	6	3.04	4.59	2	3.39	7.05
0.4043	0.71	0.5	1.72	1.85	3.5	2.00	7.97	1	2.78	4.97	6	3.04	4.58	3	3.39	9.57
0.4029	0.75	0.5	1.72	1.84	3.5	2.00	7.98	1	2.78	4.99	6	3.04	4.58	4	3.39	11.90
0.3818	-0.62	0.5	1.72	0.66	4	1.99	9.48	1	2.79	7.97	2	3.05	-1.20	1	3.41	-0.70
0.3871	-0.72	0.5	1.72	0.66	4	1.99	9.43	1	2.78	7.90	2	3.05	-0.90	2	3.41	2.96
0.3949	-0.86	0.5	1.72	0.67	4	1.99	9.38	1	2.78	7.90	2	3.05	-0.70	3	3.42	6.16
0.3825	-0.25	0.5	1.72	0.83	4	1.99	9.48	1	2.79	6.84	3	3.05	0.41	1	3.42	0.44

0.384	-0.28	0.5	1.72	0.83	4	1.99	9.46	1	2.79	6.84	3	3.05	0.69	2	3.42	4.33
0.3883	-0.37	0.5	1.72	0.85	4	1.99	9.42	1	2.79	6.88	3	3.05	0.84	3	3.42	8.00
0.3923	-0.03	0.5	1.72	0.98	4	1.99	9.47	1	2.79	5.99	4	3.04	1.80	1	3.42	1.81
0.3901	-0.04	0.5	1.72	0.99	4	1.99	9.46	1	2.79	6.02	4	3.04	2.01	2	3.41	5.71
0.3909	-0.06	0.5	1.72	0.99	4	1.99	9.44	1	2.79	6.11	4	3.04	2.10	3	3.41	9.24
0.4086	0.06	0.5	1.72	1.14	4	1.99	9.46	1	2.79	5.36	5	3.04	3.12	1	3.41	3.61
0.4028	0.08	0.5	1.72	1.15	4	1.99	9.44	1	2.79	5.42	5	3.04	3.24	2	3.40	6.97
0.4007	0.12	0.5	1.72	1.09	4	1.99	9.43	1	2.79	5.51	5	3.04	3.21	3	3.39	9.88
0.4019	-3.57	1.5	1.73	8.76	4	1.98	6.95	1	2.77	8.13	2	3.04	-0.90	1	3.39	-0.60
0.4048	-3.84	1.5	1.73	8.58	4	1.98	6.90	1	2.77	8.10	2	3.04	-0.50	2	3.39	2.77
0.4102	-4.07	1.5	1.73	8.35	4	1.98	6.87	1	2.77	8.20	2	3.04	-0.30	3	3.39	5.62
0.4034	-3.09	1.5	1.73	9.15	4	1.99	6.99	1	2.78	7.05	3	3.04	0.80	1	3.39	0.50
0.403	-3.23	1.5	1.73	8.99	4	1.98	6.96	1	2.77	7.09	3	3.04	1.08	2	3.39	4.08
0.4056	-3.37	1.5	1.73	8.85	4	1.98	6.93	1	2.77	7.17	3	3.04	1.20	3	3.39	7.00
0.4095	-3.55	1.5	1.73	8.80	4	1.98	6.91	1	2.77	7.31	3	3.04	1.22	4	3.04	10.14
0.4117	-2.76	1.5	1.73	9.40	4	1.99	7.03	1	2.78	6.18	4	3.04	2.25	1	3.39	1.73
0.4083	-2.87	1.5	1.73	9.27	4	1.99	7.01	1	2.78	6.27	4	3.04	2.42	2	3.38	5.08
0.4082	-2.95	1.5	1.73	9.19	4	1.99	6.99	1	2.77	6.39	4	3.04	2.47	3	3.38	7.86
0.41	-3.09	1.5	1.73	9.16	4	1.99	6.96	1	2.77	6.50	4	3.04	2.47	4	3.38	10.59
0.4188	-2.60	1.5	1.73	9.60	4	1.99	7.04	1	2.78	5.64	5	3.03	3.65	2	3.37	5.50
0.4163	-2.63	1.5	1.73	9.60	4	1.99	7.03	1	2.77	5.72	5	3.04	3.67	3	3.37	7.99
0.4161	-2.80	1.5	1.73	9.48	4	1.99	7.01	1	2.77	5.84	5	3.04	3.62	4	3.38	10.34
0.4063	-2.66	1.5	1.76	14.62	3	1.99	5.10	1	2.77	8.15	2	3.04	-0.70	1	3.39	-0.50
0.4095	-2.89	1.5	1.76	13.97	3	1.99	5.00	1	2.77	8.19	2	3.04	-0.40	2	3.40	3.07
0.4064	-2.00	1.5	1.77	15.85	3	2.00	5.23	1	2.78	6.92	3	3.04	1.01	1	3.93	0.60
0.4101	-2.47	1.5	1.76	14.70	3	1.99	5.08	1	2.77	7.19	3	3.04	1.34	3	3.96	7.11
0.4187	-1.41	1.5	1.77	17.01	3	2.00	5.30	1	2.78	5.65	5	3.04	3.93	3	3.38	7.96
0.437	-3.61	1.5	1.72	7.07	5	1.98	9.20	1	2.77	5.77	5	3.03	3.47	3	3.37	8.02
0.4268	-4.07	1.5	1.72	6.70	5	1.98	9.12	1	2.77	7.01	3	3.04	1.12	3	3.39	6.67
Fits below place Fe scatterer at ~3.0 Å																
0.4067	-1.09	0.5	1.72	1.18	3.5	1.99	8.11	1	3.04	2.31	4	2.82	4.79	2	3.23	0.50
0.4021	-0.81	0.5	1.72	1.21	3.5	1.99	8.12	1	3.03	2.20	4	2.83	4.56	3	3.22	2.32
0.3996	-0.83	0.5	1.72	1.44	3.5	1.99	8.04	1	3.03	3.49	4	2.81	4.04	4	3.23	8.55
0.4162	-1.01	0.5	1.72	1.15	3.5	1.99	8.08	1	3.04	1.34	5	2.84	7.21	3	3.23	0.75
0.4181	-1.17	0.5	1.72	1.50	3.5	1.99	7.93	1	3.03	2.88	5	2.82	5.66	4	3.22	7.04
0.415	-0.86	0.5	1.72	1.46	3.5	1.99	7.92	1	3.03	2.86	5	2.82	5.54	5	3.21	8.85

0.3862	-0.81	0.5	1.72	1.39	3.5	1.99	8.15	1	3.03	4.90	3	2.81	2.08	3	3.24	10.75
0.3913	-1.01	0.5	1.72	1.35	3.5	1.99	8.15	1	3.03	4.79	3	2.81	2.16	2	3.25	6.74
0.4	-1.27	0.5	1.72	1.34	3.5	1.99	8.11	1	3.03	4.95	3	2.80	2.33	1	3.26	2.33
0.3856	-1.00	0.5	1.72	1.38	3.5	1.99	8.26	1	3.04	7.17	2	2.80	0.31	1	3.32	2.32
0.3799	-0.84	0.5	1.72	1.39	3.5	1.99	8.21	1	3.04	6.25	2	2.80	0.44	2	3.30	6.24
0.3777	-0.66	0.5	1.72	1.36	3.5	1.99	8.25	1	3.03	5.91	2	2.80	0.42	3	3.29	10.00
Fits below place Fe scatterer at ~3.4 Å																
0.3748	-0.45	0.5	1.72	1.31	3.5	1.99	8.17	1	3.39	12.15	2	2.79	1.28	2	3.06	0.92
0.3818	-0.08	0.5	1.72	1.40	3.5	1.99	8.24	1	3.38	12.17	2	2.80	0.74	3	3.06	3.16
0.3941	0.13	0.5	1.72	1.47	3.5	1.99	8.28	1	3.38	11.57	2	2.80	0.30	4	3.06	5.42
0.3865	-0.94	0.5	1.72	1.22	3.5	1.99	8.01	1	3.39	12.20	3	2.80	3.79	2	3.05	0.08
0.3893	-0.44	0.5	1.72	1.31	3.5	1.99	8.14	1	3.39	12.67	3	2.79	2.88	3	3.05	2.11
0.3991	-0.31	0.5	1.72	1.51	3.5	1.99	8.13	1	3.38	12.37	3	2.80	2.27	4	3.05	3.97
0.4128	-0.15	0.5	1.72	1.60	3.5	1.99	8.15	1	3.38	11.67	3	2.80	1.80	5	3.05	5.91
0.4046	-1.39	0.5	1.72	1.02	3.5	1.98	7.91	1	3.39	12.15	4	2.80	6.43	2	3.05	-0.50
0.4055	-1.04	0.5	1.72	1.28	3.5	1.99	7.95	1	3.38	13.01	4	2.80	5.16	3	3.05	1.27
0.4137	-0.79	0.5	1.72	1.45	3.5	1.99	7.98	1	3.38	12.97	4	2.80	4.22	4	3.05	2.86
Fits below have replaced the Fe scatterer with light atoms																
0.3993	0.25	0.5	1.71	1.50	3.5	1.99	8.46	1	2.79	-2.50	4	3.08	7.64	2	3.36	2.23
0.3966	-0.01	0.5	1.71	1.63	3.5	1.99	8.27	2	2.79	0.15	4	3.06	5.56	2	3.37	4.23
0.4234	-0.53	0.5	1.72	1.63	3.5	1.99	8.07	3	2.79	2.20	4	3.06	4.11	1	3.36	3.13
0.4119	-0.45	0.5	1.72	1.60	3.5	1.99	8.10	3	2.79	2.23	4	3.06	4.04	2	3.37	5.89
0.4047	-0.51	0.5	1.72	1.57	3.5	1.99	8.08	3	2.79	2.37	4	3.06	3.82	3	3.36	8.14
0.3985	-0.43	0.5	1.72	1.54	3.5	1.99	8.07	3	2.79	2.49	4	3.06	3.56	5	3.37	12.61
0.4098	-0.90	0.5	1.72	1.45	3.5	1.99	8.02	3	2.79	2.85	3	3.05	2.06	1	3.38	3.42
0.4011	-0.80	0.5	1.72	1.46	3.5	1.99	8.03	3	2.79	2.89	3	3.06	2.11	2	3.37	6.66
0.3963	-0.74	0.5	1.72	1.44	3.5	1.99	8.03	3	2.79	2.96	3	3.06	2.06	3	3.37	9.22
0.3941	-0.68	0.5	1.72	1.43	3.5	1.99	8.02	3	2.79	3.01	3	3.06	2.00	4	3.37	11.92
0.3963	-1.09	0.5	1.72	1.22	3.5	1.99	7.98	3	2.79	3.64	2	3.05	0.08	2	3.40	5.50
0.3957	-1.03	0.5	1.72	1.28	3.5	1.99	7.98	3	2.79	3.58	2	3.06	0.21	4	3.38	12.14
0.4224	-1.60	0.5	1.72	1.14	3.5	1.98	7.85	4	2.79	6.55	2	3.05	-0.70	1	3.41	0.52
0.419	-1.62	0.5	1.72	1.12	3.5	1.98	7.89	4	2.79	6.04	2	3.05	-0.40	2	3.40	4.93
0.4172	-1.60	0.5	1.72	1.09	3.5	1.98	7.83	4	2.79	6.24	2	3.05	-0.30	3	3.39	9.24
0.4329	-1.35	0.5	1.72	1.31	3.5	1.99	7.87	4	2.79	5.18	3	3.05	1.33	1	3.38	4.49
0.4238	-1.33	0.5	1.72	1.31	3.5	1.99	7.89	4	2.79	5.16	3	3.05	1.36	2	3.37	7.40
0.4176	-1.19	0.5	1.72	1.28	3.5	1.99	7.88	4	2.79	5.35	3	3.06	1.27	3	3.36	10.61

0.4139	-1.16	0.5	1.72	1.26	3.5	1.99	7.89	4	2.79	5.43	3	3.06	1.21	4	3.36	13.29
0.3822	-0.25	0.5	1.72	1.51	3.5	1.99	8.20	2	2.79	0.71	3	3.06	3.00	3	3.38	8.08
0.3855	-0.27	0.5	1.72	1.54	3.5	1.99	8.19	2	2.79	0.63	3	3.06	3.14	2	3.37	5.56
0.3967	-0.12	0.5	1.71	1.61	3.5	1.99	8.26	2	2.79	0.17	4	3.06	5.52	2	3.37	4.21
0.3836	-0.62	0.5	1.72	1.43	3.5	1.99	8.14	2	2.79	1.10	2	3.06	0.79	1	3.39	2.00
0.3795	-0.60	0.5	1.72	1.42	3.5	1.99	8.13	2	2.79	1.11	2	3.06	0.90	2	3.39	5.54
0.3792	-0.60	0.5	1.72	1.42	3.5	1.99	8.12	2	2.79	1.15	2	3.06	0.88	3	3.39	8.48
0.3813	-0.55	0.5	1.72	1.39	3.5	1.99	8.12	2	2.79	1.19	2	3.06	0.86	4	3.39	11.72

Table S9: EXAFS fitting results for the Mn site in the 4/4 intermediate

		Component 1			Component 2			Component 3			Component 4			Component 5		
F	E_0	N	R	σ^2	N	R	σ^2	N	R	σ^2	N	R	σ^2	N	R	σ^2
0.599	0.93	1	1.85	1.19												
0.634	-3.31	2	1.83	6.51												
0.7325	-5.20	3	1.81	11.92												
0.532	1.35	2	1.85	6.65	1	2.18	5.10									
0.5267	4.21	2	1.87	6.99	2	2.21	11.46									
0.5531	4.21	1	1.85	1.04	1	2.10	42.85									
0.58	3.89	1	1.85	1.14	1	1.99	37.51									
0.5854	4.21	1	1.86	1.70	1	2.22	4.80									
0.4534	0.99	2	1.85	6.72	1	2.18	4.76	1	2.74	10.85						
0.4387	1.06	2	1.85	6.94	1	2.18	4.35	0.7	2.74	7.34						
0.4432	3.64	2	1.59	5.92	2	2.19	15.05	0.7	2.75	8.17						
0.4834	4.21	1	1.85	1.19	1	2.11	35.16	0.7	2.76	8.27						
0.4972	4.21	1	1.85	1.32	2	1.97	58.49	0.7	2.73	8.25						
0.4679	4.21	1	1.85	1.45	3	2.07	82.15	0.7	2.76	7.87						
0.4539	4.21	1	1.85	1.59	1	2.05	39.96	0.7	2.77	6.25	1	3.02	-0.70			
0.4604	3.54	1	1.85	1.29	1	2.06	55.81	0.7	2.75	7.56	2	2.94	17.42			
0.4499	4.21	1	1.85	1.65	2	2.05	58.08	0.7	2.78	5.25	1	3.01	-2.00			
0.4558	4.21	1	1.86	1.25	2	2.12	78.14	0.7	2.75	7.92	2	2.91	20.28			
0.4	2.47	2	1.86	7.38	1	2.19	4.07	0.7	2.76	4.54	1	2.99	-2.40			
0.4131	2.55	2	1.86	7.22	1	2.19	4.14	0.7	2.75	4.35	2	2.97	2.89			
0.4284	1.93	2	1.86	6.83	1	2.18	4.77	0.7	2.74	7.10	3	2.01	40.65			
0.4292	-6.57	2	1.83	8.73	1	2.16	0.84	0.7	2.70	6.54	4	2.38	25.66			
0.4453	3.68	2	1.86	5.98	2	2.18	15.04	0.7	2.77	5.30	2	3.00	3.71			
0.4142	2.41	2	1.86	7.10	2	2.21	6.94	0.7	2.71	9.34	1	2.46	-1.10			
0.4272	-1.08	2	1.85	7.25	2	2.20	6.16	0.7	2.71	6.49	2	2.46	3.99			
0.4299	-4.77	2	1.83	8.05	2	2.20	4.34	0.7	2.69	5.29	3	2.45	5.18			
0.4284	-6.46	2	1.83	8.67	2	2.19	3.34	0.7	2.68	5.28	4	2.44	8.10			
0.4267	-7.76	2	1.82	9.31	2	2.17	2.87	0.7	2.68	5.61	5	2.41	11.24			
0.4244	4.21	2	1.87	7.02	3	2.23	9.98	0.7	2.70	11.79	1	2.46	-3.30			
0.4155	3.08	2	1.87	6.53	3	2.21	10.01	0.7	2.71	8.15	2	2.47	2.48			
0.4264	0.13	2	1.86	6.71	3	2.21	9.42	0.7	2.71	6.10	3	2.47	5.99			

0.4287	-3.54	2	1.84	7.36	3	2.21	8.01	0.7	2.70	4.91	4	2.47	6.63				
0.4586	-2.55	3	1.85	12.63	1	2.16	0.59	0.7	2.72	7.49	1	2.30	9.60				
0.4467	-0.41	3	1.85	13.00	1	2.19	0.80	0.7	2.74	3.38	1	2.96	-3.00				
0.4584	-0.19	3	1.85	12.84	1	2.19	0.77	0.7	2.73	3.04	2	2.94	1.17				
0.4793	-0.55	3	1.85	12.38	1	2.18	1.22	0.7	2.73	4.41	3	2.95	8.57				
0.4624	1.36	3	1.86	10.89	2	2.19	8.09	0.7	2.76	4.53	1	2.99	-3.00				
0.4872	1.25	3	1.86	10.72	2	2.19	8.21	0.7	2.76	4.16	2	2.98	1.95				
0.5016	0.93	3	1.86	10.42	2	2.18	8.59	0.7	2.74	7.10	3	3.12	49.64				
0.4982	2.25	3	1.86	9.94	3	2.19	14.99	0.7	2.77	5.40	1	3.01	-2.70				
0.5309	1.72	3	1.85	9.75	3	2.19	15.40	0.7	2.76	5.28	2	3.01	3.11				
0.4224	-0.03	2	1.85	7.03	1	2.18	4.86	0.7	3.27	12.14	2	2.75	1.35				
0.4646	-0.52	2	1.84	6.77	1	2.18	5.91	0.7	3.28	12.41	3	2.75	4.77				
0.4228	0.15	2	1.85	7.06	1	2.18	4.75	0.5	3.28	8.45	2	2.75	1.48				
0.4645	-0.46	2	1.84	6.75	1	2.18	6.14	0.5	3.29	8.49	3	2.75	4.82				
0.4037	-1.44	2	1.84	7.45	2	2.21	5.00	0.7	2.65	6.05	2	2.78	5.12	2	2.46	0.14	
0.4061	-2.98	2	1.84	7.90	2	2.20	3.89	0.7	2.65	4.29	2	2.80	4.43	3	2.46	2.56	
0.4101	-4.09	2	1.84	7.92	2	2.19	3.25	0.7	2.65	3.12	2	2.80	2.14	4	2.45	4.99	
0.4018	-0.99	2	1.85	7.47	2	2.22	4.87	0.7	2.63	3.98	3	2.80	5.11	2	2.46	-1.30	
0.4021	-1.66	2	1.85	7.54	2	2.21	4.73	0.7	2.67	3.11	3	2.83	7.83	3	2.48	2.35	
0.4073	-3.59	2	1.84	8.27	2	2.21	3.15	0.7	2.67	1.81	3	2.83	5.39	4	2.47	3.95	
0.4095	-1.90	2	1.84	7.43	2	2.22	5.97	0.7	2.63	4.56	4	2.78	8.89	2	2.46	-1.50	
0.4083	-3.64	2	1.84	8.25	2	2.20	3.43	0.7	2.67	5.82	4	2.75	26.49	3	2.45	2.35	
0.4093	-4.57	2	1.83	8.71	2	2.19	2.91	0.7	2.68	5.61	4	2.77	33.68	4	2.44	6.20	
0.3917	2.62	2	1.86	7.24	1	2.19	4.57	0.7	2.77	5.52	1	3.01	-2.20	1	3.25	2.76	
0.3959	2.93	2	1.86	7.35	1	2.19	4.26	0.7	2.77	4.87	1	3.00	-3.00	2	3.23	13.36	
0.3944	2.64	2	1.86	7.22	1	2.19	4.41	0.7	2.75	5.09	2	3.00	4.76	1	3.28	0.00	
0.4012	3.11	2	1.86	7.22	1	2.19	4.37	0.7	2.76	4.84	2	3.00	3.26	2	3.28	6.46	
0.4119	2.96	2	1.86	7.23	1	2.19	4.15	0.7	2.75	4.41	2	2.98	2.31	3	3.28	13.79	
0.4023	2.25	2	1.86	6.96	1	2.18	4.89	0.7	2.75	6.23	3	3.01	17.20	1	3.31	-1.50	
0.4115	2.42	2	1.86	7.04	1	2.19	4.42	0.7	2.74	5.46	3	2.99	11.58	2	3.30	3.84	
0.4234	2.47	2	1.86	7.07	1	2.19	4.11	0.7	2.74	5.02	3	2.97	9.17	3	3.30	9.66	
0.4038	4.13	2	1.86	6.02	2	2.19	14.65	0.7	2.78	6.52	1	3.04	-2.50	1	3.27	1.28	
0.4122	4.21	2	1.86	6.09	2	2.18	14.57	0.7	2.78	6.58	1	3.03	-2.70	2	3.27	7.13	
0.4265	4.21	2	1.86	6.17	2	2.18	14.46	0.7	2.78	5.89	1	3.02	-3.00	3	3.27	14.95	
0.4155	3.79	2	1.86	6.00	2	2.18	15.24	0.7	2.77	6.97	2	3.06	7.37	1	3.31	-2.40	
0.4284	4.00	2	1.86	6.00	2	2.18	14.87	0.7	2.77	6.16	2	3.04	4.23	2	3.30	3.17	

0.4445	4.01	2	1.86	5.99	2	2.18	14.66	0.7	2.77	5.51	2	3.01	3.19	3	3.30	9.67
0.4194	2.87	2	1.86	5.96	2	2.19	14.89	0.7	2.75	8.12	3	2.67	126.58	1	3.32	-1.90
0.4393	2.89	2	1.86	5.99	2	2.19	14.21	0.7	2.75	7.76	3	2.68	105.22	2	3.32	3.75
Fits below place Fe scatterer at ~3.0 Å																
0.3953	0.70	2	1.85	7.15	1	2.19	4.92	0.7	3.19	24.35	1	2.75	-2.70	1	3.29	1.78
0.3996	1.20	2	1.85	7.16	1	2.19	4.87	0.7	3.10	28.90	1	2.75	-2.80	2	3.28	5.24
0.4069	1.70	2	1.85	7.17	1	2.19	4.75	0.7	3.01	24.83	1	2.75	-3.00	3	3.27	7.84
0.4025	0.29	2	1.85	6.92	1	2.18	5.77	0.7	3.08	8.34	2	2.77	3.16	2	3.29	-0.30
0.4037	0.86	2	1.85	6.96	1	2.19	5.59	0.7	3.07	6.19	2	2.78	3.40	3	3.28	1.39
0.4118	1.27	2	1.85	7.02	1	2.19	5.30	0.7	3.05	6.28	2	2.78	2.63	4	3.27	3.83
0.4237	1.49	2	1.85	7.02	1	2.18	4.95	0.7	3.02	8.17	2	2.77	1.14	5	3.26	8.07
0.4208	-1.41	2	1.84	6.69	1	2.19	7.59	0.7	3.10	5.82	3	2.76	10.62	1	3.30	-5.30
0.4081	-0.60	2	1.84	6.79	1	2.19	7.13	0.7	3.09	3.98	3	2.77	10.55	2	3.29	-2.40
0.4042	0.26	2	1.85	6.88	1	2.19	6.41	0.7	3.07	3.71	3	2.78	8.94	3	3.28	0.02
0.4094	0.65	2	1.85	6.92	1	2.19	6.06	0.7	3.06	3.60	3	2.79	8.27	4	3.27	2.09
0.4205	0.96	2	1.85	6.94	1	2.19	5.59	0.7	3.05	4.14	3	2.79	6.78	5	3.27	4.68
0.4351	1.14	2	1.85	6.95	1	2.18	5.16	0.7	3.03	5.19	3	2.79	5.08	6	3.26	8.09
0.4097	-0.74	2	1.84	6.83	1	2.19	7.67	0.7	3.08	2.48	4	2.77	16.76	3	3.28	-0.90
0.4119	-0.04	2	1.84	6.86	1	2.19	6.94	0.7	3.07	2.59	4	2.79	13.88	4	3.27	1.23
0.4214	0.29	2	1.85	6.87	1	2.19	6.57	0.7	3.06	2.83	4	2.79	12.69	5	3.27	3.23
0.4351	0.55	2	1.85	6.87	1	2.19	6.09	0.7	3.05	3.41	4	2.79	10.83	6	3.27	5.67
Fits below place Fe scatterer at ~3.2 Å																
0.3917	0.97	2	1.85	7.15	1	2.19	4.76	0.7	3.27	11.70	1	2.75	-2.90	1	3.08	26.73
0.3929	1.15	2	1.85	7.16	1	2.19	4.94	0.7	3.27	12.08	1	2.75	-2.90	2	3.10	71.75
0.4097	0.25	2	1.85	6.92	1	2.18	5.34	0.7	3.27	8.95	2	2.76	1.75	1	3.06	3.86
0.4105	0.70	2	1.85	6.96	1	2.18	5.14	0.7	3.30	9.44	2	2.76	1.48	2	3.11	15.10
0.3849	-2.11	2	1.85	8.24	1	2.38	18.43	0.7	3.25	12.31	3	2.73	4.17	1	2.18	-0.50
0.4365	-0.07	2	1.84	6.78	1	2.18	5.79	0.7	3.29	6.68	3	2.76	5.69	2	3.09	5.39
0.4393	0.31	2	1.85	6.80	1	2.18	5.66	0.7	3.31	7.74	3	2.76	5.15	3	3.12	12.96
0.449	-1.50	2	1.84	6.46	1	2.19	8.19	0.7	3.24	6.23	4	2.75	14.85	1	3.06	-4.00
0.4597	-0.97	2	1.84	6.58	1	2.18	7.41	0.7	3.27	5.04	4	2.75	11.71	2	3.09	0.87
0.4636	-0.42	2	1.84	6.64	1	2.18	6.69	0.7	3.30	5.53	4	2.76	9.96	3	3.12	6.96
0.4687	-0.13	2	1.84	6.68	1	2.18	6.72	0.7	3.32	6.72	4	2.75	9.01	4	3.14	12.54
Fits below replace Fe scatterer with light atoms																
0.3983	0.90	2	1.85	7.29	1	2.19	4.58	1	2.75	-2.80	2	2.60	103.39	2	3.27	6.80
0.4197	1.29	2	1.85	6.86	1	2.18	5.45	2	2.76	1.74	2	3.10	12.08	2	3.31	2.86

0.4106	0.83	2	1.85	6.83	1	2.18	5.92	2	2.76	2.95	1	3.11	1.85	1	3.30	-2.90
0.4116	1.21	2	1.85	6.89	1	2.18	5.63	2	2.76	2.19	1	3.07	1.67	2	3.28	2.28
0.417	1.47	2	1.85	6.94	1	2.18	5.36	2	2.76	1.61	2	3.03	1.60	3	3.28	7.13
0.4255	1.59	2	1.85	6.98	1	2.18	5.16	2	2.76	0.98	1	3.01	1.37	4	3.27	11.74
0.4145	1.12	2	1.85	6.88	1	2.18	5.59	2	2.75	2.18	2	3.15	13.70	1	3.31	-1.10
0.4197	1.27	2	1.85	6.89	1	2.18	5.47	2	2.76	1.74	2	3.10	11.92	2	3.31	2.80
0.4275	1.44	2	1.85	6.89	1	2.18	5.33	2	2.76	1.30	2	3.06	11.89	3	3.30	6.47
0.4376	1.40	2	1.85	6.89	1	2.18	5.11	2	2.75	1.00	2	3.02	11.29	4	3.29	10.19
0.4286	0.12	2	1.84	6.55	1	2.18	7.57	3	2.75	9.41	1	3.11	-3.20	1	3.29	-5.00
0.4325	0.70	2	1.85	6.63	1	2.18	6.98	3	2.76	7.63	1	3.06	-2.80	3	3.27	3.98
0.4404	0.94	2	1.85	6.71	1	2.18	6.45	3	2.77	6.42	1	3.05	-2.00	4	3.27	8.31
0.4354	0.24	2	1.84	6.56	1	2.18	7.39	3	2.75	8.06	2	3.13	3.54	1	3.31	-4.40
0.4459	0.78	2	1.85	6.66	1	2.18	6.50	3	2.76	6.11	2	3.08	3.35	3	3.30	3.15
0.4557	0.88	2	1.85	6.70	1	2.18	6.16	3	2.76	5.25	2	3.06	3.98	4	3.29	6.68
0.444	0.47	2	1.85	6.62	1	2.18	6.79	3	2.75	6.49	3	3.16	11.88	1	3.33	-2.70
0.4508	0.64	2	1.85	6.65	1	2.18	6.43	3	2.75	5.88	3	3.12	10.12	2	3.32	0.91
0.4596	0.80	2	1.85	6.66	1	2.18	6.13	3	2.75	5.27	3	3.10	9.98	3	3.32	3.97
0.4703	0.82	2	1.85	6.71	1	2.18	5.92	3	2.75	4.59	3	3.08	10.98	4	3.31	7.33
0.4424	-1.20	2	1.84	6.51	1	2.20	9.56	4	2.72	18.42	1	3.10	-6.00	1	3.27	-6.80
0.4512	-0.90	2	1.84	6.47	1	2.20	9.69	4	2.73	16.33	2	3.13	-0.50	1	3.30	-6.20
0.4544	-0.40	2	1.84	6.48	1	2.19	9.26	4	2.74	14.63	2	3.11	-0.70	2	3.29	-2.30
0.472	0.17	2	1.84	6.51	1	2.18	7.96	4	2.75	10.96	2	3.08	0.65	4	3.28	4.32
0.4889	0.15	2	1.84	6.51	1	2.18	7.55	4	2.75	9.40	3	3.09	5.02	4	3.31	4.38

Table S10: EXAFS fitting results for the Fe site in the 4/4 intermediate

		Component 1			Component 2			Component 3			Component 4			Component 5			Component 6		
F	E_0	N	R	σ^2	N	R	σ^2	N	R	σ^2	N	R	σ^2	N	R	σ^2	N	R	σ^2
0.8788	4.00	1	1.99	9.34															
0.8223	4.00	2	2.01	12.61															
0.8304	4.00	3	2.05	23.77															
0.7883	1.45	1	1.83	5.63	1	2.02	1.58												
0.7434	1.81	1	1.80	3.95	2	2.01	6.13												
0.7265	2.04	1	1.78	3.77	3	2.00	10.43												
0.7616	-0.32	2	1.85	12.44	1	2.03	2.11												
0.74	-0.18	2	1.82	9.68	2	2.03	5.49												
0.7384	-0.30	2	1.80	8.68	3	2.02	8.67												
0.7517	-0.08	2	1.78	8.84	4	2.01	12.17												
0.7514	-0.98	3	1.86	18.24	1	2.04	3.15												
0.7464	-1.74	3	1.83	14.60	2	2.03	6.03												
0.7552	-1.97	3	1.81	13.19	3	2.03	8.77												
0.7744	-2.31	3	1.79	13.03	4	2.01	11.86												
0.7091	-3.51	3	1.77	12.44	4	2.00	11.45	1	2.75	4.39									
0.6847	-3.00	3	1.80	12.60	3	2.01	8.45	1	2.75	4.43									
0.6722	-2.53	3	1.82	14.00	2	2.03	5.74	1	2.75	4.46									
0.6796	-2.46	3	1.85	16.80	1	2.03	2.55	1	2.75	4.48									
0.6889	-1.74	2	1.77	8.20	4	1.99	11.76	1	2.75	4.55									
0.6706	-1.24	2	1.79	8.40	3	2.01	8.57	1	2.75	4.59									
0.6696	-1.15	2	1.81	9.26	2	2.02	5.40	1	2.75	4.60									
0.6914	-1.64	2	1.84	11.45	1	2.02	1.85	1	2.75	4.51									
0.676	0.06	1	1.76	3.95	4	1.98	14.52	1	2.76	4.61									
0.6666	0.64	1	1.77	3.68	3	1.99	10.47	1	2.76	4.69									
0.682	0.94	1	1.80	3.94	2	2.00	6.28	1	2.76	4.73									
0.7279	0.24	1	1.82	5.50	1	2.01	1.86	1	2.76	4.65									
0.5851	-0.18	2	1.82	10.16	2	2.02	5.91	1	2.76	5.06	1	2.98	-1.10						
0.5597	0.88	2	1.83	10.70	2	2.03	6.05	1	2.77	4.43	2	2.98	1.13						
0.5476	1.42	2	1.83	10.85	2	2.03	6.05	1	2.77	4.03	3	2.99	2.70						
0.546	1.67	2	1.83	10.88	2	2.03	6.00	1	2.77	3.72	4	2.99	3.96						
0.5532	1.76	2	1.83	10.83	2	2.03	5.95	1	2.77	3.51	5	2.98	5.16						

0.5676	0.17	2	1.83	10.72	2	2.03	5.90	1	2.77	3.36	6	2.98	6.28
0.5876	1.65	2	1.83	10.45	2	2.03	5.76	1	2.76	3.28	7	2.98	7.47
0.5829	-0.63	2	1.79	8.75	3	2.01	8.77	1	2.76	5.06	1	2.98	-1.20
0.5594	-0.01	2	1.80	8.98	3	2.01	8.78	1	2.77	4.48	2	2.98	1.03
0.5496	0.51	2	1.80	9.16	3	2.02	8.80	1	2.77	4.07	3	2.99	2.59
0.5505	0.75	2	1.80	9.19	3	2.02	8.69	1	2.77	3.76	4	2.99	3.82
0.5599	1.08	2	1.80	9.13	3	2.02	8.64	1	2.77	3.59	5	2.99	5.02
0.5763	0.82	2	1.80	8.88	3	2.02	8.52	1	2.76	3.37	6	2.98	6.19
0.6023	-1.31	2	1.77	8.50	4	2.00	11.93	1	2.76	5.07	1	2.98	-1.20
0.5814	-0.85	2	1.77	8.58	4	2.00	11.86	1	2.76	4.50	2	2.98	0.93
0.5738	-0.38	2	1.78	8.72	4	2.00	11.86	1	2.76	4.07	3	2.98	2.52
0.5767	-0.22	2	1.78	8.70	4	2.00	11.78	1	2.76	3.77	4	2.98	3.75
0.5876	-0.13	2	1.78	8.70	4	2.00	11.75	1	2.76	3.54	5	2.98	4.88
0.5884	-1.55	3	1.83	15.01	2	2.03	6.42	1	2.76	4.99	1	2.98	-1.20
0.5999	-1.88	3	1.80	13.16	3	2.02	8.75	1	2.76	4.97	1	2.98	-1.10
0.626	-2.55	3	1.78	12.35	4	2.01	11.27	1	2.76	4.98	1	2.98	-1.20
0.6007	-1.84	3	1.78	13.02	4	2.01	11.55	1	2.76	4.04	3	2.98	2.51
0.5709	-1.01	3	1.81	13.67	3	2.03	8.84	1	2.76	4.03	3	2.98	2.56
0.6541	2.07	1	1.84	7.05	1	2.02	2.59	1	2.77	5.08	1	2.99	-0.90
0.6272	3.28	1	1.86	8.14	1	2.03	2.85	1	2.77	4.45	2	2.99	1.28
0.6113	3.56	1	1.86	8.12	1	2.03	2.80	1	2.77	4.05	3	2.99	2.92
0.6056	3.56	1	1.86	7.93	1	2.03	2.72	1	2.77	3.77	4	2.99	4.18
0.6089	3.45	1	1.85	7.59	1	2.03	2.60	1	2.77	3.56	5	2.99	5.39
0.6196	3.27	1	1.85	7.21	1	2.03	2.37	1	2.77	3.42	6	2.98	6.69
0.6359	3.11	1	1.85	7.08	1	2.03	2.39	1	2.77	3.37	7	2.99	7.90
0.5945	1.62	1	1.80	4.36	2	2.00	6.54	1	2.77	5.23	1	2.99	-1.10
0.5673	2.33	1	1.80	4.59	2	2.01	6.53	1	2.77	4.57	2	2.99	1.15
0.5532	2.77	1	1.80	4.75	2	2.01	6.54	1	2.77	4.14	3	2.99	2.72
0.5499	2.94	1	1.80	4.76	2	2.01	6.48	1	2.77	3.81	4	2.99	4.04
0.556	2.92	1	1.80	4.68	2	2.01	6.44	1	2.77	3.59	5	2.99	5.23
0.5699	2.79	1	1.80	4.72	2	2.01	6.43	1	2.77	3.41	6	2.99	6.36
0.5726	1.08	1	1.77	3.76	3	1.99	10.51	1	2.77	5.27	1	2.99	-1.30
0.5464	1.77	1	1.78	3.92	3	1.99	10.49	1	2.77	4.60	2	2.99	0.97
0.5347	2.13	1	1.78	3.99	3	1.99	10.45	1	2.77	4.15	3	2.99	2.55
0.5344	2.22	1	1.78	4.00	3	1.99	10.42	1	2.77	3.84	4	2.99	3.83
0.5434	2.29	1	1.78	4.00	3	1.99	10.39	1	2.77	3.60	5	2.99	5.02

0.56	2.19	1	1.78	3.95	3	1.99	10.36	1	2.77	3.43	6	2.99	6.15			
Fits below have Mn scatterer placed at ~3.0 Å																
0.6014	-1.60	2	1.78	8.40	3	2.00	9.20	1	2.98	10.04	3	2.75	1.33			
0.6351	-1.90	2	1.78	8.14	3	2.00	9.13	1	2.99	7.23	4	2.76	2.74			
0.6688	-1.90	2	1.78	8.17	3	1.99	9.13	1	2.99	4.86	5	2.77	4.34			
0.5883	0.05	1	1.78	3.91	2	1.99	7.12	1	2.98	10.23	3	2.76	1.34			
0.6146	-0.33	1	1.78	3.62	2	1.98	7.03	1	2.99	7.62	4	2.76	2.73			
0.6431	-0.41	1	1.78	3.47	2	1.98	6.92	1	3.00	5.60	5	2.77	4.45			
0.5476	-0.82	2	1.82	9.86	2	2.02	5.93	1	2.76	5.02	1	2.98	-2.60	1	3.33	-1.20
0.5274	0.53	2	1.83	10.49	2	2.03	6.03	1	2.77	4.29	2	2.98	0.00	1	3.34	-0.70
0.5383	-0.26	2	1.82	10.01	2	2.02	5.85	1	2.76	4.27	2	2.98	0.74	2	3.35	3.65
0.5507	-0.88	2	1.81	9.68	2	2.02	5.76	1	2.76	4.29	2	2.98	1.22	3	3.35	8.28
0.5566	-0.71	2	1.81	9.78	2	2.02	5.78	1	2.76	4.42	2	2.98	1.22	4	3.41	25.74
0.5192	1.27	2	1.83	10.77	2	2.03	6.04	1	2.77	3.84	3	2.98	1.82	1	3.35	0.04
0.5269	0.86	2	1.83	10.43	2	2.03	5.91	1	2.77	3.87	3	2.98	2.55	2	3.35	4.77
0.5359	0.25	2	1.82	10.19	2	2.03	5.85	1	2.76	3.92	3	2.98	2.90	3	3.36	11.17
0.5203	1.68	2	1.83	10.88	2	2.04	6.02	1	2.77	3.54	4	2.98	3.37	1	3.53	0.79
0.5241	1.39	2	1.83	10.69	2	2.03	5.96	1	2.77	3.60	4	2.98	3.97	2	3.36	5.69
0.529	0.97	2	1.83	10.59	2	2.03	5.92	1	2.76	3.66	4	2.98	4.26	3	3.36	12.32
0.5268	-0.31	2	1.79	8.79	3	2.01	8.71	1	2.77	4.33	2	2.98	0.00	1	3.34	-0.40
0.5375	-0.87	2	1.79	8.50	3	2.01	8.64	1	2.76	4.33	2	2.98	0.66	2	3.34	3.98
0.5508	-1.62	2	1.79	8.14	3	2.00	8.54	1	2.76	1.06	2	2.98	1.06	3	3.35	9.16
0.5557	-1.45	2	1.79	8.44	3	2.00	8.70	1	2.76	4.46	2	2.98	1.09	4	3.40	25.23
0.5212	0.30	2	1.80	9.11	3	2.01	8.81	1	2.79	3.87	3	2.99	1.71	1	3.35	0.04
0.5284	-0.14	2	1.79	8.89	3	2.01	8.75	1	2.76	3.90	3	2.98	2.40	2	3.35	4.72
0.5367	-0.57	2	1.79	8.68	3	2.01	8.67	1	2.76	3.96	3	2.98	2.78	3	3.36	11.39
0.525	0.90	2	1.80	9.25	3	2.02	8.79	1	2.77	3.58	4	2.98	3.28	1	3.35	0.90
0.5283	0.30	2	1.80	8.88	3	2.01	8.65	1	2.76	3.62	4	2.98	3.95	2	3.35	6.35
0.5315	0.12	2	1.80	8.88	3	2.01	8.67	1	2.76	3.72	4	2.99	4.11	3	3.35	14.23
0.5364	0.99	2	1.80	9.18	3	2.02	8.70	1	2.77	3.38	5	2.98	4.67	1	3.53	1.79
0.5347	0.70	2	1.80	9.03	3	2.02	8.66	1	2.76	3.46	5	2.98	5.26	2	3.35	7.85
0.5333	0.50	2	1.80	9.00	3	2.01	8.66	1	2.76	3.55	5	2.99	5.26	3	3.34	16.37
0.5535	0.93	2	1.80	9.04	3	2.02	8.61	1	2.76	3.24	6	2.98	6.04	1	3.35	2.91
0.5463	0.81	2	1.80	9.05	3	2.02	8.63	1	2.76	3.36	6	2.99	6.56	2	3.33	9.64
0.5498	-1.13	2	1.77	8.30	4	2.00	11.72	1	2.77	4.41	2	2.98	-0.10	1	3.34	-0.50
0.5588	-1.29	2	1.77	8.50	4	2.00	11.94	1	2.76	4.31	2	2.98	0.55	2	3.34	3.87

0.5704	-1.72	2	1.77	8.06	4	1.99	11.64	1	2.76	4.42	2	2.98	0.93	3	3.35	8.54
0.5781	-2.24	2	1.77	8.24	4	1.99	11.89	1	2.76	4.42	2	2.98	1.03	4	3.37	22.20
0.5461	-0.42	2	1.78	8.72	4	2.00	11.88	1	2.77	3.90	3	2.98	1.62	1	3.34	0.04
0.5533	-0.94	2	1.77	8.28	4	2.00	11.66	1	2.76	3.90	3	2.98	2.44	2	3.35	5.38
0.5605	-1.30	2	1.77	8.32	4	1.99	11.72	1	2.76	3.96	3	2.98	2.73	3	3.35	11.44
0.5525	-0.21	2	1.78	8.75	4	2.00	11.84	1	2.77	3.58	4	2.98	3.15	1	3.35	0.86
0.5548	-0.47	2	1.78	8.39	4	2.00	11.63	1	2.76	3.68	4	2.98	3.83	2	3.35	6.54
0.5568	-0.72	2	1.77	8.62	4	2.00	11.84	1	2.76	3.73	4	2.99	3.98	3	3.34	15.19
0.5611	0.78	1	1.79	4.24	2	2.00	6.69	1	2.77	5.24	1	2.99	-2.60	1	3.34	-1.10
0.573	-0.08	1	1.79	3.90	2	1.99	6.65	1	2.76	5.13	1	2.99	-1.80	2	3.34	3.05
0.5873	-0.76	1	1.78	3.63	2	1.98	6.60	1	2.76	5.05	1	2.99	-1.30	3	3.35	7.14
0.5388	2.15	1	1.80	4.69	2	2.01	6.67	1	2.77	4.43	2	2.99	0.08	1	3.35	-0.30
0.5496	1.51	1	1.80	4.45	2	2.00	6.63	1	2.77	4.40	2	2.99	0.78	2	3.36	3.95
0.5619	1.00	1	1.79	4.18	2	2.00	6.56	1	2.77	4.42	2	2.99	1.23	3	3.37	9.66
0.5276	2.81	1	1.80	4.88	2	2.01	6.60	1	2.77	3.96	3	2.99	1.94	1	3.36	0.30
0.5355	2.42	1	1.80	4.69	2	2.01	6.57	1	2.77	3.97	3	2.99	2.59	2	3.36	4.97
0.5445	2.13	1	1.80	4.50	2	2.00	6.51	1	2.77	4.06	3	2.99	2.87	3	3.38	13.32
0.526	3.09	1	1.81	4.90	2	2.01	6.55	1	2.77	3.65	4	2.99	3.49	1	3.36	1.05
0.53	2.93	1	1.80	4.76	2	2.01	6.50	1	2.77	3.71	4	2.99	4.08	2	3.37	6.25
0.535	2.75	1	1.80	4.69	2	2.01	6.48	1	2.77	3.79	4	2.99	4.22	3	3.38	15.37
0.5329	2.97	1	1.80	4.76	2	2.01	6.47	1	2.77	3.44	5	2.99	4.87	1	3.36	1.83
0.5321	3.10	1	1.80	4.76	2	2.01	6.47	1	2.77	3.53	5	2.99	5.44	2	3.36	7.53
0.5329	3.09	1	1.80	4.77	2	2.01	6.46	1	2.77	3.61	5	2.99	5.44	3	3.36	16.63
0.5158	1.46	1	1.77	3.99	3	1.99	10.62	1	2.77	4.49	2	2.99	-0.10	1	3.35	-0.50
0.5272	1.01	1	1.77	3.77	3	1.99	10.51	1	2.77	4.47	2	2.99	0.67	2	2.26	4.24
0.5403	0.40	1	1.77	3.68	3	1.98	10.57	1	2.77	4.46	2	2.99	1.02	3	3.37	9.43
0.5446	0.68	1	1.77	3.70	3	1.98	1.05	1	2.77	4.59	2	2.99	0.97	4	3.44	32.42
0.5076	2.09	1	1.78	4.07	3	1.99	10.53	1	2.77	4.01	3	2.99	1.78	1	3.36	0.31
0.5155	1.63	1	1.78	3.90	3	1.99	10.48	1	2.77	4.01	3	2.99	2.42	2	3.36	4.99
0.5241	1.30	1	1.77	3.84	3	1.99	10.50	1	2.77	4.07	3	2.99	2.68	3	3.37	12.49
0.5096	2.35	1	1.78	4.13	3	2.00	10.50	1	2.77	3.68	4	2.99	3.30	1	3.36	1.05
0.513	2.12	1	1.78	4.02	3	1.99	10.47	1	2.77	3.73	4	2.99	3.89	2	3.36	6.37
0.5169	1.90	1	1.78	3.95	3	1.99	10.45	1	2.77	3.81	4	2.99	4.01	3	3.37	16.11
0.5581	-1.55	3	1.86	17.77	1	2.04	3.56	1	2.76	4.88	1	2.98	-2.70	1	3.32	-1.50
0.5386	-0.06	3	1.87	18.45	1	2.05	3.74	1	2.77	4.18	2	2.98	-0.10	1	3.34	-0.80

Fits below have Mn scatterer placed at ~3.0 Å

0.581	-1.27	2	1.79	8.85	3	2.00	9.44	1	2.97	8.84	3	2.75	1.15	2	3.06	16.17			
0.5851	-1.56	2	1.78	8.67	3	2.00	9.40	1	2.94	8.19	3	2.75	0.96	1	3.04	2.69			
0.5467	-0.98	2	1.79	9.14	3	2.01	9.63	1	2.92	5.56	2	2.74	-2.10	1	3.06	-2.70			
0.5572	-1.92	2	1.78	8.37	3	2.00	9.17	1	2.99	21.10	2	2.74	-0.60	1	3.31	0.61			
0.5603	-2.30	2	1.78	8.26	3	2.00	9.18	1	3.08	23.55	2	2.74	-0.40	2	3.30	3.50			
0.5671	-2.72	2	1.78	8.38	3	2.00	9.49	1	3.12	20.32	2	2.74	-0.30	3	3.30	5.14			
0.5788	-3.26	2	1.78	8.45	3	1.99	9.52	1	3.14	18.10	2	2.74	-0.30	4	3.31	6.82			
0.595	-2.18	2	1.78	8.30	3	2.00	9.37	1	2.97	13.98	3	2.74	0.86	1	3.31	1.83			
0.5979	-2.87	2	1.78	7.89	3	1.99	9.47	1	3.01	11.78	3	2.75	1.34	2	3.26	7.17			
0.5773	-1.42	2	1.79	8.76	3	2.00	9.39	1	2.97	8.79	3	2.75	1.22	3	3.09	24.04			
0.5735	-1.04	2	1.79	9.06	3	2.00	9.61	1	3.00	0.00	4	2.80	1.19	1	3.11	-4.20			
0.5451	-0.66	2	1.79	9.25	3	2.01	9.65	1	2.99	-1.10	4	2.80	0.76	2	3.09	-2.60			
0.5311	0.18	2	1.80	9.72	3	2.01	9.83	1	2.98	-2.40	4	2.81	-0.60	3	3.08	-2.20			
0.5672	4.00	2	1.88	20.11	4	2.08	26.72	1	3.08	3.42	1	2.48	-1.70	1	3.22	-1.30			
0.5931	4.00	2	1.89	20.17	4	2.10	26.56	1	3.08	2.69	2	2.48	0.37	1	3.22	-2.10			
0.6052	4.00	2	1.89	19.64	4	2.10	24.85	1	3.09	2.00	2	2.47	0.55	2	3.21	-0.80			
0.5818	-6.61	2	1.76	11.27	4	1.98	18.91	1	3.03	2.01	2	2.44	1.82	3	3.17	2.46			
Fits below have Mn scatterer replaced by light atoms																			
0.54	-0.78	2	1.79	9.26	3	2.01	9.55	1	2.74	-2.80	3	3.07	26.49	2	3.32	2.27			
0.5032	-6.06	2	1.77	9.67	3	1.99	12.74	2	2.73	-0.40	3	2.46	7.32	2	3.30	2.87			
0.5271	-6.45	2	1.76	9.70	3	1.97	12.92	3	2.73	1.17	3	2.47	5.85	2	3.30	3.29			
0.492	-5.98	2	1.78	9.16	2	1.99	7.75	3	2.72	1.14	3	2.48	5.19	1	3.30	0.29			
0.4992	-6.37	2	1.78	9.17	2	1.99	7.95	3	2.72	1.31	3	2.48	5.25	2	3.30	3.26			
0.5144	-6.58	2	1.78	8.82	2	1.99	7.61	3	2.72	1.51	3	2.47	5.55	3	3.30	6.22			
0.514	-5.83	2	1.78	9.03	2	1.99	7.68	4	2.72	2.61	3	2.48	4.23	1	3.30	0.86			
0.5199	-5.78	2	1.78	8.32	2	1.99	7.02	4	2.72	2.87	3	2.48	4.31	2	3.30	3.69			
0.5428	-7.68	2	1.77	8.55	2	1.98	8.06	4	2.72	2.59	4	2.47	6.25	3	3.29	6.31			
0.5269	-7.10	2	1.77	8.24	2	1.98	7.59	4	2.72	2.41	4	2.47	6.35	2	3.29	4.07			
0.5225	-7.24	2	1.77	8.56	2	1.98	7.80	4	2.72	2.40	4	2.48	6.01	1	3.29	0.96			
0.5385	-5.85	2	1.78	8.99	2	1.98	7.43	4	2.72	3.65	2	2.48	1.94	3	3.30	6.03			
0.5242	-5.62	2	1.78	9.00	2	1.98	7.34	4	2.72	3.54	2	2.48	1.76	2	3.29	3.56			
0.5146	-4.98	2	1.78	9.02	2	1.99	7.18	4	2.72	3.57	2	2.48	1.63	1	3.29	0.73			
0.4703	-2.01	2	1.81	9.72	2	2.01	6.37	1	2.75	6.80	2	3.00	0.88	1	3.34	0.90	1	2.48	-0.20
0.4694	-4.04	2	1.79	9.28	2	2.00	6.63	1	2.74	5.35	2	2.99	1.15	1	3.33	1.00	2	2.48	3.32
0.4712	-5.18	2	1.79	9.14	2	2.00	6.93	1	2.74	4.51	2	2.98	0.92	1	3.33	0.90	3	2.49	6.74
0.4744	-6.21	2	1.78	8.99	2	1.99	7.16	1	2.74	4.25	2	2.97	0.66	1	3.32	0.67	4	2.48	9.68

0.4754	-2.30	2	1.81	9.40	2	2.01	6.20	1	2.75	6.81	2	3.00	1.61	2	3.34	5.59	1	2.48	-0.30
0.474	-4.48	2	1.79	9.04	2	2.00	6.52	1	2.74	5.47	2	2.99	1.99	2	3.33	5.79	2	2.48	2.96
0.4769	-5.39	2	1.79	9.00	2	2.00	6.75	1	2.74	4.56	2	2.98	1.73	2	3.33	5.74	3	2.48	6.38
0.4831	-2.92	2	1.80	9.17	2	2.01	6.16	1	2.75	6.98	2	3.01	1.85	3	3.34	10.67	1	2.48	-0.40
0.4806	-4.52	2	1.79	9.02	2	2.00	6.42	1	2.74	5.25	2	2.99	2.49	3	3.34	10.68	2	2.48	3.06
0.4854	-6.33	2	1.78	8.67	2	1.99	6.82	1	2.73	4.80	2	2.98	2.10	3	3.32	11.35	3	2.48	5.57
0.469	-0.90	2	1.82	10.12	2	2.02	6.33	1	2.75	5.64	3	2.99	3.31	1	3.34	1.74	1	2.49	0.12
0.4674	-3.14	2	1.80	9.39	2	2.01	6.38	1	2.74	4.35	3	2.98	3.44	1	3.33	1.77	2	2.49	3.85
0.4687	-4.36	2	1.79	9.22	2	2.00	6.65	1	2.74	3.86	3	2.97	3.01	1	3.33	1.78	3	2.49	7.30
0.4819	-1.32	2	1.79	9.15	3	2.01	9.66	1	2.76	5.60	3	3.00	3.38	2	3.34	6.28	1	2.48	0.39
0.4867	-2.65	2	1.79	9.35	3	2.01	10.53	1	2.75	4.88	3	2.99	3.21	2	3.34	6.65	2	2.48	4.11
0.4719	-1.57	2	1.81	9.80	2	2.02	6.25	1	2.75	5.78	3	3.00	4.07	2	3.34	6.42	1	2.49	0.00
0.47	-3.50	2	1.80	9.30	2	2.00	6.42	1	2.74	4.65	3	2.98	4.24	2	3.33	7.04	2	2.49	3.37
0.4734	-5.08	2	1.79	8.94	2	1.99	6.65	1	2.74	4.05	3	2.98	3.74	2	3.32	6.86	3	2.49	6.52
0.4771	-5.77	2	1.78	8.80	2	1.99	6.91	1	2.74	3.84	3	2.98	3.66	2	3.32	7.50	4	2.49	8.90
0.4774	-2.07	2	1.81	9.54	2	2.01	6.18	1	2.75	5.94	3	3.00	4.16	3	3.34	11.72	1	2.48	-0.10
0.4753	-4.05	2	1.79	9.09	2	2.00	6.40	1	2.74	4.90	3	2.99	4.26	3	3.33	12.54	2	2.49	3.13
0.4785	-5.42	2	1.78	8.85	2	1.99	6.66	1	2.74	4.16	3	2.98	3.87	3	3.33	14.29	3	2.49	6.26
0.479	-1.08	2	1.79	9.42	3	2.01	9.78	1	2.76	5.64	3	3.00	2.67	1	3.34	1.59	1	2.48	0.44
0.4706	-0.09	2	1.82	10.45	2	2.03	6.36	1	2.75	5.03	4	2.99	5.51	1	3.34	2.48	1	2.49	0.20
0.467	-2.05	2	1.81	9.78	2	2.01	6.36	1	2.74	3.84	4	2.97	5.42	1	3.33	2.71	2	2.50	4.00
0.4683	-3.43	2	1.80	9.42	2	2.00	6.51	1	2.75	3.39	4	2.97	4.87	1	3.33	2.67	3	2.51	7.57
0.4699	-4.17	2	1.79	9.55	2	2.01	6.87	1	2.75	3.33	4	2.97	4.31	1	3.32	2.18	4	2.50	11.40
0.47	-0.52	2	1.82	10.24	2	2.02	6.31	1	2.75	5.22	4	2.99	6.07	2	3.34	7.17	1	2.49	0.09
0.4676	-2.69	2	1.80	9.49	2	2.01	6.32	1	2.74	4.10	4	2.98	6.17	2	3.33	7.31	2	2.50	3.50
0.4703	-4.04	2	1.79	9.18	2	2.00	6.49	1	2.74	3.55	4	2.97	5.71	2	3.32	7.55	3	2.50	6.78
0.4737	-5.01	2	1.79	9.05	2	2.00	6.75	1	2.74	3.45	4	2.97	5.16	2	3.32	8.45	4	2.50	10.05
0.4736	-1.08	2	1.81	9.93	2	2.02	6.24	1	2.75	5.62	4	3.00	5.61	3	3.34	13.03	1	2.49	0.00
0.4712	-3.21	2	1.80	9.27	2	2.00	6.28	1	2.74	4.18	4	2.98	6.29	3	3.33	12.46	2	2.50	3.46
0.4735	-4.10	2	1.79	9.13	2	2.00	6.43	1	2.74	3.46	4	2.97	5.46	3	3.33	12.64	3	2.50	7.53
0.4759	0.15	2	1.82	10.43	2	2.03	6.27	1	2.75	4.69	5	2.98	7.70	1	3.33	2.78	1	2.50	0.05
0.4704	-1.50	2	1.81	9.88	2	2.02	6.29	1	2.74	3.51	5	2.97	7.29	1	3.33	3.25	2	2.51	3.86
0.471	-2.69	2	1.80	9.60	2	2.01	6.41	1	2.75	3.19	5	2.97	6.70	1	3.33	3.46	3	2.51	7.23
0.473	-3.77	2	1.80	9.42	2	2.01	6.64	1	2.75	3.09	5	2.97	6.31	1	3.32	3.93	4	2.51	10.71
0.4718	-0.12	2	1.82	10.35	2	2.03	6.30	1	2.75	4.92	5	2.99	8.24	2	3.33	7.14	1	2.50	0.00
0.4685	-2.30	2	1.80	9.54	2	2.01	6.26	1	2.74	3.81	5	2.97	8.38	2	3.32	7.49	2	2.50	3.27

0.471	-3.57	2	1.79	9.27	2	2.00	6.44	1	2.74	3.39	5	2.97	7.63	2	3.32	8.24	3	2.51	6.37
0.4731	-4.33	2	1.79	9.35	2	2.00	6.78	1	2.74	3.21	5	2.97	6.60	2	3.31	9.11	4	2.50	10.26
0.4715	-1.94	2	1.80	9.64	2	2.01	6.25	1	2.74	3.81	6	2.97	10.79	2	3.32	7.22	2	2.51	2.79
0.4771	-1.58	2	1.81	9.78	2	2.01	6.26	1	2.74	3.63	6	2.96	10.26	1	3.32	3.36	2	2.51	2.74
Fits below have Mn scatterer placed at ~2.5 Å																			
0.4812	-2.82	2	1.80	9.97	2	2.01	7.55	1	2.49	11.73	3	4.80	5.65	1	3.30	-0.70	2	2.73	-0.90
0.4668	-6.12	2	1.79	9.02	2	2.00	6.48	1	2.50	8.30	4	2.36	21.23	2	3.29	2.71	4	2.72	1.66
0.469	-5.62	2	1.79	9.02	2	2.00	6.52	1	2.50	8.04	3	2.35	17.77	2	3.29	2.67	4	2.72	1.67
0.4702	-4.58	2	1.79	9.01	2	2.00	6.37	1	2.50	7.92	2	2.34	17.23	2	3.29	2.84	4	2.72	1.75
0.4741	-3.94	2	1.79	8.99	2	2.00	6.44	1	2.49	7.55	1	2.32	10.00	2	3.29	2.86	4	2.73	1.80
Fits below have Mn scatterer placed at ~3.0 Å																			
0.4892	-4.18	2	1.79	9.52	2	2.00	7.54	1	3.01	5.64	4	2.75	4.67	2	3.15	10.10	2	2.47	2.42
0.4995	-4.24	2	1.79	9.44	2	2.00	7.41	1	3.01	5.79	4	2.75	5.79	1	3.16	5.79	2	2.47	2.38
0.4851	-5.54	2	1.78	9.01	2	1.99	7.32	1	3.02	5.60	3	2.74	3.73	3	3.18	9.88	2	2.46	2.39
Fits below have Mn scatterer replaced with light atoms																			
0.477	-4.79	2	1.80	9.78	2	2.01	7.74	1	2.73	-2.90	4	2.47	87.83	1	3.30	-0.90	2	2.46	5.88
0.4715	-5.86	2	1.80	8.97	2	2.00	6.35	3	2.72	1.57	4	2.33	29.36	1	3.29	0.16	2	2.49	2.72
0.478	-6.34	2	1.80	9.16	2	2.00	6.53	3	2.72	1.65	4	2.33	26.92	2	3.29	2.94	2	2.48	2.90
0.4795	-2.95	2	1.80	9.76	2	2.01	7.28	3	2.73	1.88	4	3.07	15.82	2	3.30	3.19	2	2.48	2.69
0.4778	-3.12	2	1.80	9.73	2	2.01	7.30	3	2.73	2.01	3	3.06	11.00	2	3.30	3.72	2	2.48	2.66
0.4781	-3.33	2	1.80	9.68	2	2.01	7.34	3	2.73	2.04	2	3.05	7.40	2	3.30	4.24	2	2.48	2.68

Literature Cited

(1) Jiang, W.; Yun, D.; Saleh, L.; Barr, E. W.; Xing, G.; Hoffart, L. M.; Maslak, M.-A.; Krebs, C.; Bollinger, J. M., Jr. *Science* **2007**, *316*, 1188–1191.
(2) Dassama, L. M. K.; Yosca, T. H.; Conner, D. A.; Lee, M. H.; Blanc, B.; Streit, B. R.; Green, M. T.; DuBois, J. L.; Krebs, C.; Bollinger, J. M., Jr. *Biochemistry* **2012**, *51*, 1607–1616.
(3) Price, J. C.; Barr, E. W.; Tirupati, B.; Bollinger, J. M., Jr.; Krebs, C. *Biochemistry* **2003**, *42*, 7497–7508.
(4) Jiang, W.; Hoffart, L. M.; Krebs, C.; Bollinger, J. M., Jr. *Biochemistry* **2007**, *46*, 8709–8716.
(5) George, G. N. *EXAFSPAK*, EXAFSPAK, SSRL, SLAC, Stanford University: Stanford, CA.
(6) Tenderholt, A.; Hedman, B.; Hodgson, K. O. *AIP Conference Proceedings* **2007,** *882*, 105–107.
(7) Rehr, J. J.; Kas, J. J.; Vila, F. D.; Prange, M. P.; Jorissen, K. *Phys. Chem. Chem. Phys.* **2010**, *12*, 5503–5513.
(8) Han, W.-G.; Giammona, D. A.; Bashford, D.; Noodleman, L. *Inorg. Chem.* **2010**, *49*, 7266–7281.
(9) Dassama, L. M. K.; Silakov, A.; Krest, C. M.; Calixto, J. C.; Krebs, C.; Bollinger, J. M., Jr.; Green, M. T. *J. Am. Chem. Soc.* **2013**, *135*, 16758–16761.
(10) Dassama, L. M. K.; Boal, A. K.; Krebs, C.; Rosenzweig, A. C.; Bollinger, J. M., Jr. *J. Am. Chem. Soc.* **2012**, *134*, 2520–2523.
(11) Delgado-Jaime, M. U.; Mewis, C. P.; Kennepohl, P. *J. Synchrotron Radiat.* **2010**, *17*, 132–137.
(12) Annino, G.; Cassettari, M.; Martinelli, M. *IEEE Trans. Microw. Theory Tech.* **2009**, *57*, 775–783.
(13) Reijerse, E.; Lendzian, F.; Isaacson, R.; Lubitz, W. *J. Magn. Reson.* **2012**, *214*, 237–243.
(14) Doan, P. E.; Hoffman, B. M. *Chem. Phys. Lett.* **1997**, *269*, 208–214.
(15) Kazan Viewer - Homepage Alexey Silakov https://sites.google.com/site/silakovalexey/kazan-viewer (accessed October 14, 2016).
(16) Stoll, S.; Schweiger, A. *J. Magn. Reson.* **2006**, *178*, 42–55.
(17) Bencini, A.; Gatteschi, D. *EPR of Exchange Coupled Systems*; Springer-Verlag: Berlin, 1990.
(18) Xue, G.; Wang, D.; Hont, R. D.; Fiedler, A. T.; Shan, X.; Münck, E.; Que, L., Jr. *Proc. Natl. Acad. Sci. U.S.A.* **2007**, *104*, 20713–20718.
(19) Hsu, H.-F.; Dong, Y.; Shu, L.; Young, V. G.; Que, L., Jr. *J. Am. Chem. Soc.* **1999**, *121*, 5230–5237.
(20) Do, L. H.; Xue, G.; Que, L., Jr.; Lippard, S. J. *Inorg. Chem.* **2012**, *51*, 2393–2402.
(21) Taktak, S.; Kryatov, S. V.; Rybak-Akimova, E. V. *Inorg. Chem.* **2004**, *43*, 7196–7209.
(22) Zang, Y.; Pan, G.; Que, L., Jr.; Fox, B. G.; Munck, E. *J. Am. Chem. Soc.* **1994**, *116*, 3653–3654.
(23) Stubna, A.; Jo, D.-H.; Costas, M.; Brenessel, W. W.; Andres, H.; Bominaar, E. L.; Münck, E.; Que, L., Jr. *Inorg. Chem.* **2004**, *43*, 3067–3079.
(24) Xue, G.; Fiedler, A. T.; Martinho, M.; Münck, E.; Que, L., Jr. *Proc. Natl. Acad. Sci. U.S.A.* **2008**, *105*, 20615–20620.

(25) Wang, D.; Farquhar, E. R.; Stubna, A.; Münck, E.; Que, L., Jr. *Nat. Chem.* **2009**, *1*, 145–150.
(26) Larson, E.; Lah, M. S.; Li, X.; Bonadies, J. A.; Pecoraro, V. L. *Inorg. Chem.* **1992**, *31*, 373–378.
(27) Baldwin, M. J.; Stemmler, T. L.; Riggs-Gelasco, P. J.; Kirk, M. L.; Penner-Hahn, J. E.; Pecoraro, V. L. *J. Am. Chem. Soc.* **1994**, *116*, 11349–11356.
(28) Schäfer, K.-O.; Bittl, R.; Zweygart, W.; Lendzian, F.; Haselhorst, G.; Weyhermüller, T.; Wieghardt, K.; Lubitz, W. *J. Am. Chem. Soc.* **1998**, *120*, 13104–13120.
(29) Jensen, A. F.; Su, Z.; Hansen, N. K.; Larsen, F. K. *Inorg. Chem.* **1995**, *34*, 4244–4252.
(30) Sturgeon, B. E.; Burdi, D.; Chen, S.; Huynh, B.-H.; Edmondson, D. E.; Stubbe, J.; Hoffman, B. M. *J. Am. Chem. Soc.* **1996**, *118*, 7551–7557.
(31) Jiang, W.; Bollinger, J. M., Jr.; Krebs, C. *J. Am. Chem. Soc.* **2007**, *129*, 7504–7505.
(32) Shu, L.; Nesheim, J. C.; Kauffmann, K.; Münck, E.; Lipscomb, J. D.; Que, L., Jr. *Science* **1997**, *275*, 515–518.
(33) Rohde, J.-U.; Torelli, S.; Shan, X.; Lim, M. H.; Klinker, E. J.; Kaizer, J.; Chen, K.; Nam, W.; Que, L., Jr. *J. Am. Chem. Soc.* **2004**, *126*, 16750–16761.
(34) Stemmler, T. L.; Sturgeon, B. E.; Randall, D. W.; Britt, R. D.; Penner-Hahn, J. E. *J. Am. Chem. Soc.* **1997**, *119*, 9215–9225.
(35) Krewald, V.; Lassalle-Kaiser, B.; Boron, T. T.; Pollock, C. J.; Kern, J.; Beckwith, M. A.; Yachandra, V. K.; Pecoraro, V. L.; Yano, J.; Neese, F.; DeBeer, S. *Inorg. Chem.* **2013**, *52*, 12904–12914.

Appendix C

Vanadyl as a Stable Structural Mimic of Reactive Ferryl Intermediates in Mononuclear Non-heme-iron Enzymes.

Reprinted with permission from

Martinie, R. J.; Pollock, C. J.; Matthews, M. L.; Bollinger, J. M., Jr.; Krebs, C.; Silakov, A. *Inorg. Chem.* **2017**, *56*, 13382–13389.

Acknowledgements

I thank Prof. Megan Matthews, who first showed the SyrB1•SyrB2 complex stabilization in the presence of the ferryl intermediate, inspiring the related size exclusion experiments herein. I also thank Dr. Chris Pollock for his help in collecting and analyzing the EXAFS data. Prof. J. Martin Bollinger, Jr. made significant and extensive revisions to the manuscript in preparation for publication. Prof. Carsten Krebs provided the original idea of using vanadyl as a substitute for the ferryl intermediate, and also contributed to revisions of the manuscript. Finally, Prof. Alexey Silakov provided valuable guidance in the analysis and presentation of the EPR data.

Inorganic Chemistry

Article

Cite This: Inorg. Chem. 2017, 56, 13382-13389

pubs.acs.org/IC

Vanadyl as a Stable Structural Mimic of Reactive Ferryl Intermediates in Mononuclear Nonheme-Iron Enzymes

Ryan J. Martinie,[†] Christopher J. Pollock,[†] Megan L. Matthews,[§] J. Martin Bollinger, Jr.,[*,†,‡] Carsten Krebs,[*,†,‡] and Alexey Silakov[*,†]

[†]Department of Chemistry and [‡]Department of Biochemistry and Molecular Biology, The Pennsylvania State University, University Park, Pennsylvania 16802, United States

[§]Department of Chemical Physiology and The Skaggs Institute for Chemical Biology, The Scripps Research Institute, 10550 North Torrey Pines Road, La Jolla, California 92037, United States

Supporting Information

ABSTRACT: The iron(II)- and 2-(oxo)glutarate-dependent (Fe/2OG) oxygenases catalyze an array of challenging transformations via a common iron(IV)-oxo (ferryl) intermediate, which in most cases abstracts hydrogen (H•) from an aliphatic carbon of the substrate. Although it has been shown that the relative disposition of the Fe−O and C−H bonds can control the rate of H• abstraction and fate of the resultant substrate radical, there remains a paucity of structural information on the actual ferryl states, owing to their high reactivity. We demonstrate here that the stable vanadyl ion [$(V^{IV}\text{-oxo})^{2+}$] binds along with 2OG or its decarboxylation product, succinate, in the active site of two different Fe/2OG enzymes to faithfully mimic their transient ferryl states. Both ferryl and vanadyl complexes of the Fe/2OG halogenase, SyrB2, remain stably bound to its carrier protein substrate (L-aminoacyl-S-SyrB1), whereas the corresponding complexes harboring transition metals (Fe, Mn) in lower oxidation states dissociate. In the well-studied taurine:2OG dioxygenase (TauD), the disposition of the substrate C−H bond relative to the vanadyl ion defined by pulse electron paramagnetic resonance methods is consistent with the crystal structure of the reactant complex and computational models of the ferryl state. Vanadyl substitution may thus afford access to structural details of the key ferryl intermediates in this important enzyme class.

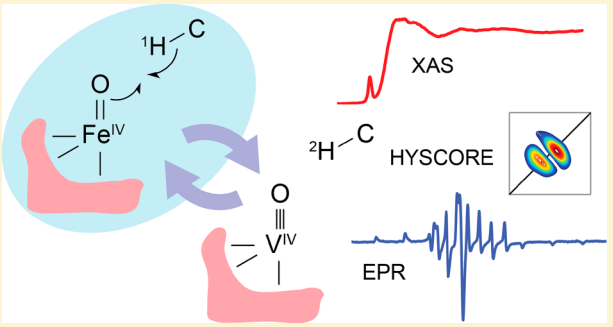

INTRODUCTION

The iron- and 2-(oxo)glutarate-dependent (Fe/2OG) oxygenases catalyze a variety of chemical transformations at unactivated carbon centers, including hydroxylation, halogenation, desaturation, cyclization, and stereoinversion reactions.[1,2] In humans, these reactions play essential roles in connective tissue biosynthesis,[3] oxygen and body mass homeostasis,[4−6] DNA repair,[7−9] epigenetic inheritance, and control of transcription.[10−12] In microbes and plants, these reactions are found in both primary metabolism and, notably, in biosynthetic pathways to specialized secondary metabolites that have been widely deployed as drugs.[1,2] Remarkably, members of this large enzyme family are believed to initiate these sundry reactions via a common Fe^{IV}-oxo (ferryl) intermediate.[2,13−18] The strategies used by individual enzymes to direct the ferryl intermediate to different outcomes remain poorly understood. A deeper understanding could facilitate deployment of their broad capabilities in biotechnological applications.[2]

The mechanistic logic employed by the enzyme class was first elucidated for members of the hydroxylase subclass.[13] Dioxygen activation occurs at a mononuclear Fe^{II} cofactor, coordinated by a $(His)_2(Glu/Asp)_1$ "facial triad" of protein ligands,[19,20] and is followed by oxidative decarboxylation of 2OG, producing succinate, CO_2, and the key ferryl complex.[13−15,21] The ferryl intermediate abstracts a hydrogen atom (H•) from a carbon of the substrate,[22] producing a substrate radical and an Fe^{III}−OH form of the cofactor. The substrate radical then couples with the hydroxo ligand (often termed "rebound") to produce the alcohol product and return the cofactor to its Fe^{II} oxidation state.[23]

Fe/2OG halogenases employ a similar strategy but divert the intermediate produced by H• abstraction; the substrate radical instead couples with a halogen (Cl or Br) coordinated *cis* to the hydroxo.[17,24] How these enzymes prevent the facile rebound step to enable *cis*-halogen transfer has been the subject of much computational and experimental analysis.[2] For the halogenase SyrB2, correlations of substrate structure with rate constants for H• abstraction and halogenation/hydroxylation partition ratios suggested that positioning of the target C−H moiety away from the oxo/hydroxo ligand is crucial for selective halogenation.[25] Subsequent direct measurements of substrate positioning by pulse electron paramagnetic resonance (EPR) methods on an iron-nitrosyl ({FeNO}^{7}) surrogate for the catalytic intermedi-

Received: August 18, 2017
Published: September 29, 2017

DOI: 10.1021/acs.inorgchem.7b02113
Inorg. Chem. 2017, 56, 13382−13389

ates confirmed that the target hydrogen is held farther from the iron center, with an Fe−H vector more nearly perpendicular to the Fe−N vector (which was assumed to mimic the Fe−O vector of the intermediate states), for a substrate that is primarily halogenated than for a substrate that is primarily hydroxylated.[26] Presumably, this configuration poises the substrate radical closer to the halogen ligand to favor its transfer over the normally facile rebound step. Computational analyses suggested that this perpendicular approach engages a π-type frontier molecular orbital of the ferryl complex in the H• abstraction step and promotes halogen transfer in the resultant *cis*-halo-hydroxo-Fe^{III}/substrate-radical state.[27,28] Importantly, these studies suggested that the perpendicular configuration is achieved not by a relocation of the substrate from its usual position above the vacant axial site of the O_2-reactive square-pyramidal Fe^{II} cofactor form (which is *trans* to the C-terminal His ligand and has been called the "inline" position; Figure 1A) but rather by relocation of the ferryl oxo

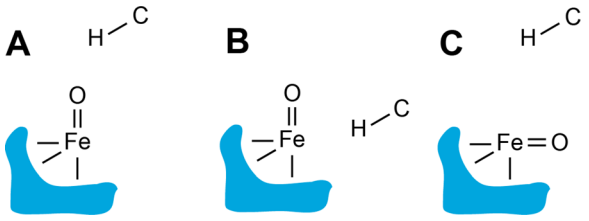

Figure 1. Possible relative dispositions of substrate and ferryl intermediate in Fe/2OG oxygenase reactions. Bonds to the facial triad protein ligands are depicted in cartoon form. (A) Canonical configuration for hydroxylation, with substrate above the inline ferryl oxo group; (B) hypothetical configuration with offline substrate and inline oxo; and (C) configuration postulated for the halogenases, with inline substrate and offline oxo.

group into an adjacent site ("offline", *cis* to the C-terminal histidine; Figure 1C).[1,27,29] The first crystal structure of an Fe/2OG halogenase with its substrate bound, that of the WelO5·Fe^{II}·2OG·12-*epi*-fischerindole U complex, confirmed substrate binding in the usual (inline) configuration (Figure 1A), lending credence to the hypothesis that the oxo must shift offline in the ferryl state to promote halogenation (Figure 1C).[30] It has been suggested that deployment of offline ferryl intermediates could be a general strategy to suppress hydroxylation in other (perhaps all) nonhydroxylation outcomes mediated by Fe/2OG enzymes,[31−34] but appropriate experimental methods to test this hypothesis have yet to emerge.

Structural characterization of high-valent iron enzyme intermediates by X-ray crystallography has been impeded by their short lifetimes, which typically do not exceed a few seconds. However, the ferryl complexes of several Fe/2OG enzymes have been trapped by rapid-mixing/freeze-quenching techniques and characterized by spectroscopic methods. Limitations of this approach are that the resultant structural information is limited to the first coordination sphere of the cofactor and interpretation often relies on comparison of measured parameters to those predicted semiempirically for a set of computationally derived structural models.

Pulse EPR methods can provide *a priori* local structural information beyond the first coordination sphere via the distance and orientation dependencies of electron−nuclear hyperfine interactions (e.g., with ^1H, ^2H, ^{13}C, etc.), but the application of such methods to ferryl complexes in Fe/2OG enzymes has been precluded by the integer-electron-spin (S = 2) ground states of the intermediates.

As introduced above, reaction of the Fe^{II}-containing enzyme−substrate complexes with nitric oxide (NO•) has been used to generate EPR-active $\{FeNO\}^7$ complexes with S = 3/2 ground states, and measurement of hyperfine (HF) couplings between the metal center and deuteria incorporated at strategic positions in the substrates has afforded details of substrate positioning.[26,35−37] However, these $\{FeNO\}^7$ complexes mimic the putative $\{FeOO\}^8$ adduct which precedes ferryl formation, and it seems unlikely that oxidative addition of NO would accurately reproduce local or global structural changes accompanying ferryl formation, for several reasons. First, NO is a diatomic ligand with greater steric bulk than the oxo group of the ferryl. Second, the iron is oxidized by NO formally to the +III oxidation state rather than the +IV state generated by O_2 activation. Finally, reaction with NO fails to bring about decarboxylation of 2OG, leaving the cosubstrate coordinated in the $\{FeNO\}^7$ complex, whereas the ferryl complex formed by O_2 activation has succinate at the corresponding site. These issues cast doubt on the extent to which structural details of the $\{FeNO\}^7$ complexes can explain or predict the reactivity of the corresponding ferryl intermediates.

Seeking a stable, more accurate mimic of the reactive ferryl state for use in EPR and crystallographic structural studies, we considered the vanadyl ion $[(V^{IV}O)^{2+}]$ as a candidate. Stable for many hours in aqueous solution, vanadyl has previously been used to probe divalent metal (e.g., Zn^{2+}, Mg^{2+}, Ca^{2+}) sites in proteins and would thus be expected to bind in the cofactor sites of Fe/2OG enzymes.[38] Structurally, the vanadyl ion has striking similarities to the ferryl moiety. Both have +2 net charges resulting from bonding between the tetravalent metal cation and divalent oxide anion.[39] Moreover, the metal−oxo bonds have similar lengths, ranging from 1.58 to 1.63 Å for octahedral vanadyl complexes with oxygen and nitrogen coordination[40−45] and from 1.61 to 1.64 Å for the ferryl intermediates in the Fe/2OG hydroxylase, TauD, and halogenases, CytC3 and SyrB2.[17,46,47] Importantly, the d^1 configuration of V^{IV} gives the vanadyl ion an S = 1/2 ground state, which makes it EPR active and amenable to accurate determination of distances between vanadium and nearby magnetic nuclei by EPR methods.

RESULTS AND DISCUSSION

To evaluate the potential of vanadyl to serve as a ferryl mimic, we first tested for its capacity to bind in the cofactor site of TauD, the most extensively studied Fe/2OG oxygenase. A sample prepared by adding vanadyl sulfate to apo TauD (metal free), along with succinate and taurine, (Figure 2A) exhibited a strong $g \sim 2$ X-band continuous-wave (CW) EPR signal with splitting characteristic of hyperfine coupling to the ^{51}V nucleus (~100% natural abundance, I = 7/2). This signal was greatly diminished in intensity in a sample from which the enzyme was omitted, as vanadyl in solution at biological pH exists in a polymeric, EPR-silent form;[48] the observed signal therefore arises from a TauD·$(V^{IV}O)$ complex (Figure S1). Global simulation of the X- and Q-band EPR spectra yielded the parameters g = [1.944, 1.979, 1.981] ± 0.001 and A_V = [519, 185, 192] ± 3 MHz (Figure S2). The $A_{//}$ component of the vanadium hyperfine tensor can be related to the identity of the ligands in the equatorial plane of the vanadyl (i.e., *cis* to the -oxo); the observed value of 519 MHz (173×10^{-4} cm^{-1}) is

DOI: 10.1021/acs.inorgchem.7b02113
Inorg. Chem. 2017, 56, 13382−13389

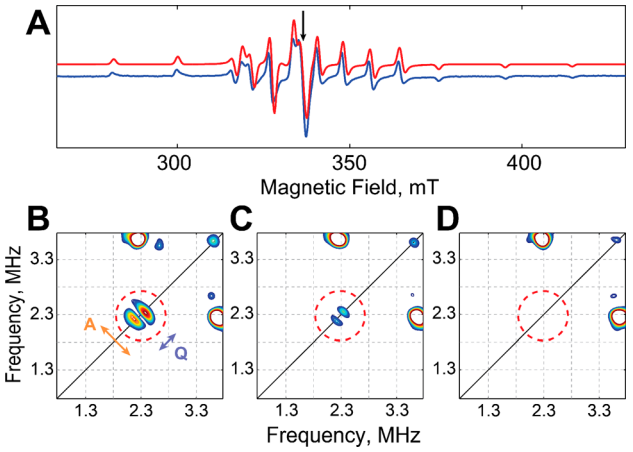

Figure 2. Characterization of the TauD·($V^{IV}O$)·taurine·succinate complex by EPR and HYSCORE spectroscopy. (A) Continuous-wave, X-band spectrum (blue) and simulation (red, shifted upward for clarity). (B–D) HYSCORE spectra collected at the maximum EPR absorbance (indicated by the arrow at 344 mT in A) on samples containing d_4-taurine (B), d_4-succinate (C), and substrate and coproduct of natural isotopic abundance (D). Splittings due to hyperfine coupling (A) and quadrupole coupling (Q) are indicated by arrows in (B). The CW spectrum was collected at 80 K, with microwave frequency 9.478 GHz and power 200 μW. HYSCORE spectra were acquired at 35 K with microwave frequency 9.685 GHz.

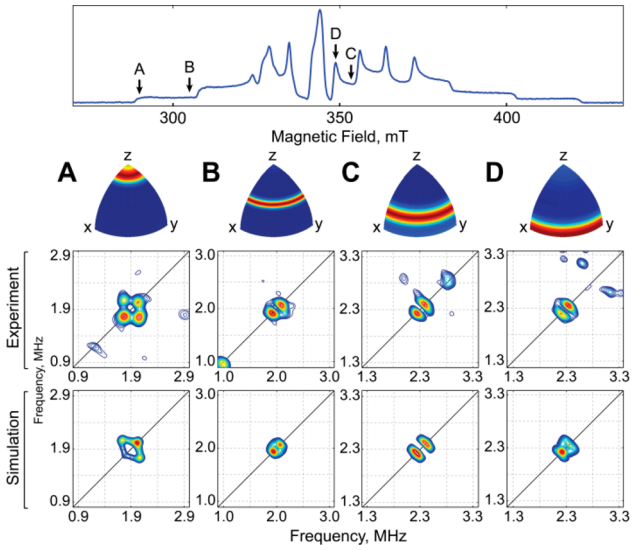

Figure 3. Field-dependent ^{2}H-HYSCORE spectra of the TauD·($V^{IV}O$)·taurine·succinate complex in the presence of d_4-taurine, recorded at 291.0 mT (A), 304.0 mT (B), 353.0 mT (C), and 348.7 mT (D). Magnetic field positions are indicated by black arrows on the one-dimensional EPR spectrum (top, presented in absorption mode); resulting orientation selectivity patterns are color coded using an "RGB" scheme (red, fully excited; blue, not excited). HYSCORE spectra were collected at 35 K with microwave frequency 9.686 GHz.

very close to the expected value of 520 MHz (174×10^{-4} cm^{-1}) for three carboxylate oxygen and one histidine nitrogen (with the plane of the histidine ring perpendicular to the V-oxo bond) ligands.[38] Although asymmetry and the presence of potentially bidentate carboxylate ligands may produce deviations from predicted values and (thus this agreement is not definitive), the observed value of $A_{//}$ is certainly compatible with the proposed geometry.

Further evidence for binding of the vanadyl in the cofactor site was provided by deuterium hyperfine sublevel correlation (^{2}H-HYSCORE) spectra (Figure 2B–D), which report on interactions between the electron spin and nearby deuterium nuclei. In ^{2}H-HYSCORE spectra, resonances are centered at the Larmor frequency of the deuterium. Hyperfine coupling is manifest by splitting along the antidiagonal, whereas nuclear quadrupolar interactions cause further splitting along the diagonal (Figure 2B). For samples of the TauD·($V^{IV}O$)·succinate·taurine complex prepared with 1,1,2,2-[$^2H_4$]-taurine (d_4-taurine), a feature centered at ν_L = 2.25 MHz was readily observed in the HYSCORE spectrum (Figure 2B) collected at the point of maximum EPR absorption (344 mT). The appearance of such a feature indicates that vanadyl does, as expected, bind in the active site, close to (<5 Å from) the taurine-binding site. In spectra of samples prepared using 2,2,3,3-[$^2H_4$]-succinate, a weaker feature was seen, showing proximity of the vanadyl to the coproduct bound in the active site (Figure 2C). No features attributable to deuterium were observed from a sample prepared with unlabeled taurine and succinate (Figure 2D).

To establish that vanadyl substitution can provide a spin probe for structural analysis, we defined the position of taurine relative to the $V^{IV}O$ unit by pulse EPR, as previously done for the {Fe-NO}^{7} complexes.[26,35,36] Field-dependent ^{2}H-HYSCORE spectra were collected for a sample of the TauD·($V^{IV}O$)·succinate·d_4-taurine complex (Figure 3). The resulting patterns were simulated with a single deuterium hyperfine coupling of [0.26, 0.26, −0.68] ± 0.05 MHz with Euler angles of [0, 35, 15] ± 10° relative to the **g** tensor (Figure 3); the deuterium nuclear quadrupole interaction was simulated as [−0.06, −0.06, 0.12] ± 0.03 MHz with Euler angles [0, −50, 15] ± 10°. That a single coupling can account for the observed signals strongly suggests that only the most proximal deuteron on C1 (inferred to be the *pro-R* hydron from crystal structures of TauD)[49,50] meaningfully contributes to these spectra. This coupling can be considered in terms of an anisotropic component, T, and an isotropic component, A_{iso}: A_{2H} = [1, 1, −2]T + A_{iso} (i.e., an axial tensor of magnitude **T** = 0.30 MHz and an isotropic component of magnitude A_{iso} = −0.04 MHz). The anisotropic component can be related to the V–^{2}H distance according to the point-dipole approximation, which yields 3.4 ± 0.2 Å. Moreover, the second Euler angle (35°) corresponds to the O≡V–^{2}H angle, as the unique axis of the (approximately axial) **g** tensor is collinear with the V≡O bond. Although the observation of isotropic hyperfine coupling is usually indicative of through-bond delocalization of spin density onto the nucleus of interest, through-space isotropic coupling has been observed for atoms in tight van der Waals contact, consistent with the small isotropic component observed here.[51–53]

Substrate positioning in TauD was previously interrogated for the aforementioned {FeNO}^{7} complex.[36,37] For comparison to the metrics provided by the $V^{IV}O$ probe, we re-examined the iron–nitrosyl complex in the presence of d_4-taurine and 2OG by field-dependent ^{2}H-HYSCORE (Figure S3). The data were simulated with a single deuterium hyperfine coupling of [0.26, 0.44, −0.70] ± 0.05 MHz with Euler angles of [0, 30, 93] ± 10° and a deuterium nuclear quadrupole interaction of [−0.04, −0.04, 0.08] ± 0.03 MHz with Euler angles [0, 40, 25] ± 10°. The anisotropic magnitude (T = 0.35 MHz) and second Euler angle (30°) are quite similar to those obtained in the previous

DOI: 10.1021/acs.inorgchem.7b02113
Inorg. Chem. 2017, 56, 13382–13389

study of the {Fe-NO}^{7} complex and above on the vanadyl complex.[36,37]

To assess the coordination geometry of the vanadyl ion in TauD and the extent to which it mimics the proposed structure of the ferryl intermediate, we interrogated the complex by X-ray absorption methods. The vanadium K-edge lies at ∼5480 eV (Figure S4), consistent with the +IV oxidation state.[54] The spectrum (Figure S5) also has an intense pre-edge feature with an intensity (99 ± 3 units) that is nearly identical to that of the six-coordinate $VO(H_2O)_5^{2+}$ ion (106 ± 4 units; Figure S5). This observed intensity is appreciably less than that seen for formally square pyramidal vanadyl complexes, likely owing to the presence of a weakly coordinating axial ligand in TauD that partially restores centrosymmetry, and hence the observed pre-edge is most consistent with an octahedral geometry distorted by the presence of an oxo ligand.[54] Such a geometry could arise from vanadium coordination by the facial triad and bidentate coordination by succinate, a first sphere that would be identical to that favored in previous spectroscopic and computational studies of the ferryl complex.[55] Fits to the extended X-ray absorption fine structure (EXAFS) data revealed a coordination sphere composed of two shells: one at 1.60 Å, corresponding to the oxo ligand, and another at 2.05 Å (Figure S6 and Table S1−S3), corresponding to the protein and succinate ligands. The fitting analysis is consistent with previous structural characterization of vanadyl complexes[40−45] and notably similar to the first-sphere metrics obtained by EXAFS on the ferryl intermediate in TauD (shells at 1.62 and 2.05 Å).[46]

From the structural metrics extracted from the HYSCORE and EXAFS analysis of the TauD vanadyl complex, a geometric model for the key atoms in the H• abstraction step effected by the ferryl complex was constructed (Scheme 1). The model has

Scheme 1. Disposition of the Taurine C1 *pro-R* Deuterium Nucleus Relative to Vanadyl in the TauD·($V^{IV}O$)·Taurine·Succinate Complex[a]

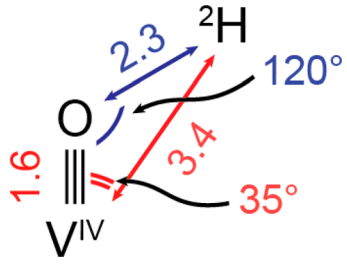

[a]Experimental measurements are denoted in red, and extrapolated values in blue; distances given are in units of angstrom.

a V≡O−^{2}H angle of (120 ± 10)° and an O−^{2}H distance of (2.3 ± 0.3) Å. Extrapolated to the ferryl complex, this geometry would be consistent with the expectation of efficient σ-channel H• abstraction by the ferryl state in this hydroxylation reaction and is compatible with previous X-ray crystal structures.[49,50]

The above experiments indicate that the complex of TauD with vanadyl, succinate, and taurine has a structure very similar to that proposed for the ferryl intermediate. Despite this agreement, we sought more compelling evidence of faithful mimicry in a biological context by testing whether binding of vanadyl can replicate a unique feature of the ferryl complex that was found for SyrB2. The substrate of SyrB2 is the carrier protein, SyrB1, with L-threonine appended via thioester linkage to its phosphopantetheine cofactor (L-threoninyl-*S*-SyrB1); it undergoes chlorination of the L-threonine methyl group. The chloroferryl complex in SyrB2 can be markedly stabilized ($t_{1/2}$ ∼ 110 min at 4 °C) by use of the alternative substrate, L-cyclopropylglycinyl-*S*-SyrB1, owing to the greater C−H bond strength of the cyclopropyl side chain.[17] Neither the apo nor the Mn^{II} form (in the presence or absence of 2OG/succinate) of SyrB2 makes a stable complex with L-threoninyl-*S*-SyrB1; consequently, the two proteins are almost completely resolved by chromatography on an appropriate size-exclusion matrix at 4 °C (Figures 4A, blue and black traces, and S7). By contrast, in

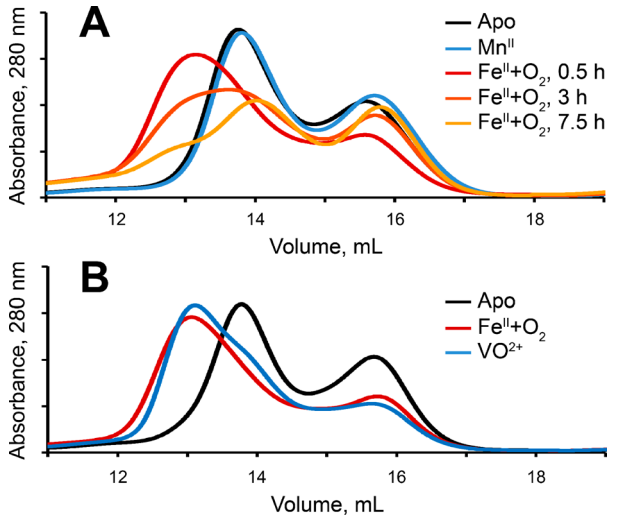

Figure 4. Size-exclusion chromatography of L-cyclopropylglycinyl-*S*-SyrB1 and SyrB2. (A) SyrB1 and Fe(II)-SyrB2 exposed to oxygen for 0 h (red), 3 h (orange), and 7.5 h (gold) prior to loading. Apo-SyrB2 (black) and Mn(II)-SyrB2 (blue) are depicted for comparison. (B) SyrB1 and SyrB2-VO (blue), Fe(II)-SyrB2 (red), and apo-SyrB2 (black). SyrB2, Fe^{II} or VO^{2+}, Cl^-, 2OG, and L-cyclopropylglycinyl-*S*-SyrB1, mixed to final concentrations of 150 μM, 140 μM, 2.7 mM, 0.8 mM, and 150 μM, respectively, were applied to a GE Healthcare Superdex 200 10/300 GL column and eluted at 0.7 mL/min with 50 mM sodium HEPES pH 7.6, 150 mM NaCl.

the cyclopropyl-stabilized ferryl intermediate state, the two proteins remain associated during chromatography under the same conditions, as evidenced by the shift to lesser elution times (Figure 4A, red trace). The elution time of the new peak is consistent with formation of a 1:1 complex of SyrB1 and SyrB2. In this experiment, chromatography was initiated as soon as possible after formation of the ferryl complex by O_2 exposure, and the elution required ∼30 min, a time scale on which the ferryl complex is stable.[17] By contrast, increasing delays between formation of the stabilized ferryl complex and the chromatography step led to decreasing intensity in the ∼13 min peak of the complex and regaining intensity in the peak of free SyrB2 (Figure 4, orange and gold traces). The time scale for this shift matched the previously published kinetics of decay of the ferryl complex formed in the presence of the non-native substrate. Incomplete formation of the complex (indicated by the presence of the SyrB2 peak at 16 mL) is likely due to the combination of decay of the ferryl complex (predicted to be ∼20% upon elution from the column) and an inactive protein fraction frequently observed in this enzyme class.[18,23] The data indicate that conformational changes coupled to ferryl formation strengthen the protein−protein interactions between SyrB1 and SyrB2 and prevent the release of the substrate

DOI: 10.1021/acs.inorgchem.7b02113
Inorg. Chem. 2017, 56, 13382−13389

during the lifetime of the reactive intermediate, presumably as an adaptation to prevent enzyme auto-oxidation. A similar observation was reported for the class I-a ribonucleotide reductase from *Escherichia coli*, in which radical translocation from the cofactor (β) subunit into the catalytic (α) subunit was seen to increase their mutual affinity by 25-fold.[56]

Remarkably, the presence of vanadyl (along with 2OG) in the active site of SyrB2 reproduces the stability of the enzyme's complex with its carrier protein substrate (Figure 4B, compare blue and red traces). Even the extent of incomplete formation of the complex is reproduced. Surprisingly, little complex formation is observed in the presence of vanadyl and succinate. The basis for this requirement for the cosubstrate rather than coproduct is currently unclear and warrants further structural studies. Nevertheless, it is clear that the surrounding protein framework of SyrB2, which has adapted to interact strongly with SyrB1 only in the ferryl state, responds to the presence of vanadyl in the same manner. This profound similarity in a global conformational effect strongly suggests that vanadyl is a faithful mimic of the ferryl state, giving credence to the utility of the vanadyl ion as a structural probe.

The data demonstrate the suitability of the vanadyl ion as an analogue of the ferryl intermediate in Fe/2OG oxygenases and its utility as a structural probe. It binds along with succinate and taurine in the TauD active site, where it adopts a distorted octahedral geometry similar to that previously proposed for the ferryl complex[55] and exhibits a metal-oxo bond length (1.60 Å) nearly identical to that determined for the key intermediate state (1.62 Å).[46] Remarkably, in addition to accurately reproducing these cofactor-proximal metrics in TauD, the vanadyl ion also reproduces the global conformational effect (manifested by stabilization of its enzyme−substrate complex) that accompanies ferryl formation in SyrB2. Although its utility as an EPR probe to extract precise substrate-positioning information is partly precedented by the prior studies on the {Fe-NO}^{7} complexes in TauD and other systems,[26,35−37] the expectation that it should more accurately mimic the geometries of the ferryl complexes makes it potentially superior for rationalizing the reactivities of the key intermediates. Moreover, the stability of the vanadyl complexes under biological conditions hints at the exciting prospect of obtaining X-ray crystal structures of the ferryl-mimicking states to map local and global protein motions that accompany ferryl formation and control its reactivity, as was recently demostrated for the Fe/2OG oxygenase VioC.[57] Thus, the new structural probe may help unravel incompletely understood mechanisms of reaction control in Fe/2OG oxygenases, thereby enabling their rational reprogramming for biotechnological applications.

MATERIALS AND METHODS

Materials. Commercially available materials were used without further purification. 1,1,2,2-[$^2H_4$]-taurine was purchased from Cambridge Isotope Laboratories. 2,2,3,3-[$^2H_4$]-succinic acid was purchased from Sigma.

Preparation of the TauD·($V^{IV}O$)·Taurine·Succinate Complex. TauD was purified as previously described.[14] Vanadyl sulfate was dissolved in 2.5 mM sulfuric acid at a concentration of 50 mM. TauD, vanadyl, succinate, and taurine were mixed to final concentrations of 1.5, 1.0, 5.0, and 5.0 mM, respectively. The solution was then transferred to an EPR tube or X-ray absorption cell and frozen in liquid N_2.

Preparation of the TauD·{FeNO}^{7}·Taurine·2OG Complex. The TauD {Fe-NO}^{7} complex was prepared in the manner previously described for SyrB2.[26] TauD, iron, 2OG, and taurine were mixed to concentrations of 1.13, 1.04, 5.67, and 5.67 mM, respectively. After exposure to NO, the resulting solution was concentrated in a centrifugal filter by approximately 4-fold, transferred to an EPR tube, and frozen in liquid N_2.

XAS Data Collection and Processing. X-ray absorption spectra were collected on beamline 7-3 at the Stanford Synchrotron Radiation Lightsource under ring conditions of 3 GeV and 500 mA. A Si(220) monochromator (φ = 90°) was used for energy selection of the incident beam; harmonic rejection was achieved using a Rh-coated mirror (9 keV) and by detuning the monochromator by 85%. The energy of the incident beam was calibrated by using a vanadium foil upstream of the sample (5465.2 eV). Scans were carried out over the energy range of 5235−6250 eV for a total exposure of 800 s. The beam intensity was measured using N_2-filled ion chambers before the sample. The sample was placed at 45° relative to the incident beam, and the Kα fluorescence was monitored using a 30 element germanium detector. Sample temperature was maintained at 10 K in a liquid helium flow cryostat.

Data processing was performed with the EXAFSPAK software package.[58] Three-segment splines (of orders 2, 3, and 3) were removed from the EXAFS using PySpline,[59] and the EXAFS data were then fit using the program OPT. Appropriate structural models were adapted from Sinnecker et al.[55] (replacing Fe with V), and scattering paths for EXAFS fits were generated using FEFF 9.0 (additional details can be found in the Supporting Information).[60] During EXAFS fitting, the distances, Debye−Waller factors, and E_0 parameter were all allowed to float while coordination numbers were systematically varied; for all fits the passive electron reduction factor (S_0^2) was fixed at 1. For XANES analysis, the pre-edge region was fit using BlueprintXAS,[61] and the edge jump obtained from the fits was normalized to 1; reported areas and intensity-weighted average energies are the average of at least 21 physically reasonable fits.

EPR Measurements. X-band continuous wave (CW) measurements were performed on a Bruker ESP 300 spectrometer with an ER 041 MR microwave bridge and an ER 4116DM resonator. All other EPR measurements were performed on a Bruker Elexsys E580 X-band spectrometer equipped with a SuperX-FT microwave bridge. For pulse EPR measurements at X-band, a Bruker ER 4118X-MS5 resonator was used in concert with an Oxford CF935 helium flow cryostat. Microwave pulses generated by the microwave bridge were amplified by a 1 kW traveling wave tube (TWT) amplifier (Applied Systems Engineering, model 117x). Pulse EPR spectra at Q-band frequencies were acquired using a home-built intermediate-frequency extension of the SuperX-FT X-band bridge that has a Millitech 5W pulse power amplifier. All experiments were conducted on a home-built TE_{011} resonator utilizing the open resonator concept developed by Annino et al.[62] and mechanical construction of the probehead similar to that presented by Reijerse et al.[63] This setup allows $t(\pi/2)$ = 12−16 ns at maximum input power with spectrometer dead time (including the resonator ring time) of 100−120 ns. Data acquisition and control of experimental parameters were performed by using Bruker XEPR software.

EPR Analysis. Data processing and spectral simulations were performed using Kazan viewer, a home-written suite of utilities in MATLAB.[64] One-dimensional EPR simulations were performed using the "pepper" utility from the EasySpin software package.[65] HYSCORE data were analyzed by simultaneous frequency domain simulation of all field-dependent spectra until a satisfactory solution was achieved. The rhombicity of the hyperfine coupling, ε, was defined as

$$[A_x, A_y, A_z] = [-1 - \varepsilon, -1 + \varepsilon, 2] \times T + A_{iso} \quad (1)$$

Euler angles (y-convention) are reported with respect to the ^{51}V hyperfine coupling tensor, which is collinear with the g matrix in our simulations.

Geometric information was calculated using a point-dipole model, according to the formula

$$T_{VD}(\mathrm{MHz}) = 12.1362 r_{VD}^{-3} \quad (2)$$

DOI: 10.1021/acs.inorgchem.7b02113
Inorg. Chem. 2017, 56, 13382−13389

Deviations from this idealized model could result from significant delocalization of spin density onto the vanadyl oxo ligand. However, available experimental and theoretical results suggest this delocalization is likely to be 5−20%.[66,67] At these levels of spin density on oxygen, deviations from the point dipole model are calculated using a geometric model to be within the stated experimental error.

Size Exclusion Chromatography. SyrB1 and SyrB2 were purified, and SyrB1 was charged with L-cyclopropylglycine as previously described.[17] Oxygen was removed from L-cyclopropylglycinyl-*S*-SyrB1 and SyrB2 as previously described. SyrB2; Fe^{2+}, Mn^{2+}, or VO^{2+}; Cl^-; 2OG; and L-cyclopropylglycinyl-*S*-SyrB1 were mixed in an MBraun (Stratham, NH) anoxic chamber to final concentrations of 0.54, 0.50, 10, 2.6, and 0.56 mM, respectively, with a final volume of 0.150 mL. After removal from the anoxic chamber, samples were mixed with 0.40 mL air-saturated buffer and then centrifuged briefly. Either immediately or after the specified delay, samples were applied to a GE Healthcare Superdex 200 10/300 GL column at 4 °C using a 100 μL sample loop and eluted at 0.7 mL/min with 1.2 column volumes of 50 mM sodium HEPES pH 7.6, 150 mM NaCl.

■ ASSOCIATED CONTENT

Supporting Information

The Supporting Information is available free of charge on the ACS Publications website at DOI: 10.1021/acs.inorgchem.7b02113.

Multifrequency EPR analysis; ^{2}H-HYSCORE analysis of TauD-{FeNO}^{7}; XAS edges, pre-edges, and corresponding fits; EXAFS data and fits; tables of EXAFS fits. (PDF)

■ AUTHOR INFORMATION

Corresponding Authors

*E-mail: jmb21@psu.edu.
*E-mail: ckrebs@psu.edu.
*E-mail: aus40@psu.edu.

ORCID

Ryan J. Martinie: 0000-0003-1257-2850
Christopher J. Pollock: 0000-0001-5736-513X
Carsten Krebs: 0000-0002-3302-7053
Alexey Silakov: 0000-0002-9285-1253

Notes

The authors declare no competing financial interest.

■ ACKNOWLEDGMENTS

This material is based upon work supported by the National Science Foundation Graduate Research Fellowship Program under grant no. DGE1255832. Any opinions, findings, and conclusions or recommendations expressed in this material are those of the author(s) and do not necessarily reflect the views of the National Science Foundation. C.J.P. thanks the NIH for a National Research Service Award (GM113389-01). This work was supported by the National Institutes of Health (GM118812 to J.M.B. and C.K. and GM069657 to C.K. and J.M.B.). Portions of this work were conducted at the Stanford Synchrotron Radiation Lightsource, SLAC National Accelerator Laboratory, which is supported by the U.S. Department of Energy, Office of Science, Office of Basic Energy Sciences under contract no. DE-AC02-76SF00515. The SSRL Structural Molecular Biology Program is supported by the DOE Office of Biological and Environmental Research and by the National Institutes of Health, National Institute of General Medical Sciences (including P41GM103393). The contents of this publication are solely the responsibility of the authors and do not necessarily represent the official views of NIGMS or NIH.

■ REFERENCES

(1) Hausinger, R. P. Fe(II)/α-Ketoglutarate-Dependent Hydroxylases and Related Enzymes. *Crit. Rev. Biochem. Mol. Biol.* **2004**, *39*, 21−68.
(2) Bollinger, J. M., Jr.; Chang, W.-c.; Matthews, M. L.; Martinie, R. J.; Boal, A. K.; Krebs, C. In *2-Oxoglutarate-Dependent Oxygenases*; Hausinger, R. P., Schofield, C. J., Eds.; RSC Metallobiology; Royal Society of Chemistry: Cambridge, UK, 2015.
(3) Kivirikko, K. I.; Myllyharju, J. Prolyl 4-hydroxylases and their protein disulfide isomerase subunit. *Matrix Biol.* **1998**, *16*, 357−368.
(4) Ivan, M.; Kondo, K.; Yang, H.; Kim, W.; Valiando, J.; Ohh, M.; Salic, A.; Asara, J. M.; Lane, W. S.; Kaelin, W. G. HIFα Targeted for VHL-Mediated Destruction by Proline Hydroxylation: Implications for O_2 Sensing. *Science* **2001**, *292*, 464−468.
(5) Jaakkola, P.; Mole, D. R.; Tian, Y.-M.; Wilson, M. I.; Gielbert, J.; Gaskell, S. J.; von Kriegsheim, A.; Hebestreit, H. F.; Mukherji, M.; Schofield, C. J.; Maxwell, P. H.; Pugh, C. W.; Ratcliffe, P. J. Targeting of HIF-α to the von Hippel-Lindau Ubiquitylation Complex by O_2-Regulated Prolyl Hydroxylation. *Science* **2001**, *292*, 468−472.
(6) Gerken, T.; Girard, C. A.; Tung, Y.-C. L.; Webby, C. J.; Saudek, V.; Hewitson, K. S.; Yeo, G. S. H.; McDonough, M. A.; Cunliffe, S.; McNeill, L. A.; Galvanovskis, J.; Rorsman, P.; Robins, P.; Prieur, X.; Coll, A. P.; Ma, M.; Jovanovic, Z.; Farooqi, I. S.; Sedgwick, B.; Barroso, I.; Lindahl, T.; Ponting, C. P.; Ashcroft, F. M.; O'Rahilly, S.; Schofield, C. J. The Obesity-Associated FTO Gene Encodes a 2-Oxoglutarate-Dependent Nucleic Acid Demethylase. *Science* **2007**, *318*, 1469−1472.
(7) Trewick, S. C.; Henshaw, T. F.; Hausinger, R. P.; Lindahl, T.; Sedgwick, B. Oxidative demethylation by *Escherichia coli* AlkB directly reverts DNA base damage. *Nature* **2002**, *419*, 174−178.
(8) Falnes, P. Ø.; Johansen, R. F.; Seeberg, E. AlkB-mediated oxidative demethylation reverses DNA damage in *Escherichia coli*. *Nature* **2002**, *419*, 178−182.
(9) Yi, C.; Jia, G.; Hou, G.; Dai, Q.; Zhang, W.; Zheng, G.; Jian, X.; Yang, C.-G.; Cui, Q.; He, C. Iron-catalysed oxidation intermediates captured in a DNA repair dioxygenase. *Nature* **2010**, *468*, 330−333.
(10) Tsukada, Y.; Fang, J.; Erdjument-Bromage, H.; Warren, M. E.; Borchers, C. H.; Tempst, P.; Zhang, Y. Histone demethylation by a family of JmjC domain-containing proteins. *Nature* **2006**, *439*, 811−816.
(11) Klose, R. J.; Yamane, K.; Bae, Y.; Zhang, D.; Erdjument-Bromage, H.; Tempst, P.; Wong, J.; Zhang, Y. The transcriptional repressor JHDM3A demethylates trimethyl histone H3 lysine 9 and lysine 36. *Nature* **2006**, *442*, 312−316.
(12) Cloos, P. A. C.; Christensen, J.; Agger, K.; Maiolica, A.; Rappsilber, J.; Antal, T.; Hansen, K. H.; Helin, K. The putative oncogene GASC1 demethylates tri- and dimethylated lysine 9 on histone H3. *Nature* **2006**, *442*, 307−311.
(13) Krebs, C.; Galonić Fujimori, D.; Walsh, C. T.; Bollinger, J. M., Jr. Non-Heme Fe(IV)−Oxo Intermediates. *Acc. Chem. Res.* **2007**, *40*, 484−492.
(14) Price, J. C.; Barr, E. W.; Tirupati, B.; Bollinger, J. M., Jr.; Krebs, C. The First Direct Characterization of a High-Valent Iron Intermediate in the Reaction of an α-Ketoglutarate-Dependent Dioxygenase: A High-Spin Fe(IV) Complex in Taurine/α-Ketoglutarate Dioxygenase (TauD) from *Escherichia coli*. *Biochemistry* **2003**, *42*, 7497−7508.
(15) Hoffart, L. M.; Barr, E. W.; Guyer, R. B.; Bollinger, J. M., Jr.; Krebs, C. Direct spectroscopic detection of a C-H-cleaving high-spin Fe(IV) complex in a prolyl-4-hydroxylase. *Proc. Natl. Acad. Sci. U. S. A.* **2006**, *103*, 14738−14743.
(16) Galonić, D. P.; Barr, E. W.; Walsh, C. T.; Bollinger, J. M., Jr.; Krebs, C. Two interconverting Fe(IV) intermediates in aliphatic chlorination by the halogenase CytC3. *Nat. Chem. Biol.* **2007**, *3*, 113−116.
(17) Matthews, M. L.; Krest, C. M.; Barr, E. W.; Vaillancourt, F. H.; Walsh, C. T.; Green, M. T.; Krebs, C.; Bollinger, J. M., Jr. Substrate-Triggered Formation and Remarkable Stability of the C−H Bond-Cleaving Chloroferryl Intermediate in the Aliphatic Halogenase, SyrB2. *Biochemistry* **2009**, *48*, 4331−4343.

DOI: 10.1021/acs.inorgchem.7b02113
Inorg. Chem. 2017, 56, 13382−13389

(18) Chang, W.-c.; Guo, Y.; Wang, C.; Butch, S. E.; Rosenzweig, A. C.; Boal, A. K.; Krebs, C.; Bollinger, J. M., Jr. Mechanism of the C5 Stereoinversion Reaction in the Biosynthesis of Carbapenem Antibiotics. *Science* **2014**, *343*, 1140−1144.
(19) Que, L., Jr. One motif - many different reactions. *Nat. Struct. Biol.* **2000**, *7*, 182−184.
(20) Koehntop, K. D.; Emerson, J. P.; Que, L., Jr. The 2-His-1-carboxylate facial triad: a versatile platform for dioxygen activation by mononuclear non-heme iron(II) enzymes. *J. Biol. Inorg. Chem.* **2005**, *10*, 87−93.
(21) Hanauske-Abel, H. M.; Günzler, V. A stereochemical concept for the catalytic mechanism of prolylhydroxylase: Applicability to classification and design of inhibitors. *J. Theor. Biol.* **1982**, *94*, 421−455.
(22) Price, J. C.; Barr, E. W.; Glass, T. E.; Krebs, C.; Bollinger, J. M., Jr. Evidence for Hydrogen Abstraction from C1 of Taurine by the High-Spin Fe(IV) Intermediate Detected during Oxygen Activation by Taurine:α-Ketoglutarate Dioxygenase (TauD). *J. Am. Chem. Soc.* **2003**, *125*, 13008−13009.
(23) Price, J. C.; Barr, E. W.; Hoffart, L. M.; Krebs, C.; Bollinger, J. M., Jr. Kinetic Dissection of the Catalytic Mechanism of Taurine:α-Ketoglutarate Dioxygenase (TauD) from *Escherichia coli*. *Biochemistry* **2005**, *44*, 8138−8147.
(24) Blasiak, L. C.; Vaillancourt, F. H.; Walsh, C. T.; Drennan, C. L. Crystal structure of the non-haem iron halogenase SyrB2 in syringomycin biosynthesis. *Nature* **2006**, *440*, 368−371.
(25) Matthews, M. L.; Neumann, C. S.; Miles, L. A.; Grove, T. L.; Booker, S. J.; Krebs, C.; Walsh, C. T.; Bollinger, J. M., Jr. Substrate positioning controls the partition between halogenation and hydroxylation in the aliphatic halogenase, SyrB2. *Proc. Natl. Acad. Sci. U. S. A.* **2009**, *106*, 17723−17728.
(26) Martinie, R. J.; Livada, J.; Chang, W.-c.; Green, M. T.; Krebs, C.; Bollinger, J. M., Jr.; Silakov, A. Experimental Correlation of Substrate Position with Reaction Outcome in the Aliphatic Halogenase, SyrB2. *J. Am. Chem. Soc.* **2015**, *137*, 6912−6919.
(27) Wong, S. D.; Srnec, M.; Matthews, M. L.; Liu, L. V.; Kwak, Y.; Park, K.; Bell, C. B. I.; Alp, E. E.; Zhao, J.; Yoda, Y.; Kitao, S.; Seto, M.; Krebs, C.; Bollinger, J. M., Jr.; Solomon, E. I. Elucidation of the Fe(IV)═O intermediate in the catalytic cycle of the halogenase SyrB2. *Nature* **2013**, *499*, 320−323.
(28) Srnec, M.; Wong, S. D.; Matthews, M. L.; Krebs, C.; Bollinger, J. M., Jr.; Solomon, E. I. Electronic Structure of the Ferryl Intermediate in the α-Ketoglutarate Dependent Non-Heme Iron Halogenase SyrB2: Contributions to H Atom Abstraction Reactivity. *J. Am. Chem. Soc.* **2016**, *138*, 5110−5122.
(29) Borowski, T.; Noack, H.; Radoń, M.; Zych, K.; Siegbahn, P. E. M. Mechanism of Selective Halogenation by SyrB2: A Computational Study. *J. Am. Chem. Soc.* **2010**, *132*, 12887−12898.
(30) Mitchell, A. J.; Zhu, Q.; Maggiolo, A. O.; Ananth, N. R.; Hillwig, M. L.; Liu, X.; Boal, A. K. Structural basis for halogenation by iron- and 2-oxo-glutarate-dependent enzyme WelO5. *Nat. Chem. Biol.* **2016**, *12*, 636−640.
(31) Boal, A. K.; Bollinger, J. M., Jr.; Chang, W. -c. Assembly of the unusual oxacycles in the orthosomycin antibiotics. *Proc. Natl. Acad. Sci. U. S. A.* **2015**, *112*, 11989−11990.
(32) McCulloch, K. M.; McCranie, E. K.; Smith, J. A.; Sarwar, M.; Mathieu, J. L.; Gitschlag, B. L.; Du, Y.; Bachmann, B. O.; Iverson, T. M. Oxidative cyclizations in orthosomycin biosynthesis expand the known chemistry of an oxygenase superfamily. *Proc. Natl. Acad. Sci. U. S. A.* **2015**, *112*, 11547−11552.
(33) Yan, W.; Song, H.; Song, F.; Guo, Y.; Wu, C.-H.; Sae Her, A.; Pu, Y.; Wang, S.; Naowarojna, N.; Weitz, A.; Hendrich, M. P.; Costello, C. E.; Zhang, L.; Liu, P.; Zhang, Y. J. Endoperoxide formation by an α-ketoglutarate-dependent mononuclear non-haem iron enzyme. *Nature* **2015**, *527*, 539−543.
(34) Zhang, Z.; Smart, T. J.; Choi, H.; Hardy, F.; Lohans, C. T.; Abboud, M. I.; Richardson, M. S. W.; Paton, R. S.; McDonough, M. A.; Schofield, C. J. Structural and stereoelectronic insights into oxygenase-catalyzed formation of ethylene from 2-oxoglutarate. *Proc. Natl. Acad. Sci. U. S. A.* **2017**, *114*, 4667−4672.
(35) Yang, T. C.; Wolfe, M. D.; Neibergall, M. B.; Mekmouche, Y.; Lipscomb, J. D.; Hoffman, B. M. Substrate Binding to NO−Ferro−Naphthalene 1,2-Dioxygenase Studied by High-Resolution Q-Band Pulsed ^{2}H-ENDOR Spectroscopy. *J. Am. Chem. Soc.* **2003**, *125*, 7056−7066.
(36) Muthukumaran, R. B.; Grzyska, P. K.; Hausinger, R. P.; McCracken, J. Probing the Iron−Substrate Orientation for Taurine/α-Ketoglutarate Dioxygenase Using Deuterium Electron Spin Echo Envelope Modulation Spectroscopy. *Biochemistry* **2007**, *46*, 5951−5959.
(37) Casey, T. M.; Grzyska, P. K.; Hausinger, R. P.; McCracken, J. Measuring the Orientation of Taurine in the Active Site of the Non-Heme Fe(II)/α-Ketoglutarate-Dependent Taurine Hydroxylase (TauD) Using Electron Spin Echo Envelope Modulation (ESEEM) Spectroscopy. *J. Phys. Chem. B* **2013**, *117*, 10384−10394.
(38) Smith, T. S., II; LoBrutto, R.; Pecoraro, V. L. Paramagnetic spectroscopy of vanadyl complexes and its applications to biological systems. *Coord. Chem. Rev.* **2002**, *228*, 1−18.
(39) Winkler, J. R.; Gray, H. B. In *Molecular Electronic Structures of Transition Metal Complexes I*; Mingos, D. M. P., Day, P., Dahl, J. P., Eds.; Structure and Bonding; Springer: Berlin, 2011; pp 17−28.
(40) Ishida, T.; Mitsubori, S.; Nogami, T.; Takeda, N.; Ishikawa, M.; Iwamura, H. Ferromagnetic Exchange Coupling of Vanadium(IV) dπ Spins across Pyrimidine Rings: Dinuclear Complexes of Oxovanadium(IV) Bis(1,1,1,5,5,5-hexafluoropentane-2,4-dionate) Bridged by Pyrimidine Derivatives. *Inorg. Chem.* **2001**, *40*, 7059−7064.
(41) Tasiopoulos, A. J.; Tolis, E. J.; Tsangaris, J. M.; Evangelou, A.; Woollins, D. J.; Slawin, A. M.; Pessoa, J.; Correia, I.; Kabanos, T. A. Model investigations for vanadium-protein interactions: vanadium(III) compounds with dipeptides and their oxovanadium(IV) analogues. *J. Biol. Inorg. Chem.* **2002**, *7*, 363−374.
(42) Manivannan, V.; Hoffman, J. T.; Dimayuga, V. L.; Dwight, T.; Carrano, C. J. A comparison of vanadyl acetylacetonate complexes of N_2O heteroscorpionate ligands that vary systematically in donor set. *Inorg. Chim. Acta* **2007**, *360*, 529−534.
(43) Yuan, C.; Lu, L.; Gao, X.; Wu, Y.; Guo, M.; Li, Y.; Fu, X.; Zhu, M. Ternary oxovanadium(IV) complexes of ONO-donor Schiff base and polypyridyl derivatives as protein tyrosine phosphatase inhibitors: synthesis, characterization, and biological activities. *J. Biol. Inorg. Chem.* **2009**, *14*, 841−851.
(44) Roy, A. S.; Saha, P.; Adhikary, N. D.; Ghosh, P. o-Iminobenzosemiquinonate and o-Imino-p-methylbenzosemiquinonate Anion Radicals Coupled VO^{2+} Stabilization. *Inorg. Chem.* **2011**, *50*, 2488−2500.
(45) Deng, Y.; Yang, Y.; Zhang, Y.; Yan, Q.; Liu, J. Formation of an asymmetrical ligand (H_3L_{cyclic}) *via* a metal-induced cyclization of symmetrical thiocarbohydrazone (H_4L) in synthesizing an oxovanadium(IV) complex $VO(HL_{cyclic})(EtOH)_2$. *J. Coord. Chem.* **2012**, *65*, 1409−1416.
(46) Riggs-Gelasco, P. J.; Price, J. C.; Guyer, R. B.; Brehm, J. H.; Barr, E. W.; Bollinger, J. M., Jr.; Krebs, C. EXAFS Spectroscopic Evidence for an FeO Unit in the Fe(IV) Intermediate Observed during Oxygen Activation by Taurine:α-Ketoglutarate Dioxygenase. *J. Am. Chem. Soc.* **2004**, *126*, 8108−8109.
(47) Galonić-Fujimori, D.; Barr, E. W.; Matthews, M. L.; Koch, G. M.; Yonce, J. R.; Walsh, C. T.; Bollinger, J. M., Jr.; Krebs, C.; Riggs-Gelasco, P. J. Spectroscopic Evidence for a High-Spin Br-Fe(IV)-Oxo Intermediate in the α-Ketoglutarate-Dependent Halogenase CytC3 from Streptomyces. *J. Am. Chem. Soc.* **2007**, *129*, 13408−13409.
(48) Chasteen, N. D. In *Biological Magnetic Resonance*; Berliner, L. J., Reuben, J., Eds.; Springer: New York, 1981; pp 53−119.
(49) Elkins, J. M.; Ryle, M. J.; Clifton, I. J.; Dunning Hotopp, J. C.; Lloyd, J. S.; Burzlaff, N. I.; Baldwin, J. E.; Hausinger, R. P.; Roach, P. L. X-ray Crystal Structure of *Escherichia coli* Taurine/α-Ketoglutarate Dioxygenase Complexed to Ferrous Iron and Substrates. *Biochemistry* **2002**, *41*, 5185−5192.

DOI: 10.1021/acs.inorgchem.7b02113
Inorg. Chem. 2017, 56, 13382−13389

(50) O'Brien, J. R.; Schuller, D. J.; Yang, V. S.; Dillard, B. D.; Lanzilotta, W. N. Substrate-Induced Conformational Changes in *Escherichia coli* Taurine/α-Ketoglutarate Dioxygenase and Insight into the Oligomeric Structure. *Biochemistry* **2003**, *42*, 5547−5554.
(51) Horitani, M.; Byer, A. S.; Shisler, K. A.; Chandra, T.; Broderick, J. B.; Hoffman, B. M. Why Nature Uses Radical SAM Enzymes so Widely: Electron Nuclear Double Resonance Studies of Lysine 2,3-Aminomutase Show the 5′-dAdo• "Free Radical" Is Never Free. *J. Am. Chem. Soc.* **2015**, *137*, 7111−7121.
(52) Foner, S. N.; Cochran, E. L.; Bowers, V. A.; Jen, C. K. Multiple Trapping Sites for Hydrogen Atoms in Rare Gas Matrices. *J. Chem. Phys.* **1960**, *32*, 963−971.
(53) Morton, J. R.; Preston, K. F.; Strach, S. J.; Adrian, F. J.; Jette, A. N. Anisotropic hyperfine interactions of rare-gas nuclei near trapped hydrogen atoms. *J. Chem. Phys.* **1979**, *70*, 2889−2893.
(54) Rees, J. A.; Wandzilak, A.; Maganas, D.; Wurster, N. I. C.; Hugenbruch, S.; Kowalska, J. K.; Pollock, C. J.; Lima, F. A.; Finkelstein, K. D.; DeBeer, S. Experimental and theoretical correlations between vanadium K-edge X-ray absorption and Kβ emission spectra. *J. Biol. Inorg. Chem.* **2016**, *21*, 793−805.
(55) Sinnecker, S.; Svensen, N.; Barr, E. W.; Ye, S.; Bollinger, J. M., Jr.; Neese, F.; Krebs, C. Spectroscopic and Computational Evaluation of the Structure of the High-Spin Fe(IV)-Oxo Intermediates in Taurine: α-Ketoglutarate Dioxygenase from *Escherichia coli* and Its His99Ala Ligand Variant. *J. Am. Chem. Soc.* **2007**, *129*, 6168−6179.
(56) Minnihan, E. C.; Ando, N.; Brignole, E. J.; Olshansky, L.; Chittuluru, J.; Asturias, F. J.; Drennan, C. L.; Nocera, D. G.; Stubbe, J. Generation of a stable, aminotyrosyl radical-induced α2β2 complex of *Escherichia coli* class Ia ribonucleotide reductase. *Proc. Natl. Acad. Sci. U. S. A.* **2013**, *110*, 3835−3840.
(57) Mitchell, A. J.; Dunham, N. P.; Martinie, R. J.; Bergman, J. A.; Pollock, C. J.; Hu, K.; Allen, B. D.; Chang, W.-c.; Silakov, A.; Bollinger, J. M., Jr.; Krebs, C.; Boal, A. K. Visualizing the Reaction Cycle in an iron(II)- and 2-(Oxo)-Glutarate-Dependent Hydroxylase. *J. Am. Chem. Soc.* **2017**. DOI: 10.1021/jacs.7b07374.
(58) George, G. N. *EXAFSPAK, EXAFSPAK, SSRL, SLAC*; Stanford University: Stanford, CA.
(59) Tenderholt, A.; Hedman, B.; Hodgson, K. O. PySpline: A ModernCross-Platform Program for the Processing of Raw Averaged XAS Edge and EXAFS Data. *AIP Conf. Proc.* **2006**, *882*, 105−107.
(60) Rehr, J. J.; Kas, J. J.; Vila, F. D.; Prange, M. P.; Jorissen, K. Parameter-free calculations of X-ray spectra with FEFF9. *Phys. Chem. Chem. Phys.* **2010**, *12*, 5503−5513.
(61) Delgado-Jaime, M. U.; Mewis, C. P.; Kennepohl, P. Blueprint XAS: a Matlab-based toolbox for the fitting and analysis of XAS spectra. *J. Synchrotron Radiat.* **2010**, *17*, 132−137.
(62) Annino, G.; Cassettari, M.; Martinelli, M. A New Concept of Open Cavity. *IEEE Trans. Microwave Theory Tech.* **2009**, *57*, 775−783.
(63) Reijerse, E.; Lendzian, F.; Isaacson, R.; Lubitz, W. A tunable general purpose Q-band resonator for CW and pulse EPR/ENDOR experiments with large sample access and optical excitation. *J. Magn. Reson.* **2012**, *214*, 237−243.
(64) *Kazan Viewer*, Homepage Alexey Silakov; https://sites.google.com/site/silakovalexey/kazan-viewer (accessed June 7, 2017).
(65) Stoll, S.; Schweiger, A. EasySpin, a comprehensive software package for spectral simulation and analysis in EPR. *J. Magn. Reson.* **2006**, *178*, 42−55.
(66) Baute, D.; Goldfarb, D. The ^{17}O Hyperfine Interaction in $V^{17}O(H_2{}^{17}O)_5{}^{2+}$ and $Mn(H_2{}^{17}O)_6{}^{2+}$ Determined by High Field ENDOR Aided by DFT Calculations. *J. Phys. Chem. A* **2005**, *109*, 7865−7871.
(67) Matsuoka, N.; Tsuchimoto, M.; Yoshioka, N. Theoretical Study of Magnetic Properties of Oxovanadium(IV) Complex Self-Assemblies with Tetradentate Schiff Base Ligands. *J. Phys. Chem. B* **2011**, *115*, 8465−8473.

DOI: 10.1021/acs.inorgchem.7b02113
Inorg. Chem. 2017, 56, 13382−13389

Supporting Information For:

Vanadyl as a Stable Structural Mimic of Reactive Ferryl Intermediates in Mononuclear Non-heme-iron Enzymes

Ryan J. Martinie[a], Christopher J. Pollock[a], Megan L. Matthews[c], J. Martin Bollinger, Jr.[a,b]* Carsten Krebs [a,b]*, and Alexey Silakov [a]*

[a]Department of Chemistry and [b]Department of Biochemistry and Molecular Biology, The Pennsylvania State University, University Park, Pennsylvania 16802, United States

[c]Department of Chemical Physiology and The Skaggs Institute for Chemical Biology, The Scripps Research Institute, 10550 North Torrey Pines Road, La Jolla, California 92037, United States

Supplementary Figures

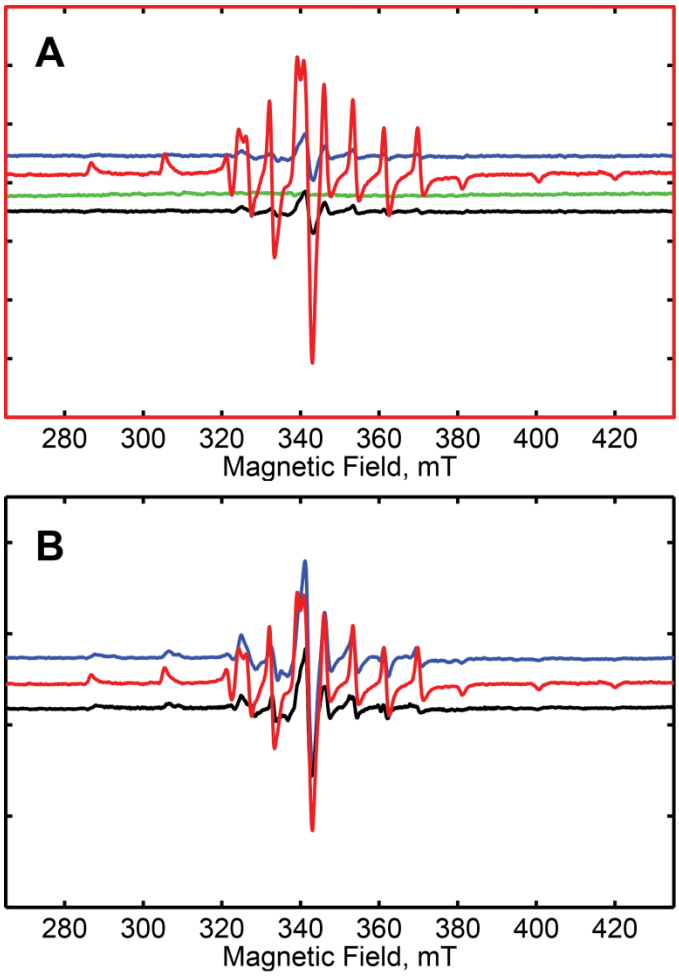

Figure S1. Comparison of continuous-wave (CW) EPR signals for solutions containing vanadyl. (**A**) Comparison of taurine only (green); succinate and taurine (blue); 2OG and taurine (black); or TauD, succinate, and taurine (red). Spectra are shifted vertically for clarity. (**B**) Comparison of TauD•vanadyl in the presence of succinate only (blue), 2OG only (black), or succinate and taurine (red). Concentration of species (if present): vanadyl sulfate (1.0 mM), succinate (3.0 mM), 2-oxo-glutarate (3.0 mM), TauD (1.6 mM) in 50 mM sodium HEPES pH 7.6. Spectra were recorded at 80 K with microwave frequency 9.625 GHz, microwave power 200 μW, 10 G modulation amplitude, and 40 ms time constant and conversion time.

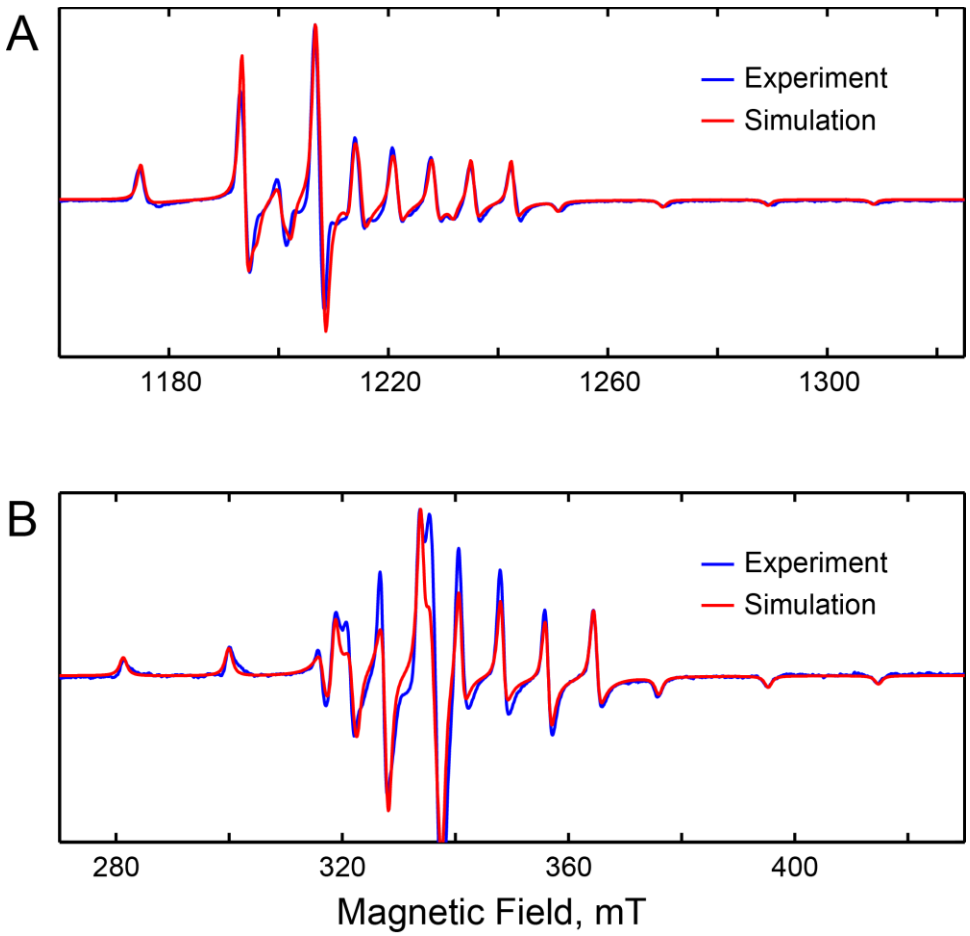

Figure S2. Experimental (blue) and simulated (red) electron paramagnetic resonance spectra of the TauD•($V^{IV}O$)•taurine•succinate complex, collected at Q-band (**A**) and X-band (**B**). The Q-band spectrum was collected as a two-pulse Hahn echo experiment with τ = 200 ns and 250 μs shot repetition time at 40 K, with the pseudo-modulated spectrum shown. X-band spectrum was acquired using continuous-wave excitation at 80 K. X- and Q-band spectra were acquired at 9.478 & 33.788 GHz, respectively. Sample composition: TauD (1.5 mM), vanadyl sulfate (1.0 mM), succinate (5.0 mM), and taurine (5.0 mM). Simulation parameters: g = [1.944, 1.979, 1.981] ± 0.001 and A_V = [519, 185, 192] ± 3 MHz.

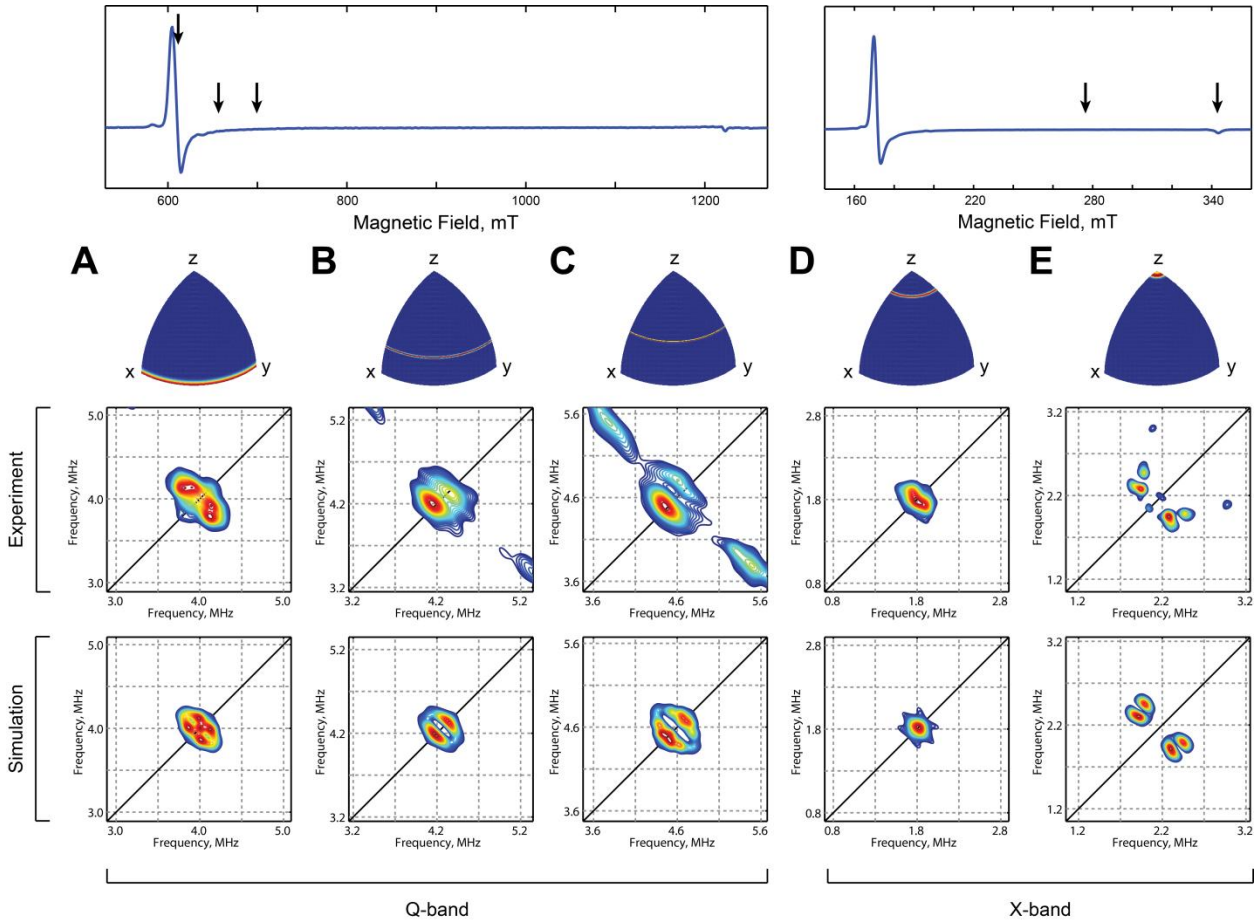

Figure S3. Field-dependent ^{2}H-HYSCORE spectra of the {Fe-NO}^{7} form of TauD in the presence of d_4-taurine and 2OG collected at Q-band (**A**-**C**) and X-band (**D**-**E**). Orientation selectivities probed by each magnetic field position (shown above the spectra) are color coded using an RGB color scheme (red - fully excited; blue, not excited). Magnetic field positions of 610 (**A**), 650 (**B**), 700 (**C**), 275 (**D**), and 329 (**E**) mT are indicated by black arrows on the one-dimensional EPR spectra (top). Spectra were collected with microwave frequency 34.276 (Q-band) and 9.308 GHz (X-band), temperature 4.0 K, $\pi/2$ pulse length of 8 ns, and τ of 140, 140, 140, 220, and 200 ns, respectively. Simulation parameters: hyperfine coupling [0.26, 0.44, -0.70] ± 0.05 MHz with Euler angles of [0, 30, 93] ± 10° and deuterium nuclear quadrupole coupling [-0.04, -0.04, 0.08] ± 0.03 MHz with Euler angles [0, 40, 25] ± 10°. Sample preparation is described in the Materials and Methods.

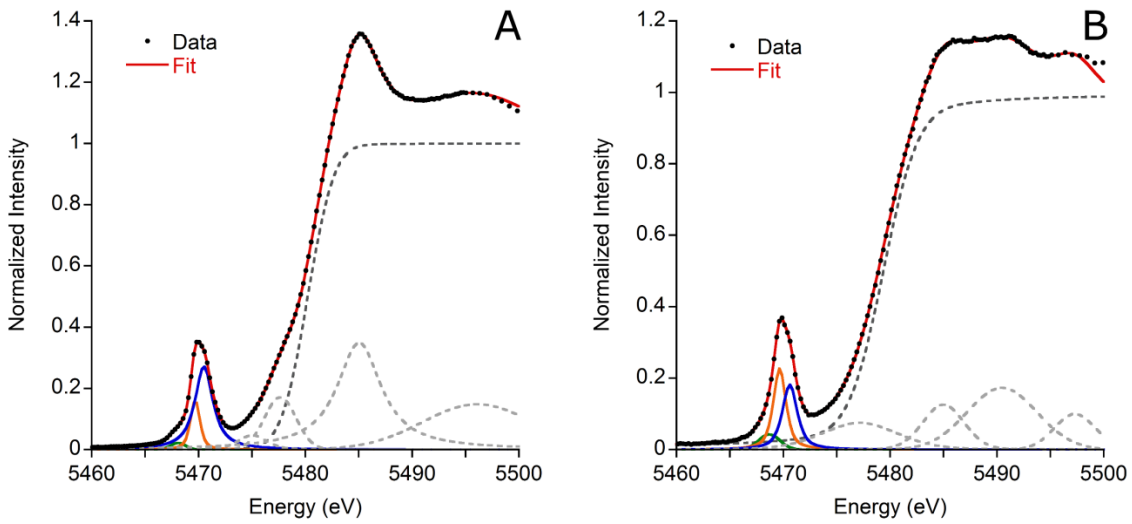

Figure S4. Representative fits of the XANES data (points) for $VO(H_2O)_5^{2+}$ (**A**) and the TauD•($V^{IV}O$)•taurine•succinate complex (**B**). Solid lines represent components of the pre-edge, whereas gray, dashed lines are background components.

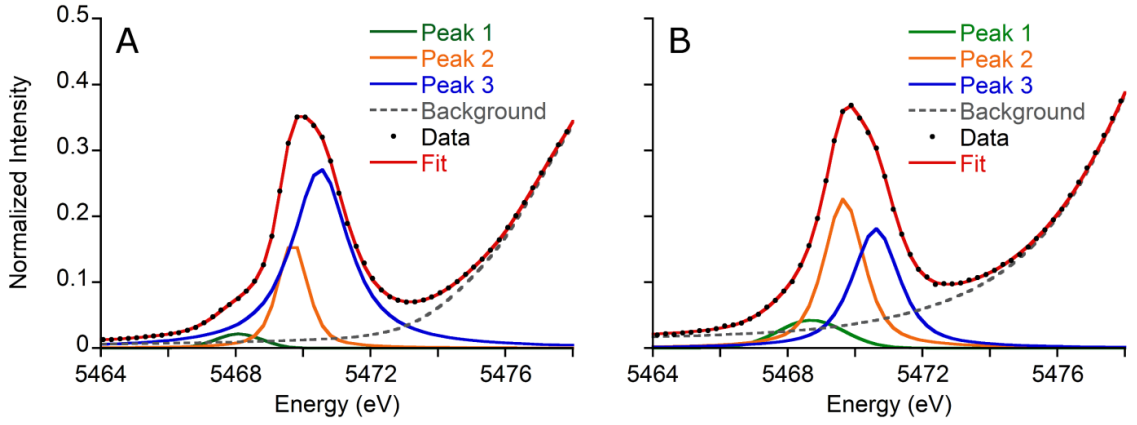

Figure S5. Representative fits of the pre-edge features in the XANES data for $VO(H_2O)_5^{2+}$ (**A**) and the TauD•($V^{IV}O$)•taurine•succinate complex (**B**). Solid, colored lines represent components that were included in calculations of the pre-edge areas.

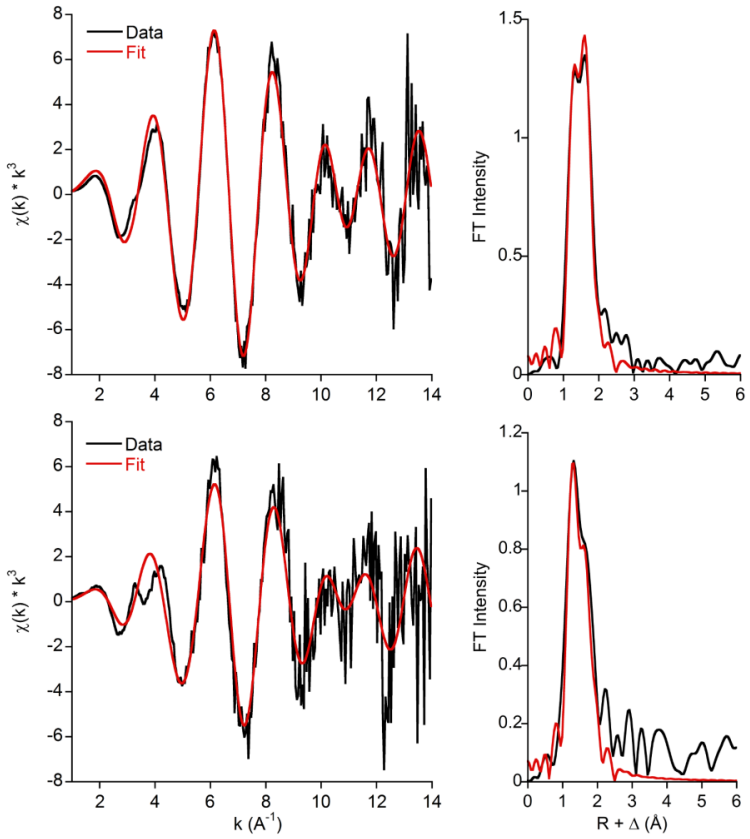

Figure S6. Fits to the k^3-weighted EXAFS data and Fourier transforms for $VO(H_2O)_5^{2+}$ (**top**) and the TauD•($V^{IV}O$)•taurine•succinate complex (**bottom**).

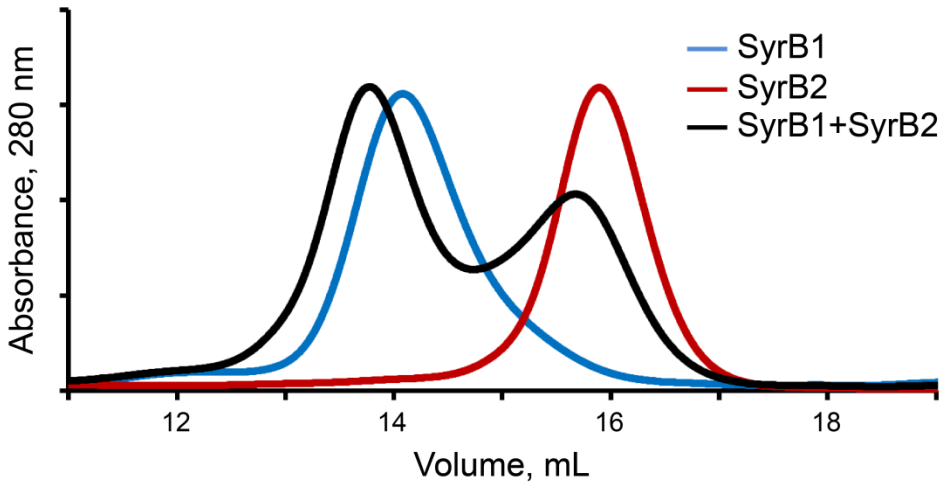

Figure S7. Elution chromatograms from size-exclusion chromatographic analysis of samples containing SyrB1 (**blue**), SyrB2 (**red**) or equi-molar quantities of both proteins (**black**). The shift of the mixed proteins relative to SyrB1 and SyrB2 alone is attributed to dynamic association during chromatography. SyrB2 (0.15 mM) and L-cyclopropylglycinyl-*S*-SyrB1 (0.15 mM) were applied to a GE Healthcare Superdex 200 10/300 GL column at 4 °C using a 100 µL sample loop and eluted at 0.7 mL/min with 1.2 column volumes of 50 mM sodium HEPES pH 7.6, 150 mM NaCl.

Supplementary Tables

Table S1: EXAFS fit parameters for $VO(H_2O)_5^{2+}$ (top) and the TauD•($V^{IV}O$)•taurine•succinate complex

$VO(H_2O)_5^{2+}$				TauD-VO			
Scatterer	**N**	**R (Å)**	**σ^2 (Å^2)**	**Scatterer**	**N**	**R (Å)**	**σ^2 (Å^2)**
V-N/O	1	1.59	0.00157	V-N/O	1	1.60	0.00136
V-N/O	4	2.02	0.00284	V-N/O	3	2.05	0.00246
F		0.3314		F		0.5716	
E_0		-0.14 eV		E_0		4.04 eV	

Table S2: EXAFS fitting results for $VO(H_2O)_5^{2+}$

			V=O			V-N/O			V-N/O		
χ^2	**F**	**E_0**	**N**	**R**	**σ^2**	**N**	**R**	**σ^2**	**N**	**R**	**σ^2**
7.4718	0.8803	3.97134	1	1.55	0.0058						
4.6009	0.6907	3.97131	2	1.58	0.00301						
9.2426	0.979	2.81078	3	1.57	0.01124						
5.1255	0.7291	-1.6467	1	2.02	-0.0027						
3.6942	0.619	-0.5603	2	2.03	-0.0003						
3.0418	0.5616	-3.0165	3	2.02	0.00146						
2.8068	0.5395	-4.091	4	2.01	0.00292						
2.8515	0.5438	-5.8326	5	2.00	0.00424						
1.6161	0.4079	-3.6211	1	1.59	0.00205	6	2.01	0.00573			
1.2644	0.3608	-1.9091	1	1.59	0.00179	5	2.02	0.00429			
1.0671	0.3314	-0.141	1	1.59	0.00157	4	2.02	0.00284			
1.13	0.3411	1.56566	1	1.60	0.00142	3	2.03	0.0013			
1.0402	0.326	0.11454	1	1.59	0.00157	4	2.02	0.00283	1	2.45	0.02339
1.181	0.3474	-1.518	1	1.59	0.00177	5	2.02	0.00426	1	2.38	0.01299

Table S3: EXAFS fitting results for the TauD•($V^{IV}O$)•taurine•succinate complex

			V=O			V-N/O			V-N/O		
χ^2	F	E_0	N	R	σ^2	N	R	σ^2	N	R	σ^2
5.4733	0.8579	3.51693	1	1.59	0.00179						
5.8301	0.8854	4.03515	2	1.60	0.00556						
6.7101	0.9499	-16.408	3	1.54	0.00882						
5.6113	0.8686	4.03522	1	2.05	0.00109						
4.635	0.7895	2.31054	2	2.05	0.00087						
4.2853	0.7591	0.03089	3	2.04	0.00266						
4.1533	0.7473	-2.9326	4	2.02	0.00417						
4.1585	0.7478	-5.6757	5	2.01	0.00548						
4.2502	0.7560	-9.2176	6	1.99	0.00664						
2.6946	0.5997	4.0352	1	1.60	0.00121	2	2.04	0.00064			
2.4478	0.5716	4.03512	1	1.60	0.00136	3	2.05	0.00246			
2.4883	0.5763	1.45792	1	1.60	0.00150	4	2.03	0.00415			
2.6389	0.5935	-0.3822	1	1.59	0.00170	5	2.03	0.00574			
2.8534	0.6171	-2.4176	1	1.59	0.00175	6	2.02	0.00734			
2.8588	0.6177	4.03522	2	1.61	0.00629	3	2.04	0.0029			
2.709	0.6013	4.03518	2	1.61	0.00610	4	2.03	0.00519			
2.7346	0.6041	2.79102	2	1.61	0.00624	5	2.03	0.0069			
2.4007	0.5639	3.55141	1	1.60	0.00137	3	2.04	0.00248	1	4.10	-0.0016
2.4951	0.5633	4.03517	1	1.60	0.00152	3	2.05	0.00254	2	2.56	0.01735
2.2906	0.5509	4.03489	1	1.60	0.00139	3	2.04	0.00254	1	2.61	-0.0009
2.4549	0.5703	4.03511	1	1.60	0.00150	3	2.04	0.00259	2	2.61	0.00371
2.4176	0.5659	4.03504	1	1.60	0.00156	3	2.05	0.00254	3	2.56	0.02223
2.3226	0.5547	2.24498	1	1.60	0.00144	4	2.04	0.0042	1	2.61	-0.0007
2.3775	0.5612	3.21365	1	1.60	0.00151	4	2.04	0.00417	2	2.50	0.02194
2.4408	0.5686	-4.875	1	1.58	0.00162	5	2.01	0.00627	1	2.34	0

Appendix D

Two-Color Valence-to-Core X-ray Emission Spectroscopy Tracks Cofactor Protonation State in a Class I Ribonucleotide Reductase

Submitted to *Angew. Chem. Int. Ed.*

Acknowledgements

C.J.P. and E.J.B. thank the National Institutes of Health for National Research Service Awards (GM113389-01 and GM116353-01). This material is based upon work supported by the National Science Foundation Graduate Research Fellowship Program under grant no. DGE1255832 (R.J.M.) and by the National Institutes of Health (GM55365 to J.M.B. and C.K.). This work is based upon research conducted at the Cornell High Energy Synchrotron Source (CHESS) which is supported by the National Science Foundation under award DMR-1332208.

Once again, I thank Dr. Beth Blasei for her role as a member of the "beam team" in the rather Herculean collection of these data. Even when things got very discouraging, Beth was always up for another go-round. Prof. Carsten Krebs and Prof. J. Martin Bollinger, Jr. provided helpful feedback on the manuscript in preparation for publication. In particular, Carsten's critical comments on our presentation of the data analysis were invaluable. Huge thanks are also due to Dr. Ken Finkelstein, the staff scientist at CHESS C-line where we collected these data. DAVES was designed and constructed by Ken, and he gave us the opportunity to be some of the first to utilize its unique capabilities. And when the experiment didn't work out as we hoped the first time, or the second, he kept giving us more and more beam time to complete our experiment, even if we were "definitely the low point in terms of performance." He was invaluable in helping us assemble and tune the setup for our experiment, was remarkably generous with his time, and was a near-constant source of optimism when things went awry. Finally, once again incredible credit is due to Dr. Chris Pollock, who first proposed that we do this study with our leftover EXAFS samples, spent countless hours at C-line with little sleep, and took the lead on analyzing these data. The whole study was done very much in partnership with Chris, and I couldn't have done it without him.

Abstract

Proton transfer reactions are of central importance to a wide variety of biochemical processes, though determining proton location and monitoring proton transfers in biological systems is often extremely challenging. Herein, we use two-color valence-to-core x-ray emission spectroscopy (VtC XES) to identify protonation events across three oxidation states of the O_2-activating, radical-initiating manganese-iron heterodinuclear cofactor in a class I-c ribonucleotide reductase. This is the first application of VtC XES to an enzyme intermediate and the first simultaneous measurement of two-color VtC spectra. In contrast to more conventional methods of assessing protonation state, VtC XES is a more direct probe applicable to a wide range of metalloenzyme systems. These data, coupled to insight provided by DFT calculations, allow the inorganic cores of the $Mn^{IV}Fe^{IV}$ and $Mn^{IV}Fe^{III}$ states of the enzyme to be assigned as $Mn^{IV}(\mu\text{-}O)_2Fe^{IV}$ and $Mn^{IV}(\mu\text{-}O)(\mu\text{-}OH)Fe^{III}$, respectively.

Nature employs metalloenzymes to catalyze some of its most challenging chemical reactions, including C-H activation, water splitting, and dinitrogen reduction.[1] In these reactions, biological systems must generate highly reactive species and control them to avoid cell damage through adventitious reactions, such as production of reactive oxygen species and enzyme auto-oxidation. To limit this danger, enzymes have evolved various mechanisms to control these reactive species, including forming intermediates in the protective environment of the enzyme and doing so only when substrate is present.[2] Another mechanism of control is to modulate reactivity via precise transfer of protons to and from the active site. Changes in protonation state can significantly influence redox potential and aid in bond activation, and, because enzymes can control access to protons via hydrogen bond networks and conformational changes, they can thereby both prevent the formation of reactive intermediates until the enzyme is poised for turnover and shield them from unproductive decay.

A classic example of enzymes harnessing the power of high valent metals occurs in class I ribonucleotide reductases (RNRs), enzymes that reduce ribonucleotides to deoxyribonucleotides.[3] The reaction is initiated when an active-site cysteine residue in the catalytic α subunit is oxidized by a stable oxidant in the β subunit through a series of proton-coupled electron transfers along a pathway of aromatic and acidic amino acids.[4] A particularly interesting example is the class I-c RNR from the pathogen *Chlamydia trachomatis* (*Ct*), which utilizes an unusual $Mn^{IV}Fe^{III}$ heterodinuclear cofactor, with the Mn^{IV} ion serving as the stable oxidant.[5] This cofactor is assembled by reaction of the $Mn^{II}Fe^{II}$ state (**2/2**) with O_2 via a transient $Mn^{IV}Fe^{IV}$ intermediate (**4/4**), which is reduced by an exogenous electron source to the catalytically active $Mn^{IV}Fe^{III}$ (**4/3**) (Scheme 1).[6]

Scheme 1. Putative protonation pattern of the inorganic core of *Ct* RNR-β during enzyme activation.

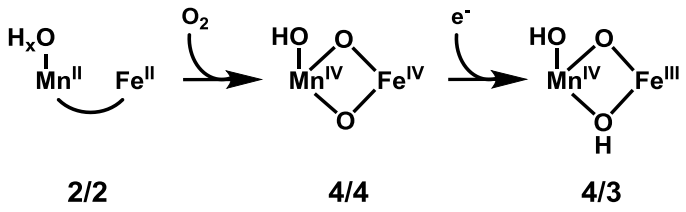

The precise structures and protonation states of these and other high-valent biological Fe and Mn complexes have excited considerable interest and investigation.[7] Unfortunately, the protonation pattern of *Ct* RNR-β remains poorly understood and is the subject of ongoing research. Only recently was a combined EXAFS / ENDOR study able to suggest, based on Mn-Fe distance and absence of strong hyperfine coupling to hydrogen, that **4/4** possesses a di-μ-oxo $Mn^{IV}(O)_2Fe^{IV}$ core and terminal OH ligand bound to Mn.[7e] Previously, **4/3** was proposed to have a $Mn^{IV}(O)(OH)Fe^{III}$ core,[7b, 8] suggesting the protonation pattern depicted in Scheme 1. These assignments rely, however, on indirect arguments, as intermetallic distances and absence of magnetic coupling are only proxies for the protonation state of the metallocofactor.

This situation exemplifies a general problem in bioinorganic chemistry; namely, despite their importance, protons are notoriously difficult to track in biological systems. Common structural methods such as crystallography and EXAFS can only infer protonation state via metrics such as metal-ligand bond lengths. Vibrational techniques like resonance Raman and nuclear resonance vibrational spectroscopy, as well as electron paramagnetic resonance methods, can more directly probe protonation, but these require isotope substitution, accessible absorption features, and half-integer spin states, limiting their applications for enzyme systems.

Valence-to-core Kβ x-ray emission spectroscopy (VtC XES) provides a more general approach to assessing protonation states in metallocofactors.[9] In this element selective

technique, a high energy x-ray photon generates a 1s core hole on an absorbing metal atom. Following ionization, electrons from higher-lying orbitals fill the core hole, emitting x-ray fluorescence; when these electrons originate in ligand-localized valence orbitals (i.e. VtC transitions),[10] the resulting spectra are sensitive to the electronic structure of the ligands. The identity[11] and number of ligands,[12] the degree of activation of diatomic ligands,[13] and, in some cases, bond angles[14] can all be probed by VtC XES. Indeed, the sensitivity of VtC XES to ligand electronic structure is sufficient to identify ligand protonation events in small molecule systems, both theoretically[15] and experimentally.[16] To date, however, VtC XES has not been used to assess protonation changes throughout an enzyme reaction.

The challenges presented by tracking protons in metalloenzymes are compounded in systems with heterometallic cofactors—a category that includes the class I-c RNRs, photosystem II, MoFe and VFe nitrogenases, and NiFe hydrogenases. *In order to fully understand reactivity of heterometallic cofactors, knowledge of the chemistry occurring at all metal centers, during each reaction step, is required.* Studies of such systems using element-specific x-ray spectroscopies typically involve serial measurement of each metal, a strategy that can lead to errors from sample variability and difficulty in assessing photoreduction of all metal centers.[7e] Serial data collection also multiplies required collection time and sample quantity, a nontrivial consideration with enzyme intermediates. Ideally, data from all metals in a heterometallic cofactor should be collected simultaneously.

To this end, XES offers an opportunity: If all metals in a sample can be excited at a common incident energy (i.e. the absorption edges are similar in energy), all will generate x-ray emission that can be collected. Indeed, such “two-color” data collection has recently been

implemented.[17] This method reduces or eliminates the impact of sample inhomogeneity and radiation damage on the two spectra.

Herein, we investigate the protonation patterns of three oxidation states of the *Ct* RNR-β metallocofactor using the dual array valence emission spectrometer (DAVES) at CHESS C-line[17a] to collect Mn and Fe XES spectra simultaneously. *These data are, to our knowledge, the first VtC spectra of an enzyme intermediate and also the first two-color VtC to be reported.* Supported by DFT calculations, these data allow for assignment of protonation state in this challenging metalloenzyme system.

The Kβ mainline XES spectra (Fig. 1) arise from metal-centered 3p → 1s transitions and are sensitive to metal spin state and metal-ligand covalency.[18] For Mn, the *S*=5/2 Mn^{II} in **2/2** is clearly distinct from the *S*=3/2 Mn^{IV} in **4/4** and **4/3**. The Fe mainline spectra for **2/2** and **4/3**, on the other hand, are nearly identical despite differences in metal oxidation state; this similarity is well-known and arises because the increased covalency of Fe^{III} complexes relative to those of Fe^{II} cancels out the effect of increased spin state.[15b, 19] The *S*=2 Fe^{IV} in **4/4** is both more covalent and of lower spin; correspondingly, it shows a slight decrease in intensity of the low energy Kβ' line (Fig. 1, red).

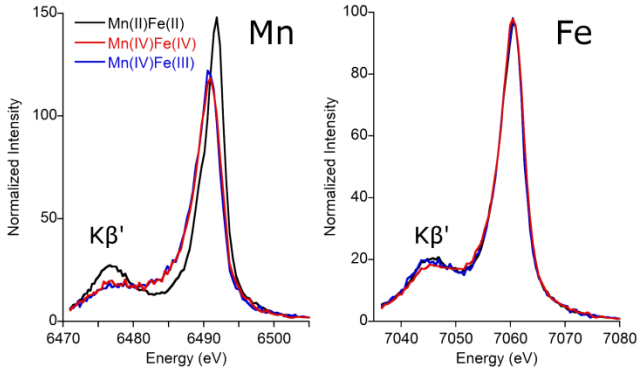

Figure 1. The Kβ mainline spectra for Mn (left) and Fe (right) in *Ct* RNR-β.

The VtC XES spectra (Fig. 2) are ~100x weaker than the Kβ mainlines and comprise two primary components: the lower-energy Kβ" region (orange fit) and the higher energy $K\beta_{2,5}$ region (blue fit). Kβ" features arise when electrons residing in ligand *n*s orbitals decay to the fill the metal 1s core hole. The $K\beta_{2,5}$ region, on the other hand, encompasses transitions arising from a mixture of ligand *n*s and *n*p orbitals and thus often requires a more complicated interpretation than the Kβ" peaks. Such an analysis can be challenging when the $K\beta_{2,5}$ transitions are poorly resolved from each other and when spectra have low signal-to-noise, as is the case here. As such, our analysis will focus on the Kβ" region, the intensity of which can be related to ligand protonation.

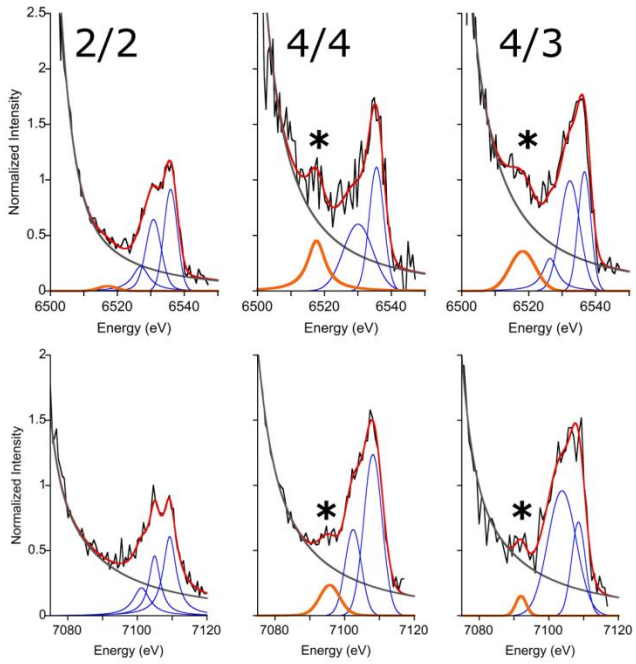

Figure 2. Representative fits to the VtC spectra for Mn (top) and Fe (bottom). In all panels: data (black), fit (red), background (grey), Kβ" (orange, also marked with *), and $K\beta_{2,5}$ peaks (blue).

The Kβ" intensity is governed by overlap between ligand 2s and the metal *n*p orbitals—larger overlap leads to greater intensity—resulting in the established exponential dependence of

Kβ" intensity on M-L bond length.[15b] Kβ" energy, meanwhile, is determined by donor 2s orbital ionization energy, with larger ionization energies yielding lower XES energies. In *Ct* RNR-β, the (hydr)oxo ligands in **4/4** and **4/3** exhibit significantly shorter M-L bonds than the rest of the ligands[7b, 7e] and therefore dominate the Kβ” region. Conversion from **4/4** to **4/3** is proposed to result in protonation of one oxo ligand in the di-μ-oxo core of **4/4** (Scheme 1), which should elongate the M-O bonds and delocalize O 2s character away from the metals; both effects would reduce metal *n*p overlap and thus reduce Kβ” intensity. As such, monitoring the Kβ” feature should allow an assessment of protonation during **4/4** to **4/3** conversion.

In order to quantify the intensity of the Kβ” feature, the VtC spectra were fit using a series of pseudo-Voigt functions; the reported values (Table 1) represent the average of statistically-equivalent, physically-reasonable fits. The declining background (Fig. 2, grey line) is the high energy tail from the fit to the Kβ mainline; because the mainlines are intense and well-resolved, errors resulting from the background are expected to be small. Additional support for these values and details of the data fitting and statistics are found in the Supporting Information.

Table 1. Numerical parameters for Mn and Fe VtC fits.[a]

Mn	VtC Area	Kβ” Area	Kβ” IWAE[b] (eV)
2/2	11.13 (11)	0.32 (1)	6517.1 (1)
4/4	17.58 (22)	4.81 (22)	6517.6 (1)
4/3	18.76 (38)	3.72 (37)	6518.2 (1)

Fe	VtC Area	Kβ” Area	Kβ” IWAE[a] (eV)
2/2	9.04 (90)	—	—
4/4	13.31 (1.70)	1.48 (76)	7095.3 (5)
4/3	13.92 (1.39)	0.58 (6)	7092.0 (1)

[a] Parenthetical values indicate uncertainty in final digits. [b] Intensity-weighted average energies.

The VtC spectra of **2/2** exhibit low total intensity and minimal Kβ” intensity for Mn and Fe (Fig. 2), as expected given the long M-L bonds of high-spin, divalent metal ions.[15b, 20] Upon conversion to **4/4**, the overall VtC intensities increase for both metals and Kβ” features become apparent in both spectra, consistent with the formation of oxo bridge(s). Subsequent reduction to **4/3** does not significantly impact the total VtC intensity for either metal but does modulate the Kβ” features. For Fe, the Kβ” is markedly diminished (by ~60%), likely due to the bond elongation associated with reduction from Fe^{IV} to Fe^{III}. Mn, on the other hand, shows a

comparatively modest decrease in Kβ" intensity (~25%). This observed reduction in Kβ" intensity suggests loss of an oxo bridge while the significant remaining intensity implies that **4/3** retains oxo ligation. The data, then, are consistent with the protonation patterns in Scheme 1; conversion of **4/4** to **4/3** results in protonation of one oxo bridge of the inorganic core, whereas the other remains intact.

Unfortunately, in the absence of detailed structural data, it is not possible to relate the magnitude of Kβ" intensity directly to the number of oxo ligands, as many other factors, including the M-O bond lengths and M-O-M bond angles, contribute to the Kβ" intensity.[14] Therefore, to interpret the experimental data more deeply, we calculated VtC spectra using DFT (Fig. 3). For both Mn and Fe, these methods have been shown to reliably reproduce experimental VtC data.[15b, 20] Previously reported models of the **2/2**, **4/4**, and **4/3** cofactors[21] were pared down to the first shell residues and geometry optimized with ORCA[22] (Fig. S6). In all cases, the obtained structures satisfactorily matched available metrical data (Table S2), and so the optimized models were used to calculate VtC spectra for all three species.

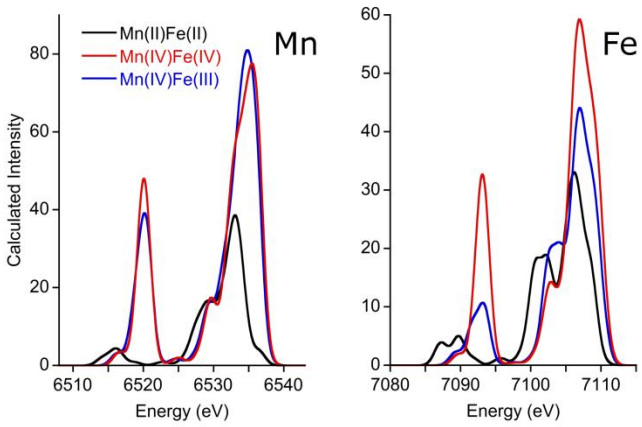

Figure 3. Calculated VtC spectra for Mn (left) and Fe (right) of **2/2**, **4/4**, and **4/3**. The calculated spectra have been broadened by 2 eV and shifted to align with experiment.

The calculated spectra generally reproduce the experimental findings, including the small reduction in Mn Kβ" intensity and the significant reduction in Fe Kβ" intensity seen for **4/3** relative to **4/4** (Fig. 3). Inspection of the optimized structures provides an immediate explanation for the Mn VtC experimental observations. On conversion of **4/4** to **4/3**, protonation of the oxo bridge results in significant (~0.12 Å) elongation of the corresponding Mn-O bond; concurrently, the extant Mn-O_{oxo} bond contracts by ~0.08 Å. This contraction of the already short Mn-O bond partially compensates for the Kβ" intensity lost upon protonation of the other oxo. Moreover, the terminal Mn-OH bond is quite short for both **4/4** and **4/3** (~1.82 Å), providing additional Kβ" intensity that further mitigates the diminution of this feature upon oxo protonation. Both of these structural elements—the short terminal Mn-OH bond and the Mn-O_{oxo} contraction in the **4/3**—have been seen in previous DFT calculations on *Ct* RNR-β.[7b, 21] The possibility of protonation occurring at the terminal Mn-bound OH was also explored and found to be inconsistent with the data (details in the Supporting Information). The calculated spectra for Fe are also consistent with experiment; specifically, an intense Kβ" peak calculated for **4/4** is predicted to become markedly less intense upon conversion to **4/3**, consistent with the loss of one oxo moiety and the generally longer bonds present for Fe^{III} compared to Fe^{IV}. We note that the calculations predict the overall Fe VtC intensity should be greater for **4/4** than for **4/3**, though the experimental areas are not statistically different. Higher quality data might permit this increase to be seen experimentally; it is also possible that the calculations systematically overestimate the intensity for Fe^{IV}, as very few experimental Fe^{IV} VtC spectra are available for comparison to computations.

In summary, the two-color VtC XES data have allowed the protonation patterns in the **4/4** and **4/3** states of *Ct* RNR-β to be assigned as $Mn^{IV}(\mu\text{-}O)_2Fe^{IV}$ and $Mn^{IV}(\mu\text{-}O)(\mu\text{-}OH)Fe^{III}$,

respectively. This study has the advantage over previous investigations of this system of probing the (hydr)oxo electronic structure and thus enabling a more direct assignment of the core protonation state. More generally, we demonstrate that, although experimentally challenging, the long-proposed application of VtC XES to enzyme intermediates is indeed feasible. For metalloenzyme intermediates with well-defined outstanding questions regarding active site structure–including such notable examples as methane monooxygenase intermediate Q and the S_2 and S_3 states of photosystem II–VtC XES investigation is thus established as a viable experimental approach.

References

[1] Lippard, S. J.; Berg, J. M., *Principles of Bioinorganic Chemistry*. University Science Books: Mill Valley, CA, 1994.

[2] Bollinger, J. M., Jr.; Chang, W.-c.; Matthews, M. L.; Martinie, R. J.; Boal, A. K.; Krebs, C., *2-Oxoglutarate-Dependent Oxygenases*. RSC Metallobiology; Royal Society of Chemistry: Cambridge, UK, 2015.

[3] Cotruvo, J. A., Jr.; Stubbe, J., *Annu. Rev. Biochem.* **2011,** *80*, 733-767.

[4] Stubbe, J.; Nocera, D. G.; Yee, C. S.; Chang, M. C. Y., *Chem. Rev.* **2003,** *103*, 2167-2202.

[5] a) Jiang, W.; Bollinger, J. M., Jr.; Krebs, C., *J. Am. Chem. Soc.* **2007,** *129*, 7504-7505; b) Jiang, W.; Yun, D.; Saleh, L.; Barr, E. W.; Xing, G.; Hoffart, L. M.; Maslak, M.-A.; Krebs, C.; Bollinger, J. M., Jr., *Science* **2007,** *316*, 1188-1191.

[6] a) Jiang, W.; Yun, D.; Saleh, L.; Bollinger, J. M., Jr.; Krebs, C., *Biochemistry* **2008,** *47*, 13736-13744; b) Jiang, W.; Hoffart, L. M.; Krebs, C.; Bollinger, J. M., Jr., *Biochemistry* **2007,** *46*, 8709-8716.

[7] a) Shu, L. J.; Nesheim, J. C.; Kauffmann, K.; Münck, E.; Lipscomb, J. D.; Que, L., Jr., *Science* **1997,** *275*, 515-518; b) Younker, J. M.; Krest, C. M.; Jiang, W.; Krebs, C.; Bollinger, J. M., Jr.; Green, M. T., *J. Am. Chem. Soc.* **2008,** *130*, 15022-15027; c) Banerjee, R.; Proshlyakov, Y.; Lipscomb, J. D.; Proshlyakov, D. A., *Nature* **2015,** *518*, 431-434; d) Doan, P. E.; Shanmugam, M.; Stubbe, J.; Hoffman, B. M., *J. Am. Chem. Soc.* **2015,** *137*, 15558-15566; e) Martinie, R. J.; Blaesi, E. J.; Krebs, C.; Bollinger, J. M., Jr.; Silakov, A.; Pollock, C. J., *J. Am. Chem. Soc.* **2017,** *139*, 1950-1957.

[8] Kwak, Y.; Jiang, W.; Dassama, L. M. K.; Park, K.; Bell, C. B.; Liu, L. V.; Wong, S. D.; Saito, M.; Kobayashi, Y.; Kitao, S.; Seto, M.; Yoda, Y.; Alp, E. E.; Zhao, J.; Bollinger, J. M., Jr.; Krebs, C.; Solomon, E. I., *J. Am. Chem. Soc.* **2013,** *135*, 17573-17584.

[9] Pollock, C. J.; DeBeer, S., *Acc. Chem. Res.* **2015,** *48*, 2967-2975.

[10] Glatzel, P.; Bergmann, U., *Coord. Chem. Rev.* **2005,** *249*, 65-95.

[11] a) Bergmann, U.; Horne, C. R.; Collins, T. J.; Workman, J. M.; Cramer, S. P., *Chem. Phys. Lett.* **1999,** *302*, 119-124; b) Lancaster, K. M.; Roemelt, M.; Ettenhuber, P.; Hu, Y.; Ribbe, M. W.; Neese, F.; Bergmann, U.; DeBeer, S., *Science* **2011,** *334*, 974-977; c) Pushkar, Y.; Long, X.; Glatzel, P.; Brudvig, G. W.; Dismukes, G. C.; Collins, T. J.; Yachandra, V. K.; Yano, J.; Bergmann, U., *Angew. Chem. Int. Ed.* **2010,** *49*, 800-803.

[12] Stieber, S. C. E.; Milsmann, C.; Hoyt, J. M.; Turner, Z. R.; Finkelstein, K. D.; Wieghardt, K.; DeBeer, S.; Chirik, P. J., *Inorg. Chem.* **2012,** *51*, 3770-3785.

[13] Pollock, C. J.; Grubel, K.; Holland, P. L.; DeBeer, S., *J. Am. Chem. Soc.* **2013,** *135*, 11803-11808.

[14] Pollock, C. J.; Lancaster, K. M.; Finkelstein, K. D.; DeBeer, S., *Inorg. Chem.* **2014,** *53*, 10378-10385.

[15] a) Smolentsev, G.; Soldatov, A. V.; Messinger, J.; Merz, K.; Weyhermuller, T.; Bergmann, U.; Pushkar, Y.; Yano, J.; Yachandra, V. K.; Glatzel, P., *J. Am. Chem. Soc.*

2009, *131*, 13161-13167; b) Lee, N.; Petrenko, T.; Bergmann, U.; Neese, F.; DeBeer, S., *J. Am. Chem. Soc.* **2010,** *132*, 9715-9727; c) Kropp, H.; King, A. E.; Khusniyarov, M. M.; Heinemann, F. W.; Lancaster, K. M.; DeBeer, S.; Bill, E.; Meyer, K., *J. Am. Chem. Soc.* **2012,** *134*, 15538-15544.

[16] a) Lassalle-Kaiser, B.; Boron, T. T.; Krewald, V.; Kern, J.; Beckwith, M. A.; Delgado-Jaime, M. U.; Schroeder, H.; Alonso-Mori, R.; Nordlund, D.; Weng, T.-C.; Sokaras, D.; Neese, F.; Bergmann, U.; Yachandra, V. K.; DeBeer, S.; Pecoraro, V. L.; Yano, J., *Inorg. Chem.* **2013,** *52*, 12915-12922; b) Mijovilovich, A.; Hamman, S.; Thomas, F.; de Groot, F. M. F.; Weckhuysen, B. M., *Phys Chem Chem Phys* **2011,** *13*, 5600-5604.

[17] a) Finkelstein, K. D.; Pollock, C. J.; Lyndaker, A.; Krawcyk, T.; Conrad, J., *AIP Conference Proceedings* **2016,** *1741*, 030009; b) Gul, S.; Ng, J. W. D.; Alonso-Mori, R.; Kern, J.; Sokaras, D.; Anzenberg, E.; Lassalle-Kaiser, B.; Gorlin, Y.; Weng, T.-C.; Zwart, P. H.; Zhang, J. Z.; Bergmann, U.; Yachandra, V. K.; Jaramillo, T. F.; Yano, J., *Phys Chem Chem Phys* **2015,** *17*, 8901-8912.

[18] a) Peng, G.; de Groot, F. M. F.; Hamalainen, K.; Moore, J. A.; Wang, X.; Grush, M. M.; Hastings, J. B.; Siddons, D. P.; Armstrong, W. H.; Mullins, O. C.; Cramer, S. P., *J. Am. Chem. Soc.* **1994,** *116*, 2914-2920; b) Pollock, C. J.; Delgado-Jaime, M. U.; Atanasov, M.; Neese, F.; DeBeer, S., *J. Am. Chem. Soc.* **2014,** *136*, 9453-9463.

[19] Gamblin, S. D.; Urch, D. S., *J. Electron Spectrosc. Relat. Phenom.* **2001,** *113*, 179-192.

[20] Beckwith, M. A.; Roemelt, M.; Collomb, M.-N. l.; DuBoc, C.; Weng, T.-C.; Bergmann, U.; Glatzel, P.; Neese, F.; DeBeer, S., *Inorg. Chem.* **2011,** *50*, 8397-8409.

[21] Han, W.-G.; Giammona, D. A.; Bashford, D.; Noodleman, L., *Inorg. Chem.* **2010,** *49*, 7266-7281.

[22] Neese, F., *Wiley Interdisciplinary Reviews: Computational Molecular Science* **2012,** *2*, 73-78.

Supporting Information

Experimental Procedures

Sample Preparation

Samples of the enzyme in various oxidation states were prepared as described previously.[1-3] In brief, apo-*Ct* RNR-β was reconstituted with aqueous solutions of Mn^{II} and $^{57}Fe^{II}$ in a N_2 atmosphere glovebox. Specifically, enzyme was added to an aqueous solution containing Mn^{II} and $^{57}Fe^{II}$ (0.75 equiv. each / β) followed by rapid pipetting to prevent precipitation. The enzyme was allowed to incubate in the presence of these metals for 30 minutes at 4 °C; at this point, samples of **2/2** were loaded into modified Mössbauer cells in which the face of the cell had been drilled out and covered in 38 μm Kapton tape and frozen on a cold block pre-chilled in liquid nitrogen.

For preparation of **4/4**, *Ct* RNR-β, Mn^{II}, Fe^{II}, and chlorite dismutase were mixed to final concentrations of 4.2 mM, 3.1 mM, 3.1 mM, and 25 μM, respectively in the absence of oxygen. This mixture was rapidly mixed at 5 °C in a 4:1 volumetric ratio with a 50 mM solution of sodium chlorite in 100 mM HEPES pH 7.6 (at 4 °C), 10% (v/v) glycerol (the same buffer used for *Ct* RNR-β). Following mixing, the sample was cryogenically quenched in liquid ethane after 230 ms. Liquid ethane was subsequently evaporated off under vacuum at temperatures below 130 K and samples were packed in modified Mössbauer cells; sample packing was performed at 77 K on an aluminum block immersed in liquid nitrogen. Following packing, samples were stored in liquid nitrogen.

For preparation of the **4/3** state, *Ct* RNR-β, Mn^{II}, and Fe^{II} were mixed to final concentrations of 1.6 mM, 1.2 mM, and 1.2 mM, respectively in the absence of oxygen. This mixture was removed from the anaerobic chamber, diluted by a factor of three with aerobic buffer, and allowed to react for 40 min. The resulting solution was dialyzed against 10 mM EDTA in buffer overnight, followed by two rounds of dialysis against buffer lacking EDTA. The resulting chelated **4/3** was concentrated in a 30 KDa cutoff filter and frozen in modified sample cells (described above).

Speciation of the samples was determined using Mössbauer spectroscopy as described previously.[3] Sample temperature was maintained at 4.2 K using a Janis SVT-400 variable-temperature cryostat. The external magnetic field (53 mT) was applied parallel to the γ beam. Subtraction of the appropriate reference spectra was conducted in WMOSS. For **4/3**, 50% of the iron present is in the form of **4/3**, while $Fe^{III}Fe^{III}$ and Fe^{III} constitute 40% and 10% of the Fe, respectively (Figure S1). For the samples enriched in **4/4**, 65% of the iron present is in the form of **4/4**. The remaining intensity is well accounted for with a reference spectrum of a sample quenched in an analogous manner to **4/4** (with the exception that 1.5 eq of iron and no manganese was used) where a mixture of $Fe^{IV}Fe^{III}$ and $Fe^{II}Fe^{II}$ is present (Figure S2).

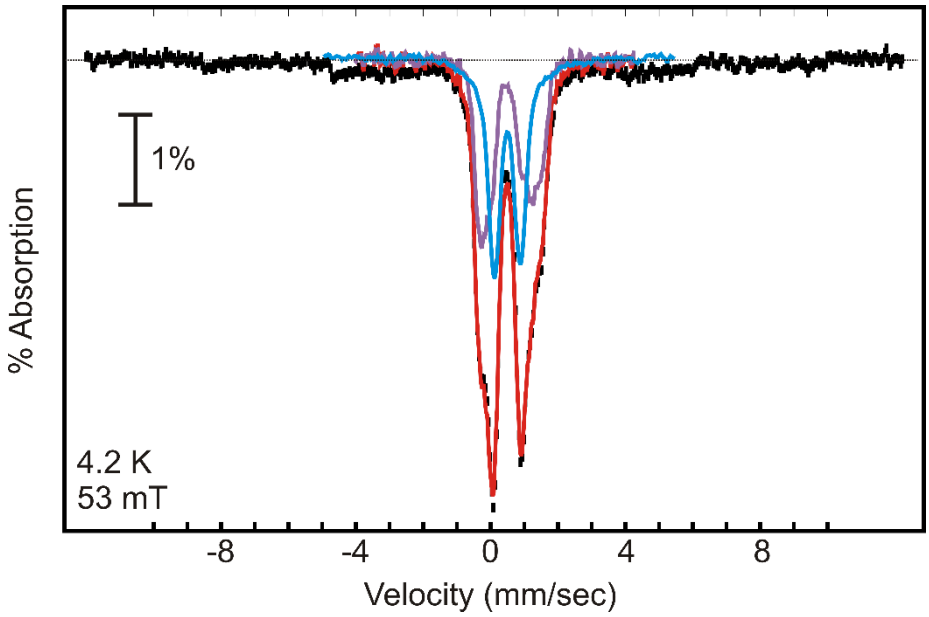

Figure S1. Mössbauer spectrum (black bars) of **4/3**, where the summation of component spectra, reference spectrum for **4/3**,[4] and reference spectrum for $Fe^{III}Fe^{III4}$ are shown as red, purple, and blue lines, respectively. An additional contribution from Fe^{III} may also be observed as a deviation in the baseline, though this species was not modelled and constitutes ~10% of the iron in the sample.

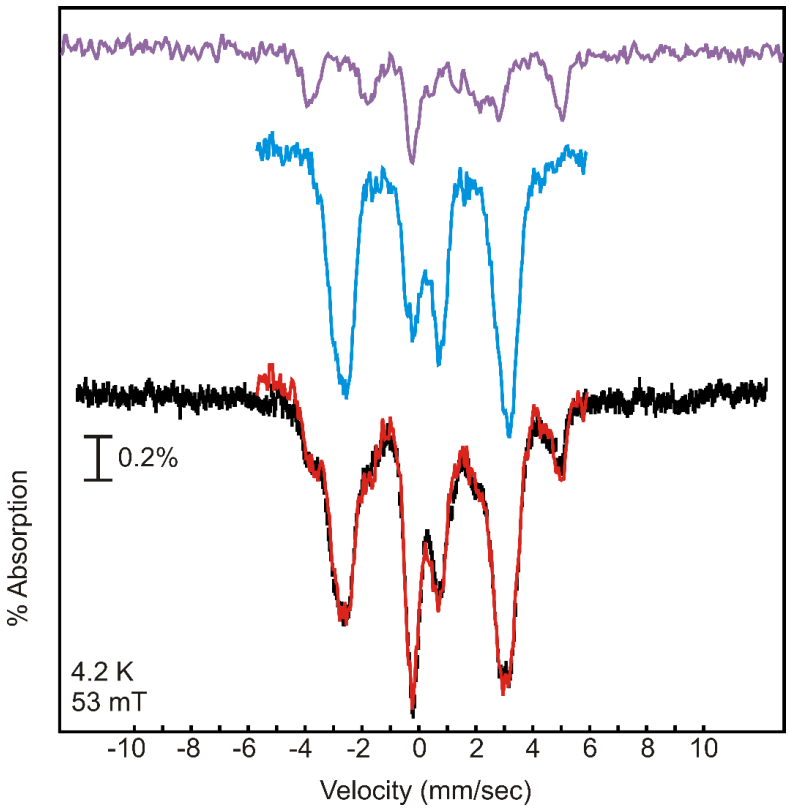

Figure S2. Mössbauer spectrum (black bars) of the sample of **4/4**, where the summation of component spectra, reference spectrum of an all-iron quenched control,[3] and reference spectrum of **4/4**[5] are shown in red, purple, and blue, respectively.

Data Collection

All data were collected at CHESS C-line under ring conditions of 5.3 GeV and ~110 mA. The energy of the incident beam was calibrated using the first inflection point of a Ni foil (8333.0 eV) and set to 8.0 keV using a Si(220) monochromator, providing ~$3x10^{11}$ photons / s in a ~1x1.25 mm spot on the sample, which was placed at 45° relative to the incident beam. A fast shutter upstream of the sample prevented sample exposure when data were not being collected. The samples were maintained <20 K using a He displex cryostat. Emitted photons were reflected using five spherically bent Si(440) and Ge(620) crystal analyzers (for Mn and Fe,

respectively) and the energy selected fluorescence from each metal was reflected onto a Pilatus 100K area detector (Dectris) with a low energy cutoff set to 3.5 keV. As much as possible, the entire flight path of the spectrometer passed through He-filled bags to prevent signal attenuation. A lead cone was placed over the window of each area detector to reduce the background intensity; for Fe the background count rate was reduced to <2 counts / s while for Mn it was <1 count / s. Intensities were extracted from the area detectors by setting a region of interest (ROI) rectangle around the reflected beam spot and integrating the intensity within this window; ROIs were set to be as small as possible without loss of signal. The background spectra were obtained by setting a second ROI of equal size and vertical position but offset in the horizontal direction by several pixels (Figure S3). Spectra for all species were collected using energy scans covering two different spectral regions: One for the mainline (Mn: 6471.0 – 6510.2 eV, 100 points; Fe: 7036.5 – 7088.5 eV, 100 points) and another for the VtC (Mn: 6503.1 – 6547.0 eV, 75 points; Fe: 7077.3 – 7119.6 eV, 75 points). The overlap between the two scans was used for splicing the scans together (*vide infra*).

Damage Assessment

In general, reduction of Mn^{IV} to Mn^{III}, Mn^{III} to Mn^{II}, and Fe^{IV} to Fe^{III} results in a characteristic shift to higher energy of the $K\beta_{1,3}$ emission line, thus allowing this feature to be used to monitor damage in these samples. Damage was assessed by collecting rapid (~10 s), sequential scans covering the maxima of the $K\beta_{1,3}$ lines for each metal. To improve signal-to-noise, this process was repeated on multiple sample spots and all first, second, third, etc scans were averaged. Exposure time was deemed acceptable until a shift in this line for either metal was observed. Emission scans were constructed such that the total accumulation time per spot

was less than that applied before damage was apparent. Note that the reduction of Fe^{III} to Fe^{II} is unlikely to result in a significant shift in the $K\beta_{1,3}$ line,[6] so for **4/3** the Mn spectrum alone was used to assess damage. The permissible dwell time for **4/3** was 125 s while for **4/4** it was 490 s.

Data Processing and Analysis

To obtain spectra for each metal, the first, second, third, etc. images from all emission scans were summed together using ImageJ to yield a single set of images corresponding to a sum of all scans (75 images for VtC spectra, 100 for mainlines). Any images affected by cosmic rays were removed prior to summing. Averaged mainline and VtC spectra were then spliced together to form a complete XES spectrum for each metal, with the overlapping region of the separate mainline and VtC spectra being used to ensure the proper relative intensities of each region prior to splicing; if needed, the VtC spectrum was multiplied by a scalar factor to align the two scans. The same procedure was followed for the background spectra. To avoid introducing additional noise into the spectra, a 20 point smoothing was applied to the background spectra and then these smoothed backgrounds were subtracted from the spliced, complete XES spectra to yield background-subtracted spectra. The energy axis was calibrated using standards of $KMnO_4$ and $(NH_4)_2Fe(SO_4)_2$. After calibration, the spectra were roughly normalized by setting the area under the curve to 1000. The spectra were then fit using BlueprintXAS.[7] After fitting, final normalizations were obtained by setting the sum of all fit peak areas to 1000 (the difference in spectral area between the rough and final normalizations was always less than 4%).

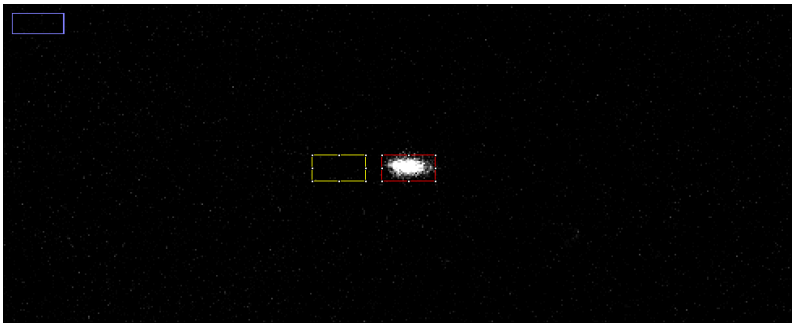

Figure S3. Example of a Pilatus image with data (red) and background (yellow) ROIs depicted.

Adjusting for Contaminating Species

The samples of both **4/4** and **4/3** each contained a mixture of species (Figures S1, S2). For some of these contaminants, they must be explicitly taken into account in order to properly analyze the XES data. Such is the case for **4/4**, where the sample contained 65% **4/4** and 35% each of Mn^{II} and $Fe^{IV}Fe^{III}$. Because Mn^{II} possesses markedly different mainline and VtC structure as compared to **4/4**, the contribution from Mn^{II} must be removed prior to analysis. To do so, 35% of the fit to the **2/2** spectrum was subtracted from the experimental **4/4** spectrum, yielding a spectrum of "pure" **4/4**. This subtracted spectrum was then renormalized to have an area under the curve of 1000 prior to fitting; all data presented are for the subtracted **4/4** spectrum. In contrast, for **4/3**, the Mn spectrum is not expected to have any contaminating species because Mn^{II} (either free or bound to the protein without Fe) does not react with O_2 and remains in the labile, divalent state throughout the reaction. It can thus be chelated from **4/3** during dialysis against EDTA and is not present in the final sample.

For the Fe spectra, the approach is simpler. First, the major Fe contaminants—$Fe^{IV}Fe^{III}$ in **4/4** and $Fe^{III}Fe^{III}$ in **4/3**—are expected, based on the available structural data, to have very similar VtC spectra to the species of interest (in contrast to the Mn^{II} in the **4/4** sample), so the presence

of these contaminants would not be expected to have nearly as dramatic an influence on the spectra as did the Mn^{II}. More pragmatically, absolute VtC intensity comparisons between the Fe spectra did not factor into our assignment of core structure, where the analysis focused simply on the presence of a Kβ" feature in **4/4** and its apparent absence in **4/3**. Because the subtraction of these contaminants is not expected to materially alter these observations, no subtractions were performed for Fe.

Calculations

All calculations were performed using ORCA 3.0.3.[8] Coordinates for **2/2**, **4/4**, **4/3**, and **4/3-H_2O** were obtained by truncating structures from a study by Noodleman and coworkers[9] to the first shell amino acid residues. Additionally, for **4/4** and **4/3**, the terminal H_2O on Mn was deprotonated to an OH^- to be in accordance with experimental observations.[3] Geometry optimizations were carried out using the BP86[10, 11] functional and def2-TZVP(-f) basis set[12] for all atoms except Fe, for which the expanded CP(PPP) basis set[13] was used. The charge on the models used was compensated by the continuum solvation model (COSMO)[14] with a dielectric constant of 4 while dispersion corrections were included using Grimme's method.[15] Relativistic effects were modeled using the zeroth order regular approximation (ZORA).[16] The broken symmetry formalism was used to account for the antiferromagnetic coupling between the metal ions. As the structures used here were greatly truncated from the original work, certain ligand hydrogen atoms (indicated with a * in the Coordinates section) were fixed in position during optimization to prevent excessive drifting of the amino acids. VtC XES spectra were calculated as described previously[17, 18] and the calculated spectra were shifted by scalar values (59.2 eV for Mn; 52.5 eV for Fe) to align with experiment.

Results and Discussion

Data Fitting

The relatively low signal-to-noise ratio of some of the Mn VtC spectra—particularly that for **4/4**—leads to the possibility that the noise exerts a non-trivial influence over the energy and intensity values obtained from the fits. To explore this possibility and to assess the robustness of the conclusions drawn from the fits, a 9-point smoothing was applied to all three Mn VtC spectra to reduce the high frequency noise while maintaining the broader spectral features. Such a procedure obviously risks obscuring sharper spectral features, though this is not expected to be a significant concern for the relatively broad peaks found in the Kβ" region. Additionally, while sharp features may be obscured, the overall spectral intensity should be maintained.

After smoothing, the spectra were fit in a manner identical to the unsmoothed data to assess the conclusions drawn. The fits to the smoothed data are shown in Figure S4 and the numerical parameters are displayed in Table S1.

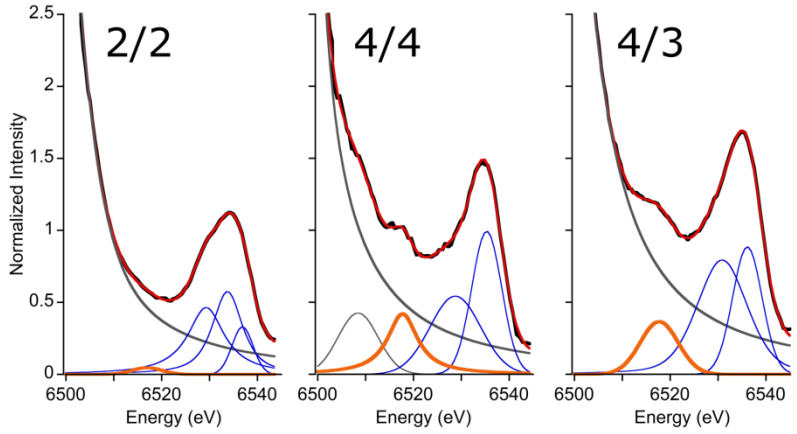

Figure S4. Fits to the Mn VtC data for **2/2**, **4/4**, and **4/3** after a 9-point smoothing has been applied to the data. For all spectra, data (black), background (grey), Kβ" (orange), and $K\beta_{2,5}$ peaks (blue) are shown.

Table S1. Fit parameters for 9-point smoothed Mn VtC data

	VtC Area	Kβ" Area	Kβ" IWAE[b] (eV)
2/2	14.23 (1.00)	0.61 (22)	6518.9 (1.4)
4/4	20.03 (21)	5.02 (16)	6517.8 (1)
4/3	23.79 (56)	3.55 (2)	6517.6 (1)

The reduced high frequency noise in the smoothed data allow the Kβ" features to be seen much more clearly than in the unsmoothed data. Importantly, the intensity trends (and to a lesser extent the absolute intensity values, as well) observed in the unsmoothed data are preserved in the smoothed data, with Kβ" intensity varying with **4/4** > **4/3** >> **2/2**. We attribute the variation in absolute intensities between the smoothed and unsmoothed data to the less well-defined backgrounds present for the smoothed data. This situation arises because, during smoothing, data points are lost at both ends of the spectrum, resulting in less data available to constrain the high

energy tail of the background. Nevertheless, even with this limitation, the trends are still clearly reproduced. Similar energies are also found for **4/4** and **4/3** while the low intensity of the Kβ" for **2/2** leads to a large uncertainty for this value in the smoothed data. The good agreement in intensities and energies seen between the original fits and the fits to the smoothed data—where the Kβ" peaks are easily seen—strongly supports the conclusions drawn in this study. Namely, the fits to the smoothed data reproduce the trends initially seen: A very weak Kβ" in **2/2** increases significantly in intensity on going to **4/4** and then modestly decreases upon reduction to **4/3**.

It is worth noting that, after smoothing, an additional apparent feature developed at the far low energy side (~6508 eV) of the VtC region for **4/4**. While VtC intensity on the low energy side of the Kβ" is not without precedent,[19] no feature has ever been observed at such low energies for Mn. Moreover, no peak at this energy can be discerned from the raw data, leading to the likely conclusion that this feature arises as an artifact of the smoothing process; as such, the intensity of this peak was not included in the VtC area reported in Table S1. In order to fully explore the possibility that this ~6508 eV peak is in fact present in the data, a fourth fit peak was added to the fit model for **4/4** and the fit was redone using the unsmoothed data (Figure S5). The addition of this peak to the unsmoothed data fit did not result in statistically improved fits; the –log(RMSE) values reported from BlueprintXAS are -0.39 for the three peak fit and -0.38 for the four peak fit. Furthermore, the change in intensity of the Kβ" peak resulting from inclusion of this fourth peak is not significant enough to affect our conclusions. Because no improvement in fit quality was observed, the inclusion of the fourth peak does not appreciably affect the Kβ"

intensity, and the presence of a peak at such low energy is unprecedented, the three peak fit was used for analysis while the four peak fit is reported here only for completeness.

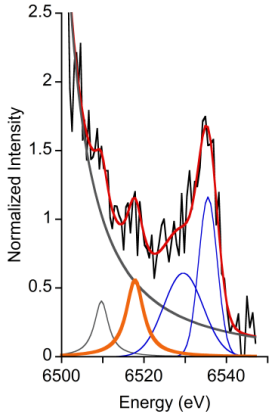

Figure S5. The four peak fit to the Mn VtC for **4/4**. No statistical improvement was seen over the three peak fit reported in the main text.

Two additional features of the fits warrant comment here, the first being the Kβ" lineshape. In both the raw and the smoothed data fits, for **4/4** the fit peak for this feature adopts a largely Lorentzian lineshape, while for **4/3** it is closer to a Gaussian. Such significantly different lineshapes would not generally be expected as these spectral features share a similar origin and were collected using identical optics. In our interpretation of these spectra, however, the Kβ" for **4/4** is dominated by contributions from the two oxo bridges, while for **4/3** a sizeable portion of the intensity gets redistributed to a hydroxo contribution at lower energies. Because the oxo and hydroxo components are not resolved, it is not surprising that a different lineshape is required to fit the Kβ" for **4/3** than is needed for the single component dominated Kβ" for **4/4**.

Lastly, we will comment on the statistics of the parameters presented in Table 1. During data fitting, many fits to the data are generated. After excluding any statistically poor and physically unreasonable fits (e.g. with linewidths below the core hole lifetime broadening), the parameters from all remaining fits are averaged together to get the intensity, energy, and standard deviation values reported in Table 1. In general, BlueprintXAS finds several distinct combinations of fit parameters—in other words, several different populations of fits—that all reproduce the experimental data equally well; in such cases, the standard deviations obtained reasonably capture the experimental uncertainty. At times, though, only a single population of acceptable fits is found, wherein the individual fit parameters vary little from fit to fit; in these instances, the standard deviations extracted are unreasonably small (e.g. <1%) and do not appear to reflect the actual experimental uncertainty. Given the signal-to-noise ratio of the data, we estimate a precision on the area determinations of around ±5% and in some cases possibly closer to ±10%. Thus, for the cases in which only a single population of fits could be found—the Fe spectra for **2/2** and **4/3** and the Mn Kβ" peak area for **4/3**—the standard deviation values reported in Table 1 were chosen at the conservative limits of ±10%.

Computations

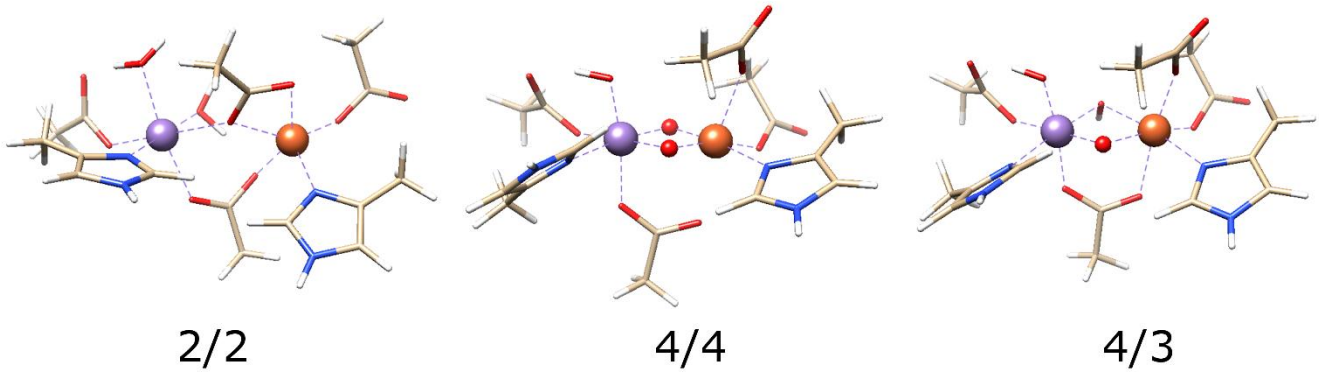

Figure S6. Geometry optimized models of the **2/2**, **4/4**, and **4/3** states of the *Ct* RNR-β cofactor.

To examine the possibility that the terminal Mn-bound OH rather than a bridging oxo is protonated in the conversion of **4/4** to **4/3** (yielding a terminal H_2O instead of μ-OH), we geometry optimized just such a model (**4/3-H_2O**) and computed its VtC spectrum (Fig. S7, S8). The calculated Kβ" intensity for **4/3-H_2O** is slightly *greater* than that for **4/4**, rendering this model inconsistent with the data. Thus, the experimental Kβ" spectra are entirely consistent with a di-μ-oxo $Mn^{IV}(O)_2Fe^{IV}$ core for **4/4** that becomes mono-protonated in **4/3** to form a $Mn^{IV}(O)(OH)Fe^{III}$ core.

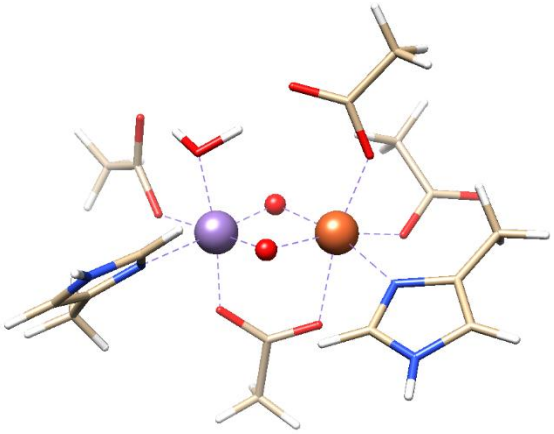

Figure S7. Geometry optimized model of **4/3-H_2O**.

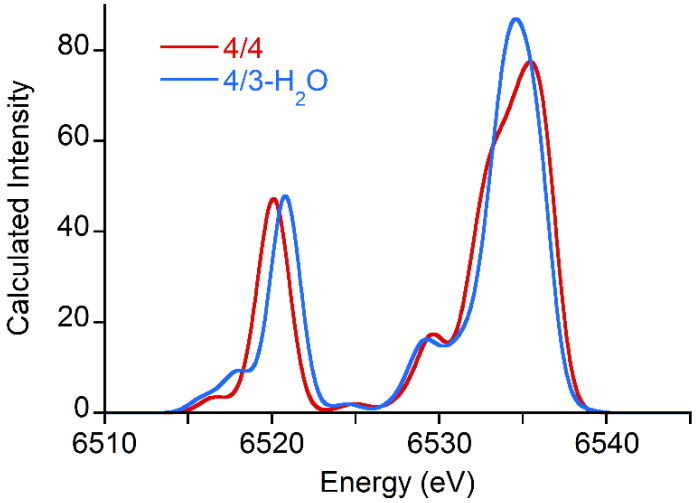

Figure S8. An overlay of the calculated Mn VtC XES spectra for **4/4** and **4/3-H_2O** shows that both species have approximately equal Kβ" intensities; thus, this protonation pattern is inconsistent with experiment.

Table S2. Comparison between experimental and calculated structural parameters for the *Ct* RNR-β models.[3, 20]

$Mn^{IV}Fe^{IV}$	Experiment	Calculation
Mn---Fe	2.74 – 2.75 Å	2.72 Å
Fe-O	1.81 Å	1.77 Å
Mn- - -H_{OH}	2.5 Å	2.3 Å

$Mn^{IV}Fe^{III}$	Experiment	Calculation
Mn---Fe	2.91 – 2.92 Å	2.88 Å
Mn-O_{oxo}	1.74 Å	1.75 Å

Coordinates

Optimized coordinates for **2/2**

Mn	-0.17172235144083	-0.03907133932665	-1.37645148188061
Fe	1.75619683919909	-3.42356200610624	-1.19880435461795
O	2.12653982042133	0.04586046881626	-1.77803590842452
O	0.25747668264865	1.09572353615552	0.48672282097805
C	0.06160220921487	4.01560586691447	-3.11441634796738
C	0.05869180259492	2.92905987384087	-2.05763757339959
O	-0.28686308974564	1.75898897187306	-2.44255761594356
O	0.37468324154305	3.23638564828911	-0.86781599236514
H	0.66821318157029	3.69481454718018	-3.97221121370091
C	0.37077070351194	-2.84459823054173	-4.86966350790302
C	0.60144676416581	-2.09841296031740	-3.57852203110871
O	-0.27811189823911	-1.29704686019893	-3.15629790326485
O	1.72420498761434	-2.31520067982311	-2.97337759719745
H	-0.66582325845526	-2.74465124045371	-5.20843305524425
C	4.60487530604233	-3.73808260651554	0.92145710602753
C	4.47856656791144	-4.46665010007789	-0.40452566256390
O	5.22478576432912	-5.39973096604764	-0.71141894210611
O	3.53663393970774	-4.02857391370956	-1.21730706268899
*H	5.43473142870339	-4.15091177447987	1.50851822372003
C	-0.44265248459918	-1.88209593657831	1.88408335693510
C	0.43212441666480	-2.49033017394948	0.82317971619393
O	0.37423555332589	-2.01828609983245	-0.39541533571709
O	1.19504972021181	-3.45704648017258	1.05456817624568
H	-1.41488727253838	-2.39859536146135	1.87485625763413
C	-3.11694963821868	2.18050804893169	-0.91362856629174
C	-3.32070901094632	0.71388450527751	-0.73041797318184
N	-2.30438969467770	-0.22841235455082	-0.89366682463814
C	-4.47902545053318	0.04555542196687	-0.39875423101698
C	-2.84456126568602	-1.42414723480196	-0.66703626249051
N	-4.15727869293711	-1.29883797935523	-0.36484520622527
*H	-4.04920730646619	2.73536163873451	-0.72436718458835
C	2.00699329927974	-6.94738340367138	-1.26219968780459
C	0.72196664234668	-6.34432408314143	-1.71606693357281
N	0.48196915040554	-4.96943604625251	-1.69861757647618
C	-0.40821476036066	-6.96954727503408	-2.19764756370725
C	-0.75880324266427	-4.78118527161879	-2.15428152953779
N	-1.32526839776891	-5.97270965664498	-2.46483114364535
*H	2.02252848093878	-8.02862919777902	-1.46449387660528
H	2.18048903824470	-0.83800006103617	-2.24600613795726
H	0.33947509972418	2.02969789614752	0.01110139529148
H	1.11431162746171	0.93647757951485	0.91840799086337
H	0.44597456496649	4.95983801808316	-2.71403785009465
H	-0.96463060620272	4.16525727931881	-3.48092556501531
H	0.63896219933725	-3.90171877494926	-4.74284453682335

H	1.04251247328579	-2.43078008439784	-5.63655737005578
H	3.66153893098359	-3.82145287258217	1.47971143227186
H	4.77757679113354	-2.66726718040300	0.73958302973779
H	-0.62315599662621	-0.81896621197907	1.68530150066749
H	0.00557505122727	-2.02568103316230	2.87366034948045
H	-2.31963242261696	-2.37164097830244	-0.70136827728615
H	-4.79203221920916	-2.05999162277573	-0.14710598571969
H	-5.48072877604181	0.40216165697751	-0.19043125800028
H	-2.78317201247847	2.39729994556159	-1.93776292640772
H	-2.34006205747342	2.56092816183486	-0.23490331796772
H	-1.24667639756904	-3.82312413418939	-2.29486789302687
H	-2.25701321493778	-6.10298661076314	-2.84396069399436
H	-0.63056219369113	-8.01633143081373	-2.36639083499411
H	2.15045164761848	-6.79731530858445	-0.18133064904932
H	2.86694830768060	-6.47999322701955	-1.76211270910390
H	2.73309180922189	-0.02521568658529	-1.02065308296054

Optimized coordinates for **4/3**

Fe	1.25263169118721	-2.65404419067677	-0.35642801416680
Mn	-0.61239676809589	-0.56627151565731	0.33891620787205
O	-0.55959496041816	-2.28419025098280	0.01456078059984
O	1.32087520090966	-0.65777751079329	0.35885605779869
O	-0.78354091491802	-0.79267762525174	2.13636464995320
C	-0.20307552221077	3.64378825887210	1.27817252383006
C	-0.62998108335137	2.20271970010810	1.51253425545367
O	-0.46291091362355	1.42288425424633	0.49441017432291
O	-1.08454776596455	1.86197399605103	2.62834409908137
H	0.88210067400055	3.71584792246705	1.44834874923083
C	-0.43122655725847	-0.48168941217815	-3.97375430300116
C	-0.04846268245105	-0.86215971436277	-2.55269701354871
O	-0.57393080610668	-0.13051451975520	-1.63608779890192
O	0.72398030836578	-1.84106356699295	-2.38333238077853
H	-0.48735148575206	0.60899608076040	-4.07843600052918
C	4.43362711053793	-1.84497610475490	0.74616288877096
C	4.28220995645653	-2.47803819645119	-0.62440191489893
O	5.26427741578342	-2.94931362331472	-1.22607085936446
O	3.07799016092458	-2.50678444753403	-1.12531690776821
*H	5.49248016457405	-1.75157939982737	1.00527457851869
C	-0.23792573473807	-4.14997584473979	2.35988904714176
C	1.26486742051670	-4.28612248292592	2.19955462914362
O	1.91487953109290	-5.08100545325785	2.89829202890158
O	1.84330944187540	-3.52718641354900	1.30352549230953
H	-0.50747038858521	-3.09101037782261	2.48892829715610
C	-3.26891148416150	1.80840786500339	-0.66703554067624
C	-3.60317929494978	0.42460909569554	-0.22568479788537
N	-2.66406055332194	-0.52549551206863	0.16619282931404

C	-4.85166981169324	-0.14756711595173	-0.10572717524696
C	-3.32163957968153	-1.62743009874633	0.51520857984550
N	-4.65021938945777	-1.43405602811225	0.36158871140710
*H	-4.16441764216317	2.31288589137821	-1.06113206259294
C	3.11901482051506	-5.74856750252457	-0.71462916134526
C	1.72116827742064	-5.73476070725110	-1.23448938291772
N	0.91284385517331	-4.60000974749012	-1.20565332059245
C	0.99191020243443	-6.75523608032344	-1.80594479243456
C	-0.26008479097912	-4.92526786962121	-1.73690135458260
N	-0.25087924896242	-6.22524995654129	-2.11497349807302
*H	3.56065895112354	-6.75533541981233	-0.77652923681848
H	-0.93911161565674	0.12648781685698	2.49334356623272
H	-0.70969676639162	4.31477229720507	1.98189844666697
H	-0.39899224957613	3.95034563388146	0.24301704177554
H	-1.43155714967478	-0.88927978008637	-4.18552169242652
H	0.28097959896230	-0.90101153842211	-4.69319732102031
H	3.91603331542065	-2.48270575664880	1.47741555283224
H	3.93554198961967	-0.86668342270611	0.77797022739668
H	-0.58200934866505	-4.75497571752663	3.20696165830947
H	-0.73540593594127	-4.47992340374770	1.43626877663051
H	-2.85299216655535	-2.54003544360651	0.86223074757123
H	-5.37018546796604	-2.11962748012964	0.56065794153109
H	-5.84048561135564	0.24641008335632	-0.30709367754711
H	-2.48110734738712	1.79120317438196	-1.43101054347647
H	-2.88907886531711	2.40373146756759	0.17389304597708
H	-1.10357618965903	-4.25318879605307	-1.84523523253632
H	-1.02188958854062	-6.72256664814108	-2.54670247277711
H	1.24242848396762	-7.78894231965262	-2.01247987303425
H	3.13513525000552	-5.41490981793902	0.33286431769237
H	3.75218986544912	-5.04864861556813	-1.27923385890497
H	1.65657489789268	-0.02101866834405	-0.29893388901448

Optimized coordinates for **4/4**

Fe	1.48649331085109	-2.32325034813808	-0.28969155747155
Mn	-0.52079340860597	-0.60439877124816	0.33447369788441
O	-0.26288353926341	-2.39404982000983	0.02518424721860
O	1.28885401551323	-0.61978077375688	0.14562616391831
O	-0.59048544949012	-0.81931820247085	2.14018813644304
C	-0.81984894726992	3.58253804761778	1.23581469563276
C	-1.03818977368880	2.09358138815443	1.44414099209674
O	-0.59683105340190	1.35392251657925	0.47239446211451
O	-1.58426599459633	1.67719375354145	2.48767056301325
H	0.19759111494252	3.83206381345256	1.57341530030976
C	-0.60431541161902	-0.36467529021896	-3.98663758325975
C	-0.17017233645681	-0.85318715640622	-2.61054923059384

O	-0.76801748215502	-0.25979520113600	-1.63397535738019
O	0.70584304059998	-1.74612928225848	-2.53439178982780
H	-1.70034062583646	-0.33825095429351	-4.05054625964228
C	4.34935845813354	-0.98986106411813	0.77764901104312
C	4.36559507263578	-1.66838340347142	-0.56957529824313
O	5.40239786731002	-1.80612528013997	-1.23074658437725
O	3.21793579047744	-2.12466381882627	-1.03501160368607
*H	5.37048245003588	-0.73184614779049	1.07191477782542
C	0.23421194212779	-4.09427394178071	2.45923865716733
C	1.74993507158797	-3.95892622066969	2.44304067472050
O	2.44208288860524	-4.58905754370603	3.27009970317026
O	2.28361550210194	-3.16835410570260	1.56320000216975
H	-0.22388841693790	-3.09625857110010	2.51967821686365
C	-3.54542463732930	1.31933870478110	-0.70820831764854
C	-3.67594195187482	-0.04023944389507	-0.11121229356263
N	-2.60136945687301	-0.80758361497655	0.32871008470859
C	-4.82971565506806	-0.75010128503673	0.14340789829431
C	-3.08929876762651	-1.93572079518186	0.83641358463172
N	-4.43698836812687	-1.93677911046780	0.73688639319131
*H	-4.51390196380038	1.66230260079572	-1.10372487463374
C	3.87215157254572	-5.06001840840007	-0.44663841492879
C	2.49005495829367	-5.28940167419304	-0.95624983857720
N	1.49408882226414	-4.31230601301887	-0.96946392214821
C	1.94486657546663	-6.43945307752137	-1.48383889913341
C	0.39446625988797	-4.85333238266862	-1.48500922354438
N	0.63128547940591	-6.14372961978628	-1.80911979545941
*H	4.44043507084370	-6.00159236946463	-0.40173551347542
H	-1.04150273485340	0.00830903893989	2.46829081540527
H	-1.53487414260091	4.16076844116177	1.83271785317946
H	-0.89508096165202	3.84874925133843	0.17445186335326
H	-0.19280563867653	-1.00692837147094	-4.77311760151612
H	-0.23847682225801	0.66238266528925	-4.13056360538867
H	3.88360339864588	-1.66136724407385	1.51288333198993
H	3.72214516535396	-0.08836090419782	0.72829640079028
H	-0.07755573539901	-4.72226034945955	3.30251751792179
H	-0.11006214365337	-4.54037132401845	1.51533243030325
H	-2.49379932792770	-2.73250127140187	1.26527375737217
H	-5.04947202037379	-2.68077737147370	1.05229945293288
H	-5.87093237716525	-0.51169284342645	-0.03720844856072
H	-2.79057310164844	1.32050781859661	-1.50492578779605
H	-3.22184252691309	2.04545239004268	0.05038049849578
H	-0.54914326333731	-4.33729500641660	-1.61479161840229
H	-0.04179705066380	-6.78211106541714	-2.21815826025104
H	2.37034380637914	-7.42225679797368	-1.64672717879671
H	3.82884269298445	-4.61127091015912	0.55585022052035
H	4.41281736799179	-4.35446427552922	-1.09297080277663

Optimized coordinates for **4/3-H_2O**

Fe	1.45281699886075	-2.41660600948799	-0.39524412927984
Mn	-0.35804332211375	-0.46909425374150	0.15820476172712
O	-0.45240011440693	-2.22112380852761	0.03682763138882
O	1.39799320600106	-0.56372244374412	0.07255701324963
O	-0.37316510783878	-0.58345781534138	2.14186678946378
C	0.18256864770922	3.78600975337689	1.01018836480207
C	-0.02783763388010	2.31167547125637	1.31100031893915
O	-0.32784358642532	1.57758976710453	0.30277755286162
O	0.11975898677609	1.90605791424921	2.49763978297602
H	1.22175855838390	3.92472024326508	0.67469936686613
C	-0.34662178410037	-0.41909287025852	-4.08597755094221
C	-0.01208935996735	-0.86586123627787	-2.67300029499093
O	-0.59686458878619	-0.17310838049392	-1.75131154335502
O	0.78477689992288	-1.81619363473969	-2.50715391025062
H	-1.41158832627193	-0.16822877036312	-4.17122570841540
C	4.70208138411154	-1.40731299316905	0.32500403346108
C	4.47384388534258	-2.43864425250760	-0.77582860040331
O	5.43781159549460	-3.10804106278183	-1.19810014975909
O	3.27536793107683	-2.53555205130678	-1.26540570393677
*H	5.49248015975616	-1.75157940125091	1.00527457667581
C	3.17562329655603	-3.76329588861325	3.39143148916552
C	2.18555122659615	-2.97276718068482	2.54627556975844
O	1.48653444428761	-2.08816542314792	3.10479135129176
O	2.16583885027498	-3.29537289548303	1.30699785302743
H	3.00809294429323	-4.84005367658002	3.25097798096353
C	-3.23300452818982	1.74187393090435	-0.91961282442832
C	-3.48652124343720	0.52618777039487	-0.09441521184460
N	-2.48838860540399	-0.35025569926466	0.32059514657530
C	-4.69293616190479	0.05287090405832	0.37618557994506
C	-3.07298801802967	-1.31976634475363	1.01611299882008
N	-4.40877827222044	-1.11039369334895	1.07186641399130
*H	-4.16441765261404	2.31288590733092	-1.06113206252252
C	3.17634998501910	-5.72594151268807	-0.71021993333583
C	1.76626875061226	-5.64943544343207	-1.18777925643420
N	1.01229646377777	-4.48351296711365	-1.11693179624449
C	0.97953961352948	-6.63648688069452	-1.74459332720562
C	-0.18865649193923	-4.75486744317021	-1.61108943678840
N	-0.25015860418513	-6.05120955859711	-2.00539776466990
*H	3.56065896639229	-6.75533543434151	-0.77652923504602
H	-0.12134671591837	0.37558022959033	2.42145376422119
H	0.02475878679900	4.39303042615821	1.90951145551219

H	-0.47653272008475	4.11973096788214	0.19883776984870
H	-0.07647224693178	-1.19912058851829	-4.80634060001875
H	0.23157340966720	0.48892264085012	-4.31299083492634
H	3.78072088983204	-1.17968723762515	0.87269159467455
H	5.04700465145526	-0.47431860924145	-0.14784923794870
H	3.08818566959333	-3.50473092912954	4.45270339784599
H	4.19491280512404	-3.54509073914383	3.04151421675115
H	-2.55144135963427	-2.15606480171937	1.46560754434204
H	-5.07907247840205	-1.70147257791341	1.55063583409178
H	-5.70244418515153	0.43371484148111	0.27611482760362
H	-2.82474183807768	1.46473313919593	-1.90217443773791
H	-2.48052551440656	2.38154639101356	-0.44109082310527
H	-1.00611539732050	-4.04560881015718	-1.67386606964861
H	-1.05531427334078	-6.50951676759133	-2.41718659239192
H	1.18019640144170	-7.67698060166312	-1.97230520859510
H	3.23814055397284	-5.37821819943740	0.33084188449397
H	3.82760345820017	-5.05618929588711	-1.29147784903532
H	0.39737140732908	-1.20469036256087	2.42452878106910

References

1. Jiang, W.; Yun, D.; Saleh, L.; Barr, E. W.; Xing, G.; Hoffart, L. M.; Maslak, M.-A.; Krebs, C.; Bollinger, J. M., Jr., *Science* **2007,** *316*, 1188-1191.
2. Dassama, L. M. K.; Yosca, T. H.; Conner, D. A.; Lee, M. H.; Blanc, B.; Streit, B. R.; Green, M. T.; DuBois, J. L.; Krebs, C.; Bollinger, J. M., Jr., *Biochemistry* **2012,** *51*, 1607-1616.
3. Martinie, R. J.; Blaesi, E. J.; Krebs, C.; Bollinger, J. M.; Silakov, A.; Pollock, C. J., *J. Am. Chem. Soc.* **2017,** *139*, 1950-1957.
4. Dassama, L. M. K.; Boal, A. K.; Krebs, C.; Rosenzweig, A. C.; Bollinger, J. M., Jr., *J. Am. Chem. Soc.* **2012,** *134*, 2520-2523.
5. Jiang, W.; Hoffart, L. M.; Krebs, C.; Bollinger, J. M., *Biochemistry* **2007,** *46*, 8709-8716.
6. Gamblin, S. D.; Urch, D. S., *J. Electron Spectrosc. Relat. Phenom.* **2001,** *113*, 179-192.
7. Delgado-Jaime, M. U.; Mewis, C. P.; Kennepohl, P., *J. Synchrotron Radiat.* **2010,** *17*, 132-137.
8. Neese, F., *Wiley Interdisciplinary Reviews: Computational Molecular Science* **2012,** *2*, 73-78.
9. Han, W.-G.; Giammona, D. A.; Bashford, D.; Noodleman, L., *Inorg. Chem.* **2010,** *49*, 7266-7281.
10. Becke, A. D., *Phys. Rev. A.* **1988,** *38*, 3098.
11. Perdew, J. P., *Phys. Rev. B.* **1986,** *33*, 8822.
12. Pantazis, D. A.; Chen, X. Y.; Landis, C. R.; Neese, F., *J Chem Theory Comput* **2008,** *4*, 908-919.
13. Neese, F., *Inorg. Chim. Acta* **2002,** *337C*, 181.
14. Klamt, A.; Schüürmann, G., *J. Chem. Soc. Perkin. Trans.* **1993,** *2*, 799-805.
15. Grimme, S.; Antony, J.; Ehrlich, S.; Krieg, H., *J. Chem. Phys.* **2010,** *132*, 154104.
16. van Lenthe, E.; van der Avoird, A.; Wormer, P. E. S., *J. Chem. Phys.* **1998,** *108*, 478.
17. Lee, N.; Petrenko, T.; Bergmann, U.; Neese, F.; DeBeer, S., *J. Am. Chem. Soc.* **2010,** *132*, 9715-9727.
18. Beckwith, M. A.; Roemelt, M.; Collomb, M.-N. l.; DuBoc, C.; Weng, T.-C.; Bergmann, U.; Glatzel, P.; Neese, F.; DeBeer, S., *Inorg. Chem.* **2011,** *50*, 8397-8409.
19. Pollock, C. J.; DeBeer, S., *Acc. Chem. Res.* **2015,** *48*, 2967-2975.
20. Younker, J. M.; Krest, C. M.; Jiang, W.; Krebs, C.; Bollinger, J. M., Jr.; Green, M. T., *J. Am. Chem. Soc.* **2008,** *130*, 15022-15027.

VITA - Ryan J. Martinie

Education

The Pennsylvania State University – University Park, PA 2013-2018
Ph.D. in Chemistry
Advisors: Prof. J. Martin Bollinger, Jr. and Prof. Carsten Krebs

Calvin College – Grand Rapids, MI 2009-2013
Bachelor of Science with Honors in Biochemistry (ACS) and Biology
Advisors: Prof. David E. Benson and Prof. Roger L. DeKock

Publications

13. Prakash, D.; Walters, K. A.; **Martinie, R. J.**; McCarver, A. C.; Lessner, D. J.; Krebs, C.; Golbeck, J. H.; Ferry, J. G. *J. Biol. Chem*. **2018**, *293*, 9198-9209.
12. Dunham, N. P.; Chang, W.-c.; Mitchell, A. J.; **Martinie, R. J.**; Zhang, B.; Bergman, J. A.; Rajakovich, L. J.; Wang, B.; Silakov, A.; Krebs, C.; Boal, A. K.; Bollinger, J. M., Jr. *J. Am. Chem. Soc.* **2018**, *140*, 7116-7126.
11. Kenney, G. E.; Dassama, L. M. K.; Pandelia, M-E.; Gizzi, A. S.; **Martinie, R. J.**; Gao, P.; DeHart, C. J.; Schachner, L. F.; Skinner, O. S.; Ro, S. Y.; Zhu, X.; Sadek, M.; Thomas, P. M.; Almo, S. C.; Bollinger, J. M., Jr.; Krebs, C; Kelleher, N. L.; Rosenzweig, A. C. *Science* **2018**, *359*, 1411–1416.
10. **Martinie, R. J.**; Pollock, C. J.; Matthews, M. L.; Bollinger, J. M., Jr.; Krebs, C.; Silakov, A. *Inorg. Chem.* **2017**, *56*, 13382–13389. Selected for cover image.
9. Mitchell, A. J.; Dunham, N. P.; **Martinie, R. J.**; Bergman, J. A.; Pollock, C. J.; Hu, K.; Allen, B. D.; Chang, W.-c.; Silakov, A.; Bollinger, J. M., Jr.; Krebs, C.; Boal, A. K. *J. Am. Chem. Soc.* **2017**, *139*, 13830–13836.
8. Tanner, A. W.; Carabetta, V. J.; **Martinie, R. J.**; Mashruwala, A. A.; Boyd, J. M.; Krebs, C.; Dubnau, D. *Mol. Microbiol.* **2017**, *104*, 837–850.
7. **Martinie, R. J.**; Blaesi, E. J.; Krebs, C.; Bollinger, J. M., Jr.; Silakov, A.; Pollock, C. J. *J. Am. Chem. Soc.* **2017**, 139, 1950-1957.
6. Livada, J.;* **Martinie, R. J.**;* Green, M. T.; Krebs, C.; Bollinger, J. M., Jr.; Silakov, A. *J. Phys. Chem. B* **2015**, *119*, 13777–13784. *Indicates equal contributions.
5. **Martinie, R. J.**; Livada, J.; Chang, W.; Green, M. T.; Krebs, C.; Bollinger, J. M., Jr.; Silakov, A. *J. Am. Chem. Soc.* **2015**, *137*, 6912–6919. Featured as a JACS Spotlight.
4. Bollinger, J. M., Jr.; Chang, W.; Matthews, M. L.; **Martinie, R. J.**; Boal, A. K.; Krebs, C. In *2-Oxoglutarate-Dependent Oxygenases*; Hausinger, R. P., Schofield, C. J., Eds.; RSC Metallobiology; Royal Society of Chemistry, 2015.
3. **Martinie, R. J.**; Godakumbura, P. I.; Porter, E. G.; Divakaran, A.; Burkhart, B. J.; Wertz, J. T.; Benson, D. E. *Metallomics* **2012**, *4*, 1037-1042. Selected for cover image.
2. **Martinie, R. J.**; Burkhart, B. J.; DeKock, R. L. *Organometallics* **2011**, *30*, 5196-5201.
1. **Martinie, R. J.**; Bultema, J. J.; Vander Wal, M. N.; Burkhart, B. J.; Vander Griend, D. A.; DeKock, R. L. *J. Chem. Educ.* **2011**, *88*, 1094–1097.

Academic Awards

Dr. John Randall Shuman Troxell Memorial Scholarship in Chemistry, 2017-2018
Pela Fay Braucher Scholarship, 2015-2016
National Science Foundation Graduate Research Fellowship, 2014
Nellie H. and Oscar L. Roberts Scholarship, 2014-2015
Schriesheim Distinguished Graduate Fellow, 2013-2014
Robert J. Albers Outstanding Senior in Biochemistry, 2013
Goldwater Scholar, 2012
Goldwater Scholar Honorable Mention, 2011
Integrated Science Research Institute Fellow, 2010-2011
National Merit Scholar, 2009